Applying novel methods to analyze structure, dynamics and intermediates of β-lactamases opening new routes for drug discovery

An der Universität Hamburg eingereichte

Dissertation

zur Erlangung des Doktorgrades der Naturwissenschaften (Dr. rer. nat.)

an der Fakultät für Mathematik, Informatik und Naturwissenschaften der

Universität Hamburg

Fachbereich Chemie

vorgelegt von

Andreas Prester

Hamburg, 2023

Die vorliegende Arbeit wurde im Zeitraum von Mai 2018 bis Dezember 2022 in der Arbeitsgruppe von Prof. Dr. med. Holger Rohde im Institut für Medizinische Mikrobiologie, Virologie und Hygiene am Universitätsklinikum Hamburg-Eppendorf und in der Arbeitsgruppe von Prof. Dr. rer. nat. Dr. Sc. Christian Betzel im Laboratorium für Strukturbiologie von Infektion und Entzündung am Institut für Biochemie und Molekularbiologie des Fachbereichs Chemie der Universität Hamburg durchgeführt.

Gutachter

1. **Prof. Dr. Dr. Christian Betzel**
2. **Prof. Dr. Holger Rohde**
3. **Prof. Dr. Thilo Stehle**

Prüfungskommission

1. **Prof. Dr. Dr. Christian Betzel**
2. **Prof. Dr. Ralph Holl**
3. **Dr. Thomas Hackl**

Datum der Disputation: **08.12.2023**

Publications

Perbandt, M., Werner, N., **Prester, A.**, Rohde, H., Aepfelbacher, M., Hinrichs, W. & Betzel, C. (2022). Structural basis to repurpose boron-based proteasome inhibitors Bortezomib and Ixazomib as β-lactamase inhibitors. *Scientific reports*, *12*(1), 1-12.

Zielinski, K. A.*, **Prester, A.***, Andaleeb, H.*, Bui, S., Yefanov, O., Catapano, L., Henkel, A., Wiedorn , M.O., Lorbeer, O., Crosas, E., Meyer, J., Mariani, V., Domaracky, M., White, T.A., Fleckenstein, H., Sarrou, I., Werner, N., Betzel, C., Rohde, H., Aepfelbacher, M., Chapman, H.N., Perbandt, M., Steiner, R.A. & Oberthuer, D. (2022). Rapid and efficient room-temperature serial synchrotron crystallography using the CFEL TapeDrive. *IUCrJ*, 9(6), 778-791.

Mehrabi, P., Sung, S., von Stetten, D., **Prester, A.**, Hatton, C. E., Kleine-Doepke, S., Berkes, A., Gore, G., Leimkohl, J., Schikora, H., Kollewe, M., Rohde, H., Wilmanns, M., Tellkamp, F. & Schulz, E. C. (2023). Millisecond cryo-trapping by the spitrobot crystal plunger simplifies time-resolved crystallography. *Nature Communications* 14, 2365.

Prester, A., Perbandt, M., Galchenkova, M., Oberthuer, D., Werner, N., Henkel, A., Maracke, J., Yefanov, O., Hakanpää, J., Pompidor, G., Meyer J., Chapman, H.N., Aepfelbacher, M., Hinrichs, W., Rohde, H. & Betzel, C. (2023). Time-resolved crystallography of boric acid binding to the active site serine of the β-lactamase CTX-M-14 and subsequent 1,2-diol esterification. *PREPRINT (Version 1) Research Square,* (Manuscript submitted for publication, under review)

*shared first authorship

Table of contents

List of abbreviations

°C	degree Celsius
Å	Ångström
APS	ammonium persulfate
AU	absorption units
BA	boric acid
BAB	boric acid bound
bp	base pair
BSA	bovine serum albumin
c	concentration
$CaCl_2$	calcium chloride
CAZ	ceftazidime
CC	correlation coefficient
CFEL	Centre for Free-Electron Laser Science
CRE	carbapenemase-producing Enterobacteriaceae
cryoMX	cryo macromolecular crystallography
CTX	cefotaxime
CTX-M	cefotaximase, β-lactamase
CV	column volume
D	diffusion constant
Da	Dalton
DBO	diazabicyclooctane
DESY	Deutsches Elektronen Synchrotron
ddH_2O	double-distilled water
DLS	dynamic light scattering
DNA	deoxyribonucleic acid
DTT	dithiothreitol; (2S,3S)-1,4-disulfanyl-2,3-butanediol
E. coli	*Escherichia coli*
EDTA	ethylenediaminetetraacetic acid
EMBL	European Molecular Biology Laboratory
ε	molar extinction coefficient

ESBL	extended-spectrum β-Lactamase
et *al*.	et *alii*/et *aliae*
η	greek letter eta, dynamic viscosity
g	gram
GBE	glycerol – boric acid ester
GHS	Global Harmonized System of Classification and Labelling of Chemicals
GOL	glycerol
h	hour
HCl	hydrochloric acid
IC_{50}	50 % inhibitory concentration
IEX	ion exchange chromatography
IPTG	isopropyl β-d-1-thiogalactopyranoside
k	kilo
K	kelvin
k_B	Boltzmann constant
k_{cat}	turnover rate
kDa	kilodalton
K_2HPO_4	dipotassium hydrogen phosphate
KH_2PO_4	potassium dihydrogen phosphate
K_m	Michaelis-Menten constant
KPC	*Klebsiella pneumoniae* carbapenemase
K. pneumoniae	*Klebsiella pneumoniae*
l	liter
LB medium	lysogeny broth medium
Li_2SO_4	lithium sulfate
m	meter
M	molar (mol/l)
MBL	metallo-β-lactamase
MDR	multi-drug resistance
MES	2-(N-morpholino)ethane sulfonic acid
$MgCl_2$	magnesium chloride
$MgSO_4$	magnesium sulfate

ml	milliliter
mol	mole
min	minute
MISC	mix-and-inject serial crystallography
MRSA	methicillin-resistant *Staphylococcus aureus*
ms	millisecond
MW	molecular weight
MWCO	molecular weight cut-off
NaCl	sodium chloride
NaOAc	sodium acetate
NaOH	sodium hydroxide
Na_2HPO_4	sodium phosphate dibasic
NaH_2PO_4	sodium dihydrogen phosphate
NDM	New Delhi metallo-β-lactamase
nm	nanometer
OD_{600}	optical density at 600 nM wavelength
OXA	oxacillinase, β-lactamase
PAGE	polyacrylamide gel electrophoresis
PBP	penicillin-binding protein
PBS	phosphate buffered saline
PCR	polymerase chain reaction
PDB	Protein Data Bank
PEG	polyethylene glycol
pH	*potentia hydrogenii*
R_H	hydrodynamic radius
RMS	root mean square
RMSD	root mean square deviation
RNA	ribonucleic acid
rpm	rounds per minute
RT	room temperature
s	second
SAD	single-wavelength anomalous dispersion

S. aureus	*Staphylococcus aureus*
SAXS	small-angle X-ray scattering
SBL	serine β-lactamase
SDS	sodium dodecyl sulfate
SEC	size-exclusion chromatography
SFX	serial femtosecond crystallography
SO4	sulfate
spp.	*species pluralis*
SSX	serial synchrotron crystallography
T	temperature
TB	terrific broth medium
TEMED	N,N,N',N'-tetramethylethane-1,2-diamine
Tris	tris(hydroxymethyl)aminomethane
TRX	time-resolved crystallography
UHH	Universität Hamburg
UKE	Universitätsklinikum Hamburg-Eppendorf
UV	ultraviolet
V	volt
VRE	vancomycin-resistant *enterococci*
v/v	volume per volume
w/v	weight per volume
wat	water molecule
WHO	World Health Organization
XFEL	*X-ray free electron laser*
x g	relative centrifugal force (rcf), multiples of g (9.81 m/s^2)
α	alpha
β	beta
γ	gamma
ε	epsilon
μ	micro
Ω	Omega
σ	sigma

One letter Code	Three letter Code	Amino acid
A	Ala	alanine
C	Cys	cysteine
D	Asp	aspartate
E	Glu	glutamate
F	Phe	phenylalanine
G	Gly	glycine
H	His	histidine
I	Ile	isoleucine
K	Lys	lysine
L	Leu	leucine
M	Met	methionine
N	Asn	asparagine
P	Pro	proline
Q	Gln	glutamine
R	Arg	arginine
S	Ser	serine
T	Thr	threonine
V	Val	valine
W	Trp	tryptophan
Y	Tyr	tyrosine

Abbreviation	Base
A	adenine
C	cytosine
G	guanine
U	uracil
T	thymine

Zusammenfassung

Das Auftreten und die Verbreitung von Antibiotikaresistenzen stellen eine wachsende Bedrohung für die Gesundheit der Menschen dar. Besonders besorgniserregend ist die Produktion von β-Laktamasen vor allem durch gramnegative Bakterien, da diese Enzyme die Fähigkeit haben, die wichtigste Klasse von Antibiotika, die β-Laktame, zu hydrolysieren und zu inaktivieren. Trotz jahrelanger umfangreicher β-Laktamase-Forschung bleiben einige Aspekte umstritten, besonders der Reaktionsmechanismus und welche Aminosäurereste tatsächlich an dem Acylierungsmechanismus zur Bildung des Acyl-Enzym-Zwischenprodukts beteiligt sind.

Gleichzeitig gab es bemerkenswerte Fortschritte auf dem Gebiet der zeitaufgelösten seriellen Kristallographie (TRX), die die Beobachtung molekularer Prozesse mit atomarer Auflösung und in Zeiträumen von Millisekunden ermöglicht. Diese Arbeit beschreibt einen Ansatz zur Aufklärung der Katalyse- und Hemmungsmechanismen der Klasse A β-Laktamase mit erweitertem Spektrum CTX-M-14 aus *Klebsiella pneumoniae* durch die Anwendung neuartiger zeitaufgelöster kristallographischer Methoden. Dabei wurden ihre Struktur, Dynamik und Zwischenprodukte im Komplex mit Substraten, Inhibitoren und Inhibitormodellen bestimmt.

Zunächst wurden Vorversuche durchgeführt, um optimale Bedingungen für die zeitaufgelöste Kristallographie zu ermitteln. Dazu gehörten die Optimierung der Proteinexpression und -reinigung, die Herstellung von Mikrokristallen mit der für die verschiedenen Methoden geeigneten Größe und die Bestimmung der kinetischen Parameter des Enzyms. Außerdem musste das am besten geeignete Substrat und die besten Umgebungsbedingungen gefunden und ein geeigneter Zeitrahmen für TRX-Experimente abgeschätzt werden. Eine Verringerung des pH-Wertes von 7.4 auf 3 führte zu einer Abnahme der Umsatzzahl k_{cat} um einen Faktor von 2.5 – 5, und eine Verringerung der Temperatur von 28 °C auf 4 °C führte zu einer Abnahme von k_{cat} um einen Faktor von 2.5. Darüber hinaus wurde eine Zeitreihe mit einem Lichtmikroskop aufgezeichnet, die die katalytische Hydrolyse des chromogenen β-Laktams Nitrocefin durch einen CTX-M-14 Kristall im makroskopischen Maßstab durch einen Farbwechsel der Substratlösung zeigte. Damit wurde die enzymatische Aktivität auch im Proteinkristall bestätigt.

Das β-Laktam-Antibiotikum mit dem langsamsten Umsatz, Ceftazidim mit $k_{cat} = 0.9 \pm 0.2$, wurde für erste TRX-Experimente mit dem am CFEL entwickelten TapeDrive an einer

Synchrotron-Beamline (DESY, P11) verwendet. Leider konnte für das Ceftazidim-Molekül im aktiven Zentrum von CTX-M-14 zu keinem der analysierten Zeitpunkte zwischen 62 ms und 5 s eine Elektronendichte beobachtet werden, auch nicht beim Screening verschiedener pH-Werte. Anschließend wurden weitere potenzielle Antibiotika-Kandidaten unter Verwendung des HARE-Chips mit LAMA-Reaktionsinitiierung für Fixed-Target-TRX an einer Synchrotron-Beamline (EMBL, P14.2) untersucht, bis schließlich Piperacillin als geeignetes Substrat identifiziert wurde. Unter Verwendung von Piperacillin wurde der Zeitverlauf der Hydrolysereaktion durch CTX-M-14 mit der Bildung eines Michaelis-Menten-Zustands, eines kovalenten Acyl-Enzym-Zwischenprodukts und eines Enzymproduktkomplexes innerhalb eines Zeitrahmens von 2 s – 12 s verfolgt. Diese Reaktion wurde unter Verwendung von TRX bei 30 °C (303 K) beobachtet. Es wurden wesentliche strukturelle Unterschiede zu bestehenden Proteinstrukturen von inaktiven CTX-M-Mutantenvarianten gefunden, die in der Proteindatenbank (PDB) hinterlegt sind, insbesondere im Enzymproduktkomplex, was die großen Vorteile von TRX mit Wildtyp-Enzymen bei nahezu physiologischen Temperaturen hervorhebt. Die Unterschiede ergeben sich aus der Tatsache, dass die mutierten Varianten künstlich induzierte Veränderungen aufweisen.

β-Laktamase-Inhibitoren sind von großer Bedeutung, da sie die Aktivität von β-Laktamasen hemmen und somit in Kombination mit β-Laktam-Antibiotika zur Überwindung von Resistenzen eingesetzt werden können. In einem weiteren Teil der Arbeit wurden die zeitlichen Abläufe bei der Bindung von Inhibitoren an CTX-M-14 mit dem CFEL TapeDrive untersucht. Dabei zeigte sich, dass der neuartige Diazabicyclooctan-β-Laktamase-Inhibitor Relebactam bereits nach 250 ms bei nahezu vollständiger Besetzung bindet. Unter Verwendung von Borsäure als vereinfachtes Inhibitormodell für eine Klasse von kürzlich zugelassenen Boronat-basierten β-Laktamase-Inhibitoren wurde TRX eingesetzt, um mechanistische Einblicke in die Bindung an das Serin im aktiven Zentrum von CTX-M-14 zu erhalten, wobei ein Reaktionszeitrahmen von 80 – 100 ms ermittelt wurde. In einem nachfolgenden Reaktionsschritt wurde die anschließende 1,2-Diol-Borsäureesterbildung mit Glycerin im aktiven Zentrum in einem Zeitrahmen von 100 – 250 ms beobachtet. Darüber hinaus wurde die Verdrängung des entscheidenden Anions im aktiven Zentrum der β-Laktamase als wesentlicher Bestandteil des Bindungsmechanismus von Substraten und Inhibitoren bestätigt. Aus diesen Erkenntnissen und dem Vergleich verschiedener Inhibitoren

konnten besondere Merkmale für die Entwicklung neuer β-Laktamase-Inhibitoren identifiziert werden.

Die gewonnenen mechanistischen Einblicke in die Serin-β-Laktamase-vermittelte Hydrolyse und ihre Hemmung tragen zu einem besseren Verständnis der Resistenz bei und liefern wichtige Informationen für den Kampf gegen Antibiotikaresistenzen. Darüber hinaus sind diese Informationen von großer Bedeutung für die zukünftige Entwicklung von β-Laktam-Antibiotika und β-Laktamase-Inhibitoren.

Abstract

The emergence and spread of antibiotic resistance represent a growing threat to public health. Of particular concern is the production of β-lactamases mostly by Gram-negative bacteria, as these enzymes have the ability to hydrolyze and inactivate the most important class of antibiotics, the β-lactams. Despite years of extensive β-lactamase research, some aspects remain controversial, particularly the reaction mechanism and which amino acid residues are actually involved in the acylation mechanism to form the acyl-enzyme intermediate.

Concurrently, there have been remarkable advances in the field of time-resolved serial crystallography (TRX), enabling the observation of molecular processes at atomic resolution and millisecond time frames. This thesis describes an approach to elucidate the catalysis and inhibition mechanisms of the Class A extended-spectrum serine β-lactamase CTX-M-14 from *Klebsiella pneumoniae* by applying novel time-resolved crystallographic methods, thereby determining its structure, dynamics, and intermediates in complex with substrates, inhibitors and inhibitor models.

First, preliminary experiments were conducted to find optimal conditions for time-resolved crystallography. This included optimization of protein expression and purification, production of microcrystals with the appropriate size for the different methods, and determination of enzyme kinetic parameters to find the most suitable substrate and environment and to estimate an appropriate time frame for TRX experiments. A reduction of pH from 7.4 to 3 resulted in a decrease of turnover number k_{cat} by a factor of 2.5 – 5, and a reduction of temperature from 28 °C to 4 °C resulted in a decrease of k_{cat} by a factor of 2.5. Furthermore, a time series was recorded with a light microscope, demonstrating the catalytic hydrolysis of the chromogenic β-lactam nitrocefin by a CTX-M-14 crystal on a macroscopic scale by a color change of the substrate solution. Thus, the enzymatic activity was also confirmed in the protein crystal.

The β-lactam antibiotic with the slowest turnover, ceftazidime $k_{cat} = 0.9 \pm 0.2$, was used for initial TRX experiments at a synchrotron beamline (DESY, P11) using the TapeDrive developed at CFEL. Unfortunately, no electron density could be observed for the ceftazidime molecule in the active site of CTX-M-14 at any of the time points analyzed between 62 ms and 5 s, even when screening different pH values. Then, more potential antibiotic candidates were screened using the HARE chip with LAMA reaction initiation for fixed target TRX at a synchrotron beamline (EMBL, P14.2) until finally piperacillin was identified as a suitable substrate. Using

piperacillin, the time course of the hydrolysis reaction by CTX-M-14 was followed by the formation of a Michaelis-Menten state, a covalent acyl-enzyme intermediate, and an enzyme product complex within a time frame of 2 s – 12 s. This reaction was observed using TRX at 30 °C (303 K). Essential differences to existing protein structures of inactive CTX-M mutant variant structures, deposited at the protein data bank (PDB) were found, especially in the enzyme product complex, highlighting the major advantages of TRX with wild-type enzymes at near-physiological temperatures. The differences arise from the fact that the mutant variants have artificially induced changes.

β-Lactamase inhibitors are of great relevance as they inhibit the activity of β-lactamases and thus can be used to overcome resistance when combined with β-lactam antibiotics. In another part of the thesis, the temporal processes during inhibitor binding to CTX-M-14 were investigated using the CFEL TapeDrive. This revealed binding of the novel diazabicyclooctane β-lactamase inhibitor relebactam after only 250 ms with nearly complete occupancy. Utilizing boric acid as a simplified inhibitor model for a class of recently approved boronate-based β-lactamase inhibitors, mechanistic and structural insights into binding to the serine in the active site of CTX-M-14 were obtained by applying TRX, identifying a reaction time frame of 80 – 100 ms. In a next step, the reaction time frame of the subsequent 1,2-diol boric acid ester formation with glycerol in the active site was determined to be within 100 – 250 ms. In addition, the displacement of the crucial anion in the active site of the β-lactamase was confirmed to be an essential aspect of the binding mechanism for both substrates and inhibitors. From these experiments and data, and the comparison of several inhibitors, particular features for the development of new β-lactamase inhibitors could be identified.

The obtained mechanistic insights in serine β-lactamase mediated hydrolysis and its inhibition contribute to a better understanding of resistance and provide important information for the fight against antibiotic resistance. Moreover, this information will be of great importance for future development of β-lactam antibiotics and β-lactamase inhibitors.

1. Introduction

1.1. Antimicrobial resistance and the importance of multidrug-resistant bacterial pathogens

The discovery of penicillin in 1929 became one of the greatest milestones in clinical therapy (Fleming, 1929). However, it took more than 10 years before the structure of penicillin G was elucidated and large-scale production became possible, so that it entered clinical use in 1940 and helped safe millions of lives (Abraham & Chain, 1940).Only a few years later in 1945, the first resistances to penicillin in therapy were already observed (Lewis, 2013).
This was the beginning of an arms race between scientists developing new antibiotics and microorganisms that already possess, develop, or acquire, and spread diverse resistance mechanisms through conjugation, transformation, or transduction of the resistance genes. Usually, bacterial organisms manage to develop resistance within two to three years after the introduction of a new antibiotic (Davies, 2006). This is particularly evident in the continuous evolution of β-lactamases under the selection pressure of the frequent introduction of new penicillins, cephalosporins, carbapenems, and monobactams. Irrational and improper use of antibiotics has led to the emergence of multidrug-resistant pathogens that are spreading at a dangerous rate (Jacoby & Bush, 2005). Antibiotic resistance is linked to 1.2 million deaths worldwide in 2019 (Murray et al., 2022). Based on scenarios for increasing drug resistance, it is estimated that the number of deaths related to antibiotic resistance could rise to 10 million per year by 2050 if no action is taken (O'Neill, 2016). While it is nearly impossible to predict the course of evolving antibiotic resistance, there is a clear trend and without intervention, this trend is likely to continue.

For a long time, there was no precise definition of what an MDR organism is. Strictly speaking, multidrug-resistant organisms (MDROs) are referred to as such because they are resistant to more than one antimicrobial agent in vitro (Magiorakos et al., 2012). However, precise standardized international terminology needed to be defined to improve the comparability of surveillance data for these MDROs and to better assess their global, regional, and local epidemiological significance and public health impact (Magiorakos et al., 2012). Thus, as part of a joint initiative of the European Center for Disease Prevention and Control (ECDC) and the

US Centers for Disease Control and Prevention (CDC), a group of experts proposed a systematic approach to defining MDRs and other categories. Epidemiologically significant antimicrobial categories were established for each bacterium and corresponding lists were proposed for antimicrobial susceptibility testing (Magiorakos et al., 2012). Accordingly, multidrug-resistance (MDR) is defined as non-susceptibility to at least one agent from three or more antimicrobial categories. Extensively drug-resistance (XDR) is defined as non-susceptibility to at least one agent in all but two or fewer antimicrobial categories. The most critical classification, pandrug-resistance (PDR), is defined as non-susceptibility to all agents in all antimicrobial categories. Thus, organisms that are characterized as PDR are always also characterized as XDR, and these in turn are always also characterized as MDR. (Magiorakos et al., 2012)

While in recent decades multidrug-resistant Gram-positive bacteria such as methicillin-resistant *Staphylococcus aureus* (MRSA) and vancomycin-resistant *enterococci* (VRE) were the main cause of nosocomial infections (hospital-acquired infections), since the end of the 20th century an increasing number of Gram-negative bacteria have been primarily responsible (Livermore, 2012). These include MDR Gram-negative bacteria such as *Acinetobacter baumannii, Pseudomonas aeruginosa*, extended-spectrum β-lactamase (ESBL) producing enterobacteria, and carbapenem-resistant enterobacteria (CRE) (Laxminarayan et al., 2013; Teerawattanapong et al., 2017). The MDR enterobacteria are mainly represented by *Escherichia coli* and *Klebsiella pneumoniae*. Enterobacteriaceae are naturally occurring bacteria of the human bowel flora, but they can also be pathogenic and cause urinary tract infections, pneumonia, and bloodstream infections (Bevan et al., 2017). The resistance of these Gram-negative pathogens is mostly based on the production of β-lactamases, enzymes that degrade or modify β-lactam antibiotics, rendering them ineffective (Drawz & Bonomo, 2010). Due to the increased use of these β-lactam antibiotics, the bacteria have developed extended-spectrum β-lactamase (ESBL) enzymes that allow them to survive by inactivating a much broader spectrum of antibiotics like penicillins, cephalosporins and monobactams. This has severely limited the options in the treatment of infections caused by ESBL-producing Gram-negative enterobacteria, leaving only the combination with β-lactamase inhibitors or the use of carbapenems (Laxminarayan et al., 2013). This in turn has led to increased use of carbapenems and the emergence of carbapenemase-producing Enterobacteriaceae (CRE)

(Hawkey, 2015). Treatment of infections with these organisms is particularly difficult because multidrug-resistance often leaves only few options, resulting in high mortality rates. CRE often have multiple mechanisms of antibiotic resistance such as co-production of ESBLs together with carbapenemases as well as other mechanisms and are therefore classified as MDR or XDR Gram-negative bacteria. Recently, an increasing number of clinical isolates have been found to produce even more than one carbapenemase. Of these, *Klebsiella pneumoniae* is the most frequently reported enterobacterial species of CRE (Meletis et al., 2015). Especially the rapid spread of carbapenemase-producing *Klebsiella pneumoniae* strains is of concern and highlights the urgent need for novel therapeutic options (Munoz-Price et al., 2013). In addition, bacteria that produce β-lactamase enzymes can acquire an extended-spectrum of these enzymes through point mutation during treatment with an antibiotic, resulting in non-susceptibility and treatment failure (Both et al., 2017). Moreover, the corresponding genes for the resistance mechanisms are often encoded on plasmids and can thus be easily transferred to other bacteria (including different bacterial species) by horizontal gene transfer, which extremely accelerates the spread of resistance and the emergence of MDR (Livermore, 2012).

Having effective antibiotics available has made a variety of medical advances possible in the first place, including organ transplants, cancer chemotherapy, and complex surgeries. Many of these procedures would no longer be possible with rising antimicrobial resistance because patients' risk of infection is increased due to their weakened immune systems (O'Neill, 2016). This puts pressure on drug development because there is no obvious next line of antibiotics that can be used against carbapenemase producing bacteria as there was with carbapenems against ESBL producing bacteria (Livermore, 2012). As a result, an increasing number of β-lactam/β-lactamase inhibitor combinations are being developed that are also effective against MDR and especially CRE organisms (Bush, 2015; Yahav et al., 2020; Zhanel et al., 2018).

However, according to a 2019 World Health Organization (WHO) report, the clinical pipeline remains insufficient to address the challenge of the increasing emergence and spread of antibiotic resistance (WHO, 2019). One reason for this is that, unfortunately, most large pharmaceutical companies have withdrawn from the field of anti-microbial drug discovery, so this work is now mainly done by academic laboratories and small to medium-sized companies (Hutchings et al., 2019). The development of new antibiotics is difficult, complex and involves

high costs for clinical trials (Finch et al., 2011; Livermore et al., 2011). Approved antibiotics are usually only used for a relatively short time for acute infections or can be classified as reserve antibiotics and thus only used for severe cases of XDR infections (White et al., 2011). This makes them less profitable than, for example, drugs for the treatment of chronic diseases.
This makes academic research even more important in order to gain new insights into the mechanisms of antibiotic resistance. Ideally, the new findings can be used for the development of new antimicrobial substances. The focus on β-lactamase inhibitors is particularly important because it enables antibiotics that have already been approved to regain efficacy. However, it should be clear that the emergence of new antibiotic resistance is practically inevitable, but it is possible to slow it down through responsible use of antibiotics and development of new therapeutic options (Chawla et al., 2022).

1.2. Antibiotics and their mode of action

As previously mentioned, antibiotics are utilized in the treatment of infections caused by bacteria. Most antibiotics are either derived from natural products or natural product derivatives, while some are fully synthetic (see Figure 1) (Hutchings et al., 2019; Newman & Cragg, 2016). Antibiotics can exhibit bactericidal or bacteriostatic activity, depending on the specific antibiotic and the targeted bacterial organism (Ocampo et al., 2014; Pankey & Sabath, 2004). Bactericidal antibiotics typically act on the bacterial cell wall, cell membrane, or essential enzymes, leading to bacterial lysis. In contrast, antibiotics that target protein synthesis often exhibit a bacteriostatic effect and only prevent bacterial growth. Although the bactericidal activity of an antibiotic seems preferable to the bacteriostatic, there is little clinical evidence to support this proposition (Pankey & Sabath, 2004).
In fact, bacteriostatic antibiotics may be beneficial in certain situations, such as when rapid lysis of bacteria would result in the release of exotoxins and cause toxic shock syndromes, as occurs in infections with staphylococci and streptococci. In these cases, it has been observed that a bacteriostatic antibiotic such as clindamycin can effectively fight the infection while inhibiting exotoxin production (van Langevelde et al., 1997).
Antibiotics are usually classified according to their mode of action, chemical structure, or spectrum of activity and usually target bacterial functions or growth processes that are not present in human cells, thus achieving high specificity (Calderón & Sabundayo, 2007).

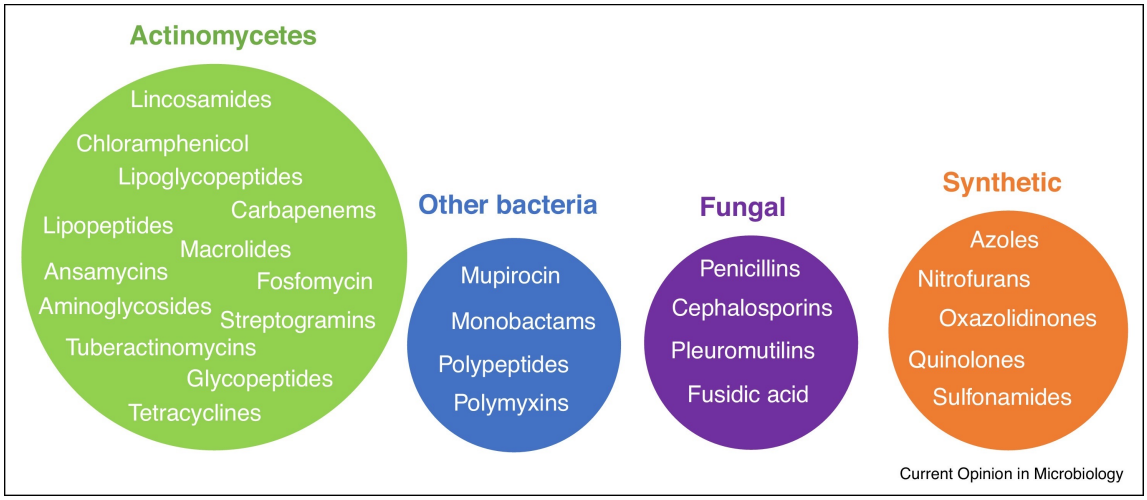

Figure 1: Clinically relevant classes of antibiotics are until today mostly derived from natural sources. From Hutchings et al. (2019).

For example, one mode of action of antibiotics is the inhibition of bacterial cell wall synthesis, which is essential for both Gram-positive and Gram-negative bacteria (Figure 2). These antibiotics include the β-lactams, glycopeptides, bacitracin, and fosfomycin. The most successful class of antibiotics, the β-lactams, target the DD-transpeptidases, also known as penicillin-binding proteins (PBPs), which are necessary for crosslinking of peptidoglycan strands and therefore the formation of the bacterial cell wall. The β-lactam moiety of these antibiotics mimics the terminal D-Ala-D-Ala motif (Tipper & Strominger, 1965) of the nascent peptidoglycan and therefore acts as an analogue but forms a covalent acyl-enzyme complex that is stable against hydrolysis and therefore inhibits the transpeptidase. As a result, the amount of peptidoglycan precursors increases, triggering the activation of autolytic cell wall hydrolases (autolysins) and leading to lysis and death of the bacteria (Höltje, 1995; Kitano & Tomasz, 1979; Tomasz, 1979).

The four main classes of β-lactam antibiotics include penicillins, cephalosporins, carbapenems and monobactams which are based on the four membered 2-azetidinone ring (Figure 3). However, some pathogens have acquired resistance through expression of β-lactamases, which are able to hydrolyze the antibiotics and thus render them ineffective as previously described.

β-Lactam antibiotics are by far the most commonly used drugs to treat bacterial infections (Hamad, 2010). During 2004 – 2014, the antibiotic class of β-lactams was the most commonly prescribed injectable antibiotic at 65.24 % (Figure 4)(Bush & Bradford, 2016). According to the Centers for Disease Control and Prevention (USA), penicillins and cephalosporins were the

most commonly prescribed oral antibiotics in the U.S. in 2021 with 77.8 million prescriptions out of a total of 211.1 million (CDC, 2022). This highlights the important role of this class of antibiotics and the significance of research on resistance mechanisms to them.

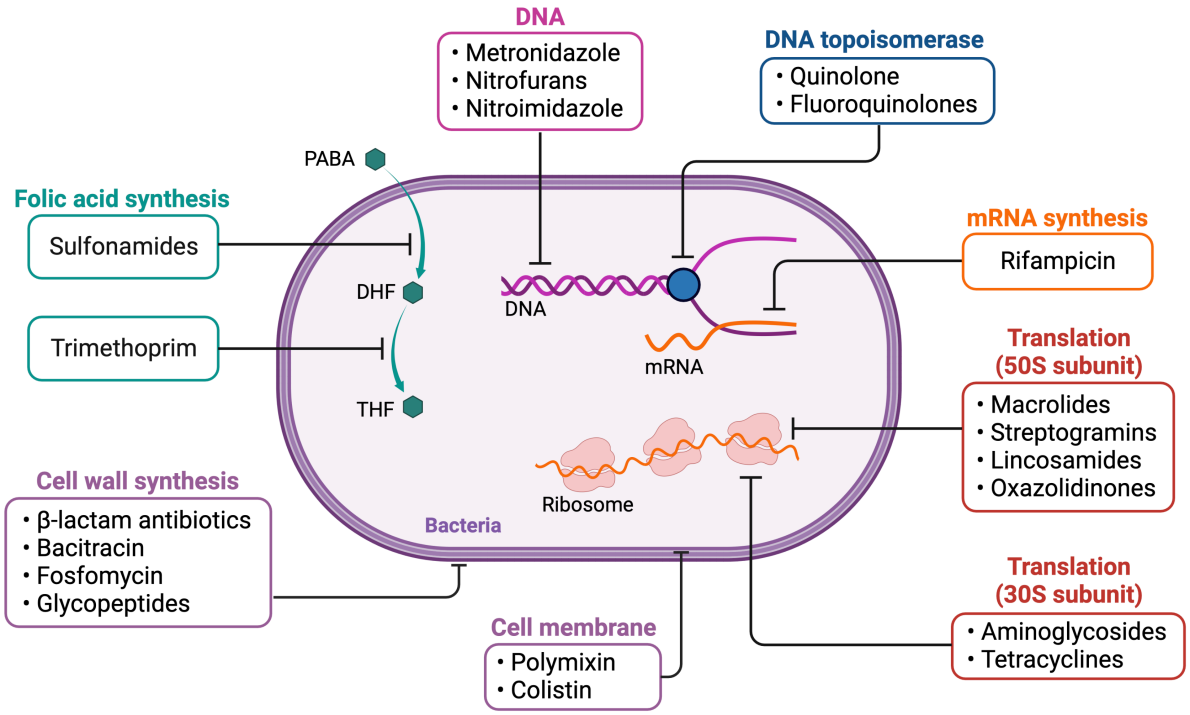

Figure 2: Mode of action of different classes of antibiotics on various bacterial targets. Adapted from "Antimicrobial Therapy Strategies", by BioRender.com (2023). PABA: 4-aminobenzoic acid; DHF: dihydrofolate; THF: tetrahydrofolate.

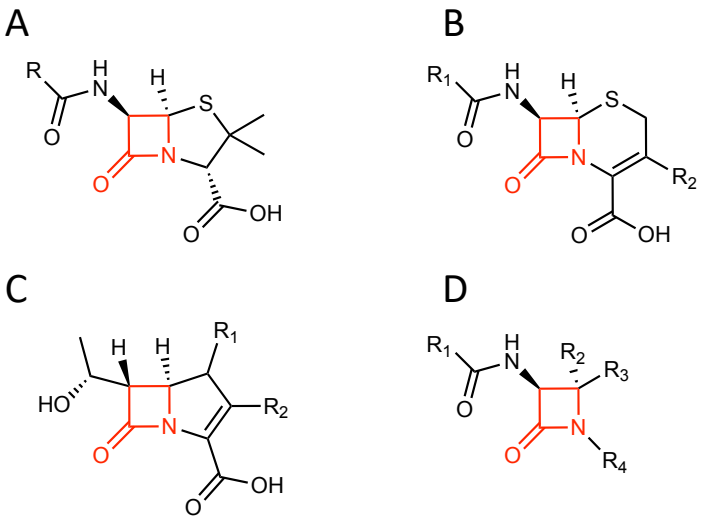

Figure 3: Core structures of penicillins (A), cephalosporins (B), carbapenems (C) and monobactams (D) with the β-lactam ring (2-azetidinone) highlighted in red.

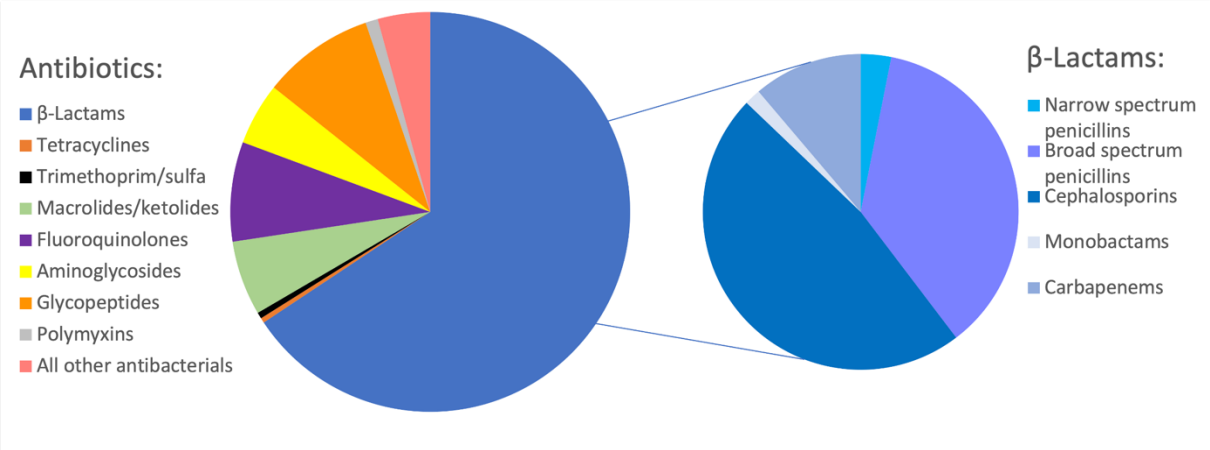

Figure 4: Proportion of prescriptions in the United States for injectable antibiotics by class (left) and the percentage of β-lactam class used (right) in 2004 – 2014. The percentage of standard units for the injectable antibiotics: β-lactams 65 %; glycopeptides 9 %; fluoroquinolones 8 %; macrolides/ketolides 6 %; aminoglycosides 5 %; polymyxins 1 %; trimethoprim/sulfamethoxazole 0.5 %; tetracyclines (excluding tigecycline) 0.4 %; all other antibiotics (including daptomycin, linezolid, and tigecycline) 4 %. The percentage of β-lactams by class: narrow spectrum penicillins 3 %; broad spectrum penicillins 37 %; cephalosporins 47 %; monobactams 2 %; carbapenems 11 %. Adapted from Bush and Bradford (2016).

Some antibiotics, such as polymyxins, colistin, and daptomycin target the membranes of either Gram-negative or Gram-positive bacteria, causing permeabilization of the outer and inner membranes, resulting in lysis and cell death. The disruption of the membrane results in the formation of visible protrusions that facilitate the uptake of molecules that were previously unable to permeate the membrane (e.g. other antibiotics), as well as the leakage of periplasmic proteins (Straus & Hancock, 2006; Trimble et al., 2016).

Other antibiotics target the protein synthesis that is essential for bacterial cell function and survival. These antibiotics inhibit the prokaryotic 70S ribosome by various mechanisms, preventing the correct translation of mRNA into bacterial proteins.

Prokaryotic 70S ribosomes consist of a large 50S and a small 30S subunit and are very different from eukaryotic 80S ribosomes consisting of a 60S and a 40S subunit. Both ribosomes differ not only in size but also in protein composition, which is why antibiotics specifically target bacterial ribosomes. While tetracyclines bind to the 30S subunit and prevent the entry of aminoacyl-tRNA into the ribosome, aminoglycosides cause reading errors of the mRNA, leading to the production of defective proteins (Krause et al., 2016; Mohr, 2016). In contrast, macrolides, lincosamides and streptogramin antibiotics bind to the 50S ribosomal subunit and inhibit the protein synthesis by blocking peptide elongation (Tenson et al., 2003; Zhanel et al.,

2001). Rifampicin, on the other hand, prevents the synthesis of mRNA by inhibiting bacterial DNA-dependent RNA polymerase (Campbell et al., 2001).

A few antibiotics target the synthesis of bacterial DNA, disrupting the replication and transcription of DNA and ultimately leading to the death of the bacteria (Newman & Cragg, 2016). Nitroimidazoles, such as metronidazole inhibit nucleic acid synthesis by forming reactive nitroso species in anaerobic bacteria, disrupting the DNA of bacterial cells (Engleberg et al., 2007; Freeman et al., 1997). Quinolone antibiotics inhibit the ligase activity of DNA gyrase and topoisomerase IV while leaving nuclease activity unaffected, resulting in the release of DNA with single- and double-strand breaks, leading to cell death (Aldred et al., 2014). DNA gyrase and topoisomerase IV are bacterial enzymes that usually cut DNA and introduce supercoiling.

Antibiotics can also target the synthesis of folic acid, which is essential for the formation of nucleic acids. Sulfonamides inhibit the enzyme dihydropteroate synthase in the folic acid pathway, thus preventing the synthesis of dihydropteroate, a precursor of dihydrofolate (DHF) (Sköld, 2000). The subsequent step in folic acid synthesis can be inhibited by trimethoprim, that binds to dihydrofolate reductase and inhibits the reduction of dihydrofolic acid (DHF) to tetrahydrofolic acid (THF) (Brogden et al., 1982).

Unlike bacteria, mammalian cells have a folate uptake system, so they do not require their own folic acid synthesis and generally do not possess the inhibited enzymes.

The emergence and spread of antimicrobial resistance to classical antibiotics have led to the investigation of alternative ways to treat bacterial infections. These include new structure-based drug design in addition to classical natural-product based drug discovery (Ferreira et al., 2015; Hutchings et al., 2019; Moloney, 2016). Furthermore, antibody treatments, phage therapy, antisense RNA-based treatments and CRISPR-Cas9-based treatments are also being developed (Abedon et al., 2011; Ghosh et al., 2019; Theuretzbacher & Piddock, 2019).

1.3. Mechanisms of antimicrobial resistance

Due to the use of antibiotics to treat bacterial infections, some pathogens have developed resistance to these drugs. These mechanisms of antimicrobial resistance are as diverse as the modes of action of antibiotics and the understanding of the molecular processes provide the essential knowledge for new drug development (Blair et al., 2015). They can be divided into antibiotic resistance mechanisms of individual bacteria (Figure 5 A), mechanisms that depend on bacterial communities (Figure 5 B) or on the environment of the bacteria (Figure 5 C).

Mechanisms of individual bacteria include reduced membrane permeability, expression of efflux pumps, antibiotic target alteration and protection, and most importantly, enzyme-catalyzed modifications of antibiotics, such as the expression of β-lactamases (Darby et al., 2022; Drawz & Bonomo, 2010; Llarrull et al., 2010). In some bacterial genera, certain of these mechanisms occur naturally and therefore provide intrinsic resistance, whereas in other bacterial genera these mechanisms can be obtained through the acquisition or mutation of new genetic material, resulting in acquired antibiotic resistance (Darby et al., 2022). The error rate of bacterial DNA polymerase is low, but in the context of millions of bacterial cells and rapid generation times, accumulation of mutations in bacterial populations is unavoidable. In the presence of antibiotics, these mutations can then provide an advantage, for example, if they enable one of the aforementioned mechanisms, ultimately allowing the mutants to rapidly dominate in a population, leading to the emergence of resistance (Cook & Wright, 2022). The interplay of multiple molecular mechanisms can result in high levels of resistance.

Starting with reduced permeability, a mechanism of antibiotic resistance that is intrinsic to some microbes, particularly Gram-negative bacteria that results in reduced drug influx (Figure 5 A). Many antimicrobial agents need to pass through the bacterial cell envelope to reach their target and thus exert their effect. Since Gram-negative bacteria have a double cell wall, penetration of the cell envelope is more difficult and thus intrinsic resistance to many antibiotics, that are otherwise effective for Gram-positive bacteria, is provided (Darby et al., 2022).

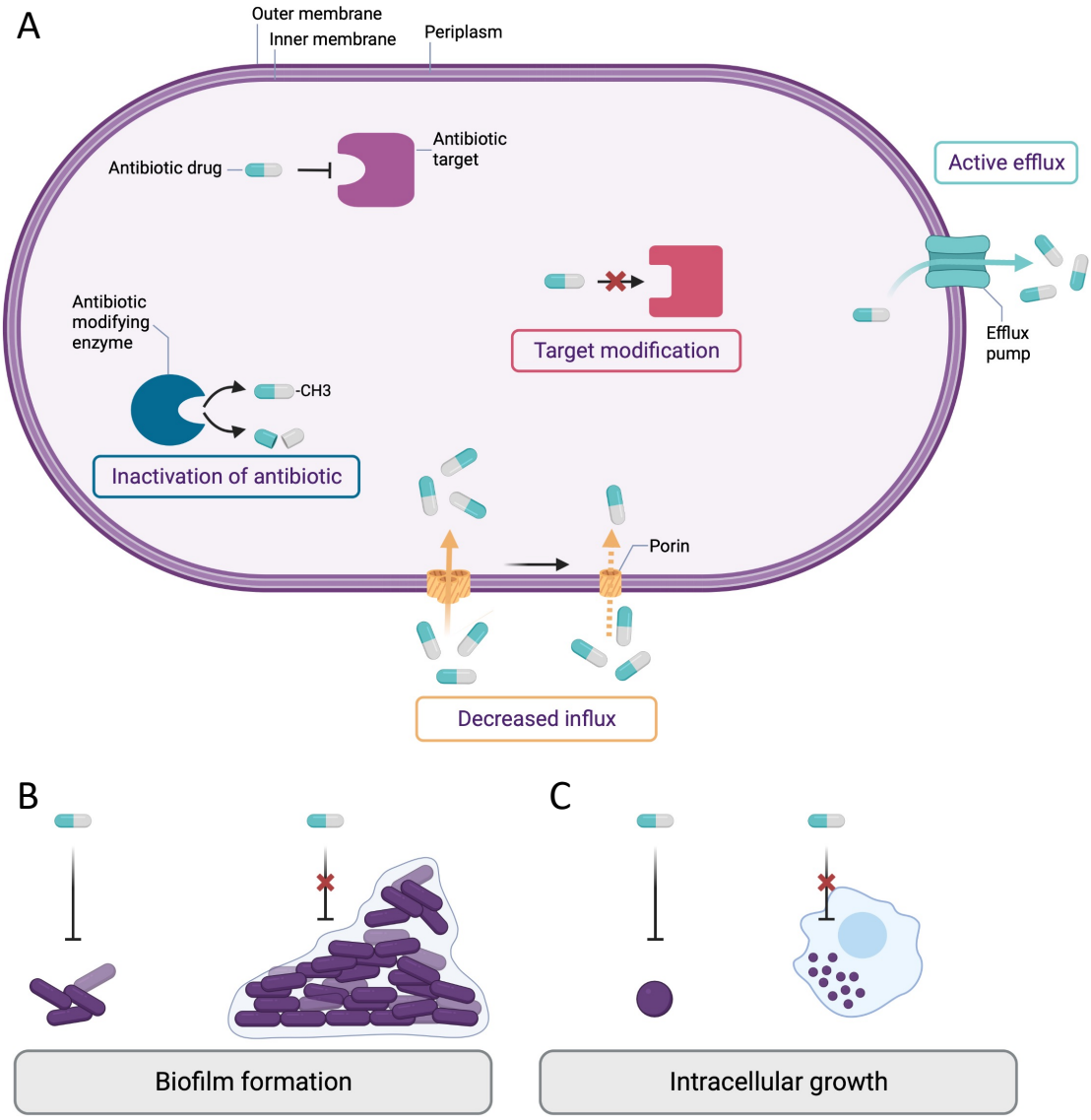

Figure 5: Individual antimicrobial resistance mechanisms (A) and resistance based on bacterial lifestyle (B) and environment (C). Created with BioRender.com (2022)

In addition, alteration of the cell envelope due to a reduced number of porins or altered phospholipid and fatty acid content of the cytoplasmic membrane may impair drug passage (Mishra et al., 2012). The bacterial membranes provide protection and a barrier function while allowing the sufficient uptake of nutrients, through various porins. These porins extend across the membrane, forming pores and allowing for diffusion-driven uptake of hydrophilic compounds up to a certain size, including some antibiotics like β-lactams (Fernández & Hancock, 2012). However, mutations in porin-encoding genes can lead to decreased expression of porins, a narrower porin channel not suitable for antibiotics, or the complete loss of some porins, resulting in the development of resistance due to reduced permeability

(Fernández & Hancock, 2012). In the development of new active substances, therefore, it is not only efficacy against the individual target that is important, but more importantly reaching the target site. (Darby et al., 2022)

Bacteria can not only prevent antibiotics from entering the cell, but also selectively remove them from inside the cell into the extracellular space via active transport with efflux pumps (Figure 5 A). All bacteria possess multiple efflux pumps, which transfer a large variety of harmful compounds, including antibiotics, out of the bacteria (Darby et al., 2022) and generally allow rapid adaptation and survival in challenging environments. These are transmembrane proteins, which, in contrast to porins, provide energy-dependent transport of molecules. Because efflux pumps occur naturally in bacteria, they can provide intrinsic antibiotic resistance, which can have a synergistic effect with the previously mentioned decreased permeability (Poole et al., 1993). However, the occurrence of a mutation that leads to an increased expression level of a given efflux pump can result in the acquisition or boost of resistance to the antibiotics transported by that pump (Fernández & Hancock, 2012; Salehi et al., 2021). Furthermore, mutations can also lead to improved efflux pump efficiency (Vettoretti et al., 2009). Since efflux pumps can transport and thus remove multiple classes of antibiotics, they contribute strongly to MDR. Understanding the molecular mechanisms of efflux pumps is beneficial for rational development of suitable inhibitors to prevent drug efflux and restore antibiotic susceptibility (Zwama & Nishino, 2021).

Another mechanism of resistance to antibiotics is the alteration, protection or bypass of the primary target (Figure 5 A). This is particularly effective because a central component of the high efficacy of antibiotics relies on specific targeting of bacterial proteins and binding with high affinity to the main target that has an essential cellular function (Baquero & Levin, 2021). In case the target is not accessible, either because it has been altered or it is protected, the antibiotic cannot exert its effect, leading to resistance. For example, one possible type of resistance to β-lactam antibiotics is achieved by mutations in the penicillin-binding protein (PBP) that result in decreased affinity of the aforementioned antibiotics (Periasamy et al., 2020). In addition, the target molecule can be chemically modified to prevent interaction with the antibiotic. In this way, a resistance mechanism against macrolides works by methylation of the 16S rRNA, which prevents macrolide binding (Bhujbalrao & Anand, 2019) and therefore

prevents inhibition of the ribosome. One of the best studied examples of target protection is tetracycline resistance by Tet(M) and Tet(O) (Munita & Arias, 2016). These proteins belong to the translational factor superfamily and bind to the ribosome, resulting in an altered ribosomal conformation that displaces the tetracycline from its binding site and prevents its rebinding. This allows protein synthesis to resume unhindered. Bacteria are also capable of evolving new variants of the antibiotic target that perform similar biochemical functions to the original protein but are not inhibited by the antimicrobial molecule. Key clinical examples include methicillin resistance of *S. aureus* due to acquisition of a gene for PBP2a, a PBP that has low affinity for all β-lactams (Munita & Arias, 2016).
The three target-related mechanisms, mutation, protection, and bypass of the target site, can in combination lead to greatly reduced susceptibility to antibiotics (Darby et al., 2022).

One of the most important resistance mechanisms is mediated by the expression of enzymes that alter or degrade the antibiotic agent, resulting in inactivation of the antibiotic (Figure 5 A) (Drawz & Bonomo, 2010; Forsberg et al., 2015). Enzyme-catalyzed inactivation of antibiotics by hydrolysis is the oldest and the most relevant mechanism since the first use of antibiotics, with the discovery of a β-lactamase in 1940 (Abraham & Chain, 1940). Thousands of such enzymes have been identified to date and enable the degradation of various classes of antibiotics, including β-lactams, aminoglycosides, phenols, and macrolides (Blair et al., 2015). Particularly noteworthy are the β-lactamases, which are able to inactivate one of the most widely used classes of antibiotics, the β-lactams. The development of increasingly broad-spectrum β-lactam antibiotics has also driven the evolution of β-lactamases with an increasingly extended hydrolysis spectrum (ESBLs), ultimately resulting in the emergence of bacterial isolates resistant to all available β-lactam antibiotics (Lima et al., 2020; Lynch III et al., 2013). In addition, the rapid spread of these β-lactamases via plasmids poses a threat to the health care system, hence they are discussed in more detail in section 1.4. In addition to hydrolysis, bacteria have evolved proteins that can modify antibiotics by transferring a chemical group such as a methyl, acetyl, phosphate, or nucleotidyl group and thus achieve antibiotic resistance by preventing antibiotic binding through steric hindrance (Blair et al., 2015). Such antibiotic-modifying enzymes have been discovered for several classes of antibiotics, including aminoglycosides, macrolides, rifamycins, streptogramins, and lincosamides (Darby et al., 2022). Among the best-known examples is the group of

chloramphenicol acetyltransferases, which are used as a selection marker on plasmids in molecular biology. These enzymes transfer an acetyl group to chloramphenicol, thus preventing binding to the ribosome and conferring resistance to this antibiotic (Roberts & Schwarz, 2017).

In addition to individual antibiotic resistance mechanisms, particular bacterial lifestyles are capable of generating resistance to certain antibiotics. This category also includes growth in a biofilm, a surface-adherent group of bacteria that are enclosed in an extracellular matrix, making them less susceptible or even resistant to antibiotics (Figure 5 B). This extracellular matrix is composed of exopolysaccharides, extracellular DNA (eDNA), proteins, and lipids that compromise antibiotic access to bacteria (Flemming & Wingender, 2010). Enzymes secreted in the matrix, such as β-lactamases, can degrade antibiotics. Furthermore, the cells in a biofilm are in different metabolic states, which is why individual cells of the biofilm can survive antibiotic treatment due to reduced permeability, reduced metabolic activity and therefore reduced expression of the antibiotic target, and production of persister cells (Darby et al., 2022).

Many bacterial species can grow in a biofilm, including, for example, *Staphylococcus aureus, Klebsiella pneumoniae, Escherichia coli, Pseudomonas aeruginosa,* and *Acinetobacter calcoaceticus* (Hall & Mah, 2017; Stewart & Costerton, 2001; Yuan et al., 2020).

Biofilm formation is initiated by the interaction of the bacteria with a surface. With time, accumulations of multiple cells in small biofilm colonies mature into large macrocolonies. Subsequently, cells can escape from mature biofilms and then colonize new surfaces (Hall & Mah, 2017; Petrova & Sauer, 2016). This prevalence and the difficulty of treating biofilms with antibiotics makes them particularly important in medicine, as they often lead to chronic infections. In particular, colonization of indwelling medical devices such as prostheses or pacemakers by *S. aureus* biofilms threatens many advances in modern medicine and poses a high risk to patients (Hall & Mah, 2017). It is widely accepted that the basis of antibiotic resistance due to biofilm formation is multifactorial and the underlying molecular mechanisms vary depending on the antibiotic, bacterial strain and species, stage of biofilm development, and biofilm growth conditions (Alhede et al., 2011; Craft et al., 2019; Ito et al., 2009; Stewart, 2015). However, it is clear that survival in biofilms is not based on just one mechanism, but on a combination of multiple mechanisms (Uruén et al., 2020).

The environment in which bacteria reside is critical to whether and how antibiotics can affect them, and thus represents an important mechanism of antibiotic resistance (Figure 5 C). Some organisms classified as extracellular pathogens have the ability to replicate inside cells. These include *Escherichia coli* (Subramanian et al., 2008), *Pseudomonas aeruginosa* (Heimer et al., 2013), *Staphylococcus aureus* (Horn et al., 2018), *Yersinia spp.* (Pujol & Bliska, 2003) and several more (Casadevall & Fang, 2020). A good example of this is the adoption of an intracellular lifestyle by *S. aureus* in eukaryotic host cells (Flannagan et al., 2016; Lowy, 2000). *S. aureus* is a commensal pathogen found on the human skin but is also equipped with virulence factors and can cause severe infections. The adoption of an intracellular lifestyle by *S. aureus* is an important aspect of its pathogenesis, as it allows to evade host immunity and antibiotics (Soe et al., 2021).

A better understanding of the molecular mechanisms of antibiotic resistance can guide the development of new strategies to treat infectious diseases and address current health threats.

1.4. β-Lactamases

Since the structure and function of β-lactamases have been extensively studied in this thesis, these enzymes are addressed in more detail in this separate chapter of the introduction. As described above, they represent an antibiotic resistance mechanism that ensures the survival of the bacteria by degrading the drug itself. Expression of these enzymes provides one of the most important resistance mechanisms, as they cause inactivation of the most widely used class of antibiotics, the β-lactams (Drawz & Bonomo, 2010; Forsberg et al., 2015). The list of characterized β-lactamases continues to grow, resulting in the Beta-Lactamase DataBase (BLDB) reporting over 7,800 different β-lactamase variants (Naas et al., 2017; accessed 12.02.2023). These β-lactamases can be categorized into four Ambler classes (A-D) according to their sequence (Ambler et al., 1991; Bush, 2013; Bush & Jacoby, 2010; Hall & Barlow, 2005). Classes A, C and D belong to the serine β-lactamases (SBLs), which have a catalytic serine in the active site. Class B enzymes, represent the metallo-β-lactamases (MBLs), which have two Zn-ions facilitating the hydrolysis of β-lactam antibiotics.

The early β-lactamases, also called penicillinases, like some TEM and SHV variants were mainly active against first-generation β-lactams. To counteract resistance by expression of these β-lactamases, antibiotic classes have been expanded to include derivatives with improved

properties and hydrolytic stability. However, simple point mutations in the ubiquitous TEM and SHV plasmid-encoded *bla* genes altered key amino acid residues of the active site, allowing the new enzyme variants to degrade the new derivatives (Bonnet, 2004). These are a new class of extended-spectrum β-lactamases (ESBLs) that have gained the greatest clinical importance due to their extended hydrolysis spectrum, which allows them to hydrolyze penicillins, narrow-spectrum and broad-spectrum cephalosporins and monobactams (Nepal et al., 2017). Rapid spread on plasmid-encoded *bla* genes ensured that the ESBLs represent the most prevalent class of β-lactamases with over 10 enzyme families associated with ESBL, including CTX-M, SHV, TEM, PER, VEB, BES, GES, TLA, SFO and OXA (Paterson & Bonomo, 2005; Zhao & Hu, 2013). Apart from the OXA family (class D), all ESBLs belong to Ambler class A and are particularly widespread in Enterobacteriaceae such as *K. pneumoniae* and *E. coli* (Paterson & Bonomo, 2005). Consequently, class A β-lactamases are the most intensively studied of all β-lactamases (Tooke et al., 2019a).

Among the ESBLs, the strong increase of CTX-M variants stands out, with CTX-M-14 and CTX-M-15 being the most widely isolated variants worldwide (Blair et al., 2015; Cantón et al., 2012; Cantón et al., 2008; Zhao & Hu, 2013). This explosive spread around the world has been even referred to as the CTX-M pandemic, with CTX-M ESBLs becoming dominant (Cantón & Coque, 2006; Livermore et al., 2007). The name of CTX-M β-lactamases is originated from the highly effective hydrolysis of the oxyimino-cephalosporin cefotaxime (CTX) and the first reported isolation in Munich (M) (Bauernfeind et al., 1990). CTX-M-14 β-lactamase is also widely used as a model system for the study of CTX-M structure and function (Brown et al., 2020; Chen et al., 2005a; Patel et al., 2018; Patel et al., 2017).

CTX-M enzymes were initially described in *K. pneumoniae*, *E. coli*, and *Salmonella spp.* but rapidly emerged in other Enterobacteriaceae (Cantón et al., 2012). These β-lactamases originated from mobilization of chromosomal *bla* genes from *Kluyvera spp.* into mobile genetic elements (Cantón et al., 2008). These $bla_{\text{CTX-M}}$ genes can be integrated into plasmids or transposons for effective transfer, which has enabled the rapid dissemination (Coelho et al., 2010). As a result, CTX-M enzymes have become the most prevalent ESBL in the world and are considered responsible for a large proportion of cephalosporin resistance in *E. coli* and *K. pneumoniae* (Munita & Arias, 2016). Like other ESBLs, CTX-Ms have diverged from an evolutionary perspective through point mutations, probably as a consequence of antibiotic

selection pressure, resulting in at least six main clusters, including the five CTX-M lineage groups (CTX-M-1-group, CTX-M-2-group, CTX-M-8-group, CTX-M-9-group, CTX-M-25-group) and one *Kluyvera spp.* group (KLUC) (Cantón et al., 2012; D'Andrea et al., 2013). These groups are distinguished from each other by differences of more than 10 % in amino acid sequence, while within a group they have only minor allelic variants and less than 5 % differences in amino acid sequence. The CTX-M-14 lactamase studied in this thesis is a member of the CTX-M-9 lineage group (D'Andrea et al., 2013). According to the BLDB, 230 CTX-M variants have now been identified (Naas et al., 2017; accessed 12.02.2023).

The success of CTX-M dissemination is likely to be based on a combination of factors, such as efficient propagation of the bla_{CTX-M} genes by mobile genetic elements, the low fitness costs of CTX-M production, and the high selection pressure caused by the massive use of extended-spectrum cephalosporins. The CTX-M pandemic has been a key factor in the rapid spread of resistance to extended-spectrum cephalosporins among enterobacteria. This in turn has facilitated the use of carbapenems, thus leading to the emergence of carbapenem-resistant pathogens. Therefore, it is particularly important to address CTX-M β-lactamases in drug discovery and antibiotic resistance research and to classify them as a major target in infection control (D'Andrea et al., 2013).

Carbapenems are now becoming the first choice in the treatment of hospital-associated Gram-negative infections, as they are the only β-lactam antibiotics that are still effective against ESBL-producing pathogens (Paterson, 2000). However, carbapenem resistance is mediated by the expression of carbapenemases capable of inactivating a wide range of β-lactams, including extended-spectrum cephalosporins and carbapenems (Blair et al., 2015). These enzymes include members of Ambler class A, B and D β-lactamases, are now mostly plasmid-mediated, and have been reported in Enterobacteriaceae, *A.baumannii,* and *P.aeruginosa* (Queenan & Bush, 2007; Tzouvelekis et al., 2012). Especially important representatives are *Klebsiella pneumoniae* carbapenemases (KPC; class A), New Delhi metallo-β-lactamases (NDM; class B), and oxacillinases (OXA-48 type; class D), which are spreading worldwide and therefore become a major concern in clinical therapy (Tooke et al., 2019a). In 2017, WHO published a list of priority pathogens for research and development of new antibiotics. All three bacterial species listed in the highest category "Priority 1: Critical" exhibit carbapenem resistance (Tacconelli et al., 2018; WHO, 2017). A better understanding of ESBLs

and new agents against them, as an alternative to carbapenems, may slow the spread of carbapenem resistant bacteria by reducing the need to use carbapenem antibiotics. Since there are currently no last resort drugs against carbapenemase-producing bacteria, combinations of β-lactam antibiotics with β-lactamase inhibitors are becoming increasingly important (see section 1.5).

β-Lactamases hydrolyze the amide bond of the β-lactam ring, degrading the drug (Darby et al., 2022). A proposed general mechanism of a serine β-lactamase is shown in Scheme 1. All three serine β-lactamase classes (Ambler class A, C, and D) use an acylation and deacylation mechanism via an acyl-enzyme intermediate for the hydrolysis of β-lactams (Scheme 1).

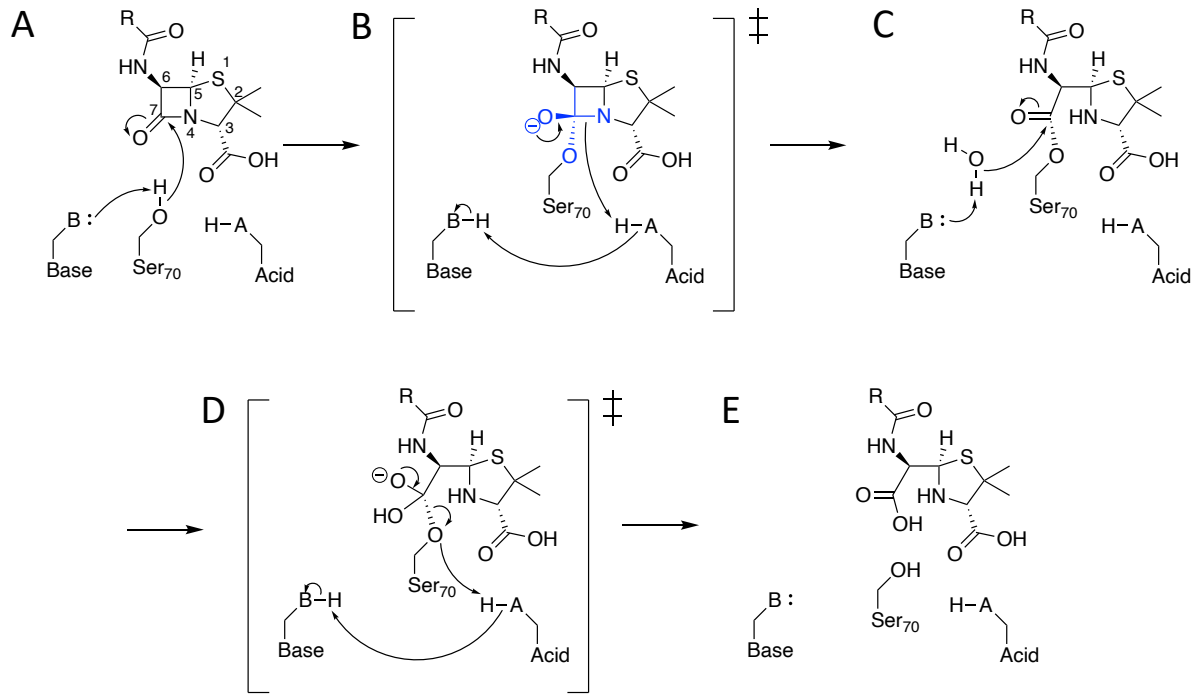

Scheme 1: Overview of the proposed general serine β-lactamase acylation (A-C) and subsequent deacylation (C-E) mechanism for hydrolysis of a generic penicillin substrate. The acylation reaction begins with the convergence of enzyme and substrate into a non-covalent Michaelis complex (A). Subsequently, a general base activates Ser70 for a nucleophilic attack on the amide carbonyl carbon atom (atom C7), resulting in a tetrahedral acylation transition state (blue, B). The transition state is resolved by formation of a covalent acyl-enzyme intermediate (C). For the deacylation step, a general base activates the catalytic/deacylating water molecule for a nucleophilic attack on the acyl-enzyme carbonyl carbon atom (C), resulting in a tetrahedral deacylation transition state (D) that finally releases the hydrolyzed penicilloate product after hydrolysis (E). The identity of the general base varies between the different β-lactamase classes and may also vary in the acylation or deacylation mechanism (Chen et al., 2007; Tooke et al., 2019a; Vandavasi et al., 2016).

This mechanism is reminiscent of that of serine proteases and indeed they possess similar structural key features. The catalytic serine is activated by a general base and performs a nucleophilic attack on the carbonyl carbon atom of the scissile β-lactam-amide bond, resulting in the acyl-enzyme intermediate via a tetrahedral transition state. Resolution of the acyl-enzyme involves activation of a catalytic/deacylating water by a general base to hydrolyze the ester bond. The three Ambler classes differ substantially in their amino acid sequence and therefore it is not surprising that they also differ in the mechanistically relevant identities of the bases and precise interactions of these (Tooke et al., 2019a). Furthermore, it is not clear which amino acid residues actually act as the general bases. Thus, the exact mechanism is still debated since the 1990s.

In the class A β-lactamases investigated in this study, activation for nucleophilic attack of Ser70 is mediated by either Lys73 or Glu166 via a water molecule (Tooke et al., 2019a). As early as the 1980s, Fourier transform infrared (FTIR) spectroscopy first indicated an acyl-enzyme intermediate for class A β-lactamases, and initial mutagenic studies replacing the active site serine have clearly demonstrated that Ser70 is involved in the hydrolysis of β-lactam antibiotics (Chen et al., 1996; Fisher et al., 1980). Moreover, the role of Ser130 as a general acid in the transfer of a proton to the β-lactam nitrogen of the substrate during acylation is well established (Scheme 1 B) (Galleni et al., 1995; Tooke et al., 2019a).

However, there has been controversy regarding the involvement of Lys73 and Glu166 in the hydrolysis mechanism of class A β-lactamases resulting in two main proposals that have been put forward (Majiduddin et al., 2002; Tooke et al., 2019a). They differ mainly in which of the two conserved amino acid residues, Lys73 or Glu166, acts as a general base in the acylation mechanism and thus activate Ser70 for nucleophilic attack on the β-lactam carbonyl carbon. In contrast, for the deacylation mechanism, there is agreement that Glu166 provides optimal conditions for deacylation of the enzyme-substrate complex via a water molecule (Fisher et al., 2005; Tooke et al., 2019a). Both acylation mechanism proposals are supported by experimental evidence from biochemical and crystallographic studies of enzyme mutant variants, as well as by modern computational simulations (Tooke et al., 2019a). In particular, high-resolution crystal structures of native enzymes as well as covalent enzyme substrate complexes obtained by X-ray or neutron diffraction provide direct evidence for protonation states in the active site of β-lactamases and thus about possible hydrogen bonds and proton transfers involved in the reaction mechanism.

Support for the involvement of Glu166 as a general base for acylation is provided by high-resolution X-ray and neutron diffraction structures of native CTX-M enzymes, showing that Glu166 is linked to Ser70 through a conserved water molecule by a hydrogen bonding network (Scheme 2 B) (Tooke et al., 2019a). Moreover, in these native structures, Lys73 is present in the protonated state and therefore unable to activate Ser70 (Scheme 2 A) (Chen et al., 2007; Tomanicek et al., 2011). This is also confirmed by combined quantum mechanical/molecular mechanical (QM/MM) studies on TEM-1 class A β-lactamase, according to which no stable species with neutral Lys73 and protonated Glu166 were observed in the simulations (Hermann et al., 2005; Hermann et al., 2009; Hermann et al., 2003).

Support for Lys73 acting as a general base for acylation is provided by mutational studies at the Glu166 position, as these mutant variants were able to form stable acyl-enzyme complexes but were unable for deacylation (Adachi et al., 1991; Guillaume et al., 1997; Strynadka et al., 1992). This is consistent with the essential role of Glu166 in the deacylation reaction but indicates the presence of an acylation mechanism via Lys73 (Fisher et al., 2005; Tooke et al., 2019a). X-ray and neutron diffraction structures of these Glu166 mutant and substrate acyl-enzyme complexes show that Lys73 is neutral/deprotonated and therefore able for activation of Ser70 (Pan et al., 2017; Vandavasi et al., 2017). This indicates that the binding of the substrate can sufficiently lower the pK_a of Lys73 side chain and thus deprotonate it (Scheme 2 C) (Tooke et al., 2019a). Further studies with alanine mutants of Lys73 showed that formation of an acyl-enzyme complex was impaired but formation of a non-covalent Michaelis complex was obtained, indicating an essential role of Lys73 in acylation (Tremblay et al., 2010). An *ab initio* QM/MM study of TEM-1 with penicillin supports the competitive coexistence of both a Lys73-dependent and a Glu166-dependent pathway (Meroueh et al., 2005). Another study demonstrated ligand-induced proton transfer using an acylation transition state analogue, revealing a low barrier hydrogen bond between Lys73 and Ser70 for stabilization (Scheme 2 C) (Nichols et al., 2015).

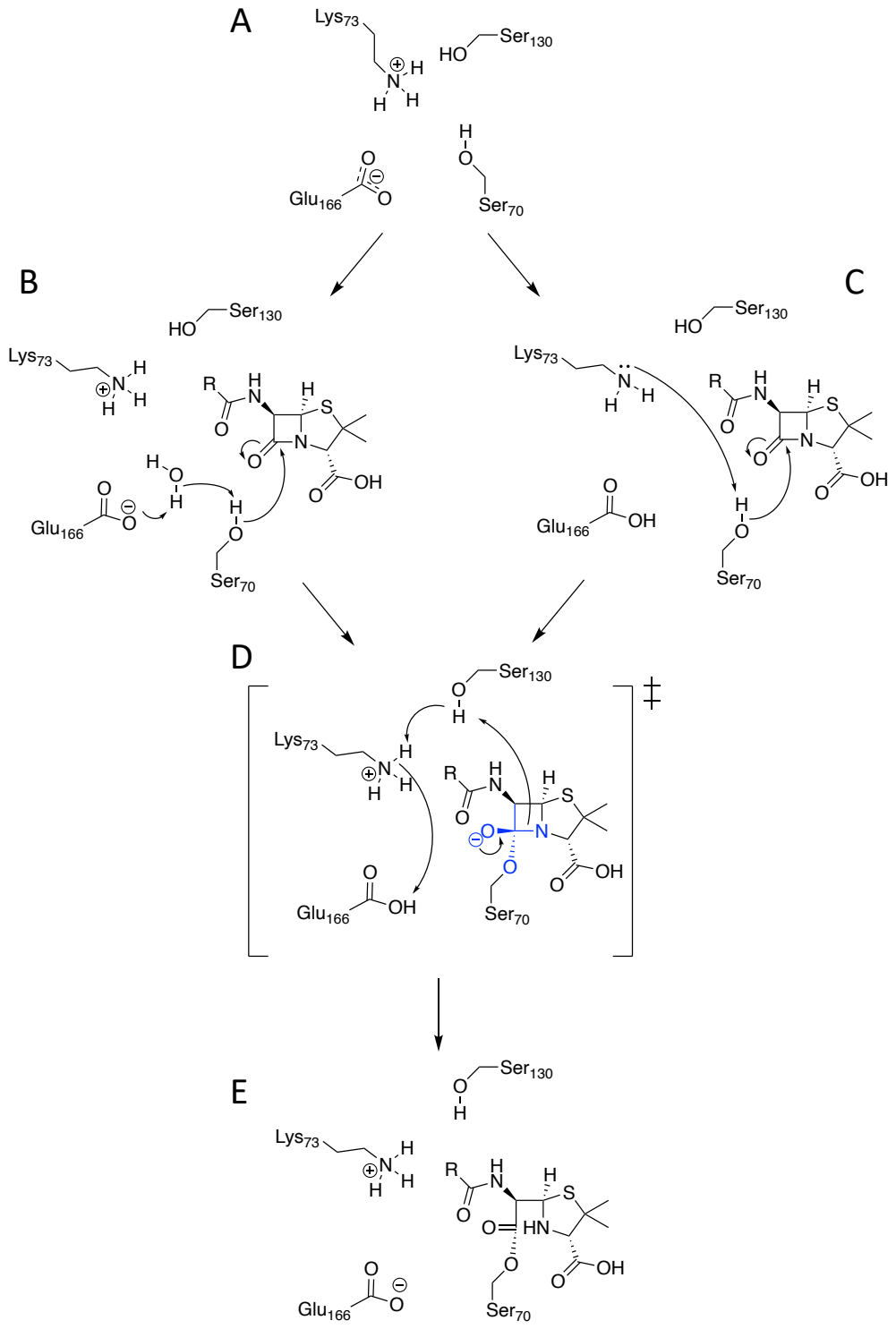

Scheme 2: Two potential acylation mechanisms of class A β-lactamases with either Lys73 or Glu166 acting as the general base for activation of Ser70, as proposed by several studies. (A) The active site of the native protein shows protonated Lys73 and deprotonated Glu166. Activation of Ser70 for nucleophilic attack on the amide carbonyl carbon atom of β-lactam then occurs either by (B) Glu166 via a water molecule or by (C) Lys73 after the protonation states have changed due to substrate binding and Lys73 has become neutral. This forms a tetrahedral acylation transition state (blue, D), which is resolved by protonation of the amide nitrogen by Ser130 resulting in the acyl-enzyme intermediate (E) (Tooke et al., 2019a; Vandavasi et al., 2016).

Despite the wealth of information on the mechanism, no clear conclusion can yet be drawn as to which of the two possible bases, Lys73 or Glu166, is ultimately responsible for the activation of the catalytic Ser70. This is due to the fact that mainly mutant variants or artificial substrate analogues have been used for structural characterization resulting in altered hydrogen bonding networks compared to the wild type enzyme or genuine substrates. Furthermore, QM/MM simulations are sensitive with respect to the initial model and the respective QM method.

Recent advances in fast-mixing technologies and the availability of X-ray free-electron lasers as well as bright X-ray synchrotrons facilitate the application of time-resolved serial femtosecond crystallography (TR-SFX) and time-resolved serial synchrotron crystallography (TR-SSX) (Martin-Garcia et al., 2016; Schulz et al., 2022). This eliminates the need for catalytically defective mutant variants and artificial substrate analogues to capture mechanistically relevant but transient reaction states. In particular, the major medical impact of β-lactamases and the rapid spread of antibiotic resistance have led first groups to conduct such studies on β-lactamases (Kupitz et al., 2017; Olmos et al., 2018; Schmidt et al., 2023; Wiedorn et al., 2018; Mateusz Wilamowski et al., 2022; Zielinski et al., 2022). However, the great diversity of β-lactamases and β-lactam antibiotics requires a comprehensive analysis of several β-lactamase enzyme and substrate classes to allow any general conclusions to be drawn.

1.5. β-lactamase inhibitors

Many β-lactam antibiotics are used in combination with β-lactamase inhibitors (BLI) such as tazobactam or avibactam because multidrug resistant bacteria will develop resistance to all β-lactam antibiotics unless the enzyme is inhibited (Craig & Andes, 2013; Takeda et al., 2007; Zhanel et al., 2014). Blocking resistance mechanisms by inhibiting resistance elements, such as β-lactamases, is a proven therapeutic strategy in medical practice (Wright, 2011). The development of BLIs enables already approved antibiotics to restore efficacy to otherwise resistant pathogens when combined with an inhibitor (González-Bello et al., 2019). These inhibitors are able to effectively acylate most serine-β-lactamases and form long-lived acyl-enzymes, thereby blocking the β-lactamase function.

The first generation β-lactam-based β-lactamase-inhibitors clavulanic acid, sulbactam and tazobactam were approved in the 1980s and 1990s (Bush & Jacoby, 2010; Vena et al., 2019; Watkins et al., 2013) but they only inhibit a subset of serine β-lactamases and are increasingly susceptible to evolved resistance. They act irreversibly and form a stable acyl-enzyme complex with serine β-lactamases. Even most extended-spectrum β-lactamases (ESBLs) are inhibited by β-lactam inhibitors, making the clinical use of classic β-lactam/β-lactamase inhibitor (BLBLI) combinations such as amoxicillin-clavulanic acid, ampicillin-sulbactam, and piperacillin-tazobactam effective against ESBL producers in the absence of other resistance mechanisms (Paterson & Bonomo, 2005; Pitout & Laupland, 2008; Rodríguez-Baño et al., 2018).

However, expression of multiple β-lactamases can impede therapy with classic BLBLIs as demonstrated in a *Klebsiella pneumoniae* isolate expressing CTX-M and OXA enzymes (Both et al., 2017).

The susceptibility of β-lactams and β-lactam-based inhibitors to β-lactamases has long sparked interest in the development of non-β-lactam inhibitors. A notable recent advance was the discovery of diazabicyclooctanes (DBO) such as avibactam and relebactam, which were approved in 2015 and 2019, respectively (Andrei et al., 2019; Liscio et al., 2015). Unlike previous inhibitors, these non-β-lactam BLIs bind in a reversible way that the active BLI can be released after re-cyclization and thus can inhibit additional β-lactamases. They exhibit broader specificity than previous BLIs and can inhibit Ambler class A (including KPC), C and D serine β-lactamases, but not class B metallo-β-lactamases (Bush & Bradford, 2016).

However, as the clinical incidence of metallo-β-lactamases increased, the identification of effective inhibitors targeting these enzymes became more important (Mojica et al., 2022; Wright, 2011). This resulted in the development of another new class of BLIs represented by boronate-based compounds such as vaborbactam and taniborbactam (Hecker et al., 2015; Krajnc et al., 2019). The inhibitory effect of boronic acid derivatives on serine proteases has long been known and served as a basis for the study of similar effects on serine β-lactamases, because the active sites of these enzymes share the same key structural features required for the catalytic mechanism (Nakatani et al., 1975). Subsequently, inhibition of serine β-lactamases by various boronic acid derivatives was demonstrated as early as the 1980s (Beesley et al., 1983; Cartwright & Waley, 1984; Kiener & Waley, 1978). Additionally, boric acid itself is known to function as a reversible competitive inhibitor of serine-β-lactamases (Beesley et al., 1983; Kiener & Waley, 1978).

Nevertheless, it took until 2017 for Vabomere (meropenem-vaborbactam combination), the first inhibitor in this class and the first carbapenem/β-lactamase-inhibitor combination with activity against carbapenemases in CRE infections, to actually be approved for clinical use by the FDA (Lee et al., 2019). Boronate-based inhibitors are of particular interest for two reasons. First, Boron has the ability to mimic the tetrahedral transition state of the catalytic reaction mechanism of serine β-lactamases, and second, unlike their predecessors, these BLIs can also inhibit some clinically important metallo-β-lactamases (Krajnc et al., 2019).

Moreover, the application of 3-aminophenylboronic acid as a potentiator in disc diffusion sensitivity assays facilitates the identification of *Klebsiella pneumoniae* carbapenemase (KPC)-type β-lactamase positive isolates. This compound enhances the inhibition zone diameter on the agar plate, enabling differentiation from isolates that produce other types of β-lactamases (Doi et al., 2008; Prester et al., 2023).

Because of these properties, further investigation and optimization on boronate-based BLIs is certainly of high relevance. The ability to repurpose inhibitors of protease enzymes, such as the boronate based proteasome inhibitors bortezomib and ixazomib to inhibit serine β-lactamases, supports the particular importance and potential of boronate-based BLIs (Perbandt et al., 2022). In addition, an increasing number of these boronate-based BLIs have recently been investigated (FDA.gov, 2018; Hecker et al., 2015; Krajnc et al., 2019; Lomovskaya et al., 2017), such as mono- and bicyclic boronates that provide inhibition of carbapenemases like KPC-2 β-lactamase (Tooke et al., 2020). This is particularly important as the development of new BLIs is crucial for the treatment of extensively or pandrug-resistant pathogens due to the continued emergence of extended-spectrum β-lactamases and carbapenemases.

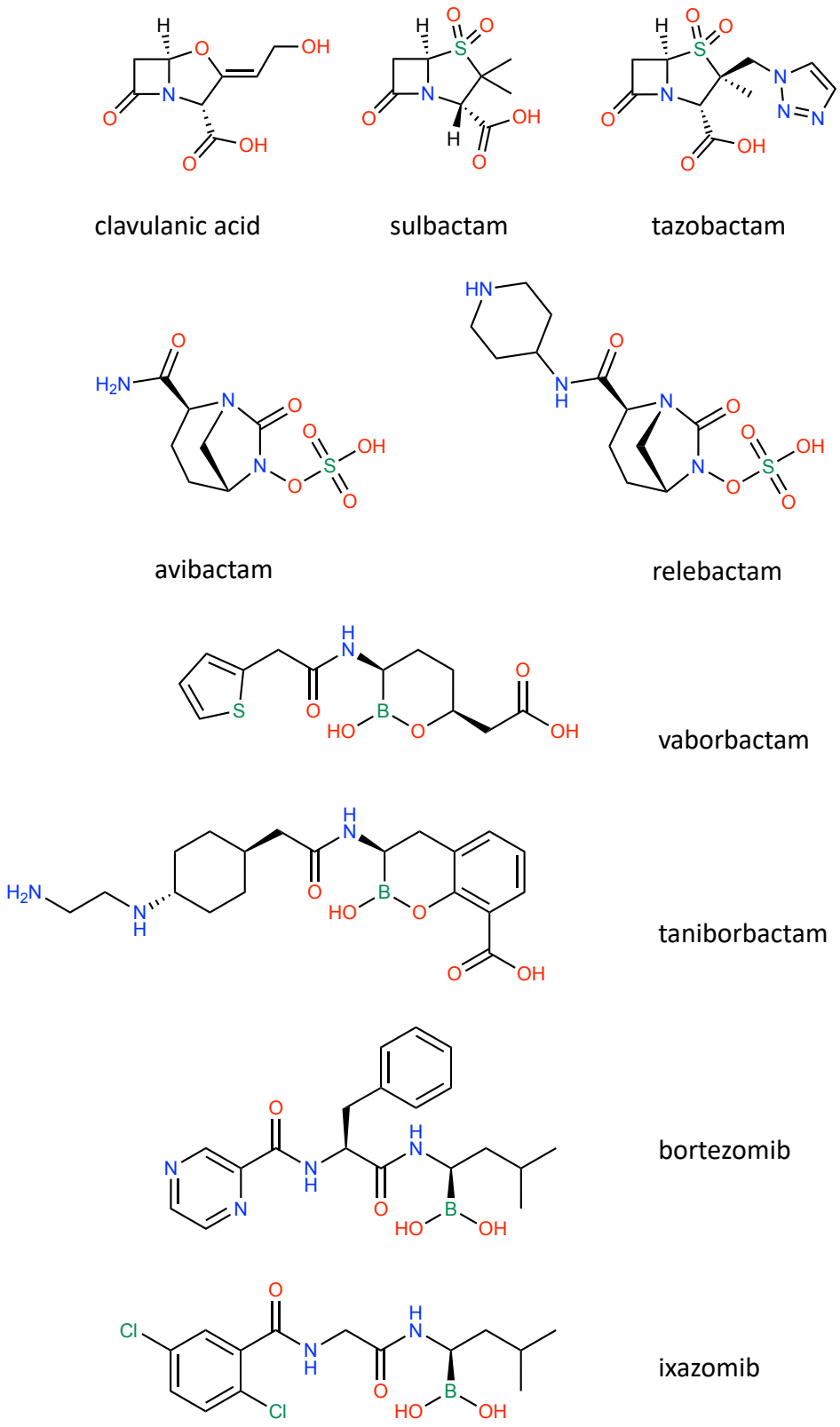

Figure 6: Chemical structures of several β-lactamase inhibitors. The classic β-lactam-based inhibitors clavulanic acid, sulbactam, tazobactam, the diazabicyclooctane inhibitors avibactam and relebactam, the monocyclic and bicyclic boronic acid derivative inhibitors vaborbactam and taniborbactam, as well as the proteasome inhibitors bortezomib and ixazomib are shown.

1.6. X-ray Crystallography

1.6.1. The meaning and origin of X-ray crystallography

The correlation of regulation, mechanism, and function of proteins with their atomic molecular structure has become a major interest in modern biochemistry and molecular biology (McPHERSON, 1991). Understanding these complex relationships is essential for the understanding of biological systems in detail and for many practical applications such as disease prevention and treatment in modern medicine, including antibiotic resistance management.

Proteins represent by far the most important molecules in the biological world, and their function is often closely related to the atomic structure and the interaction with other biological components (Yang et al., 2015). Insights into the atomic structure allow conclusions to be drawn about the specificity of active sites and binding sites, providing valuable information for biotechnological and medical research, such as structure-based drug design (Ferreira et al., 2015). Proteins are built from a set of only 20 standard proteinogenic amino acids (excluding selenocysteine and pyrrolysine) that differ chemically only in their side chains. Nevertheless, the wide variety of compositions in a primary chain allows for tremendous structural diversity and variety of proteins. Thus, proteins can handle important tasks in many parts of cellular life, such as enzymatic catalysis of reactions in metabolism as well as in DNA replication. Proteins are also an important component of the immune system, are involved in cell signaling and signal transduction, and can form transport proteins or structural proteins necessary for cellular integrity. Because proteins are generally too small to observe with a light microscope, various alternative methods have been developed to determine the unique three-dimensional structure of proteins and thus also to draw important conclusions about their function and how it can be affected. These methods include X-ray crystallography (Kendrew et al., 1958; Shi, 2014), electron crystallography (Shi et al., 2013), neutron crystallography (Blakeley et al., 2008; O'Dell et al., 2016), X-ray scattering methods (SAXS) (Lipfert & Doniach, 2007; Mertens & Svergun, 2010), cryo-electron microscopy (Danev et al., 2019; García-Nafría & Tate, 2020; Yip et al., 2020) and nuclear magnetic resonance spectroscopy (NMR) (Cavalli et al., 2007; Kay, 2011).

To date, X-ray crystallography is the most widely used method for the determination of three-dimensional protein structures with atomic resolution for proteins of any size. Thus, about 85.7 % of the more than 202.764 structures in the Protein Data Bank (PDB) have been elucidated by this method (Berman et al., 2000; RCSB.org on 27.03.2023). However, it should be noted that cryo-EM has caught up in the number of PDB structures published annually in recent years. For example, in 2022, 4113 new structures were determined using cryo-EM, which is almost half the number of the 9846 structures determined using X-ray crystallography (Berman et al., 2000; RCSB.org on 27.03.2023). Despite the many entries of already solved structures in the PDB, we are far from knowing the structure, let alone the function, of all known proteins. Recently developed deep learning algorithms like the neural-network based system AlphaFold are trained with the existing database of protein structures and can predict unknown three-dimensional structures of proteins based on their amino acid sequence with relatively high precision (Jumper et al., 2021). Current limitations of these algorithms are the prediction of interactions with protein partners, multimers and post-translational modifications. In addition, the prediction of interactions with metal ions, cofactors and ligands, which is a very crucial part of structural biology and crystallography, is still limited. However, the latest research indicates that this could also be possible at some point (Evans et al., 2022; Hekkelman et al., 2023).

X-rays were discovered by Wilhelm Conrad Röntgen in 1895 and have been fundamental to the investigation of molecular processes and atomic structures ever since (Röntgen, 1895). In 1912, Max von Laue and colleagues confirmed that X-rays are a form of electromagnetic wave radiation by exposing a copper sulfate crystal with X-rays and observing the resulting diffraction pattern of well-defined spots (Friedrich et al., 1913).

Crystals are regular arrangements of atoms. When exposed to X-ray waves, they scatter them mainly through their electrons, which generate secondary spherical waves by elastic scattering. Since the scatterers (electrons) are regularly arranged in a crystal, they also produce a regular array of spherical waves. These waves cancel each other out in most directions by destructive interference, but in some specific directions, determined by Bragg's law, they add constructively. This fundamental discovery was made by Henry and William Bragg (Bragg & Bragg, 1913; Bragg, 1912), allowing information about the three-dimensional structures of any crystallized molecule to be obtained from the diffraction pattern. Therefore,

the arrangement in a crystal acts like an amplifier of the signal. The waves with constructive interference appear on a detector/film as spots called reflections or Bragg peaks, resulting in a diffraction pattern.

Father and son Bragg interpreted the diffraction patterns as the result of reflections of X-rays from the evenly spaced planes of the crystal. They derived the previously mentioned Bragg's law from these findings as a special interpretation of Laue diffraction, where specular reflected waves from the various crystal lattice planes interfere constructively at specific incident angles and wavelengths:

$$n\lambda = 2d \sin\theta$$

Equation 1: Bragg's law for constructive interference in X-ray diffraction.
Where n is any integer, λ is the wavelength of the beam, d is the distance between diffracting crystal planes and θ is the incidence angle of the beam.

They found that the diffraction phenomenon could be considered geometrically as shown in Figure 7. The Bragg condition for constructive interference of X-ray waves by scattering in a crystal is then obtained as follows: The crystal is considered as crystal planes uniformly distributed with the spacing of d. When an X-ray wave with the incident angle θ hits the crystal, it is specularly scattered by the electrons of the atoms of the individual crystal planes. In Figure 7 this is exemplarily shown with 2 atoms A and B. Wave 2 obviously passes a longer distance (by CB and BD) than wave 1. Based on the geometric consideration of the path-difference, two right triangles in the form of ABC and ABD can be formed and the sides CB and BD can be calculated by $d \sin\theta$ respectively. Wave 2 thus travels a distance $2d \sin\theta$ longer than wave 1. If this path-difference is a multiple n (any integer) of the wavelength λ, then the two waves arrive in phase at the detector and thus have constructive interference and contribute to the diffraction pattern. In such a case the Bragg condition from Equation 1 is fulfilled. Using this method, William Henry Bragg and William Lawrence Bragg succeeded in solving the first crystal structure on an atomic level, which was that of a sodium chloride crystal (Bragg & Bragg, 1913). With this technique, it was possible for the first time to determine the atomic bond distances and bond angles, making this method one of the biggest breakthroughs in scientific research. Nevertheless, it took several years before the atomic structure of the first protein, sperm whale myoglobin, was solved in 1958 (Kendrew et al., 1958).

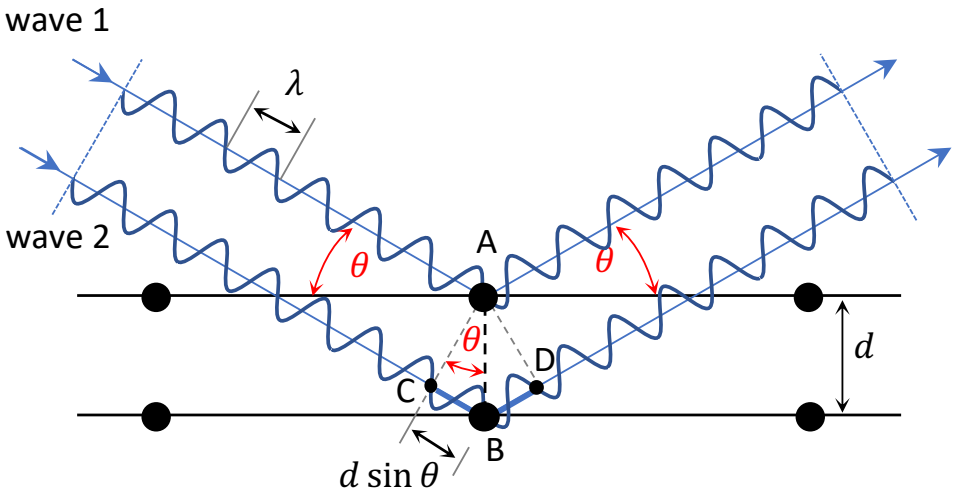

Figure 7: Schematic representation of Bragg diffraction. Where λ is the wavelength of the beam, d is the distance between diffracting crystal planes and θ is the incidence angle of the beam.

1.6.2. Protein crystallization

To determine a protein structure by X-ray crystallography, a protein crystal has to be grown first. Crystallization is a phase transition phenomenon that can be visualized by a phase diagram, which indicates the state of the protein (liquid, crystalline, or precipitate) under a variety of crystallization parameters (Figure 8). Crystallization is so complex because it is not possible to know the individual conditions of the phase diagram in advance. Ultimately, it also represents only a small part of the parameters relevant to crystallization.

The phase diagram shows an undersaturated area, where the protein is fully soluble, and a supersaturation area, that can be divided into three zones represented by the precipitation zone, where proteins form amorphous aggregates, the nucleation zone, where both nucleation and growth of crystals occur, and the metastable zone, where only crystal growth is sustained. Various techniques are used to reach the nucleation zone, which is crucial for crystallization. The most commonly used techniques include (A) batch, (B) vapor diffusion, (C) dialysis, and (D) free-interface diffusion (Figure 8) (Chayen & Saridakis, 2008). In the batch process, protein solution and crystallizing agent are mixed to directly reach the nucleation zone and allow crystal nucleation and growth to occur. Vapor diffusion is the most widely used method of crystallization. A drop of the protein solution is mixed with the crystallizing agent and equilibrated in a sealed chamber (e.g., sealed 24 well plate) against a reservoir containing the crystallizing agent at a higher concentration than in the drop. The advantage of this method is that both the concentration of protein and crystallizing agent increase over time

due to vapor diffusion, and thus a larger overall area of the phase diagram is covered. This increases the probability that the nucleation zone will be reached. The dialysis method separates the protein solution from the solution containing the crystallizing agent by a semipermeable membrane. Thus, the concentration of the crystallizing agent in the crystallization solution is slowly increased, while the protein concentration remains constant until the nucleation zone is eventually reached. Free interface diffusion is a technique in which the protein and crystallizing solutions are positioned side by side and a concentration gradient that changes with time is established by slow diffusion of the solution into each other. However, not all methods always lead to protein crystals, as it can also happen that the nucleation zone cannot be reached at all or only with a certain method.

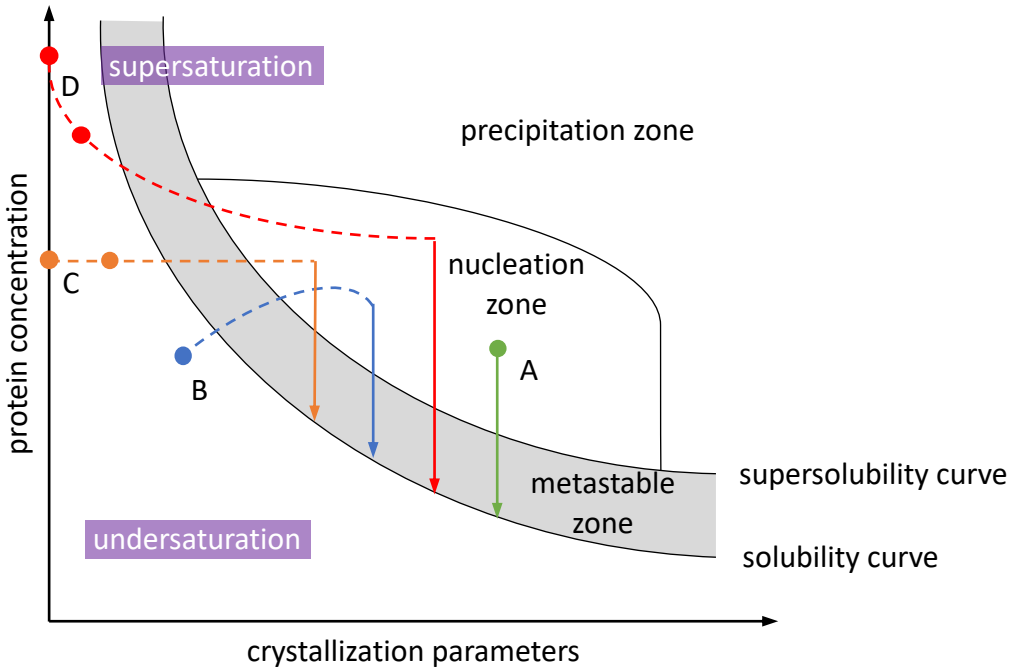

Figure 8: Schematic representation of a phase diagram depicting the kinetics of protein crystallization of the four main techniques (A) batch, (B) vapor diffusion, (C) dialysis, and (D) free-interface diffusion. The state of the protein is shown depending on the concentration of the protein against the crystallization parameters. A protein solution becomes supersaturated, when it is pushed above its solubility limit by increasing the concentration of the protein and/or the crystallizing agent. Each crystallization technique involves a different pathway to reach the nucleation and metastable zones. The colored circles represent the starting conditions with two alternative starting points for dialysis and free-interface diffusion as the starting solution can contain either protein alone or protein already mixed with the crystallizing agents. Adapted from Chayen and Saridakis (2008).

1.6.3. Conventional single crystal protein X-ray crystallography

Conventional single crystal protein X-ray crystallography, often referred to as macromolecular X-ray crystallography (MX), generally provides static snapshots of systems at equilibrium (Brändén & Neutze, 2021). X-rays relevant for protein crystallography are in a wavelength range of ~0.8 – 2.3 Å (Rupp, 2009). Originally, sealed vacuum tubes like the Coolidge tube were used as X-ray sources (Coolidge, 1913). For this, a filament cathode and an anode were located in a sealed vacuum tube. When a high voltage current was applied, electrons generated at the cathode accelerated to the anode and emitted X-rays upon collision. Due to the high stress on the anode, this method was later improved by using a rotating anode target that rotates at high speed to efficiently distribute and dissipate the generated heat. This allowed the use of higher energies and thus the emission of X-rays with higher intensities. Such X-ray sources are still frequently used nowadays as in-house sources and thus allow simple X-ray crystallography experiments in the laboratory. However, the intensity of these X-rays is much lower than that of a synchrotron and the emitted wavelength is fixed by the choice of the rotating anode material.

In conventional X-ray crystallography, synchrotrons are currently the X-ray source of choice for obtaining the best diffraction data from protein crystals. These are facilities that accelerate bunches of electrons with several GeV in energy and maintain them in a storage ring. Electrons are kept in orbit by bending magnets. The resulting acceleration causes the electrons to emit intense polychromatic radiation from soft UV to hard X-rays at a defined angle tangential to the ring. Monochromators can then be used to selectively pass the wavelength required for a particular experiment. Due to the high intensity of X-rays generated by modern 3rd generation synchrotron sources, radiation damage of crystals has become a major concern. Therefore, almost all conventional single crystal X-ray crystallography experiments are nowadays performed under cryogenic conditions to minimize radiation damage (Garman & Schneider, 1997; Rupp, 2009). Upon sample freezing, ice crystals can form, creating strong diffraction patterns that can contaminate the diffraction pattern of the protein crystals (Rupp, 2009). To prevent ice crystal formation during freezing, it is necessary to apply a cryoprotectant to the crystals beforehand (Pflugrath, 2015). The choice of cryoprotectant must be determined in advance.

In conventional protein crystallography, a single protein crystal with dimensions typically in the order of 50 µm – 500 µm is mounted on a goniometer and exposed to an X-ray beam to collect diffraction patterns (Figure 9) (Hunter et al., 2011). During this procedure, the crystal is kept at cryogenic temperature and rotated in the X-ray beam to obtain a complete dataset. At modern synchrotron facilities such as PETRA III (DESY, Hamburg, Germany), a complete dataset can be collected in a few minutes.

After diffraction data collection, the data is processed, which starts with the determination of the crystal system and the unit cell dimensions as well as the orientation of the crystal in the beam. Then each spot of the diffraction pattern is indexed and the intensity is measured. The intensity of the diffracted spots depends on both the amplitude and the phase difference of the diffracted waves (Smyth & Martin, 2000). The amplitude and phase can be used to determine the structure factor, a parameter from which an electron density map can be calculated that provides information about the arrangement of atoms in the unit cell. While amplitudes can usually be calculated using the square root of the intensity, the phase information cannot typically be obtained directly from the diffraction data, which represents a fundamental limitation in macromolecular crystallography.

The most common method for solving the phase problem is molecular replacement, which requires the availability of an already known homologous protein structure (Rossmann, 1990). The method involves the reverse crystallographic calculation. Thus, the phases are extracted from the structure factors of the known coordinates and applied to the new dataset to calculate the new structure factors. Therefore, this method always introduces a bias towards the molecular replacement model.

An alternative method for structures where no homologues are known is isomorphous replacement, where a dataset of a native crystal and a dataset of a derivative crystal with introduced heavy atoms are collected (Ke, 1997; Otwinowski, 1991). The differences in the scattering amplitudes can then be used to calculate the phases.

Another alternative is anomalous X-ray scattering (Multi-wavelength anomalous diffraction, MAD or single-wavelength anomalous diffraction, SAD), which is used to determine the phase and the substructure of the anomalously diffracting atoms and thus the phase for the entire molecule (Hendrickson et al., 1985; Hendrickson & Teeter, 1981). Often seleno-methionine, which has a different scattering power, is used to introduce anomalous scattering atoms into protein crystals.

With the obtained amplitudes and phases, the structure factors can then be calculated using the fast Fourier transform method (Ten Eyck, 1973). Subsequently, a protein model can be placed in the obtained electron density map. The fit between model and electron density can be improved with multiple rounds of manual and computational refinement (Liebschner et al., 2019). Once the structure refinement is finished, it can be deposited in the PDB and is thus accessible to everyone. X-ray crystallography structures have several quality factors for the data collection and the refined structures that provide an indication of the quality of the data and the agreement of the model with the experimental data.

1.6.4. Serial X-ray crystallography

In contrast to single crystal macromolecular X-ray crystallography, in which a single crystal is typically rotated to obtain a complete diffraction dataset as described in section 1.6.3, serial crystallography exposes thousands of microcrystals in random orientations at room temperature to collect a complete dataset (Barends et al., 2022; Chapman et al., 2011; Zielinski et al., 2022).

As the brightness of new synchrotron radiation sources (3rd and 4th generation) increased, the minimum crystal size required to measure Bragg spots steadily decreased (Smith et al., 2012; Su et al., 2015). The achievable high flux densities made it necessary to distribute the total X-ray dose either by exposing multiple positions of a single crystal or by exposing multiple microcrystals to avoid global and specific radiation damage (Riekel et al., 2005). By exposing and measuring multiple crystals at random orientation, in sequence and each crystal only once to collect a complete merged dataset, this type of data collection is described as serial X-ray crystallography. When performed at a synchrotron, it is called serial synchrotron crystallography (SSX).

Another advance in recent years has been the development of X-ray free electron lasers (XFELs) with a peak brilliance of about 10 orders of magnitude higher compared to 3rd generation synchrotrons that has enabled the use of even smaller crystals in the nanometer regime (Bostedt et al., 2016; Liu & Lee, 2019). XFELs are usually large facilities that produce fully coherent, ultrabright, femtosecond X-ray pulses by passing high energy free electrons through periodic alternating magnetic fields (Liu & Lee, 2019; Madey, 1971). When serial X-ray crystallography experiments are performed at an XFEL with its femtosecond X-ray pulses,

the term serial femtosecond crystallography (SFX) is used to distinguish it from serial synchrotron crystallography (SSX).

The difference between the two methods lies mainly in the exposure time and the intensity of the X-rays, which, however, cause major differences in their application. X-ray intensity at modern 3rd and 4th generation synchrotron sources enables exposure times for microcrystals in the low millisecond to microsecond range in SSX. Thus, the exposure time is much longer than at XFELs for SFX, which is typically in the femtosecond range. This influences especially the maximum temporal resolution of time-resolved experiments (Zielinski et al., 2022).

Radiation damage is an unavoidable phenomenon in macromolecular X-ray crystallography experiments. Nowadays, two types of radiation damage are known. The global radiation damage, which mainly corresponds to a degradation of the diffraction properties of a protein crystal, and the specific damage, which mainly corresponds to the breakage of covalent bonds (for example disulfide bridges), decarboxylation of acidic residues, the photoreduction of metal centers, and the photoreduction of photoactive protein chromophores (Burmeister, 2000; Gotthard et al., 2019; Ravelli & McSweeney, 2000).

While cryogenic conditions are used in conventional X-ray crystallography to increase the absorbed dose that a crystal can tolerate before the radiation affects its diffraction properties (see Section 1.6.3), in serial X-ray crystallography a crystal is exposed only once and therefore does not necessarily need to be cooled. The radiation damage is distributed among all measured crystals, so that the collection of a complete diffraction dataset is possible even at room temperature. Global and specific radiation damage are decoupled under cryogenic conditions (Gotthard et al., 2019). These conditions minimize mainly the global damage, while the specific damage may increase due to the prolonged X-ray exposure time.

In contrast, global and specific radiation damage are again coupled at room temperature, making specific radiation damage a much smaller problem (Gotthard et al., 2019). Therefore, serial crystallography structures show less specific radiation damage compared to conventional cryoMX structures, since they are exposed to the X-rays only once and for a short time.

This even extends to the fact that the intense short XFEL pulses in SFX experiments are powerful enough to destroy the crystal. However, the phenomenon of "diffraction-before-destruction" is observed, as the radiation damage (destruction) occurs only after the

diffracted radiation has left the sample (Chapman et al., 2014; Chapman et al., 2011; Neutze et al., 2000). Moreover, the diffraction signals were shown to be self-terminating when measured with XFEL pulses, since the diffraction intensity decreases when the crystalline order is damaged by the radiation damage (Barty et al., 2012).

In addition to the potential artifacts induced by specific radiation damage, a second potential problem with X-ray crystallography at cryogenic conditions is the fact that the cooling process can artificially trap biologically inactive conformations of amino acid side chains (Gotthard et al., 2019). This can result in the misinterpretation of enzyme mechanisms. Therefore, it is advisable to perform such studies using serial X-ray crystallography methods at room temperature. This has also made the development of time-resolved X-ray crystallography methods at synchrotron sources attractive again.

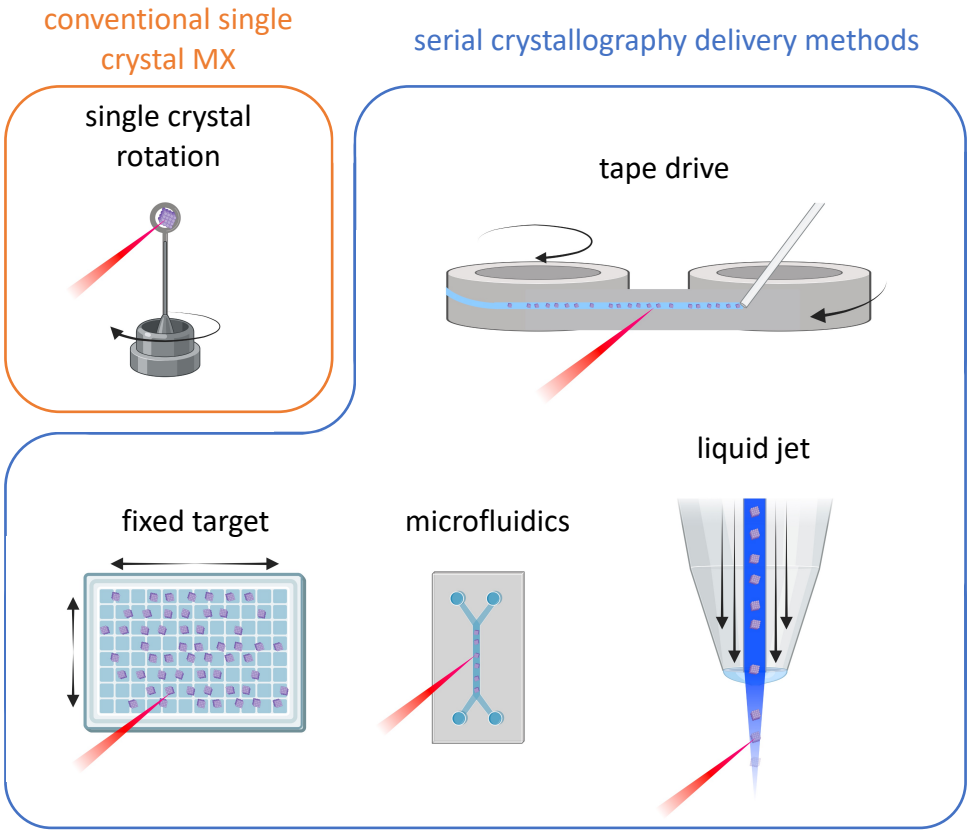

Figure 9: Schematic representation of conventional single crystal MX in comparison with serial crystallography sample delivery methods. While in conventional rotation crystallography only a single protein crystal (purple cube) is rotated during diffraction data collection, serial crystallography requires new methods to continuously deliver new crystals into the X-ray beam (red line). These sample delivery methods include fixed target approaches on a chip, liquid jet injectors, hybrid methods such as tape drive and microfluidic devices. Created with BioRender.com (2022).

To prevent re-exposure of destroyed or damaged crystals, it requires entirely new sample delivery methods that rapidly provide large quantities of microcrystals passing through the X-ray beam (Figure 9).

Starting with liquid jet injectors, the first sample delivery technique utilized at XFELs. It is best suited for SFX with short and intense X-ray pulses in the femtosecond range, but less ideal for SSX due to the fast flow and high sample consumption. Liquid jet injectors come in a variety of configurations. The gas dynamic virtual focusing nozzle (GDVN) is a device that uses a gas sheath to focus a crystal suspension stream into a jet with a diameter of a few micrometers (Martiel et al., 2019). Further developments of the device resulted in the double-flow focusing nozzle (DFFN), which uses an additional liquid sheath around the crystal suspension stream to increase the focusing, reduce the sample consumption, and stabilize the flow (Oberthuer et al., 2017). Liquid jet injectors also allow the use of viscous media such as LCP. At the same time, this usually reduces the flow rate, making this approach is also suitable for SSX (Weierstall et al., 2012).

Fixed target approaches are typically either mesh loops on conventional spine mounts for SSX or one of the various solid-support solutions that can be either used at SSX or SFX (Schulz et al., 2022). The solid-support solutions are mostly chips with notches for the crystals (Gati et al., 2014; Meents et al., 2017; Owen et al., 2017). Moving these crystals into the X-ray beam requires a setup with high positioning accuracy and extreme dynamic capabilities. SFX equipment usually has to allow faster translation of the crystal mounts and has to withstand the extremely bright XFEL pulses. The advantage of solid support devices is the very low sample consumption compared to the other methods and the high hit rate of up to 100 %. In addition, the crystals can also be imaged several times in SSX experiments, which allows unique data collection schemes such as the hit-and-return (HARE) approach (Schulz et al., 2018).

Microfluidic devices are 3D printed and X-ray compatible designs with multiple channels. Syringe pumps allow the crystal suspensions to pass through these channels and into the X-ray beam while still in a closed environment. These devices, although still underrepresented, allow SSX data collection of protein microcrystals with very high hit and indexing rates while keeping the sample consumption low (Monteiro et al., 2020).

Finally, hybrid methods such as the tape drive setups (based on a conveyor belt apparatus) are also used for SSX (Beyerlein et al., 2017; Zielinski et al., 2022) and SFX (Fuller et al., 2017).

Either individual drops or a stream of the microcrystal suspension are deposited on a Kapton film and transported into the X-ray beam via the movement of the tape.
All of these methods deliver single microcrystals in such a rapid rate that collection of complete diffraction datasets is facilitated because only a single diffraction pattern is recorded from each microcrystal in a microcrystal suspension. The development of SFX and SSX has since introduced a new era for protein structure determination.

1.6.5. Time-resolved serial crystallography

Enzymes in crystals, can maintain the conformational flexibility required to carry out biological processes, making crystallographic studies of protein dynamics possible (Martiel et al., 2019). Previously, mechanisms of proteins were unraveled by combining conventional structural biology approaches with other biochemical or biophysical methods, resulting in mutation studies, studies of substrate analogs, or freeze-trapping experiments (Schulz et al., 2022). Macromolecular X-ray crystallography usually provides static snapshots of biological systems at equilibrium and protein structures derived from mutant variants or substrate analogs and inhibitors may reflect artifacts that are present only because of the artificially introduced modifications (Brändén & Neutze, 2021). For a complete insight into the function of an enzyme, it is therefore important to combine the structural information with temporal changes during the enzymatic reaction. Furthermore, the true dynamics of the protein can only be displayed by the wild-type enzyme, as it is not affected by artificially introduced modifications. This information can reveal metastable intermediates and previously hidden features of protein function that can provide new insights into catalysis, allostery, oxidation states, side chain motions, isomerization reactions, molecular breathing, and molecular binding events (Schulz et al., 2022).

Theoretically, it is possible to trap reaction states of an enzyme either by soaking a typical protein crystal for X-ray single crystal crystallography with the substrate or by inducing light-activated reactions with a laser pump and subsequently freeze the crystal after defined time points. However, the disadvantage is that diffusion in the large crystal takes a relatively long time (Schmidt, 2013), which leads to an uneven distribution of reaction states in the crystal. Similarly, in laser-pumped experiments, laser penetration may not be sufficient for large crystals to activate all active sites/caged compounds. These limitations lead to an overlapping

of the different reaction states in the collected protein structure, which ultimately prevents a clear conclusion about the reaction state. Since it takes a few milliseconds for a crystal to freeze, thermodynamically stable states are trapped. However, the goal of time-resolved crystallography is to detect kinetic transition states that may not be thermodynamically stable.

Another important consideration of time-resolved experiments is reaction kinetics, as intermediate states can only be observed if they are sufficiently populated in the active site of the enzymes (Schmidt, 2013). Assuming a chemical kinetic reaction proceeds according to the typical Michaelis-Menten pattern as shown in Equation 2. If the reaction kinetics of individual steps are particularly fast and substrate diffusion times are relatively slow (e.g., large crystals), the preceding intermediate states may not obtain a sufficiently high population to be observed with TRX. To observe reactions with a fast turnover, it is therefore crucial that the concentration of the substrate in the crystal is very high right at the beginning. This can only be achieved by using microcrystals.

$$E + S \overset{k_1}{\leftrightarrow} [ES] \overset{k_2}{\rightarrow} [E-S] \overset{k_3}{\rightarrow} [EP] \overset{k_4}{\rightarrow} E + P$$

Equation 2: Kinetic mechanism of a hypothetical enzymatic reaction similar to β-lactamases. Where $E + S$ is the free enzyme and the substrate, $[ES]$ the Michaelis-Menten complex, $[E - S]$ the covalent bound acyl-enzyme intermediate, $[EP]$ the enzyme product complex, $[E + P]$ the free enzyme and product, and k_n as the respective rate.

Advancements in serial crystallography techniques at synchrotrons and free-electron lasers have expanded the range of applicable crystal sizes for macromolecular crystallography, encompassing the low micro- and nanometer scale. The use of microcrystals shortens diffusion times tremendously and allows for homogenous reaction initiation, which has enabled the measurement of many new interesting biological targets (Schmidt, 2013). The same applies to crystal penetration of laser beams for reaction initiation.
Thus, time-resolved serial crystallography (TRX) enables to capture structure and dynamics in various biomolecules. Nevertheless, the delay time and temporal resolution limiting factors such as diffusion times and laser penetration have to be considered for TRX.

Reaction initiation often is triggered via laser pump or diffusion of the substrate via mix-and-inject (Olmos et al., 2018; Schmidt, 2013) mix-and-diffuse (Beyerlein et al., 2017; Zielinski et

al., 2022), and Liquid application method for time-resolved analyses (LAMA) (Mehrabi et al., 2019a). All sample delivery techniques for serial crystallography already presented in section 1.6.4 are suitable for this purpose.

Liquid jet injectors for TRX can mix the microcrystal suspension with the substrate already in the nozzle, thus the time for the solution to reach the X-ray interaction region can be considered as the delay time. In addition, a laser beam can be directed at the liquid jet to initiate a light-induced reaction. For fixed target approaches, each well of the chip can be laser pumped, or the substrate can be deposited using LAMA technique (Mehrabi et al., 2019a). The chip can be placed in an environmental control box and thus diffraction data can be collected at different temperatures, enabling 5D crystallography (Mehrabi et al., 2021). Recently, it has become possible to perform TRX experiments with microcrystals on mesh loops at microfocus beamlines initially designed for conventional rotation crystallography data collections. This is facilitated by automation devices such as the so-called spitrobot, a device that sprays substrate solution via LAMA nozzles onto microcrystals that are on a mesh mounted on a standard spine base to initiate the enzymatic reaction and plunge-freezes the microcrystals after defined time points (Mehrabi et al., 2022). This approach, while fast and simple, generally requires cryo-conditions and thus has the some disadvantages of cryo X-ray crystallography.

Microfluidic devices can have an additional channel for a substrate to mix with the microcrystal suspension (Monteiro et al., 2020). For tape drive devices, the microcrystalline suspension can pass through different environments (e.g. temperature, different gases) or is pumped with a laser while the tape transports the droplets into the X-ray beam. In addition, mix-and-diffuse or drop-on-drop methods can be used to mix the microcrystal suspension with a substrate solution in the nozzle or directly on the Kapton tape, so that the path from mixing to the X-ray beam can be considered as the delay time for time-resolved studies (Beyerlein et al., 2017; Fuller et al., 2017).

In principle, laser pumped TRX can achieve much shorter delay times. However, caged compounds or light-induced enzymatic reactions that are suitable for laser activation are necessary for this but very rare. Therefore, laser induced TRX is not an option for the determination of structure and dynamics of many biologically relevant and interesting enzymes. However, if very short delay times are desired for fast light-inducible reactions with

a time resolution in the femtosecond regime, this method in combination with SFX is particularly suitable.

Since most reactions in biological systems cannot be initiated by light, it must be achieved by simple mixing of protein crystals and substrate. The diffusion time for the distribution of a substrate in very small microcrystals is fast enough for protein dynamics to be observed on millisecond or longer timescales, which is a suitable time frame for many biological processes (Schmidt, 2020).
Furthermore, there are increasing possibilities to adapt the environmental conditions during a time-resolved TRX data collection to physiological conditions of the investigated protein and thus to observe reaction processes and times as close to nature as possible (Mehrabi et al., 2021). This also allows the observation of an enzymatic reaction at various temperatures, which can be used to create a free energy landscape of the reaction mechanism.

Ultimately, the goal of TRX is to record the protein structure after various delay times following reaction initiation and thus, in the optimal case, to obtain a time course of the binding process and the enzymatic reaction. Ideally, this allows to draw conclusions about the mechanistic processes involved and about any transient or intermediate states. This information can be used for a better understanding of biological function and also for improved targeted structure-based drug development.
First experiments with this aim have already been performed and have revealed groundbreaking results and very promising perspectives for the future of time-resolved serial crystallography (Kupitz et al., 2014; Kupitz et al., 2017; Olmos et al., 2018; Schmidt et al., 2023; Tenboer et al., 2014; Wiedorn et al., 2018; Mateusz Wilamowski et al., 2022).

2. Aim of the thesis

Antibiotic resistance is one of the major challenges in modern medicine and the spread of multidrug-resistant pathogens urgently requires a better understanding of the underlying mechanisms to facilitate development of new compounds. In this context, this thesis will investigate understanding of molecular resistance mechanisms as an essential prerequisite to develop novel strategies (e.g. anti-resistant, anti-virulent) to combat multidrug-resistant bacteria. The special focus is on resistance to β-lactam antibiotics caused by expression of β-lactamases. These β-lactamases are bacterial enzymes that can inactivate β-lactam antibiotics by hydrolyzing the β-lactam ring. In this context, the CTX-M β-lactamases, which constitute the majority of extended-spectrum β-lactamases in clinical isolates, should be highlighted in particular. This work will mainly involve research on CTX-M-14, one of the most widely spread β-lactamases worldwide. To analyze the extended substrate spectrum of this β-lactamase in detail and to prepare for intended time-resolved studies, extensive screening experiments with substrates and inhibitors shall be conducted. Time-resolved structural analyses with the most suited substrates and inhibitors shall then be performed, to provide insights into the dynamics and structure of enzymatic reaction mechanisms at atomic resolution and millisecond time frames. In particular, the acylation and deacylation mechanisms of β-lactamases have long been the subject of scientific debate and shall be investigated by applying novel *mix-and-diffuse serial crystallography* techniques with synchrotron and XFEL radiation. Corresponding workflows for the use of the β-lactamase CTX-M-14 with the TapeDrive and HARE chips shall be established and conducted in this context. Many previous scientific efforts to elucidate the hydrolysis mechanism were based on inactive mutant variants of different β-lactamases or computational studies. However, in this work, the function of the wild-type enzyme shall be investigated to avoid misinterpretation of the mechanism caused by artificially inserted mutations. These findings shall support future structure-based development of novel antibiotics as well as specific inhibitors to treat antibiotic resistance.

3. Materials and Methods

3.1. Materials

3.1.1. Chemicals

All chemicals used in this work were purchased in analytical grade from AppliChem GmbH (Germany), Carl Roth GmbH + Co. KG (Germany), Honywell Fluka (USA), Lonza Group AG (Switzerland), MedChemExpress LLC (USA), Merck KGaA (Germany), Molecular Dimensions Limited (USA), Sigma-Aldrich Corp. (USA) or Thermo Scientific Inc. (USA).

3.1.2. Consumables

Table 1: Consumables overview.

Description	Manufacturer
48-well SWISSCI MRC plates	Hampton Research Corp., USA
96-well UV-Star® plates	Greiner AG, Austria
96-well plates	Greiner AG, Austria
Amicon® Ultra 3, Ultra 15, MWCO 10 kDa	Merck Millipore (Merck KGaA), Germany
Bottle top filter, Filtropur BT 50	Sarstedt AG & Co. KG, Germany
Celltrics gravity flow filter	Sysmex Corp, Japan
Cuvettes, semi-micro	Brand GmbH, Germany
Cuvettes, ultra-micro quartz glass	Hellma GmbH & Co. KG, Germany
Crystal Crusher glass rod	Hampton Research Corp, USA
Dialysis Cassettes, 30ml, MWCO 10 kDa	Thermo Fisher Scientific Inc., USA
Falcon Tubes	Sarstedt AG & Co. KG, Germany Greiner AG, Austria
Neubauer cell counting chamber C-Chip	NanoEnTek, South Korea
Pipette tips	Sarstedt AG & Co. KG

Description	Manufacturer
Reaction tubes	Sarstedt AG & Co. KG, Germany Eppendorf AG, Germany
Seed Bead Glass Kit	Hampton Research Corp, USA
Serological Pipettes	Sarstedt AG & Co. KG
Syringes 1ml, 2ml, 5ml, 10ml, 20ml	BD (Becton, Dickinson and Company), USA
Syringe Filter 0.22 µm, Millex®	Merck Millipore (Merck KGaA), Germany

3.1.3. Equipment

Table 2: Overview of used Equipment.

Device	Model/Manufacturer
Agarose gel electrophoresis	- Owl agarose gel system, Thermo Fisher Scientific Inc., USA - Power Supply PS3002, Life Technologies GmbH, Germany
Beamlines	- P11, DESY, PETRA III, DESY, Hamburg, Germany - T-REXX, P14.EH2, EMBL, Petra III, DESY, Hamburg, Germany
Centrifuges	- 5415 R (Eppendorf AG, Germany) - 5418 R (Eppendorf AG, Germany) - 5424 R (Eppendorf AG, Germany) - 5810 R (Eppendorf AG, Germany) - Multifuge 1 S-R (Heraeus GmbH, Germany) - Sorvall Lynx 6000 (Thermo Fisher Scientific Inc., USA) - Sigma 3-18K (Sigma Laborzentrifugen GmbH, Germany)
Crystallization robots	- Honeybee 961 (Genomics Solutions, USA) - Oryx4 (Douglas Instruments, UK)
DLS device	- SpectroLight 300 (Xtal Concepts GmbH, Germany)
FPLC	- ÄKTA purifier 10 (GE Healthcare, USA) - ÄKTA pure 25 (GE Healthcare, USA)
FPLC columns	- Hitrap SP FF 5 ml (GE Healthcare, USA)

Device	Model/Manufacturer
	- HisTrap FF 5 ml (GE Healthcare, USA) - Superdex 200 Increase 10/300 GL (GE Healthcare, USA)
Freezer -20 °C	- Liebherr premium (Liebherr International S.A., Switzerland) - Liebherr comfort (Liebherr International S.A., Switzerland)
Freezer -80 °C	- B35-85 (FRYKA-Kältetechnik GmbH, Germany) - HERAfreeze basic (Thermo Fisher Scientific Inc., USA)
Fridge	- Liebherr profi line (Liebherr International S.A., Switzerland) - Kirsch super (Philipp Kirsch GmbH, Germany)
Imaging	- Leica M205 C (Leica Microsystems GmbH, Germany) - Microscope SZX12 with camera DP10 (Olympus, Japan)
Incubator	- Heraeus B 5060 (Heraeus GmbH, Germany)
Incubation shaker	- Multitron Pro (Infors AG, Germany) - Ecotron (Infors AG, Germany) - Certomat BS-1 (Sartorius Stedim Biotech GmbH, Germany)
Magnetic stirrer	- RCT basic (IKA Werke GmbH & Co. KG, Germany)
Microbalance	- TE3102S (Sartorius AG, Germany) - CP224S-OCE (Sartorius AG, Germany)
PCR thermocycler	- peqSTAR (Peqlab Biotechnologie GmbH, Germany)
pH meter	- SevenEasy (Mettler-Toledo Inc., USA)
Photospectrometer	- Nanodrop 1000 (Thermo Fisher Scientific Inc., USA) - Nanodrop 2000c (Thermo Fisher Scientific Inc., USA) - DS-11 FX µVolume (DeNovix Inc., USA) - OD600 DiluPhotometer (Implen GmbH, Germany)
Pipettes	- Eppendorf Research and Research plus, 2 µl, 10 µl, 200 µl, 1000 µl (Eppendorf AG, Germany) - PIPETBOY (INTEGRA Biosciences AG, Switzerland)
Plate reader	- BioTek Synergy H1 (BioTek Instruments Inc., USA) - Tecan infinite M200 (Tecan Group AG, Switzerland)
SDS-PAGE	- Mini-PROTEAN Tetra System (Bio-Rad Laboratories Inc., USA)

Device	Model/Manufacturer
	- Bio-Rad PowerPac 1000 (Bio-Rad Laboratories Inc., USA)
Sonifier	- Digital Sonifier 400 (Branson Ultrasonics Corporation, USA)
Thermomixer	- Thermomixer 5436 (Eppendorf AG, Germany)
In house X-ray source	- IμS (Incoatec GmbH, Germany)
In house X-ray detector	- Mar345S (MarXperts GmbH, Germany)
Vortex mixer	- VF2 (IKA Werke GmbH & Co. KG, Germany)

3.1.4. Buffer, Media and Solutions

The individual buffer, media and solutions were prepared with double distilled water (ddH_2O). The pH was adjusted with HCl or NaOH solution.

Table 3: Generally used buffers and solutions.

Name of buffer/solution	Composition	Concentration
Isopropyl-β-D-thiogalactopyranosid (IPTG)	IPTG	1 M
Citrate-phosphate buffer	Citric acid	40 mM
	Na_2HPO_4	20 mM
Coomassie staining solution	ddH2O	50 % (v/v)
	Methanol	40 % (v/v)
	Acetic acid	10 % (v/v)
	Coomassie Brilliant Blue R-250	0.025 % (w/v)
Coomassie destaining solution	ddH2O	50 % (v/v)
	Methanol	40 % (v/v)
	Acetic acid	10 % (v/v)
NuPage LDS sample buffer (4x)	Glycerol	40 – 70 % (w/v)
	Lithium Dodecyl Sulfate	< 10 % (w/v)
	SERVA Blue G250 & Phenolrot	

Name of buffer/solution	Composition	Concentration
NuPage MES SDS running buffer (20x)	MES	-
	SDS	1 – 5 % (w/v)
Rothiphorese NF-Acrylamid/Bis-solution	Acrylamide	29 % (w/v)
	N,N'-Methylen-bis-acrylamide	1 % (w/v)
Agarose gel staining solution	RedSafe DNA stain	20000x
PBS	NaCl	135 mM
	KCl	2.6 mM
	K_2HPO_4	8 mM
	KH_2PO_4	2.6 mM
Separating gel buffer	Tris-HCl, pH 8.8	1.5 M
	SDS	0.4 % (w/v)
Stacking gel buffer	Tris-HCl, pH 6.8	0.5 M
	SDS	0.4 % (w/v)
DNA loading dye (5x)	Bromophenol blue	0.05 % (w/v)
	Xylene cyanol	0.35 % (w/v)
	EDTA	1 mM
	Glycerol	60 % (w/v)

Table 4: Buffers for protein purification.

Name of buffer /solution	Composition	Concentration
His-tag binding buffer pH 7.4	NaCl	500 mM
	NaH_2PO_4	20 mM
	Imidazol	40 mM
His-tag elution buffer pH 7.4	NaCl	500 mM
	NaH_2PO_4	20 mM
	Imidazol	250 mM
IEX binding buffer pH 6	MES	20 mM

Name of buffer /solution	Composition	Concentration
IEX elution buffer pH 6	MES	20 mM
	NaCl	1 M
SEC buffer pH 6	MES	50 mM
	NaCl	150 mM

Table 5: Buffers for protein crystallization.

Name of buffer /solution	Composition	Concentration
Cryo-solution	Li_2SO_4	200 mM
	NaOAc	100 mM
	PEG 8000	30 % (w/v)
	Glycerol	25 % (w/v)
Crystallization buffer pH 4.5	Li_2SO_4	200 mM
	NaOAc	100 mM
	PEG 8000	30 % (w/v)
Crystallization buffer for microcrystals pH 4.5	Li_2SO_4	200 mM
	NaOAc	100 mM
	PEG 8000	40 % (w/v)
Microcrystal stabilization buffer pH 4.5	MES	6 mM
	NaCl	21 mM
	Li_2SO_4	140 mM
	NaOAc	70 mM
	PEG 8000	28 % (w/v)
Ligand solution buffer pH 4.5	MES	10 mM
	NaCl	35 mM
	Li_2SO_4	100 mM
	NaOAc	50 mM
	PEG 8000	20 % (w/v)

Table 6: Growth media and antibiotics for bacterial cultures.

Media	Composition	Concentration
LB-Agar (Luria/Miller, pH 7)	Tryptone	10 g/l
	Yeast extract	5 g/l
	NaCl	10 g/l
	Agar agar	15 g/l
LB medium (Luria/Miller, pH 7)	Tryptone	10 g/l
	Nacl	5 g/l
	Yeast Extract	10 g/l
SOC medium	Tryptone	20 g/l
	Yeast extract	5 g/l
	NaCl	10 mM
	KCl	2.5 mM
	$MgCl_2$	10 mM
	$MgSO_4$	10 mM
	Glucose	20 mM
TB medium (pH 7.2)	Casein	12 g/l
	Yeast extract	24 g/l
	K2HPO4	12.5 g/l
	KH2PO4	2.3 g/l
	Glycerol	0.4 % (v/v)
Ampicillin stock (1000x)	Ampicillin sodium salt in 100 % Methanol	100 mg/ml
Chloramphenicol stock (1000x)	Chloramphenicol in 100 % Methanol	34 mg/ml
Kanamycin stock (1000x)	Kanamycin sulfate in ddH2O	50 mg/ml

3.1.5. Molecular weight size markers

Table 7: Molecular weight size marker overview.

Name	Size range	Supplier
PageRuler Prestained Protein Ladder	10 kDa – 180 kDa	Thermo Fisher Scientific Inc., USA
Generuler 1 kb Plus DNA Ladder	75 bp – 20 kbp	Thermo Fisher Scientific Inc., USA

3.1.6. Commercial kits

The commercially available QIAprep Spin Miniprep Kit (Qiagen N.V., Netherlands) was used for plasmid purifications. The Phusion High Fidelity PCR Kit (Thermo Fisher Scientific Inc., USA) was used for PCR reactions. The NucleoSpin Gel and PCR Clean-up Kit (Macherey-Nagel GmbH & Co. KG, Germany) was used for agarose gel extraction and purification of PCR products. The NEB Gibson Assembly Cloning Kit (New England BioLabs Inc., USA) was used for cloning.

3.1.7. Bacterial plasmids

Table 8: Overview of the bacterial plasmids used.

Plasmid	Properties	Supplier/Reference
pCR4::Prom+CTX-M-14	CTX-M-14 WT sequence with bacterial promoter, T7 promoter for overexpression	(Both et al., 2017)
pCR4::Prom+CTX-M-14 P167S	CTX-M-14 P167S variant sequence with bacterial promoter, T7 promoter for overexpression	(Both et al., 2017)
pCR4::Prom+CTX-M-14 P167S T262I	CTX-M-14 P167S T264I variant sequence with bacterial promoter, T7 promoter for overexpression	(Both et al., 2017)
pET302-nt-His::CTX-M-14	CTX-M-14 WT sequence with His-tag, T7 promoter for overexpression	This work

Plasmid	Properties	Supplier/Reference
pET302-nt-His::CTX-M-14 P167S	CTX-M-14 P167S T264I variant sequence with His-tag, T7 promoter for overexpression	This work
pET302-nt-His::CTX-M-14 P167S T262I	CTX-M-14 P167S T264I variant sequence with His-tag, T7 promoter for overexpression	This work
pET302-nt-His::CTX-M-14 Δsignal	CTX-M-14 WT Sequence with His-tag and without signal peptide, T7 promoter for overexpression	This work
pET302-nt-His::CTX-M-14 P167S Δsignal	CTX-M-14 P167S T264I variant sequence with His-tag and without signal peptide, T7 promoter for overexpression	This work
pET302-nt-His::CTX-M-14 P167S T262I Δsignal	CTX-M-14 P167S T264I variant sequence with His-tag and without signal peptide, T7 promoter for overexpression	This work
pET24a(+)::CTX-M-14 E166A	CTX-M-14 E166A variant sequence with His-tag, T7 promoter for overexpression	This work; BioCat GmbH, Germany

3.1.8. Bacterial strains

E. coli strains DH5α and Top10 were used for plasmid transformation and plasmid storage, while various BL21 (DE3) strain derivatives were used for recombinant protein production. The β-lactamase CTX-M-14 discussed in this thesis was found in a clinical isolate of a multidrug-resistant *K. pneumonia* (isolate DT1, (Both et al., 2017)).

Table 9: Overview of the bacterial strains used.

Strain	Genotype	Supplier/Reference
K. pneumoniae	Isolate DT1	(Both et al., 2017)
E. coli BL21 (DE3)	F– ompT hsdSB (rB–, mB–) gal dcm (DE3)	Thermo Fisher Scientific Inc., USA
E. coli BL21 (DE3) star	F– ompT hsdSB (rB–, mB–) gal dcm (DE3) pLysS (CamR)	Thermo Fisher Scientific Inc., USA

Strain	Genotype	Supplier/Reference
E. coli DH5α	F– ϕ80lacZΔ M15 Δ (lacZYA-argF) U169 recA1 endA1 hsdR17 (rK– mK+) phoA supE44 λ- thi–1 gyrA96 relA1	Thermo Fisher Scientific Inc., USA
E. coli Top10	F–mcrA Δ(mrr–hsdRMS–mcrBC) Φ80LacZΔM15 Δ LacX74 recA1 araD139 Δ(araleu) 7697 galU galK rpsL (StrR) endA1 nupG	Thermo Fisher Scientific Inc., USA

3.1.9. Software

Table 10: Overview of the software used.

Software	Application	Reference
APBS electrostatics	PyMOL plugin for electrostatic surface representation	(Jurrus et al., 2018; Lerner & Carlson, 2006)
Benchling	DNA plasmid sequence management	(www.benchling.com, 2022)
BioRender	Creation of illustrations for figures	(BioRender.com, 2022)
CCP4i (v.8.0.007)	Dimple, Refinement, Matthews Cell Content Analysis	(Winn et al., 2011)
ChemDraw	Illustration of chemical structures and reaction equations	(v.20.1, PerkinElmer, USA)
Clustal Omega (1.2.4)	Multiple sequence alignment	(Madeira et al., 2022)
CrystFEL (v.0.8.0; v.0.9.1; v0.10.1)	Processing of serial crystallography data	(White et al., 2012; White et al., 2016)
ESPript 3.0	Representation of multiple sequence alignment	(Robert & Gouet, 2014)
Expasy	Calculation of MW and extinction coefficient	(Gasteiger et al., 2005)
GraphPad Prism	Diagrams, data statistics, regressions and calculations	(v.5.0.0, GraphPad Software, USA)
LigPlot+, v.2.2	2D representation of protein and ligand interactions	(Laskowski & Swindells, 2011)
MolProbity	Evaluation of protein models	(Chen et al., 2010; Williams et al., 2018)

Software	Application	Reference
NEBioCalculator	Calculation of DNA mass and moles	(nebiocalculator.neb.com, 2022)
NEBuilder Assembly Tool	Design of Gibson Assembly primer	(nebuilder.neb.com, 2022)
PHENIX	Refinement	(Paul D Adams et al., 2010)
PyMOL	Preparation of figures of protein structures	(DeLano, 2002)
XDS	Data processing	(Kabsch, 2010b)

3.2. Molecular biology and biochemical Methods

3.2.1. Agarose gel electrophoresis

In this work, 1 % agarose (w/v) gels were used to separate nucleic acids by size. To prepare these gels, 1 g agarose was dissolved in 100 ml TBE buffer by heating the suspension for 1 – 3 min. in the microwave. After cooling for 2 min., 5 µl of RedSafe was added, the liquid agarose was poured into a horizontal gel caster and a suitable comb was inserted. After polymerization the gel was covered with TBE- buffer, the combs were pulled out and the gel was loaded with 7 µl DNA. The DNA was previously mixed with 5x DNA loading dye. In addition, 4 µl of the DNA size standard was applied in one pocket. A constant voltage of 120 V was applied for 45 – 60 min. The resulting band pattern was visualized by UV light and documented using a BioRad imager.

3.2.2. DNA PCR cleanup and gel extraction

For the ligation of DNA fragments or the sequencing of DNA sections, it is necessary to purify this DNA beforehand. This can be done either by purification after PCR or by extraction of the DNA from an agarose gel. PCR cleanup and gel extraction was performed using the NucleoSpin Gel and PCR Clean-up Kit (Macherey-Nagel GmbH & Co. KG, Germany) according to the manufacturer's instructions. Elution was performed using 30 – 50 µl ddH2O or elution buffer. The isolated DNA was stored at -20 °C.

3.2.3. Restriction digestion

Restriction digestion was performed either to prepare plasmid DNA for a ligation method or to verify the correct plasmid DNA. For a reaction batch of 20 µl, 2 µl of the corresponding 10x restriction buffer and an appropriate amount of ddH2O as well as 1 µg of DNA were added to a reaction tube. For the digestion of 1 µg DNA, 1 µl (20 units) per restriction enzyme was added. The reaction mixture was briefly mixed and incubated at 37 °C for 3 h in a PCR thermo cycler. The result of the restriction digestion was verified by agarose gel electrophoresis.

3.2.4. Determination of nucleic acid concentration and purity

The concentration of a nucleic acid solution can be estimated by photometric measurement of absorbance at a wavelength of 260 nm. At this wavelength, the nucleic acids have an absorption maximum. For an accurate measurement of the concentration, an extinction coefficient for the respective nucleic acid sequence would have to be determined, which would make the measurement in the laboratory much more difficult. Therefore, the concentration can be estimated according to a rule of thumb for longer nucleic acid sequences. An absorbance A_{260} of 1.0 (at 1 cm path length) corresponds to a concentration of 50 ng/µl for double-stranded DNA and 40 ng/µl for RNA.

Protein impurities in the DNA sample can be estimated by the ratio of absorbance at 260 nm to 280 nm, since proteins have their maximum absorbance at 280 nm. For pure DNA the A_{260}/A_{280} ratio should be 1.8 and for pure RNA 2.0. In addition, high absorbance at 230 nm may indicate contamination with phenol, EDTA or carbohydrates.

The measurements were performed on a DeNovix DS-11 or a Nanodrop instrument using 1 µl of sample. Before the measurement, the device was blanked with either ddH2O or elution buffer. The concentration can be calculated using the modified Lambert-Beer equation in Equation 3.

$$c = \frac{A_{260} \cdot MW}{\varepsilon \cdot d}$$

Equation 3: Calculation of nucleic acid concentration according to the Lambert-Beer Law. With c = concentration of nucleic acid solution in g/l; A_{260} = measured Absorption at 260 nm; MW = molecular weight of nucleic acid sequence in g/mol; ε = molar extinction coefficient of specific nucleic acid sequence at 260 nm in $M^{-1} \cdot cm^{-1}$; d = pathlength in cm.

3.2.5. Preparation of chemically competent *E. coli*

To transform a DNA plasmid containing the protein of interest for recombinant expression into an *E. coli* strain, the strain must first be prepared to be chemically competent. For this purpose, 5 ml LB medium, which was optionally supplemented with an appropriate selection antibiotic, was inoculated with either a colony from a cultivated plate or cells from a cryogenic stock of an *E. coli* strain. The preculture was grown overnight at 37 °C and 180 rpm in a shaking incubator. For the main culture, 100 ml LB medium was inoculated with 1 ml of the preculture. The LB medium was optionally supplemented with an appropriate selection antibiotic. The main culture was incubated at 37 °C and 180 rpm until it reached an OD_{600} of 0.5. It was then transferred into 50 ml falcon tubes and cooled on ice for 15 min. From this point on, all further steps had to be done under cooling. The culture was then centrifuged for 10 min at 5000 x g and 4 °C and the supernatant was discarded. Each pellet was resuspended with 5 ml of an ice-cold sterile filtered 100 mM $CaCl_2$ solution and then centrifuged again for 10 min at 5000 x g and 4 °C. The supernatant was discarded, the pellets were resuspended with 1 ml of ice-cold 100 mM $CaCl_2$ and flash frozen in 50 µl aliquots using liquid nitrogen. Competent cells were stored at -80 °C until use.

3.2.6. Transformation of competent *E. coli*

For transformation of a DNA plasmids into an *E. coli* strain, an aliquot (50 µl) of a chemically competent cell line in a reaction tube was thawed on ice for 10 min. The cells were briefly mixed with 100 ng plasmid DNA and incubated on ice for 30 min. A heat shock at 42 °C for 45 s was then performed to transform the DNA into the cells. The cells were directly placed on ice for 5 min and then incubated with 950 ml of sterile SOC medium for 1 h at 37 °C and 800 rpm in a thermomixer. From this preparation, 50 – 100 µl were plated on LB agar with the appropriate selection antibiotics and incubated overnight at 37 °C.

3.2.7. Bacterial plasmid DNA isolation

For isolation of plasmid DNA, 5 ml of LB medium was mixed with the antibiotic (1:1000 stock) and a single colony, of the colonies obtained from transformation, was inoculated with a pipette tip. The cultures were incubated overnight at 37 °C and 180 rpm. The following day, cultures were centrifuged at 5000 x g for 10 min at room temperature. Plasmid DNA was extracted using the QIAprep Spin Miniprep Kit according to the manufacturer's instructions.

Elution was performed using 30 – 50 µl ddH2O or elution buffer. The isolated plasmid DNA was stored at -20 °C.

3.2.8. DNA sequencing

To verify that the DNA plasmids were correct or that ligation had worked, the plasmids were sent to Eurofins Genomics Germany GmbH (Germany) for sequencing using their TubeSeq service. The reaction tube was enclosed in an envelope and placed in a Eurofins collection box. Sequencing results were usually available the following day and were compared using the online tool Benchling via a sequence alignment.

3.2.9. DNA assembly and cloning

The NEB Gibson Assembly Cloning Kit was used for cloning of DNA plasmids. Gibson assembly enables the successful assembly of multiple DNA fragments and was used to transfer the sequence of CTX-M-14 wildtype and variants into a pET302 vector for enhanced overexpression of the target proteins. The kit was used according to the manufacturer's instructions. Specific primers were designed using the NEBuilder Assembly Tool and the molar amount of fragments for assembly was calculated using NEBioCalculator.

3.3. Protein biochemistry Methods

3.3.1. Recombinant gene expression of CTX-M-14 variants in *E. coli*

For recombinant expression of the target protein CTX-M-14, a preculture of 70 ml LB medium with the appropriate antibiotic was inoculated with one colony of the plasmid carrying *E. coli* BL21 (DE3) or *E. coli* BL21 (DE3) star strain from an agar plate or from a glycerol stock. Cultivation of the preculture was performed overnight at 37 °C and 180 rpm. For the main culture, 10 ml of preculture was added to 1 l of LB with the appropriate antibiotics. The culture was incubated at 37 °C and 180 rpm. The growth of *E. coli* bacteria was monitored by measuring OD_{600} until the culture reached log phase at OD_{600} of 0.5 – 0.7. At this point, protein expression was induced by adding 150 µl of 1 M IPTG. After 3 – 4 h of protein expression, the cell suspension was transferred to 1 l centrifuging buckets and centrifuged at 5500 x g and 4 °C for 10 min. The supernatant was discarded, and the cell pellet was transferred into a 50 ml falcon tube and frozen at -80 °C.

3.3.2. Cell lysis

Cell pellets of a 1 l culture were thawed at room temperature and then resuspended with 10 ml of IEX binding buffer. The cell suspension was then sonicated five times for 30 s with 30 s break intervals in between. Cell debris was removed by centrifugation for 30 min at 4 °C and 20000 × g. The supernatant containing the soluble cell lysate was filtered with a 0.22 µm bottle top filter before dialysis or purification.

3.3.3. Dialysis

Dialysis of the cell lysate was used primarily to reduce the salt concentration of the sample to allow later purification by ion exchange chromatography. In addition, the use of a 10 kDa molecular weight cut off (MWCO) membrane also removed low molecular weight compounds. Dialysis cassettes (Thermo Fisher Scientific Inc., USA) were used for this purpose according to the manufacturer's instructions. The membrane of the cassettes was hydrated in IEX binding buffer for 2 min before loading the sample. Depending on the sample volume, 30 – 60 ml of cell lysate was dialyzed against 4 – 5 l of IEX binding buffer. Dialysis was carried out overnight at 4 °C with constant stirring.

3.3.4. Cation-exchange chromatography

In cation exchange chromatography, positively charged molecules are separated from negatively charged molecules. The cation exchange chromatography column is composed of a Sepharose matrix with negatively charged groups so that only positively charged molecules such as the CTX-M-14 protein (pI = 8.0) bind to it while the negatively charged molecules flow through. The bound molecules can be eluted from the column by an increasing salt gradient.
For cation exchange chromatography of CTX-M-14, the HiTrap SP FF 5ml column was used on an ÄKTA purifier or ÄKTA pure system according to the manufacturer's instructions. The column was equilibrated with 5 column volumes (CV) of ddH2O followed by 5 CV of IEX binding buffer at a constant flow rate of 3 ml/min. The previously filtered cell lysate was applied using a 50 ml super loop. The column was then washed with 10 CV of IEX binding buffer to remove non-specific or weakly bound molecules. CTX-M-14 was eluted at a flowrate of 1 ml/min using an increasing gradient of IEX elution buffer from 0 – 5 % over 5 CV. The UV monitor of the ÄKTA systems can measure the light absorption of aromatic amino acids of proteins at a wavelength of 280 nm, which enables the detection of protein peaks and thus the correct

selection of elution fractions. CTX-M-14 was eluted at a salt concentration of approx. 40 mM NaCl. The proteins from the cell lysate that bind more strongly to the column were removed with 5 CV of 100 % IEX elution buffer. The column was rinsed with 0.5 M NaOH for 2 CV and then with ddH2O for 10 CV to regenerate it. For long-term storage, the column was rinsed with 5 CV of 20 % EtOH and stored at 4 °C. The purity of CTX-M-14 fractions was checked by SDS-PAGE as standard.

3.3.5. SDS-Polyacrylamide gel electrophoresis (SDS-PAGE)

SDS-PAGE was used to separate proteins according to their size (Laemmli, 1970). For this, the main component acrylamide is polymerized in a reaction catalyzed by ammonium persulfate (APS) and TEMED forming a molecular sieve. The pore size of the molecular sieve is determined by the amount of Acrylamide and is usually smaller than that of agarose, which enables the separation of smaller molecules such as proteins from 5 – 250 kDa.

The addition of SDS (or LDS) and, if required, reducing agents such as DTT, enables the complete denaturation of proteins. The hydrophobic part of the SDS accumulates on the hydrophobic regions of the denatured proteins so that the negatively charged sulfate group is directed outwards. All reduced polypeptides bind the same amount of SDS on a weight basis independent of the amino acid composition. This covers the intrinsic charge of the protein so that all proteins are negatively charged and have the same charge density, which is why separation is based on size only (Shi & Jackowski, 1998).

In a discontinuous buffer system, an SDS gel consists of a large pore stacking gel with pH 6.8 and a small pore separation gel with pH 8.8 (Laemmli, 1970). The composition of the used SDS gels is summarized in Table 11. The protein mixture is first focused in the stacking gel and then separated by size in the separation gel. Smaller molecules migrate faster through the molecular sieve. The Mini-PROTEAN Tetra System (Bio-Rad Laboratories Inc., USA) was used for SDS-PAGE. Protein samples were mixed with 4x NuPAGE LDS sample buffer and denatured at 95 °C for 10 min. Samples were centrifuged and 10 – 20 µl as well as 5 µl of a protein size standard were applied onto the gel. The SDS PAGE chamber was filled with 1x NuPage MES SDS running buffer and the gels were run at a constant voltage of 120 – 140 V for 1 – 1.5 h. Then, the SDS gels were stained in the Coomassie staining solution for 30 min to overnight. Subsequently, the gels were destained in the Coomassie destaining solution until protein bands were visible and the background was destained.

Table 11: SDS-PAGE gel composition. Volume specification for casting 4 SDS gels.

Gel type	Compound/solution	Volume
Stacking gel (4 %)	ddH2O	6.1 ml
	Rothiphorese NF-Acrylamid/Bis-solution	1.3 ml
	Stacking gel buffer pH 6.8	2.5 ml
	10 % (w/v) SDS	100 µl
	TEMED	10 µl
	10 % (w/v) APS	50 µl
Separating gel (12 %)	ddH2O	6.8 ml
	Rothiphorese NF-Acrylamid/Bis-solution	8.0 ml
	Separating gel buffer pH 8.8	5.0 ml
	10 % (w/v) SDS	200 µl
	TEMED	10 µl
	10 % (w/v) APS	100 µl

3.3.6. Sample concentration

Protein samples were concentrated using an Amicon centrifugal concentrator (Merck KGaA, Germany) with a MWCO of 10 kDa according to the manufacturer's instructions. The protein solutions were repeatedly centrifuged for 10 min at 4000 x g and 4 °C until the desired concentration was reached. Between each centrifugation step, the sample was thoroughly mixed with a pipette. The protein was stored at 4 °C.

3.3.7. Determination of protein concentration

The concentration of a protein solution can be estimated by photometric measurement of absorbance at a wavelength of 280 nm. At this wavelength, the aromatic amino acids have an absorption maximum. Based on the protein sequence, a specific extinction coefficient is thus obtained. DNA has an absorption maximum at 260 nm, which allows to determine DNA impurities in the protein sample by using the absorbance ratio at 260/280 nm. A 260/280 ratio of less than 0.60 is a good indication of pure protein with minimal nucleic acid contamination. Protein concentration is calculated via a derivation of the Lambert-Beer law as in Equation 4.

$$c = \frac{A_{280} \cdot MW}{\varepsilon \cdot d}$$

Equation 4: Calculation of protein concentration according to the Lambert-Beer Law.
With A_{280} = measured Absorption at 280 nm; MW = molecular weight of CTX-M-14 in g/mol; c = concentration of protein solution in g/l; ε = molar extinction coefficient of CTX-M-14 at 280 nm in $M^{-1} \cdot cm^{-1}$; d = pathlength in cm.

The specific molar extinction coefficient and the molecular weight of CTX-M-14 were calculated based on the peptide sequence using the ProtParam tool (Gasteiger et al., 2005). CTX-M-14 without its signal peptide has a molecular weight of 27.96 kDa and a molar extinction coefficient of 23.950 $M^{-1}cm^{-1}$. The actual measurement was performed on a DeNovix DS-11 or a Nanodrop instrument using only 2 µl of sample. Before the measurement, the device was blanked with the elution buffer.

3.3.8. Enzyme kinetic assays

The CTX-M-14 steady-state parameters k_{cat} and K_m were determined for several antibiotic substrates by photometrically measuring the initial hydrolysis rates of the antibiotics at various concentrations. Moreover, these kinetic parameters were studied at different temperatures and in various buffer systems with pH values ranging from pH 7.4 to pH 3. Kinetic assays were performed in triplicates. Substrates were added to a 96-well UV-Star microplate (Greiner AG, Austria) at the appropriate final concentration. Enzyme was added at a final concentration of 100 nM and the sample was mixed well. The absorbance at the specific wavelength for each antibiotic was measured in a BioTek Synergy H1 microplate reader (BioTek Instruments, Inc., USA). For the calculation of k_{cat} and K_m for each antibiotic, the initial velocity rates were plotted against the corresponding antibiotic concentrations and calculated using the k_{cat} equation of GraphPad Prism (GraphPad Software, USA).

3.3.9. Enzyme inhibition assays

Enzyme inhibition assays were performed as we have previously published in scientific reports (Perbandt et al., 2022). The 50 % inhibitory concentration (IC_{50}) of CTX-M-14 was determined as the concentration of inhibitor required to decrease the initial rate of hydrolysis of the substrate by 50 %. Inhibition assays were performed in triplicates. Dilution series of the various compounds were prepared in PBS buffer at pH 7.4. The enzyme was added to the

inhibitor solution at a final concentration of 100 nM and the solution was incubated at 37 °C for 15 min. The substrate cefotaxime was then added at a final concentration of 100 µM, and hydrolysis of the cefotaxime was monitored in 96-well UV-Star microplates (Greiner AG, Austria) at 260 nm for 10 min using a BioTek Synergy H1 microplate reader (BioTek Instruments, Inc., USA). Initial hydrolysis rates were plotted against the logarithm of inhibitor concentration and the IC_{50} was calculated using the nonlinear regression function of GraphPad Prism (GraphPad Software, USA).

3.4. Biophysical Methods

3.4.1. Dynamic light scattering (DLS)

Dynamic light scattering (DLS) was used to characterize the protein sample in solution before crystallization. DLS provides information about the hydrodynamic radius R_H of a protein in solution and thus about the size distribution of particles in a polydisperse sample. Thus, impurities due to other proteins or multiple oligomerization states can be indicated by a large size distribution of particles. However, to increase the probability of successful crystallization, a monodisperse sample with a small size distribution of particles is beneficial (D'Arcy, 1994; Niesen et al., 2008; Price Ii et al., 2009). The hydrodynamic radius R_H of a globular protein can be estimated using the Stokes-Einstein equation.

$$R_H = \frac{k_B T}{6\pi\eta D}$$

Equation 5: Calculation of hydrodynamic radius R_H according to the Stokes-Einstein relation. k_B = Boltzmann constant, T = absolute temperature, η = dynamic viscosity, D = diffusion constant

For DLS measurement, the sample was centrifuged for 60 min at 20000 x g and 4 °C. Then, 20 µl of the sample was pipetted into a DLS suitable quartz cuvette (Hellma GmbH & Co. KG, Germany) and measured at a constant temperature of 20 °C in a SpectroSize 300 (XtalConcepts, Germany). Scattered light was measured at an angle of 90°. Each measurement was performed for 20 s and was repeated 20 times to obtain reliable data.

3.5. Protein crystallization

3.5.1. Sitting drop vapor diffusion crystallization

The optimal crystallization conditions for macrocrystals have already been determined in a high-throughput screening (Werner, 2020). The JCSG-plus-screen provided the best conditions, which were further optimized. The best results were obtained with the optimized conditions of 25 – 35 % (w/v) PEG8000, 200 mM Li_2SO_4, 100 mM NaOAc at pH 4.5 as a crystallizing agent.

For the preparation of macrocrystals, sitting drop vapor diffusion experiments were performed in MRC maxi plates. The reservoir was filled with 100 µl crystallizing agent and 1.5 µl CTX-M-14 protein solution (20 mg/ml) were mixed with 1.5 µl crystallizing agent in the sitting drop well. The plates were then sealed with adhesive tape and stored at RT. The plates were checked for crystal growth at regular intervals.

3.5.2. Seeding

Seeding allows crystals to grow in the metastable zone, where crystal growth from seeds can occur, but not spontaneous nucleation. This can be used to increase reproducibility and to increase the probability of a successful crystallization attempt. Furthermore, by adding seeds to a droplet in a vapor diffusion crystallization experiment that is in the metastable zone, the number and size of crystals grown can be controlled. The number of seeds introduced is determined by testing a dilution series of the prepared seed stock.

To prepare such a seed stock, existing macrocrystals were crushed with a Crystal Crusher glass rod (Hampton Research Corp, USA) and pipetted into a 1.5 ml reaction tube together with 50 µl reservoir solution. Then 3 glass beads were added and the tube was vortexed for 3 min, stopping every 30 sec to cool the tube on ice. A dilution series of this seed stock was made and used for further vapor diffusion experiments. The crystal seeds were transferred to a crystallization droplet using a horse hair.

3.5.3. Batch crystallization for microcrystals

The batch crystallization method is particularly suitable for producing a very large quantity of microcrystals. This requires the seed stock to be highly concentrated and as homogeneous as possible. A first batch crystallization experiment was performed with the undiluted previously described seed stock and the crystals obtained were used to prepare the new highly concentrated seed stock. This preparation was performed by mixing 50 % (v/v) CTX-M-14 protein solution (20 mg/ml) with 45 % (v/v) crystallizing agent (40 % (w/v) PEG8000, 200 mM Li_2SO_4, 100 mM NaOAc at pH 4.5) and 5 % (v/v) undiluted seed stock in a 1.5 ml reaction tube. The resulting microcrystals grew over night at 20 °C, were centrifuged for 5 min at 200 × g and 20 °C and the crystal pellet was crushed with the Crystal Crusher (Hampton Research Corp, USA). This procedure was repeated 10 times. In a final centrifugation step, the supernatant containing the crystal seeds was separated, resulting in a highly concentrated seed stock.

This seed stock was then used to produce the homogeneous microcrystals for serial synchrotron crystallography (SSX) and serial femtosecond crystallography (SFX) experiments. The size of the crystals was determined by adding different amounts of seed stock. In a typical approach, volumes of 50 % (v/v) CTX-M-14 protein solution (20 mg/ml) and 40 – 49 % (v/v) crystallizing agent (40 % (w/v) PEG8000, 200 mM Li_2SO_4, 100 mM NaOAc at pH 4.5) and 1 – 10 % (v/v) highly concentrated seed stock were mixed in a 1.5 ml reaction tube. The prepared CTX-M-14 microcrystals grew within 1 – 5 hours and had a homogeneous size distribution from 5 – 12 µm for SFX or 11 – 23 µm for SSX experiments, which was measured by light microscopy. To prevent further crystal growth, these microcrystals were centrifuged for 10 min at 200 x g and 20 °C, the supernatant was removed and replaced with microcrystal stabilization buffer (28 % (w/v) PEG8000, 140 mM Li_2SO_4, 70 mM NaOAc, 6 mM MES and 15 mM NaCl at pH 4.5).

3.6. X-ray crystallography

3.6.1. Single-crystal X-ray crystallography

The rotation oscillation technique was used for data collection applying single crystal X-ray crystallography. A macrocrystal was rotated in the X-ray beam during multiple exposures. If a crystal structure with ligands was to be determined, then the macrocrystals, prepared in the vapor diffusion experiment, were placed in a crystallizing agent solution containing the ligand and soaked for a defined amount of time. Data collection was performed at cryogenic temperatures because radiation damage is significantly reduced at this temperature. Therefore, this technique is later referred to as cryoMX (cryo macromolecular crystallography). To prevent the formation of crystalline ice, the crystals had to be protected with a cryo protection solution. Crystals were picked up with a polymer loop, immersed in cryo solution (crystallizing agent with 25 % (w/v) glycerol) and frozen in liquid nitrogen. Data collection was performed either at the Laboratory for Structural Biology of Infection and Inflammation (DESY, Build. 22a, Hamburg, Germany) in-house source IμS (Incoatec GmbH, Germany) with a Mar345S detector (MarXperts GmbH, Germany) or at the P11 beamline at Petra III (DESY, Hamburg, Germany) with a Pilatus 6M-F detector (Dectris Ltd., Switzerland). Frozen crystals were placed on a goniometer and cooled to 100 K with a stream of nitrogen gas. The crystals were exposed to an X-ray beam with a diameter suitable for the crystal size. Diffraction data were processed using auto processing pipelines or XDS (Kabsch, 2010a, 2010b).

3.6.2. Time-resolved serial X-Ray crystallography

In serial X-ray crystallography, individual microcrystals are measured in random orientation. The crystals are usually exposed to an X-ray beam only once. This reduces radiation damage and allows data collection at RT and without cryoprotectants. Furthermore, it is possible to perform mix-and-diffuse experiments at very short delay times, since very small microcrystals are used and thus the diffusion times are significantly shortened (Schmidt, 2013).

3.6.2.1. CFEL TapeDrive

The application of the CFEL TapeDrive was described in detail in our recently published paper (Zielinski et al., 2022). A microcrystal suspension with a homogenous size distribution of 11 – 15 µm was produced in a batch crystallization setup and filtered using a 30 µm Celltrics gravity flow filter (Sysmex Corp, Japan). Ligands have been dissolved in ligand solution buffer (20 % (w/v) PEG8000, 100 mM Li_2SO_4, 50 mM NaOAc, 10 mM MES and 25 mM NaCl at pH 4.5) for mix-and-diffuse experiments. The microcrystal suspension and the ligand solution vials were each connected to a channel of the Elveflow OB1 flow controller (ElveSys, France). A microfluidic flow sensor allowed to monitor and control the flow rates of the sample solutions. In mix-and-diffuse experiments, the same flow rate was chosen for microcrystal suspension and for ligand solution to achieve 1:1 (v/v) mixing. The samples flowed through a capillary onto a non-sticky polyimide tape (Caplinq, Netherlands), creating a continuous stream of the mixed microcrystal suspension. This tape was part of the conveyor belt apparatus called TapeDrive. It was moved continuously and thus ensured that the stream of microcrystal suspension was carried into the X-ray beam. For time-resolved experiments, the delay time between the mixing of the microcrystals with the ligand and the measurement by the X-ray beam was adjusted by varying the tape speed and changing the distance of the capillary to the X-ray beam. The CFEL TapeDrive was mounted on the crystallography endstation at the P11 beamline at Petra III (DESY, Hamburg, Germany). Data collection was performed using the Eiger 2 16M detector and data processing was carried out using the CrystFEL package (White et al., 2012; White et al., 2016).

3.6.2.2. Chip data collection using a combination of HARE and LAMA

Additionally, a second method for time-resolved serial synchrotron data collection was used with a combination of the hit-and-return (HARE) method (Schulz et al., 2018) and the liquid application method for time-resolved analyses (LAMA) (Mehrabi et al., 2019a). For this purpose, a fixed target approach was employed for sample delivery using HARE chips (Mehrabi et al., 2020). The microcrystal suspension with a homogenous size distribution of 15 – 20 µm was produced in a batch crystallization setup. Microcrystal concentration was measured by depositing 10 µl of the crystal slurry into a Neubauer cell counting chamber (NanoEnTek, Korea) and counting the crystals using a benchtop light microscope. The HARE chip was loaded with 125 µl of a microcrystal suspension at a concentration of 1 x 10^6 – 1.5 x 10^6 ml^{-1} crystals.

Residual mother liquor was removed during the chip loading procedure by applying a vacuum to the chip-loading block. The substrate piperacillin was dissolved at a concentration of 333 mM in ligand solution buffer without PEG8000 to reduce viscosity for optimal droplet formation (140 mM Li_2SO_4, 70 mM NaOAc, 6 mM MES and 15 mM NaCl at pH 4.5). The reaction was initiated using LAMA, a mixing approach for serial crystallography that shoots picoliter sized drops of the substrate into each feature of a chip containing protein crystals. In addition, the advantages of the HARE approach were exploited to collect diffraction data and reduce the total data collection time while minimizing sample consumption for crystals and ligands. This technique involved measuring a chip according to a specific pattern. According to the desired delay time, a dark image (no reaction initiation) of one feature of the chip was recorded and then the reaction was initiated by substrate droplet deposition using LAMA. This was repeated for the next features until the desired delay time has elapsed. Then the chip was moved back to the position of the first feature to collect diffraction data after the set delay time. The other features were then measured in the same order. This process is fully automated and was repeated until the whole chip was collected. Thus, two datasets were collected. A dark image dataset without reaction initiation and a dataset after reaction initiation. The dark image was used to check for contamination with the ligand (misaligned ligand nozzle, big ligand droplets) and thus evaluate the quality of the time-resolved dataset with respect to the delay time. Due to the multiple X-ray exposures, the crystals had to be checked for radiation damage. These data collections were performed at the P14.2 endstation of beamline P14 operated by EMBL Hamburg at PETRA III (DESY, Hamburg, Germany). Data processing was carried out employing the CrystFEL package (White et al., 2012; White et al., 2016) using an automated script by David von Stetten (EMBL, Hamburg).

3.6.3. Structure solution and refinement

The published structure of CTX-M-14 (PDB 6gth, Wiedorn et al. (2018)) collected at the European XFEL was used as the initial model for molecular replacement by phaser (McCoy et al., 2007) after removal of the water molecules and the ligand. Initial refinement was carried out using phenix.refine (Afonine et al., 2012) with all isotropic atomic displacement parameters (ADPs) set to 20 $Å^2$ and using simulated annealing. Repeated cycles of TLS refinement with phenix.refine and manual model building with Coot (Emsley et al., 2010) were

performed until convergence. A thorough manual inspection as well as the programs Polygon and Molprobity (Chen et al., 2010) were used for validation of the final models.

3.6.4. Generation of polder maps

The crystallographic maps used for structure solution are almost always model-biased since model information is used for their calculation. Any small molecule added to the model will manifest itself in the map, hindering validation. Therefore, it is difficult to see whether a low occupancy ligand is actually present or not. To overcome this problem, polder (OMIT) maps can be generated (Liebschner et al., 2017). These polder maps are calculated by excluding selected atoms and bulk solvent mask. The newly generated polder map then shows a less biased map of the selected atoms. Since the bulk solvent is also excluded, this method is excellent for improving the map of parts of the structure with weak density. This is especially useful for the interpretation of electron density maps in time-resolved structural analyses, since small changes in the map will not be obscured by bulk solvent.

Polder maps were generated using the *phenix.polder* tool from the PHENIX software suite (P. D. Adams et al., 2010; Liebschner et al., 2017). The model file and the reflection file of the refined structure were used for the calculation and the region for which the polder map was generated was defined in the OMIT selection.

4. Results

4.1. CTX-M-14 expression, purification and characterization

Anna Both provided the pCR4::Prom+CTX-M-14 plasmid containing the $bla_{CTX\text{-}M\text{-}14}$ gene that is derived from a clinical *K. pneumoniae* isolate (Both et al., 2017). The $bla_{CTX\text{-}M\text{-}14}$ gene contains the genetic information for the expression of a 291 amino acid protein (Figure S2), 28 amino acids of which encode a signal peptide. This protein is the investigated CTX-M-14 β-lactamase, which provides resistance of bacteria to β-lactam antibiotics by hydrolyzing the β-lactam ring. Upon expression, CTX-M-14 is guided by the signal peptide to the periplasm of Gram-negative bacteria, the site of action of β-lactam antibiotics (Laminet & Plückthun, 1989; Mansell et al., 2010; Selas Castiñeiras et al., 2018). Once at the target site, the signal peptide is removed, resulting in a 27.96 kDa protein.

A protocol for expression and purification of the CTX-M-14 construct was previously established by Nadine Werner, a colleague from the group of Prof. Betzel (Werner, 2020). This protocol was adapted and optimized to achieve optimal protein yields in our laboratory.

Expression, cell lysis, dialysis, and purification with a cation exchange column were performed as described in the methods section 3.3. A 5 ml HiTrap SP FF column (GE Healthcare, USA) was used for purification (Figure 10 A). For elution of CTX-M-14, the salt concentration was increased by a linear gradient of IEX elution buffer (20mM MES, 1 M NaCl, pH 6) from 0 – 5 %. As a result, weakly bound impurities were removed in a first peak (peak I) before eluting the target protein at about 40 mM NaCl after 65 ml retention volume (Figure 10 A, peak II). CTX-M-14 purified by this approach was particularly pure and required no further purification steps. In addition, a 12 % SDS-PAGE (Figure 10 B) was performed to monitor protein expression and purity. The lane with the applied lysate (L) showed a strong overexpressed band at the level of about 28 kDa, confirming the successful expression of CTX-M-14. Whereas the absence of this band in the lane for the cation exchange flow through (FT) confirmed successful binding to the column. The elution (E) lane of the pooled fractions showed only one band at the level of about 28 kDa, indicating successful purification of CTX-M-14.

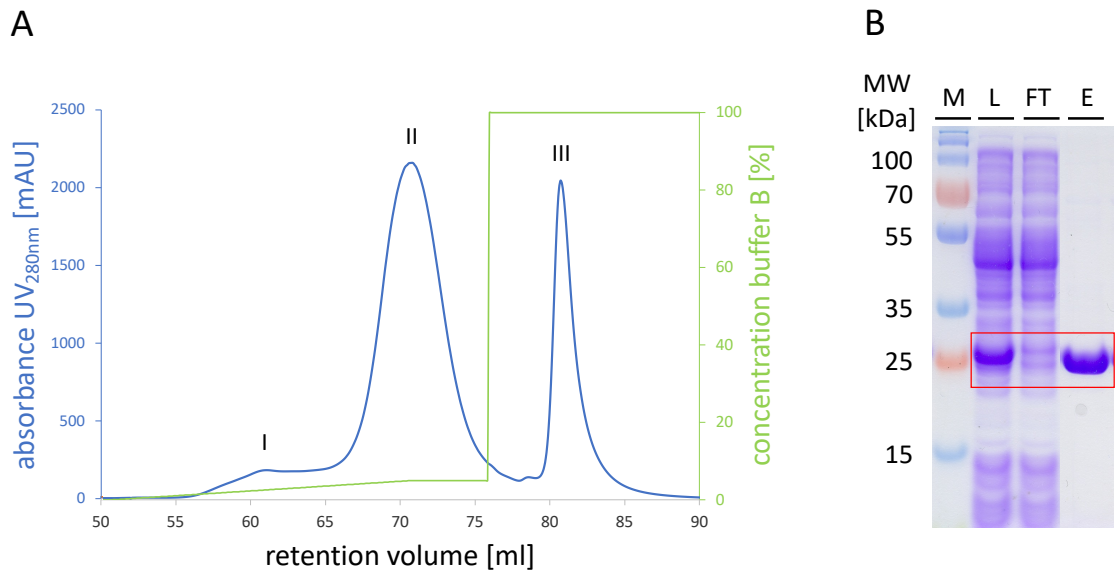

Figure 10: Purification of CTX-M-14. (A) Exemplary representation of the elution profile of CTX-M-14 purification with a HiTrap SP FF cation exchange column. The target protein was eluted in the highest absorption peak (II, blue) of 2200 mAU at a concentration of about 3 – 5 % of the elution buffer (green). This corresponded to a salt concentration of about 40 mM NaCl. **(B)** 12 % SDS polyacrylamide gel of an SDS-PAGE for analysis of the protein purification. Samples of the lysate (L), the flow through of the purification (FT), the eluted fraction of CTX-M-14 (E) and a protein molecular weight marker (M, PageRuler Prestained Protein Ladder) were applied on the gel. The bands corresponding to CTX-M-14 were circled in red. In the pooled elution fraction, a single band was observed at about 28 kDa, which matches the MW of CTX-M-14.

Prior to crystallization, characterization by DLS was performed to ensure that the sample is free of impurities and is in a monodisperse state best suited for crystallization. DLS measurements were performed as described in the methods section 3.4.1. The purified CTX-M-14 sample was concentrated to 11 mg/ml using an Amicon centrifugal concentrator (Merck KGaA, Germany) with a MWCO of 10 kDa. This concentration was chosen as it corresponds to the final concentration present in the crystallization droplet after mixing protein und crystallizing agent. Before DLS measurements, the sample was centrifuged for 60 min at 20000 x g and 4 °C. Calculations for the hydrodynamic radius determined a value of R_H = 2.37 ± 0.03 nm (Figure 11). Assuming a globular protein, this corresponds to a MW of 23.85 kDa, which is slightly smaller than the actual MW of 27.96 kDa. The slight deviation may be due to the fact that CTX-M-14 is not a perfectly globular protein. Nevertheless, the DLS measurements indicated that CTX-M-14 was present as a monomer in a monodisperse solution, providing perfect conditions for crystallization.

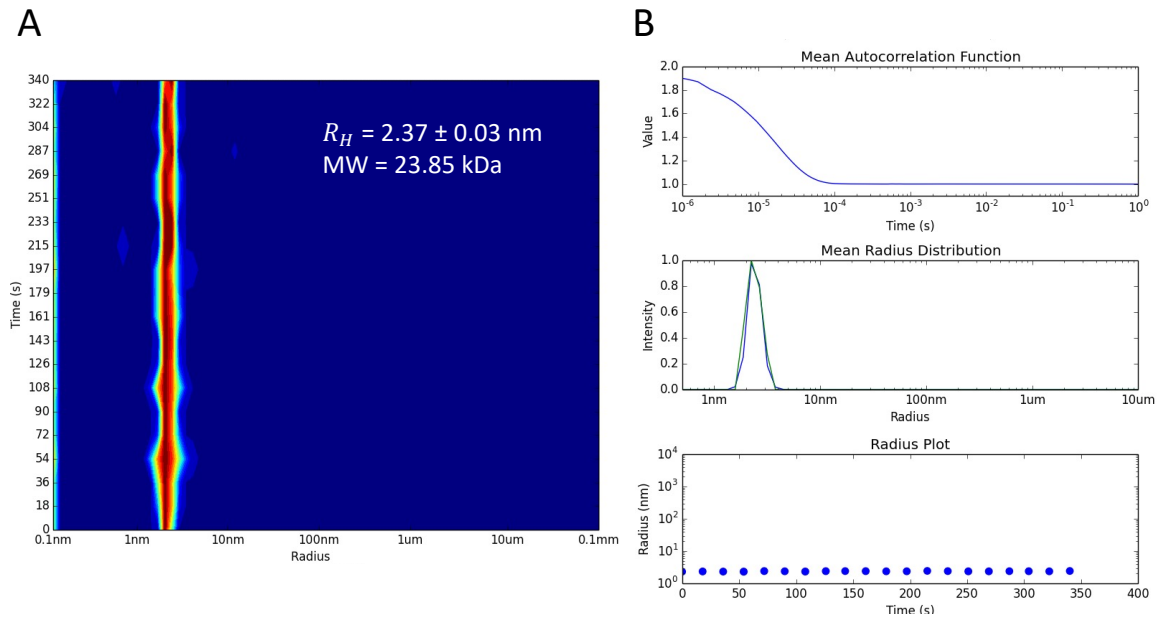

Figure 11: DLS measurements of purified CTX-M-14. (A) Radius distribution over time for CTX-M-14 after purification. The contour plot's color scale indicates the relative intensity of the particle, where blue corresponds to zero intensity, and dark red to the maximum intensity. **(B)** Mean autocorrelation function, mean radius distribution and radius plot showing that CTX-M-14 is pure and monodisperse as only one particle size species is present. The calculated hydrodynamic radius R_H = 2.37 ± 0.03 nm indicates that CTX-M-14 is present as a monomer.

4.2. CTX-M-14 crystallization

Macrocrystals of CTX-M-14 were prepared by the vapor diffusion technique as described in the methods section 3.5.1. For this purpose, a CTX-M-14 protein solution with a concentration of 20 mg/ml and a crystallizing agent containing 25 – 35 % (w/v) PEG8000, 200 mM Li_2SO_4, 100 mM NaOAc at pH 4.5 were used. To cover a wide range of crystallization conditions, the concentration of PEG8000 was varied from 25 – 35 % (w/v). However, most crystals were formed at a concentration of 30 % (w/v) PEG8000. Initial crystals grew over night, looked intergrown (Figure 12 A, B) and were therefore used for a seed stock preparation. Seeding approaches as described in section 3.5.2 increased the number of successful crystallization experiments and improved the crystal morphology (Figure 12 C, D). The obtained crystals had either a hexagonal (Figure 12 C) or trigonal (Figure 12 D) shape, depending on the main crystal shape of the used seed stock. Thus, the seed stock had a significant influence on the crystal shape. These macrocrystals were used to determine the high resolution cryo-crystal structure of the CTX-M-14 native enzyme and for soaking experiments with antibiotic substrates and inhibitors.

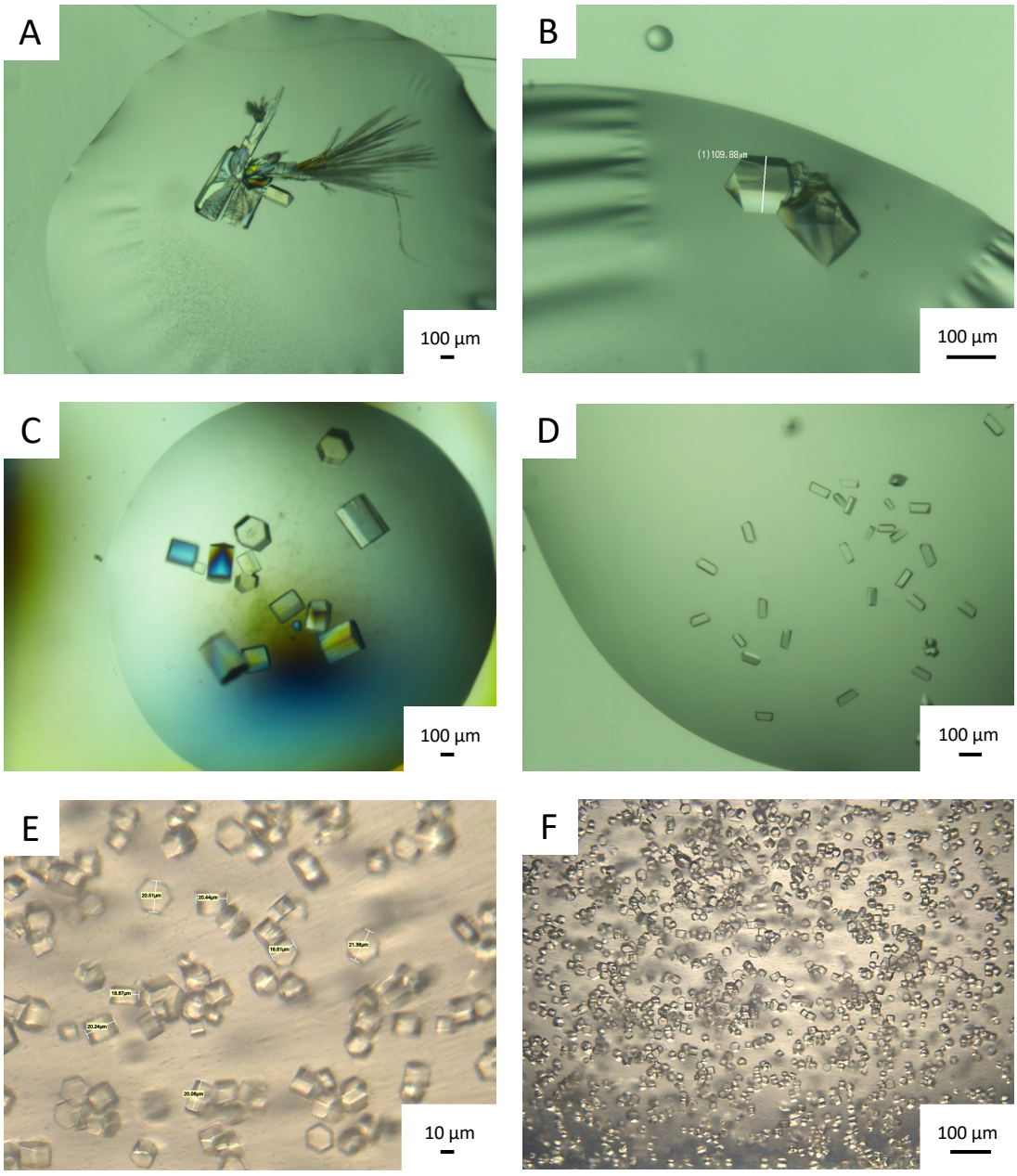

Figure 12: Crystallization of CTX-M-14. (A-B) Macrocrystals with different morphologies obtained by vapor diffusion crystallization experiments with 25 – 35 % (w/v) PEG8000, 200 mM Li_2SO_4, 100 mM NaOAc at pH 4.5. **(C-D)** Macrocrystals obtained by vapor diffusion crystallization experiments optimized by a seeding approach. As a result, only one crystal morphology is present in each crystallization droplet. **(E-F)** Microcrystals with a homogeneous size distribution of 16 – 21 µm obtained by batch crystallization experiments with 40 % (w/v) PEG8000, 200 mM Li_2SO_4, 100 mM NaOAc at pH 4.5 used for SFX and SSX data collection.

Time-resolved structural analysis of CTX-M-14 with various substrates and inhibitors requires very small and well-diffracting microcrystals with a homogeneous size distribution suitable for serial crystallography. Such microcrystals were prepared by batch crystallization method as described in section 3.5.3. In a typical batch crystallization approach, volumes of 50 % (v/v) CTX-M-14 protein solution (20 mg/ml) and 40 – 49 % (v/v) crystallizing agent (40 % (w/v)

PEG8000, 200 mM Li_2SO_4, 100 mM NaOAc at pH 4.5) and 1 – 10 % (v/v) highly concentrated seed stock were mixed in a 1.5 ml reaction tube. Resulting microcrystals had a homogenous size distribution of 16 – 21 µm (Figure 12 E, F). However, the crystal size could be varied by changing the percentage of seed stock in the batch crystallization setup. A higher percentage of seed stock increases the number of crystallization nuclei added to the batch, resulting in the growth of more and smaller crystals. Once the microcrystals reached the desired size, they were centrifuged for 10 min at 200 x g and 20 °C and the supernatant was replaced with microcrystal stabilization buffer (28 % (w/v) PEG8000, 140 mM Li_2SO_4, 70 mM NaOAc, 6 mM MES and 21 mM NaCl at pH 4.5). The prepared CTX-M-14 microcrystals diffracted very well and were stable for at least 6 months.

4.3. Stability of CTX-M-14 microcrystals at low PEG8000 concentrations

The PEG8000 concentration in the microcrystal stabilization buffer (28 % (w/v) PEG8000, 140 mM Li_2SO_4, 70 mM NaOAc, 6 mM MES and 21 mM NaCl at pH 4.5) was chosen slightly higher than in the actual crystallization conditions to keep the equilibrium on the side of the crystals, since the free protein has been removed. The intention was to prevent the crystals from dissolving and keep them stable for a longer time. However, the increased PEG8000 concentration leads to a higher viscosity of the sample, which was a disadvantage in some serial crystallography procedures. Using the LAMA approach (described in section 3.6.2.2) for mix-and-diffuse time-resolved crystallography experiments, a small droplet of a few picoliter of the substrate is injected onto an individual well of a chip containing a microcrystal. For substrate solutions with high viscosity, the formation of a uniform drop was problematic. Adding the substrate in a solution with a lower PEG8000 concentration than in the microcrystal approach could have a negative impact on the microcrystal stability. Therefore, it was investigated to what extent the PEG8000 concentration could be decreased while the concentration of all other buffer components remained the same. The CTX-M-14 microcrystals were centrifuged for 10 min at 200 x g and 20 °C and the supernatant was replaced with microcrystal stabilization buffer (140 mM Li_2SO_4, 70 mM NaOAc, 6 mM MES and 21 mM NaCl at pH 4.5) containing 28 % (w/v) PEG8000, 10 % (w/v) PEG8000 or 5 % (w/v) PEG8000 (Figure 13). While the crystals at 28 % PEG8000 did not show any microscopically visible limitations in crystal stability over the time course of 60 min., the condition at 10 % (w/v) PEG8000 has resulted in a slightly cracked surface of the crystals after 30 min. After 60 min, many crystals

are still present, but a clear crystal surface is hardly visible. However, the crystals at 10 % (w/v) PEG8000 after 10 min. still look comparable to the crystals at 28 % (w/v) PEG8000, so it can be assumed that they have not been damaged during this time period. Thus, it could be shown that the CTX-M-14 microcrystals survive a short-term reduction of the PEG8000 concentration to 10 % (w/v). The 5 % (w/v) PEG8000 exhibited a drastically reduced number of microcrystals after only 10 min. Therefore, the PEG8000 concentration can be reduced to 10 % (w/v) for up to 10 min. in time-resolved serial crystallography setups with viscosity constraints.

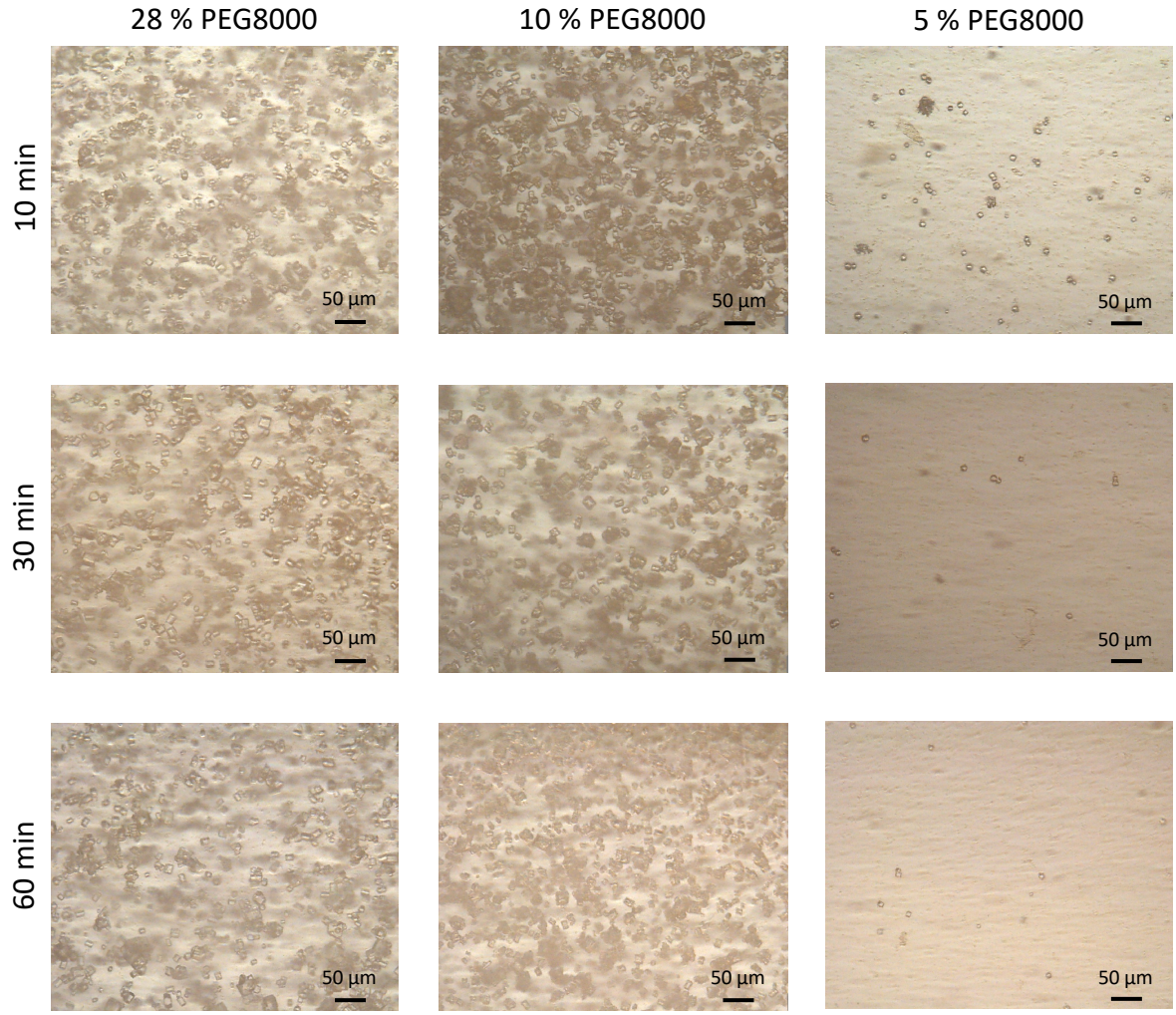

Figure 13: CTX-M-14 microcrystals tested for stability by exposure to low PEG8000 concentrations in crystallizing agent for 10, 30 and 60 min. 28 % PEG8000 corresponds to the standard concentration in the stabilization buffer and is shown for comparison. With 10 % PEG8000, the crystals begin to show the first changes after 30 min., whereas with 5 % PEG8000 the majority of all crystals have dissolved in less than 10 min.

4.4. Hydrolysis activity of the CTX-M-14 crystal

It has been demonstrated several times that enzymes arranged in the crystal lattice retain their catalytic activity, allowing time-resolved structural analysis (Brändén & Neutze, 2021; Kupitz et al., 2014; Mehrabi et al., 2019b). To visualize the hydrolysis activity of CTX-M-14 within the crystal, a CTX-M-14 crystal was placed in a crystallization drop containing nitrocefin and was observed over a period of 40 min. Nitrocefin is a chromogenic cephalosporin routinely used to detect the presence of β-lactamase enzymes produced by various microbes. It comprises a β-lactam ring that is susceptible to β-lactamase mediated hydrolysis. The hydrolysis results in a shift of the absorption maximum from 390 nm to 486 nm, which is reflected in a color change from yellow/green to red and allows visual detection of β-lactamase activity on a macroscopic level.

A CTX-M-14 crystal with the size of 200 x 200 x 300 µm was transferred into a fresh droplet of crystallizing solution (20 % (w/v) PEG8000, 100 mM Li_2SO_4, 50 mM NaOAc at pH 4.5) to remove residual free protein. Subsequently, the crystal was transferred into a droplet of crystallizing solution (20 % (w/v) PEG8000, 100 mM Li_2SO_4, 50 mM NaOAc at pH 4.5) containing 2 mM nitrocefin (Figure 14). Due to the nitrocefin, this droplet was colored yellow/green. A slight red coloration around the crystal could be observed as early as 0.5 min after the addition of the CTX-M-14 crystal to the droplet, indicating the β-lactamase activity of the crystal (Figure 14, 0.5 min). The red coloration continues to spread due to diffusion and further hydrolytic cleavage of nitrocefin. Thus, this experiment successfully demonstrated that CTX-M-14 retains its catalytic activity in the crystal.

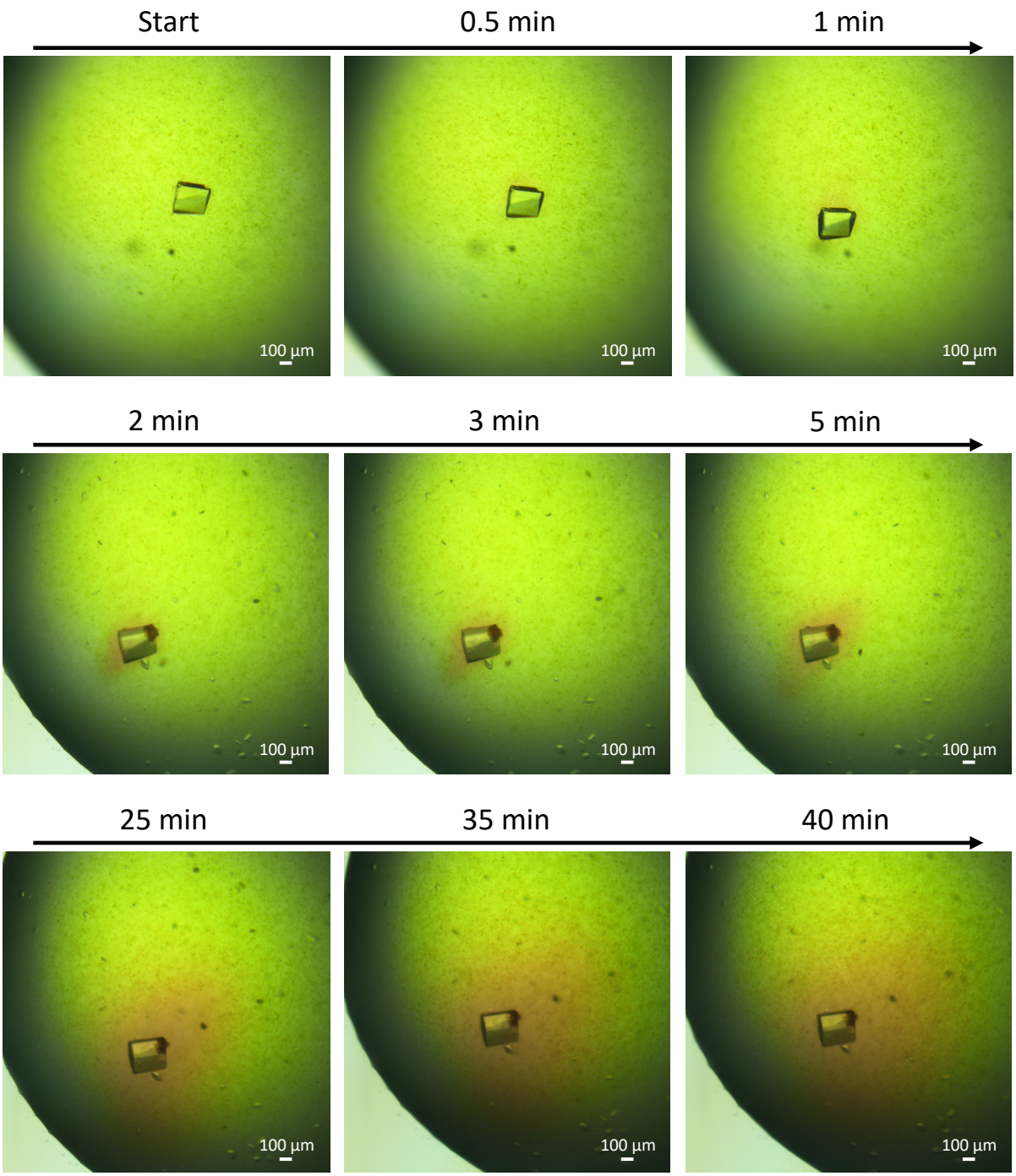

Figure 14: Nitrocefin hydrolysis by CTX-M-14 crystal in a crystallization droplet. CTX-M-14 crystal was placed in a crystallization droplet containing 2 mM nitrocefin and the color change (yellow/green to red) due to the hydrolysis of nitrocefin was observed over a time period of 0.5 – 40 min.

4.5. Determination of enzyme kinetic parameters

The steady state parameters such as the turnover number k_{cat} and the Michaelis constant K_m are important quantities of enzyme kinetics. The rate constant of the rate-determining step of the reaction is denoted by k_{cat} and indicates the number of substrate molecules that are converted in one second. In addition, the Michaelis constant K_m indicates the substrate concentration at which the turnover rate is half-maximal.

Literature survey of the kinetic parameters of CTX-M-14 revealed turnover numbers ranging from 3 – 2700 molecules per second for the hydrolysis of various antibiotics (Bonnet, 2004; Ishii et al., 2007). Thus, even with the slowest substrate ceftazidime (CAZ) with a k_{cat} of 3 s^{-1} (Bonnet, 2004), the probability of detecting transient intermediate states in time-resolved crystallography approaches is very limited as a single ceftazidime molecule would be hydrolyzed in about 333 ms. Initial time-resolved serial crystallography diffraction data collections using the CFEL TapeDrive failed to show electron density for ceftazidime in the active site of CTX-M-14 after a mixing delay time of 250 ms (see section 4.6.1.3). Therefore, the turnover number of CTX-M-14 had to be decreased. In addition to the adaptation of chemical parameters (viscosity, pH, concentrations), temperature is an important parameter for regulating the catalytic rate of an enzyme according to van't Hoff's rule and Eyring transition state theory. The influence of these parameters on the environment-dependent enzymatic turnover number was investigated by determining the steady state kinetic parameters k_{cat} and K_m. Furthermore, the kinetic parameters of 10 different antibiotics were tested to determine the best substrate for the time-resolved structural analyses. In addition, the efficacy of different β-lactamase inhibitors on CTX-M-14 were investigated by determining the 50 % inhibitory concentration IC_{50}. Inhibitors have the advantage of having a relatively long lasting terminal state bound to the β-lactamase, making them easier to capture by time-resolved data collections. For example, it is easier to estimate whether the selected time point is suitable for the experiment. If there was no electron density for the inhibitor, the chosen time point probably represented a state before the binding process, so a longer delay time point should be chosen.

4.5.1. Kinetic parameters of CTX-M-14 at various pH values

Since crystallization was performed at pH 4.5, alkaline pH values were not considered for determining the kinetic parameters of CTX-M-14. Alkaline pH values could not have been

applied to time-resolved serial crystallography experiments because such a large change in pH could have a negative impact on the stability and diffraction quality of the microcrystals. Therefore, the steady state parameters k_{cat} and K_m (Table 12) for the hydrolysis of ampicillin and cefotaxime by CTX-M-14 were determined at pH 7.4 (PBS), pH 6 (20 mM MES), pH 4.5 (20 % (w/v) PEG8000, 100 mM Li_2SO_4, 50 mM NaOAc) and pH 3 (40 mM citric acid, 20 mM Na_2HPO_4). It should be noted that the conditions at pH 4.5 correspond to the crystallization conditions and thus also consider the viscosity of the solution. The experiments were performed as described in section 3.3.8.

For ampicillin, lowering the pH from 7.4 to 3 reduced the enzymatic turnover number by a factor of 5 from 77 ± 2 s^{-1} to 15 ± 8 s^{-1} (Table 12). At the same time, the Michaelis constant K_m increased and thus the half-maximal velocity is only reached at higher substrate concentrations. Cefotaxime showed the same decreasing tendency in turnover number at acidic pH, but with a smaller reduction by a factor of about 2.5 when the pH was reduced to pH 3. Thus, a possibility of reducing the reaction rate of CTX-M-14 β-lactamase by lowering the pH was demonstrated. However, the effect of pH change on the diffraction quality of the crystals would need to be investigated if applied to time-resolved serial crystallography experiments.

Table 12: CTX-M-14 WT steady-state parameters k_{cat} and K_m for ampicillin and cefotaxime at various pH.

Antibiotic	k_{cat} [s^{-1}]				K_m [µM]			
	pH 7.4	pH 6	pH 4.5	pH 3	pH 7.4	pH 6	pH 4.5	pH 3
ampicillin	77 ± 2	49 ± 1	40 ± 23	15 ± 8	130 ± 11	62 ± 6	850 ± 400	1250 ± 400
cefotaxime	81 ± 4	75 ± 3	49 ± 3	33 ± 4	158 ± 19	23 ± 5	680 ± 74	313 ± 74

4.5.2. Kinetic parameters of CTX-M-14 at various temperatures

The temperature dependence of β-lactam hydrolysis by CTX-M-14 was investigated using ampicillin (Figure 15) and cefotaxime as substrates at 28 °C and 4 °C. Low temperatures were of particular interest as reaction rates needed to be reduced for time-resolved experiments. Unfortunately, this turned out to be a problem, as most photometric instruments do not have a refrigeration function. Therefore, the experiments were performed in the cold room at a

temperature of 4 °C. Nevertheless, the comparison of the reaction rate at the two temperatures showed a reduction of the turnover number k_{cat} by a factor of 2.5 for both investigated substrates (Table 13). For ampicillin, the turnover number k_{cat} decreased from 49 ± 1 s^{-1} at 28 °C to 19 ± 1 s^{-1} at 4 °C and for cefotaxime from 75 ± 3 s^{-1} to 31 ± 3 s^{-1}. With this information, time-resolved structural analysis can be optimized after introducing temperature control features in time-resolved serial crystallography setups at the CFEL TapeDrive. Thus, the reaction rate can be reduced accordingly, and possible transient states can be investigated with high temporal resolution.

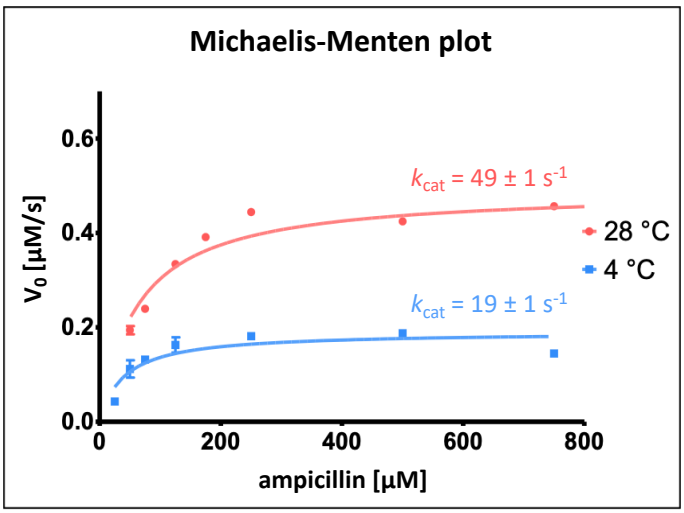

Figure 15: Michaelis-Menten plot of ampicillin hydrolysis by CTX-M-14 β-lactamase at pH 6 (20 mM MES) and 28 °C or 4 °C. Initial rates of enzymatic hydrolysis were plotted against the corresponding concentration of the antibiotic. A reduction in the initial rate of hydrolysis of ampicillin at colder temperatures is evident, which is also reflected in the reduction of the corresponding k_{cat} values by a factor of 2.5.

Table 13: CTX-M-14 WT steady-state parameters k_{cat} and K_m for ampicillin and cefotaxime at pH 6 and different temperatures.

Antibiotic	k_{cat} [s^{-1}]		K_m [µM]	
	28 °C	4 °C	28 °C	4 °C
ampicillin	49 ± 1	19 ± 1	62 ± 6	40 ± 12
cefotaxime	75 ± 3	31 ± 3	70 ± 8	12 ± 6

4.5.3. Kinetic parameters of CTX-M-14 with various antibiotics

In search of a relatively slowly hydrolyzed substrate, the kinetic parameters of hydrolysis of 10 different β-lactam antibiotics (Table 14) by CTX-M-14 β-lactamase were determined using a photometric approach as described in section 3.3.8. Corresponding Michaelis-Menten-plots of these antibiotics are shown in the appendix in Figure S3 and the corresponding molar extinction coefficients used for calculations in Table S1. Chemical structures of the antibiotics are shown in Figure S4. The penicillin antibiotics ampicillin, benzylpenicillin and piperacillin showed a wide range of turnover numbers. While ampicillin and piperacillin had very similar turnover numbers with a k_{cat} of 49 ± 0.9 s^{-1} and 45 ± 2.0 s^{-1}, respectively, benzylpenicillin was the second fastest hydrolyzed of the studied antibiotics with a k_{cat} of 254 ± 5.7 s^{-1}. Interestingly, although having a similar turnover number to ampicillin, piperacillin had a much lower K_m of 10 ± 6.5 µM and thus the half-maximal rate was reached at much lower concentrations of the antibiotic. The only tested first-generation cephalosporin, cefalotin, was by far the most rapidly hydrolyzed antibiotic with a k_{cat} of 565 ± 13.2 s^{-1}, which made it unsuitable for later time-resolved experiments. The second-generation cephalosporin cefuroxime and the fourth-generation cephalosporin cefepime yielded k_{cat} values of 96 ± 3.1 s^{-1} and 129 ± 13.1 s^{-1}, respectively. Thus, these antibiotics were also hydrolyzed faster than ampicillin or cefotaxime and were therefore also not suitable for the time-resolved experiments. Only the third generation cephalosporins showed relatively low turnover numbers, except for cefotaxime with a k_{cat} of 75 ± 2.6 s^{-1}. The hydrolysis of ceftriaxone was the third slowest of the antibiotics measured, with a k_{cat} of 25 ± 0.8 s^{-1}. Ceftazidime and cefdinir exhibited the smallest turnover rates with a k_{cat} of 0.9 ± 0.2 s^{-1} and 2 ± 0.1 s^{-1}, respectively. Thus, these two antibiotics were particularly well suited for the following time-resolved serial crystallography experiments. However, it should be noted that ceftazidime showed a relatively high K_m of 676 ± 177 µM compared to the other antibiotics investigated, which could be caused by a low affinity for the CTX-M-14 active site. In contrast, ceftriaxone and piperacillin could be also considered for the time-resolved experiments due to their low K_m values of 7.5 ± 1.4 µM and 10 ± 6.5 µM, respectively.

Table 14: Kinetic parameters of CTX-M-14 with various substrates at 28 °C and pH 6.

Antibiotic	k_{cat} [s^{-1}]	K_m [µM]
ampicillin	49 ± 0.9	62 ± 5.9
benzylpenicillin	254 ± 5.7	38 ± 8.3
cefalotin	565 ± 13.2	16 ± 3.3
cefdinir	2 ± 0.1	7.4 ± 1.2
cefepime	129 ± 13.1	381 ± 69.2
cefotaxime	75 ± 2.6	70 ± 8.1
ceftazidime	0.9 ± 0.2	676 ± 177
ceftriaxone	25 ± 0.8	7.5 ± 1.4
cefuroxime	96 ± 3.1	41 ± 7.9
piperacillin	45 ± 2.0	10 ± 6.5

4.5.4. Inhibition of CTX-M-14

In addition to the substrates of CTX-M-14, β-lactamase inhibitors were investigated in this work. To assess the inhibitory effect of the compounds on CTX-M-14, the 50 % inhibitory concentration IC_{50} was determined as described in section 3.3.9. The IC_{50} corresponds to the concentration of inhibitor required to decrease the initial rate of hydrolysis of the substrate by 50 %. The approved non-β-lactam based β-lactamase inhibitor avibactam was used to investigate the feasibility of the assay. Avibactam showed an inhibitory effect on CTX-M-14 even at low concentrations, reaching an IC_{50} value of 3.4 ± 0.3 nM (Figure 16).

Furthermore, the proteasome inhibitors bortezomib and ixazomib were studied in a repurposing approach in search of new opportunities for inhibitor development (Perbandt et al., 2022). Both proteasome inhibitors exhibited a dual mode of inhibition, so in addition to inhibition of proteases, they were able to effectively reduce the hydrolysis activity of CTX-M-14. However, the inhibitory effect was observed only at relatively high concentrations for inhibitors in the micromolar rather than nanomolar range, resulting in IC_{50} values of 68 ± 19 µM for bortezomib and 13 ± 2.4 µM for ixazomib (Figure 16) (Perbandt et al., 2022).

Nevertheless, the inhibitory effect of ixazomib was about five times stronger than that of bortezomib.

In addition, boric acid was tested in combination with glycerol as an inhibitor model to further investigate the basis of many new boronate-based β-lactamase inhibitors and the proteasome inhibitors mentioned here. The boric acid and glycerol combination, however, only achieved an IC_{50} value of 913 ± 342 µM (Figure 16), which is about 3×10^5 times higher than that of avibactam. Additionally, it should be noted that the standard error is very large compared to the other tested compounds, which could be attributed to the generally low inhibition of the boric acid and glycerol combination.

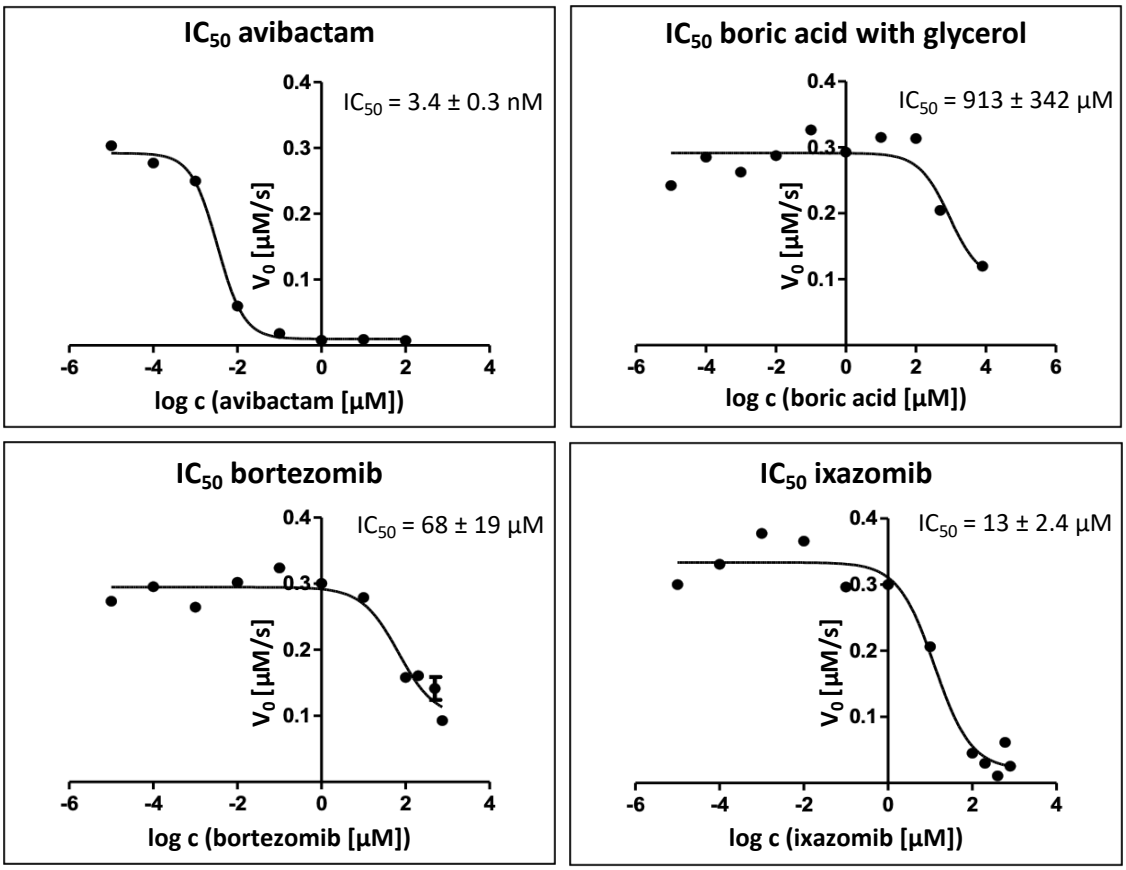

Figure 16: Inhibition assays showing the effect of avibactam, boric acid with glycerol, bortezomib and ixazomib on β-lactam hydrolysis by CTX-M-14 β-lactamase. The initial velocities of cefotaxime hydrolysis were plotted against the log concentration of each inhibitor, showing the decrease in hydrolysis rates at higher concentrations of the compounds. Calculated IC_{50} values are 3.4 ± 0.3 nM for avibactam, 913 ± 342 µM for boric acid with glycerol, 68 ± 19 µM for bortezomib and 13 ± 2.4 µM for ixazomib.

4.6. Time-resolved serial crystallography experiments

4.6.1. Serial synchrotron crystallography using the CFEL TapeDrive

The results described in this section were obtained using the CFEL TapeDrive (Beyerlein et al., 2017) at the P11 beamline (Burkhardt et al., 2016) of the PETRA III synchrotron (DESY, Hamburg, Germany) as described in section 3.6.2.1. A research article in which I am co-first author, describing the procedure and the first serial crystallography data in detail, was published in the International Union of Crystallography Journal IUCrJ (Zielinski et al., 2022).

4.6.1.1. First room temperature structure of inhibitor-free CTX-M-14

In the initial experiments with the CFEL TapeDrive, microcrystals of CTX-M-14 were measured to determine a native reference structure at room temperature and to evaluate the feasibility of the TapeDrive for this project. In addition, the sample consumption was evaluated to adjust the production quantities of the protein, if necessary. Furthermore, the time required for the collection of a complete dataset was determined in order to plan the following beam times accordingly. CTX-M-14 diffraction data was collected at room temperature resulting in datasets with 5000 detector images (5k, represents first 5000 images of the full dataset), 10000 detector images (10k) and a full dataset with 127171 detector images (full dataset). Data processing was performed using CrystFEL (White et al., 2012; White et al., 2016), and structure solution and refinement was performed using the Phenix software suite (Paul D Adams et al., 2010; Liebschner et al., 2019). Corresponding data collection and refinement statistics are shown in Table 15. The Matthews coefficient of the crystals was 2.15 $Å^3$/Da, corresponding to a solvent content of 43 %. According to Matthews Cell Content Analysis (CCP4i; Winn et al., 2011) the asymmetric comprised a single protein molecule. All datasets were complete and could be used to solve the crystal structure of CTX-M-14. Thus, it was shown that a complete dataset with only 5k images could be acquired in 200 s at an acquisition rate of 25 Hz. This consumed a total of no more than 34 µg of protein in about 3.3 µl of microcrystal suspension (Zielinski et al., 2022). The resolution cut-off during processing was set to $CC_{1/2}$ = 0.15. Of the 5000 detector images, 5109 crystals could be indexed by CrystFEL, resulting in a complete dataset with a resolution of about 1.55 Å. The 10k dataset yielded only 4286 indexed lattices by CrystFEL, likely due to a lower hit rate than the 5k dataset.

Table 15. Data collection and refinement statistics for CTX-M-14 β-lactamase native enzyme using the CFEL TapeDrive (Zielinski et al., 2022).

	CTX-M-14 (full dataset)	CTX-M-14 (10000 frames)	CTX-M-14 (5000 frames)
PDB entry	7zpv	8af7	8af8
Temperature (K)	293	293	293
Crystal size (µm)	10-20	10-20	10-20
No. of collected images	127170	10382	5000
Total measuring time (s)	5086	415.3	200
Average acquisition rate (Hz)	25	25	25
Indexed patterns	61331	4286	5109
Indexed per second	12.1	10.3	25.6
Space group	$P3_221$	$P3_221$	$P3_221$
a, *b*, c (Å)	42.2, 42.2, 234.4	42.2, 42.2, 234.4	42.2, 42.2, 234.4
α, β, γ (°)	90, 90, 120	90, 90, 120	90, 90, 120
Solvent content	0.397	0.397	0.397
Resolution (Å)	1.40-17.77 (1.40-1.42)	1.55-17.77 (1.55-1.58)	1.55-17.77 (1.55-1.58)
Unique reflections	49225 (4733)	36504 (3514)	36495 (3514)
$\langle I/\sigma(I)\rangle$	9.11(0.69)	3.25 (0.62)	3.75 (0.63)
Completeness (%)	100 (100)	99.98 (100)	99.98 (100)
Multiplicity	2217 (1400)	114 (65.0)	149 (75.1)
R_{split}	7.2 (165.91)	27.8 (172.41)	22.97 (170.30)
$CC_{1/2}$	0.991 (0.266)	0.815 (0.268)	0.907 (0.262)
CC*	0.998 (0.648)	0.948 (0.650)	0.975 (0.644)
Wilson *B* factor (Å^2)	24.22	23.58	23.14
Resolution range in refinement (Å)	1.40-17.78 (1.40-1.47)	1.55-16.54 (1.55-1.61)	1.55–14.95 (1.55–1.61)
Reflections used in refinement	49225 (4832)	36504 (3523)	36495 (3521)
Reflections used for R_{free}	1033 (100)	768 (74)	765 (73)
R_{work}	0.1410 (0.3338)	0.1797 (0.3015)	0.1758 (0.3775)
R_{free}	0.1561 (0.3827)	0.2147 (0.3192)	0.1988 (0.3643)
RMS (bonds)	0.009	0.006	0.011
RMS (angles)	1.01	0.82	1.18
Ramachandran favored (%)	97.68	97.27	98.06
Ramachandran allowed (%)	1.93	2.34	1.55
Ramachandran outliers (%)	0.39	0.39	0.39
Rotamer outliers (%)	1.87	1.83	0.95
Clashscore	2.19	6.90	3.47
Average *B*-factor	34.26	32.61	34.56
macromolecules	33.23	31.50	32.66
ligands	78.08	45.56	46.35
solvent	45.06	44.97	123.90
MolProbity score	1.27	1.27	0.89

Statistics for the highest-resolution shell are shown in parentheses.

Nevertheless, a structure with a similar resolution and similar R_{work} and R_{free} values could be determined with this dataset (Table 15). However, the full dataset with 127171 detector images and 61331 indexed crystals yielded an even higher resolution of 1.40 Å. This is mainly due to the higher multiplicity and better I/sigma and therefore more observed unique reflections of the full dataset. This also resulted in the R_{work} = 0.141 and R_{free} = 0.156 values of

the full dataset being lower than those of the 5k dataset with R_{work} = 0.176 and R_{free} = 0.199. Nevertheless, the calculated electron density maps of the three datasets did not show any significant differences. Thus, it could be shown that a complete dataset could be acquired after 200 s of data collection. However, a longer measurement of the sample offered a slightly better data quality, so that priorities can be set accordingly when planning beam times. These initial experiments demonstrated the potential of the TapeDrive for serial crystallography data collection, so this method was utilized to collect time-resolved data to study biological questions. (Zielinski et al., 2022)

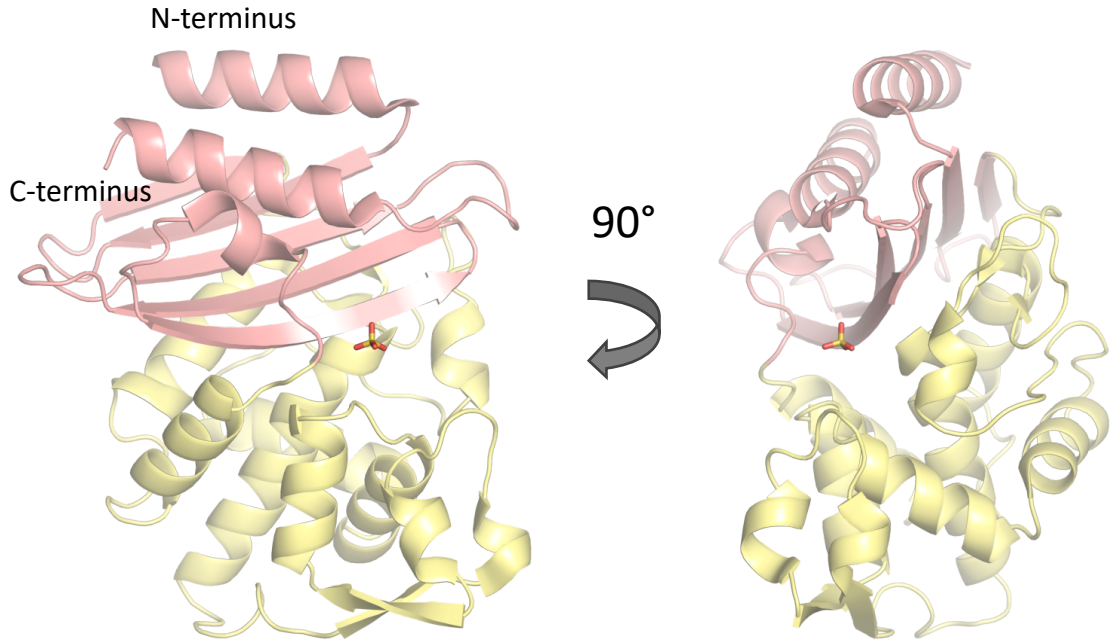

Figure 17: X-ray structure of CTX-M-14 with a resolution of 1.4 Å collected at room temperature using the CFEL TapeDrive (PDB 7zpv, Zielinski et al. (2022)). The structure consists of an α+β-domain (salmon) and an α-domain (yellow). A sulfate ion is located in the anion binding site in close proximity to the active site, which is located in the groove between the two domains.

The resulting model of CTX-M-14 demonstrates excellent geometry and the overall structure is similar to other Ambler class A β-lactamases and other members of the CTX-M family (Lahiri et al., 2013). CTX-M-14 consists of two domains, an α+β-domain and an α-domain (Figure 17). The α+β-domain (residues 27 – 60 and 216 – 289) comprises the N- and C-terminal helices of the protein and five antiparallel β-sheets. The α-domain (residues 61 – 215) consists of the other α-helices and four small β-sheets. A sulfate ion is present in the anion binding site in close proximity to the active site, which is located in the groove between the two domains and consists of conserved amino acid residues of Ambler class A β-lactamases (Figure 18).

Ser70 is responsible for the covalent binding of substrates. The core catalytic residues are Ser70, which forms a covalent bond with the substrate, and the three main residues Lys73, Ser130 and Glu166 involved in the proton shuttling mechanism for β-lactam hydrolysis (Chen et al., 2007; Chen et al., 2005b). In this native structure without a substrate, however, only a sulfate ion is present in the anion binding site and is coordinated by the side chains of Ser130, Lys234, Thr235 and Ser237 (Figure 18).

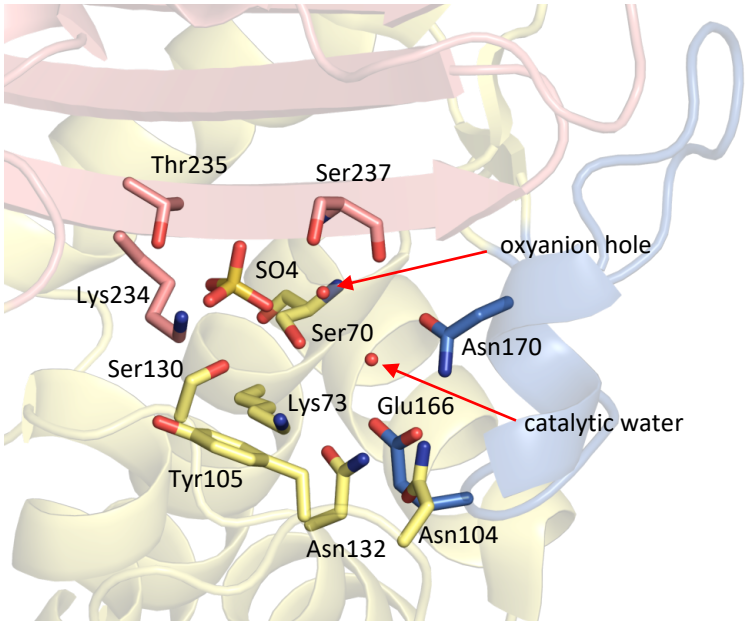

Figure 18: Active site of CTX-M-14 (PDB 7zpv) with a stick representation of residues conserved in Ambler class A β-lactamases. The groove between the α+β-domain (salmon) and the α-domain (yellow) forms the active site that is flanked by the Ω-loop (blue). The water molecule in the oxyanion hole and the catalytic water molecule are marked with a red arrow.

Looking at the surface charge of the protein, the anion binding site is represented by a positively charged pocket (Figure 19). Right next to the anion binding site is the oxyanion hole formed by the backbone amide groups of Ser70 and Ser237, which is important for stabilizing a negatively charged oxygen and is occupied by a water molecule in the native structure (Murphy & Pratt, 1988; Rodkey et al., 2012). At this site, an acyl carbonyl of covalently bound substrates or inhibitors is usually stabilized (e.g., relebactam, section 4.6.1.4). The side chains of Asn104 and Asn132 are located close to each other forming a part of the cationic patch in the active site that interacts with carboxamide carbonyl oxygens of the core β-lactam structure (Lahiri et al., 2013). However, in the native enzyme, these residues coordinate a network of water molecules.

The Ω-loop (Figure 18) consists of the amino acid residues 161 – 179 and plays an important role in substrate and inhibitor binding (Poirel et al., 2001; Shurina & Page, 2021). Specific mutations (e.g., P167S) in this Ω-loop cause an extended-spectrum of the β-lactamase, primarily by increasing the size and flexibility of the binding pocket and thus eliminating steric hindrance (Both et al., 2017).

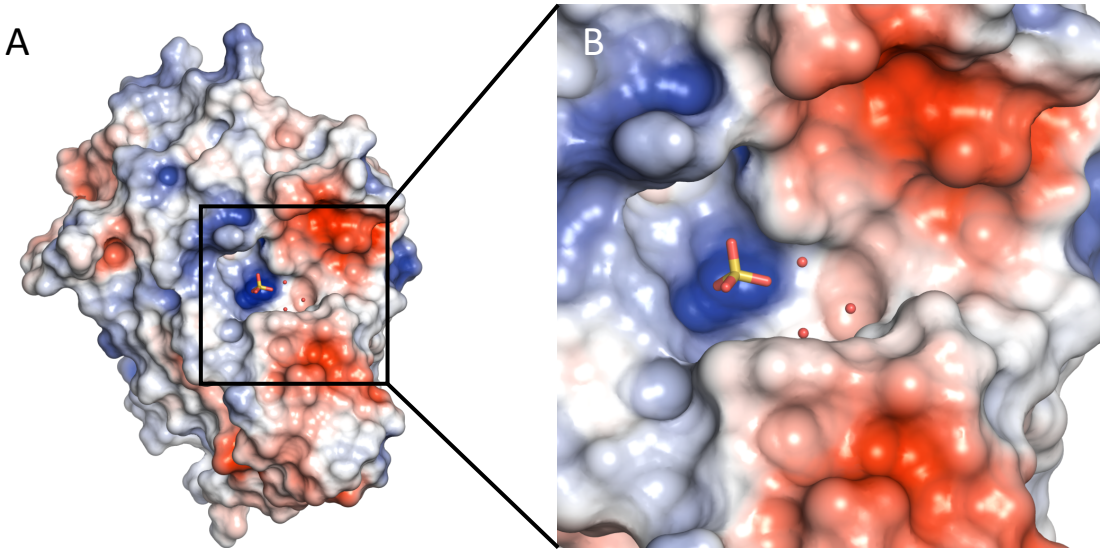

Figure 19: Electrostatic surface representation of (A) CTX-M-14 and (B) a focus on the active site. Positively charged areas of the enzyme surface are displayed in blue and negatively charged areas in red. The binding pocket of CTX-M-14 forms a strong positively charged region in which a sulfate is present in the native structure. This region is referred to as the anion binding site. The electrostatic surface representation is calculated and visualized by the APBS Electrostatics plugin in Pymol (Jurrus et al., 2018; Lerner & Carlson, 2006).

4.6.1.2. Comparison of CTX-M-14 X-ray structures at room temperature and cryogenic temperature

The CTX-M-14 X-ray structures at room temperature were determined by serial synchrotron crystallography (Zielinski et al., 2022) or serial femtosecond crystallography (Wiedorn et al., 2018) using microcrystals, while the X-ray structures at cryogenic temperature were determined by standard rotational series single crystal crystallography using macrocrystals at cryogenic temperatures (Perbandt et al., 2022). In this chapter the already mentioned TapeDrive structure 7zpv (1.4 Å) and the CTX-M-14 cryoMX structure 7q0z (1.0 Å) are being compared. It should be noted that the cryoMX structure (7q0z) was solved by the colleague Nadine Werner from the group of Prof. Betzel (Hamburg University) and published in a joint

research article (Perbandt et al., 2022). However, it is the best structure for this comparison because it was produced according to the same protocol and crystallization conditions. Although the micro and macrocrystals were produced under similar conditions, they differ in their symmetry and unit cell parameters. The macrocrystals were arranged in the orthorhombic $P2_12_12_1$ space group, while the microcrystals were arranged in the trigonal $P3_221$ space group (Figure 21). In addition, the microcrystals did not require cryo protection since data collection was performed at room temperature, whereas the macrocrystals were briefly soaked in glycerol to protect them from freezing solvent molecules that might otherwise disrupt the crystal lattice. As a result, three glycerol molecules are present in the cryoMX structure. Due to the sulfate-containing crystallization conditions, both structures include sulfate ions. In both structures, a sulfate ion is present in the anion binding site as it can be stabilized by the amino acid side chains described above. The cryoMX structure has four more sulfate ions distributed in the periphery of the protein, whereas the TapeDrive structure has only one more sulfate ion.

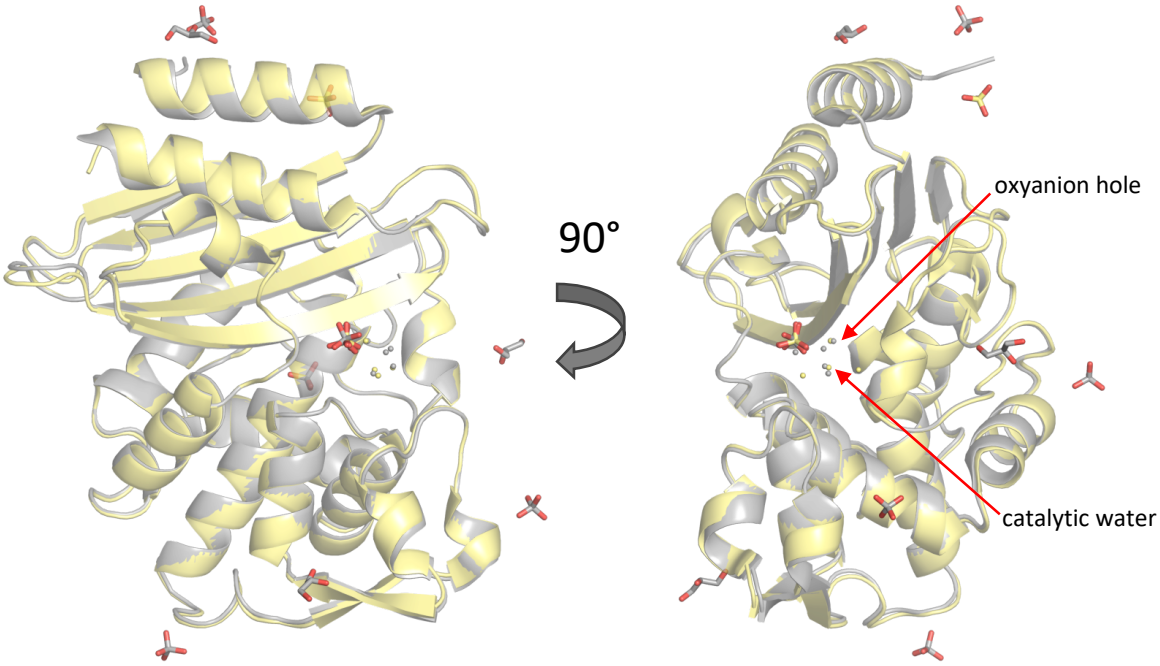

Figure 20: Comparison of the overall structures of CTX-M-14 collected at room temperature (yellow, PDB 7zpv, Zielinski et al. (2022)) and the cryoMX structure (grey, PDB 7q0z, Perbandt et al. (2022)). Good alignment of the asymmetric unit with an RMSD of 0.293 Å despite the differences in space group symmetry and unit cell dimensions.

Furthermore, it is noticeable that 490 water molecules are present in the CryoMX structure, while only 154 water molecules are present in the TapeDrive structure. Nevertheless, both structures include the well-coordinated water molecules in the active site, such as the catalytic water or the water in the oxyanion hole (Figure 20).

Alignment of both structures was performed using PyMOL and showed that the structures matched very well despite the differences in symmetry and unit cell dimensions resulting in an RMSD of 0.293 Å (Figure 20). Solvent channels within the crystals were calculated using the MAP_CHANNELS tool (Juers & Ruffin, 2014), revealing slightly larger solvent channels for the microcrystals used for TapeDrive experiments compared to the macrocrystals used for cryoMX, making mix-and-diffuse studies more feasible (Zielinski et al., 2022).

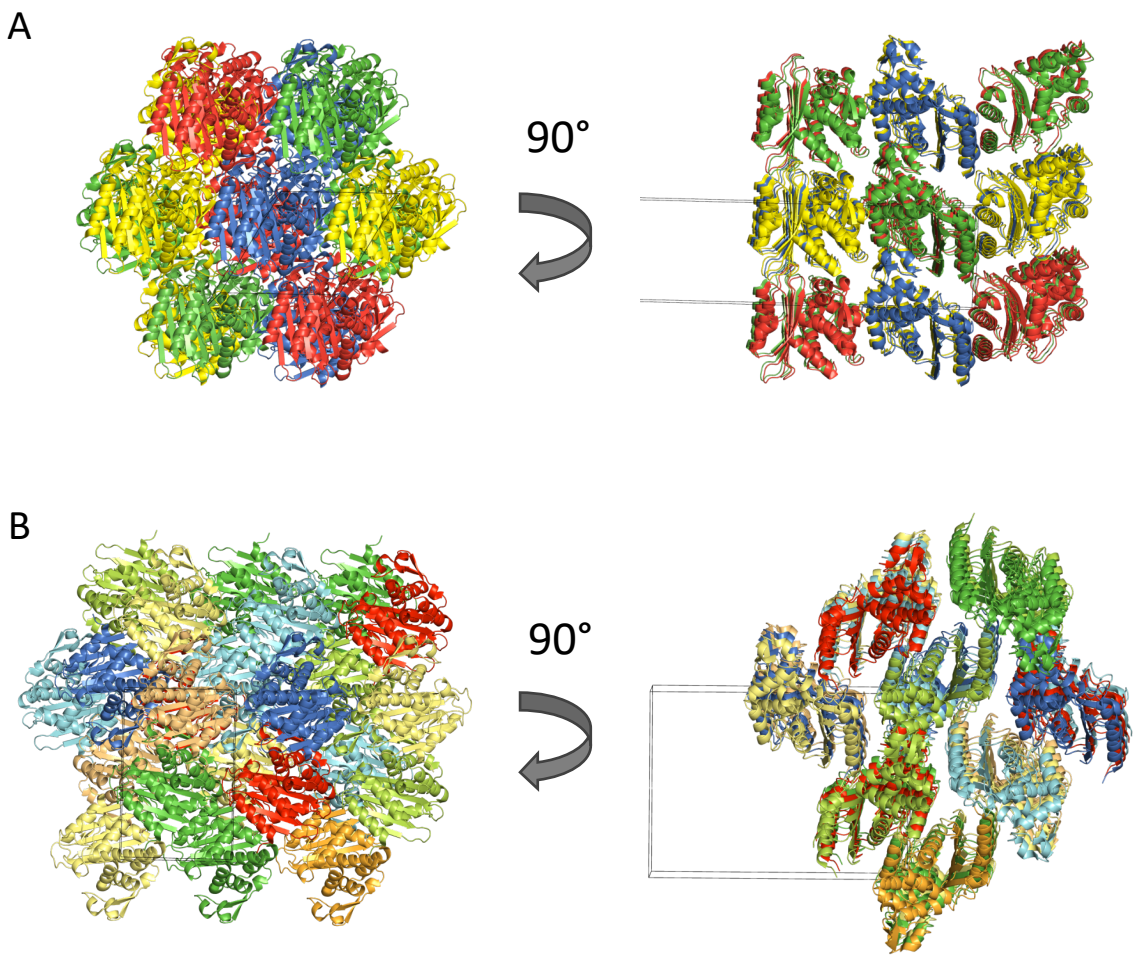

Figure 21: Crystal packing of (A) CTX-M-14 microcrystals used for serial synchrotron crystallography and (B) macrocrystals used for cryoMX. The microcrystal packing is represented by the TapeDrive CTX-M-14 native structure (7zpv) with symmetry pairs of space group $P3_221$ in the unit cell, which is outlined in black **(A)**. The macrocrystal packing is represented by the cryoMX CTX-M-14 native structure (7q0z) with symmetry pairs of space group $P2_12_12_1$ in the unit cell **(B)**.

4.6.1.3. Optimization of the measurement environment for the detection of ceftazidime binding to CTX-M-14

Initial experiments with the CFEL TapeDrive were used to mix CTX-M-14 with 100 mM ceftazidime (Figure 22) with the goal to obtain time-resolved structural information of the catalytic mechanism. To ensure that the measured datasets were complete, and due to the limited amount of microcrystal suspension, diffraction data were collected for only a single time point with a delay time of 250 ms. The crystals diffracted well to a resolution of 1.70 Å, yielding *R*-factor values of R_{work} = 0.163 and R_{free} = 0.201 for the refined model (Table 16).

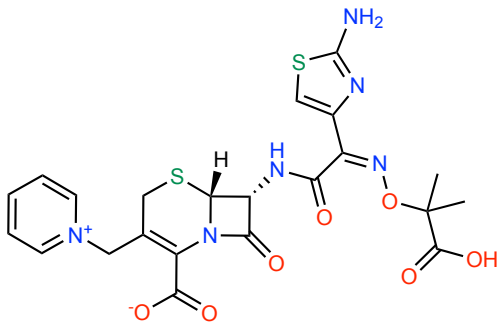

Figure 22: Chemical structure of ceftazidime.

Unfortunately, the obtained structure did not show difference electron density for a ceftazidime molecule. To further confirm the absence or presence of ceftazidime, a polder map was generated omitting the Ser70, the sulfate ion and some water molecules in the active site. Polder maps are particularly well suited to visualize weak electron density of ligands, since bulk solvent is excluded in the calculation (Liebschner et al., 2017). Therefore, these polder maps can be used to verify the presence of atoms in the model. However, the polder map also showed no electron density for ceftazidime. To be more precise, absolutely no differences could be found compared to the structure of the native enzyme (Figure 23). Thus, in the structure of CTX-M-14 mixed with ceftazidime at 250 ms, the sulfate ion was also present in the anion binding site as well as the catalytic water (wat10) and the water molecule in the oxyanion hole (wat353). In addition, the other water molecules in the active site were also distributed very similarly (Figure 23). Consequently, it can be assumed that ceftazidime did not bind in the active site of CTX-M-14 during the 250 ms period.

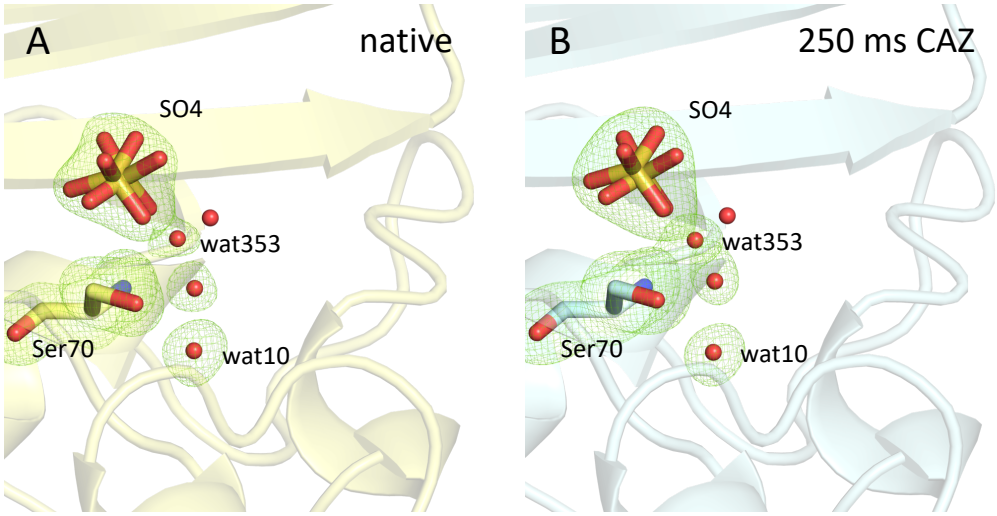

Figure 23: Active site of (A) CTX-M-14 native enzyme and (B) CTX-M-14 mixed with ceftazidime with a delay time of 250 ms. Both structures were determined using the CFEL TapeDrive. For the CTX-M-14 native, no ligand was added, while for the other structure CTX-M-14 was mixed with ceftazidime and measured with a delay time of 250 ms. Both structures and the corresponding polder electron density maps contoured at 5 σ (green mesh) of the active site looked identical. Ceftazidime could not be observed in the active site of CTX-M-14.

It is assumed that the ceftazidime molecule was hydrolyzed and released too quickly to generate clear electron density. Based on this, the reaction rate of the β-lactamase should be reduced. Measurement of the kinetic parameters k_{cat} and K_m of CTX-M-14 against different antibiotics revealed that ceftazidime was already the slowest hydrolyzed substrate with a turnover rate k_{cat} of 0.9 ± 0.2 s^{-1} (section 4.5.3, Table 14). However, it was also shown that the reaction rate could be further reduced by lowering the temperature (section 4.5.2) or the pH (section 4.5.1). Since temperature control for the CFEL TapeDrive was not available at this time, the pH of the measurement environment was lowered. The initial data collection was performed at pH 4.5 provided by the crystallization conditions. To lower the pH in TapeDrive experiments, a microcrystal stabilization buffer (28 % (w/v) PEG8000, 140 mM Li_2SO_4, 70 mM NaOAc, 6 mM MES and 15 mM NaCl) with the appropriate pH was injected into the microcrystal lane at a 1:1 (v/v) ratio. This allowed the crystals to mix with the buffer for a few seconds until they were applied to the tape via a capillary and mixed with the substrate directly on the tape. Timelines of CTX-M-14 mixed with ceftazidime at pH 4 (Figure 24) and pH 3 (Figure 25) were collected with delay times ranging from 62 ms to 5000 ms. Data collection and refinement statistics are shown in Table 16. The achieved resolution was in the range of 1.60 Å – 1.76 Å. Differences in resolution could be explained by number of images per dataset and thus a different number of unique reflections. The structure of CTX-M-14

mixed with ceftazidime at pH 3 and a delay time of 100 ms had the lowest number of unique reflections (24756) and the lowest resolution of 1.76 Å. Nevertheless, the resolution should be sufficient for the identification of ligands in the active site. Resulting structures had *R* factor values in the range of R_{work} = 0.138 – 0.153 and R_{free} = 0.171 – 0.185 for the refined models (Table 16).

Despite the wide range of delay times and pH adjustments to lower reaction rates, it was not possible to detect ceftazidime in the active site of CTX-M-14 β-lactamase (Figure 24 and Figure 25). The polder electron density showed the same state as in the structure of the native enzyme described above.

It could not be concluded with certainty whether the chosen delay times were too early or too late to observe the reaction of ceftazidime, as reaction rates in the crystal may differ from those observed in solution. Therefore, an inhibitor was used for the following TapeDrive experiments.

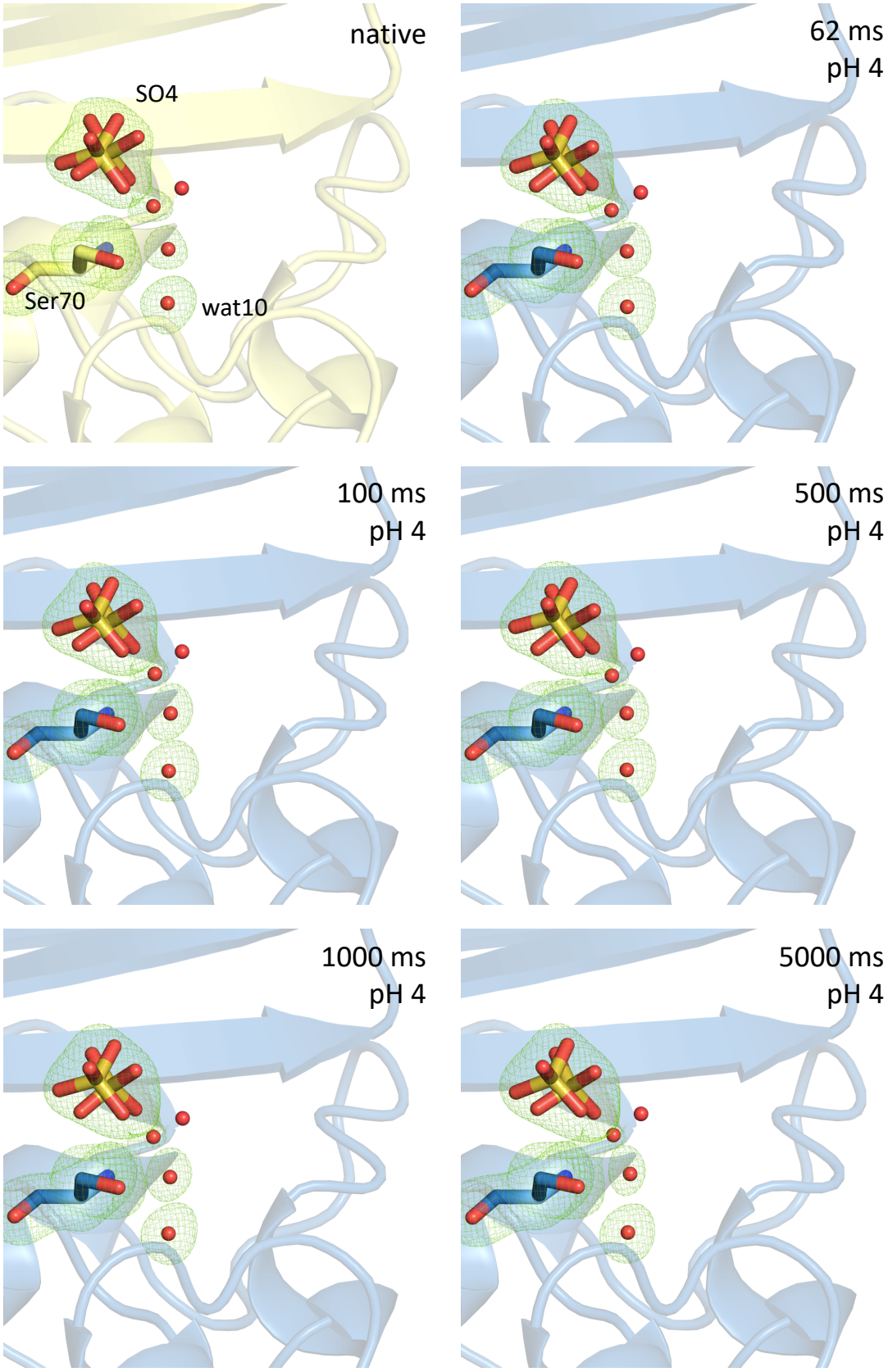

Figure 24: Timeline of the active site of CTX-M-14 mixed with ceftazidime (blue) at pH 4 and delay times of 62 ms – 5000 ms. Also shown is a structure of the native enzyme (yellow) for comparison. As before, no sufficient polder electron density contoured at 5 σ (green mesh) for ceftazidime was observed over the entire time course of the experiment.

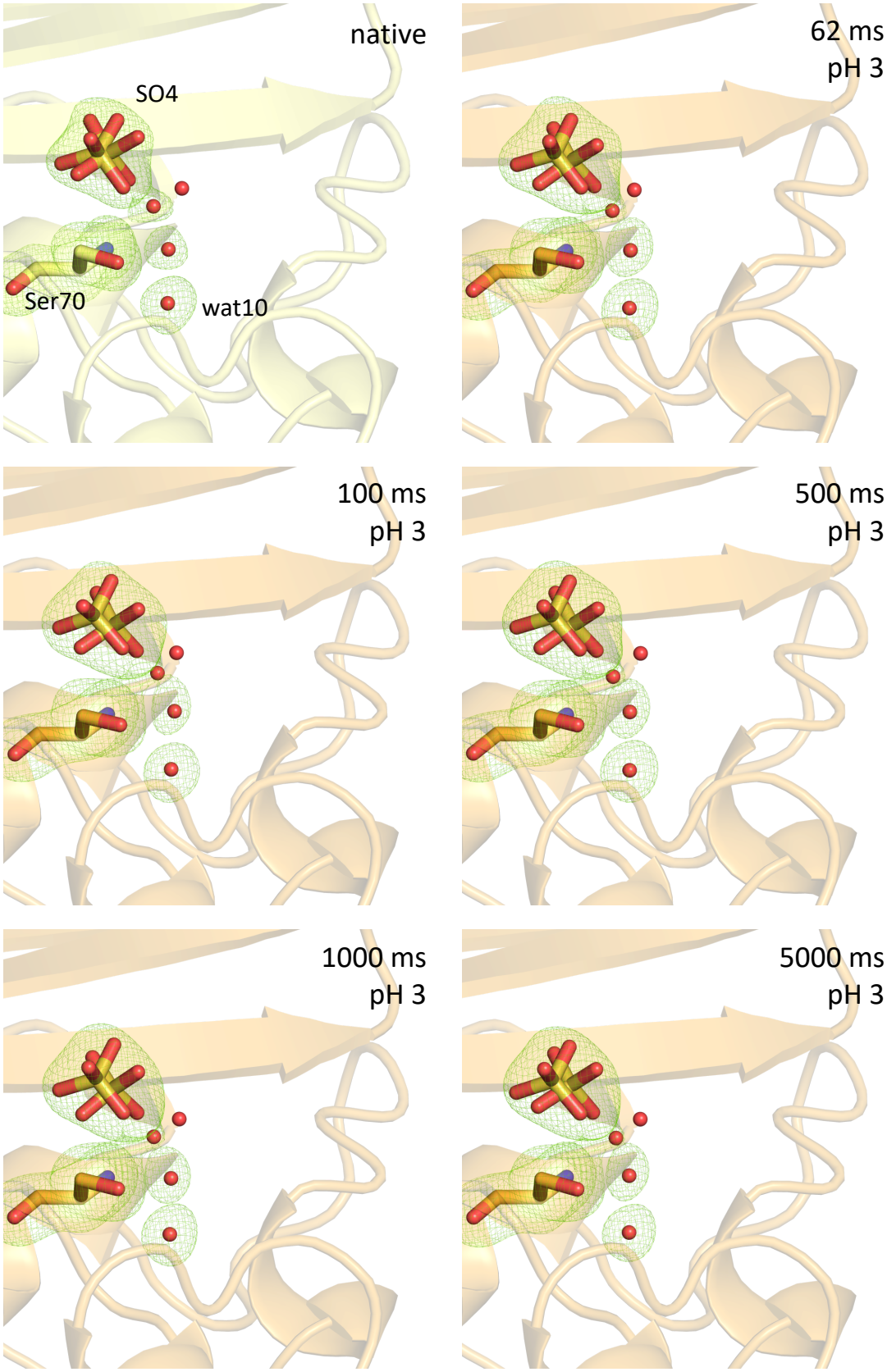

Figure 25: Timeline of the active site of CTX-M-14 mixed with ceftazidime (orange) at pH 3 and delay times of 62 ms – 5000 ms. The structure of the native enzyme (yellow) is shown for comparison. Even at lower pH values and thus slower reaction rates, sufficient polder electron density contoured at 5 σ (green mesh) for ceftazidime was not observed over the entire time course of the experiments.

Table 16. Data collection and refinement statistics for CTX-M-14 mixing with ceftazidime (CAZ) at pH 4 and pH 3 using the CFEL TapeDrive.

	CTX-M-14 CAZ pH4.5 250 ms	CTX-M-14 CAZ pH4 5000 ms	CTX-M-14 CAZ pH4 1000 ms	CTX-M-14 CAZ pH4 500 ms	CTX-M-14 CAZ pH4 100 ms	CTX-M-14 CAZ pH4 62ms	CTX-M-14 CAZ pH3 5000 ms	CTX-M-14 CAZ pH3 1000 ms	CTX-M-14 CAZ pH3 500 ms	CTX-M-14 CAZ pH3 100 ms	CTX-M-14 CAZ pH3 62ms
Resolution range (Å)	17.12.-1.70 (1.72-1.70)	38.88-1.64 (1.70-1.64)	38.88-1.60 (1.66-1.60)	38.88-1.60 (1.66-1.60)	38.88-1.65 (1.71-1.65)	38.88-1.62 (1.68-1.62)	38.88-1.65 (1.71-1.65)	38.88-1.63 (1.69-1.63)	38.88-1.67 (1.73-1.67)	38.88-1.76 (1.83-1.76)	38.88-1.67 (1.73-1.67)
Space group	$P3_221$	$P3_221$	$P3_221$	$P3_221$	$P3_221$	$P3_221$	$P3_221$	$P3_221$	$P3_221$	$P3_221$	$P3_221$
a, b, c (Å)	42.2, 42.2, 234.8	41.84, 41.84, 233.28	41.84, 41.84, 233.28	41.84, 41.84, 233.28	41.84, 41.84, 233.28	41.84, 41.84, 233.28	41.84, 41.84, 233.28	41.84, 41.84, 233.28	41.84, 41.84, 233.28	41.84, 41.84, 233.28	41.84, 41.84, 233.28
α, β, γ (°)	90, 90, 120	90, 90, 120	90, 90, 120	90, 90, 120	90, 90, 120	90, 90, 120	90, 90, 120	90, 90, 120	90, 90, 120	90, 90, 120	90, 90, 120
Unique reflections	36720 (3578)	30532 (2023)	32763 (2081)	32763 (2081)	29969 (1934)	31635 (2064)	29969 (1934)	31073 (2037)	28922 (1854)	24841 (1602)	28922 (1854)
⟨I/σ(I)⟩	9.34 (0.81)	11.69 (0.34)	17.87 (0.37)	14.72 (0.37)	10.78 (0.35)	15.23 (0.55)	14.31 (0.39)	20.89 (0.54)	15.39 (0.35)	10.52 (0.43)	11.12 (0.34)
Completeness (%)	100 (100)	100 (100)	100 (100)	100 (100)	100 (100)	100 (100)	100 (100)	100 (100)	100 (100)	100 (100)	100 (100)
Multiplicity	2168 (1444.6)	1482 (493.9)	3594 (507.3)	2786 (72.2)	2254 (33.9)	3000 (57.9)	2723 (736.5)	5899 (1738.3)	3705 (651.1)	2900 (478.3)	2218 (70.3)
Rsplit	6.56 (140.39)	5.02 (230.28)	3.67 (266.99)	5.20 (279.77)	7.59 (311.63)	5.38 (194.06)	3.76 (231.64)	2.81 (186.02)	4.22 (276.17)	6.07 (230.22)	7.01 (292.37)
CC1/2	0.996 (0.162)	0.995 (0.0809)	0.996 (0.126)	0.992 (0.072)	0.997 (0.071)	0.995 (0.151)	0.999 (0.170)	0.999 (0.185)	0.998 (0.133)	0.998 (0.165)	0.996 (0.079)
CC*	0.999 (0.528)	0.999 (0.404)	0.999 (0.473)	0.998 (0.367)	0.999 (0.365)	0.999 (0.512)	1.000 (0.539)	1.000 (0.559)	1.000 (0.485)	0.999 (0.532)	0.999 (0.382)
Wilson *B*-factor (Å^2)	30.82	33.93	31.59	26.68	23.93	23.08	35.70	34.24	32.38	33.12	25.73
Resolution range in refinement (Å)	17.12.-1.70 (1.72-1.70)	38.88-1.64 (1.70-1.64)	38.88-1.60 (1.66-1.60)	38.88-1.60 (1.66-1.60)	38.88-1.65 (1.71-1.65)	38.88-1.62 (1.68-1.62)	38.88-1.65 (1.71-1.65)	38.88-1.63 (1.69-1.63)	38.88-1.67 (1.73-1.67)	38.88-1.76 (1.83-1.76)	38.88-1.67 (1.73-1.67)
Reflections used in refinement	27886 (2691)	30440 (2599)	32669 (2979)	32665 (3008)	29878 (2755)	31542 (3098)	29878 (2845)	30980 (3008)	28832 (2674)	24756 (2374)	28832 (2707)
Reflections used for R_{free}	1616 (153)	1737 (142)	1875 (167)	1880 (171)	1720 (153)	1829 (180)	1727 (160)	1795 (174)	1666 (156)	1434 (140)	1669 (159)
R_{work}	0.1630 (0.3743)	0.1461 (0.3989)	0.1432 (0.4498)	0.1406 (0.3906)	0.1492 (0.3913)	0.1408 (0.3558)	0.1423 (0.4011)	0.1384 (0.4178)	0.1408 (0.4417)	0.1534 (0.3732)	0.1480 (0.3807)
R_{free}	0.2007 (0.4288)	0.1804 (0.4393)	0.1713 (0.4256)	0.1725 (0.4228)	0.1825 (0.4495)	0.1705 (0.3590)	0.1788 (0.4084)	0.1712 (0.4227)	0.1768 (0.4640)	0.1849 (0.3404)	0.1802 (0.4248)
RMS (bonds)	0.005	0.003	0.006	0.005	0.005	0.006	0.005	0.009	0.007	0.005	0.006
RMS (angles)	0.74	0.66	0.88	0.86	0.80	0.86	0.82	1.09	0.94	0.73	0.93
Ramachandran favored (%)	98.08	98.08	98.08	98.08	98.08	98.08	98.08	97.70	97.70	98.08	98.08
Ramachandran allowed (%)	1.53	1.53	1.53	1.53	1.53	1.53	1.53	1.92	1.92	1.53	1.53
Ramachandran outliers (%)	0.39	0.38	0.38	0.38	0.38	0.38	0.38	0.38	0.38	0.38	0.38
Rotamer outliers (%)	0.90	0.93	0.93	0.93	0.93	0.93	0.93	0.93	0.93	0.93	0.93
Clashscore	1.44	2.19	2.44	2.92	2.44	1.95	1.70	3.17	2.92	2.68	3.17
Average *B*-factor	39.18	43.97	39.99	36.32	34.15	32.77	44.95	43.66	41.04	41.45	34.83
macromolecules	37.37	42.90	38.99	35.00	32.86	31.46	43.87	42.58	39.87	40.64	33.63
ligands	42.12	43.11	36.58	34.65	34.09	31.90	42.59	43.34	40.74	38.75	32.55
Solvent	53.39	53.75	49.26	48.34	45.82	44.78	54.90	53.58	51.66	48.96	45.83
MolProbity score	0.84	0.73	0.92	1.00	0.84	0.79	0.88	1.03	1.06	0.88	1.12

Statistics for the highest-resolution shell are shown in parentheses.

4.6.1.4. Time-resolved analysis of relebactam binding processes to CTX-M-14

Inhibitors have the advantage of having a relatively long-lasting endpoint with a covalent bond to the enzyme. Therefore, it is easier to estimate whether a chosen delay time has been too early or too late to observe a reaction mechanism. If no inhibitor was yet present in the active site, the delay time was probably too short and had to be increased. This circumvents the problem encountered with the substrate ceftazidime and allowed the observation of binding processes.

Previously, the novel diazabicyclooctane (DBO) derivative inhibitor avibactam has been shown to bind in the active site of CTX-M-14 β-lactamase with high occupancy (Wiedorn et al., 2018). However, at the time of these experiments, another promising DBO β-lactamase inhibitor, relebactam, was already available and was used for time-resolved experiments (Figure 26).

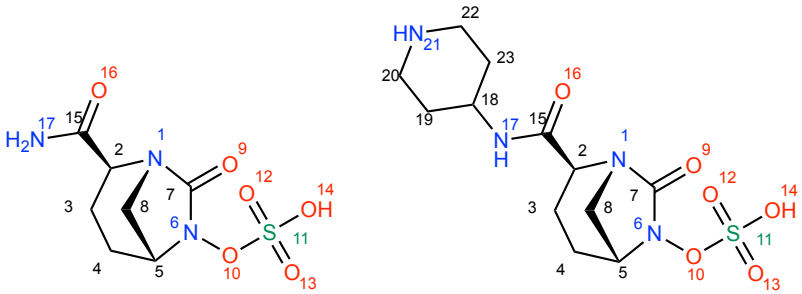

Figure 26: Chemical structures of the diazabicyclooctane inhibitors avibactam and relebactam.

Time-resolved diffraction data of CTX-M-14 mixed with relebactam at delay times of 0.25 s, 1.7 s, 40 s, 100 s and 140 s were collected using the CFEL TapeDrive as described in section 3.6.2.1. In addition, a cryoMX structure of CTX-M-14 soaked with relebactam was collected. The above described CTX-M-14 native structure (7zpv), also collected using the TapeDrive (Zielinski et al., 2022), was used for comparison. Data collection and refinement statistics are shown in Table 17 and Table 18. All time-resolved crystallography (TRX) TapeDrive structures have reached a resolution of about 1.52 Å, except for the structure with a delay time of 0.25 s with a resolution of only 1.70 Å. It should be noted that the achieved resolution is also reflected in Wilson-*B*-factor. While the data of the time points 1.7 s – 140 s have Wilson-*B*-factor of approx. 20 Å^2, the 0.25 s data only had Wilson-*B*-factor of 33.18 Å^2. This was also reflected in the calculated *R* factors.

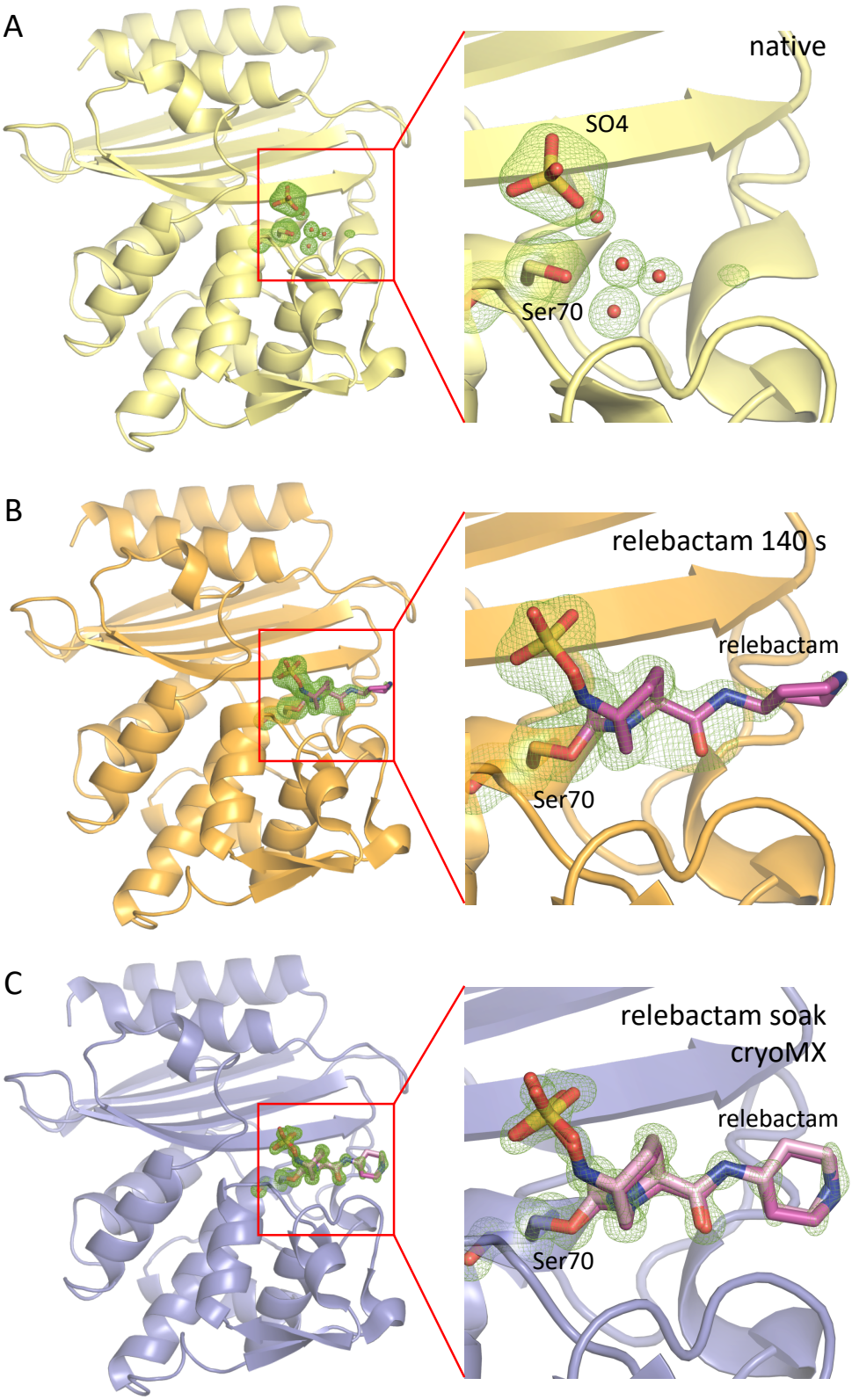

Figure 27: Crystal structure and zoom in the active site of (A) TapeDrive CTX-M-14 native (7zpv), (B) TapeDrive CTX-M-14 mixed with the inhibitor relebactam with a delay time of 140 s and (C) cryoMX CTX-M-14 soaked with relebactam. In the active site, the catalytic Ser70, the sulfate ions, the water molecules and the bound relebactam are highlighted as stick representation. The corresponding polder map (green mesh) contoured at 5 σ verifies the presence of relebactam (magenta) in the active site. Relebactam shows a second conformation (pink) in the cryoMX structure.

The structure with a delay time of 0.25 s showed *R* factors of R_{work} = 0.206 and R_{free} = 0.256, while the other TapeDrive structures showed *R* factors of R_{work} = 0.145 – 0.163 and R_{free} = 0.166 – 0.186. Nevertheless, this resulted in qualitatively very good structures that allowed a reliable interpretation of the processes. The cryoMX structure of CTX-M-14 soaked with relebactam achieved a resolution of 1.14 Å and the obtained model yielded *R* factors of R_{work} = 0.102 and R_{free} = 0.131.

For TapeDrive and cryoMX relebactam structures there was clear Fo-Fc difference electron density for relebactam in the active site of the enzyme. In combination with the high resolution, this allowed modeling of the bound inhibitor in the active site with a high degree of confidence. As before, polder maps were generated to verify the presence of molecules in the active site (Figure 27). There is a clear difference from the polder electron density of the native structure to the structures with relebactam. The structures mixed or soaked with relebactam show distinct polder electron density for the relebactam molecule, confirming the presence of the inhibitor. Thus, a room temperature and a cryo structure of CTX-M-14 with bound relebactam were successfully obtained. The polder electron density clearly reveals the covalent bonding of relebactam and the nucleophilic Ser70 via formation of a carbamoyl ester, which is accompanied by the opening of the DBO ring by cleavage of the N6 – C7 bond (Figure 26, Figure 28). In addition to the covalent carbamoyl ester with Ser70, relebactam is stabilized by interaction with various other side chains in the active site (Figure 28). The relebactam molecules of both structures (TRX-140 s/cryoMX) form polar contacts with the same conserved amino acid residues. The coordination of relebactam thus occurs via the same hydrogen bonds in both structures. The relebactam sulfate moiety is stabilized by Lys234 (3.5 Å/3.3 Å), Thr235 (3.2 Å/3.1 Å) and Ser237 (3.1 Å/3.0 Å) in the anion binding site. Furthermore, the oxygen of the carbamoyl group is stabilized in the oxyanion hole by the main chain amide groups of Ser70 (2.7 Å/2.6 Å) and Ser237 (2.9 Å/2.8 Å). Stabilizing interactions also include hydrogen bonding of the side chains of Asn104 (3.4 Å/3.1 Å), Asn132 (2.9 Å/2.9 Å) and Asn170 (3.5 Å/3.5 Å) with the carboxamide group of relebactam. Further hydrogen bonds with relebactam are formed by the side chains of Lys73 (3.5 Å/3.5 Å) and Ser130 (3.1 Å/3.1 Å). The catalytic water is positioned by Glu166 and Asn170 with close distance of 3.3 Å/3.0 Å to the C7 atom (Figure 26) of relebactam in the TapeDrive and cryoMX structure, respectively. It is apparently positioned for decarbamoylation and recyclization of relebactam to ensure the reversible pathway of the inhibitor.

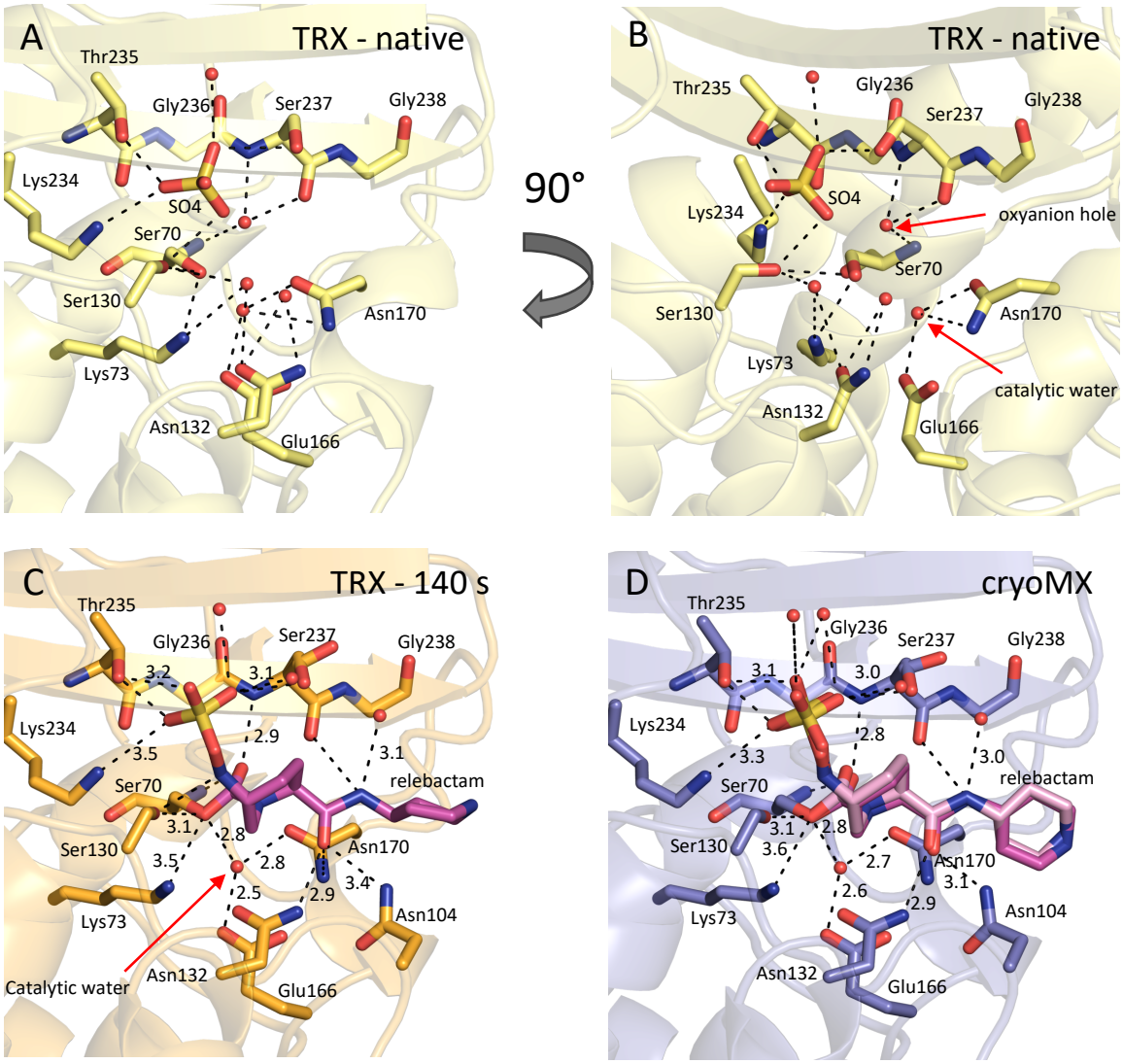

Figure 28: Visualization of polar contacts of ambient sulfate ions and water molecules in the active site of CTX-M-14 (TRX-native; PDB 7zpv; A and B). Furthermore, the polar contacts of CTX-M-14 and relebactam are shown in the (C) CTX-M-14 (TRX-140 s-relebactam) structure and in the (D) CTX-M-14 (CryoMX-relebactam) structure. Potential hydrogen bonds are depicted as black dashes with the atomic distance in Ångström.

Both relebactam structures show only small differences in their polder electron density. The piperidine ring adopts the energetically preferred chair configuration in both, cryo and RT structures. The cryoMX structure could display the electron density for the relebactam much better due to the high resolution, especially the coverage of the piperidine ring. Moreover, the electron density of the cryoMX structure allows interpretation of a second alternative orientation of the relebactam. However, in the cryoMX structure it can adopt two orientations, and both are twisted slightly differently towards the Asn104 residue compared to the TapeDrive structure (Figure 27 B and C). This is not surprising, since the terminal piperidine ring is not directly stabilized by any interactions with the enzyme and is exposed to

the solvent. It also explains why the piperidine ring is less well defined in the polder electron density than the rest of the relebactam.

Binding of relebactam does not cause any apparent global conformational changes or major changes in the active site of CTX-M-14 compared to the native structure. This is represented by the small RMSDs of 0.109 Å (TapeDrive: relebactam-140s versus native) and 0.151 Å (cryoMX: relebactam versus native) for superposition of the structures. Furthermore, the position of amino acid residues conserved in Ambler class A β-lactamases in the active site is also almost unchanged compared to the native protein (Figure 28).

The time-resolved structures (Figure 29) of CTX-M-14 mixed with relebactam reveal a distinct polder electron density for the inhibitor in the active site of CTX-M-14 after a delay time of only 0.25 s. In particular, the highly coordinated parts of relebactam, such as the sulfate, the carbamoyl and the carbamide moieties, are covered in strong polder electron density (Figure 29). At this point, the relebactam is refined with an occupancy of 77 %, indicating that the binding processes proceed much faster. After a delay time of 1.7 s, the cleaved diazabicyclooctane ring is covered in stronger polder electron density compared to 0.25 s. This also raises the refined occupancy of relebactam to 96 %. The longer delay time of 40 s appears to show weaker polder electron density than before at 1.7 s. However, the polder maps are contoured at 5 σ and therefore display only very strong electron density. Moreover, even at the delay time of 40 s, the refined occupancy for relebactam is 94 %, which is only a small decrease and within an acceptable tolerance range. The occupancy of relebactam reaches 100 % at a delay time of 100 s. In addition, the polder electron density for the nitrogen of the piperidine ring is visible for the first time in this observed time series. After 140 s, the piperidine ring is slightly better defined in polder electron density and the occupancy remains at 100 %.

Unfortunately, no changes in the orientation of relebactam, active site residues, or displacement of surrounding water molecules were observed over the investigated time.

For comparison, in the cryoMX CTX-M-14 structure, relebactam is completely covered in polder electron density contoured at 5 σ, except for one carbon atom in the piperidine ring. Due to the high resolution, it is possible to define the exact position of the individual atoms. The occupancy of the two relebactam molecules in alternative positions is refined to 29 % and 56 %.

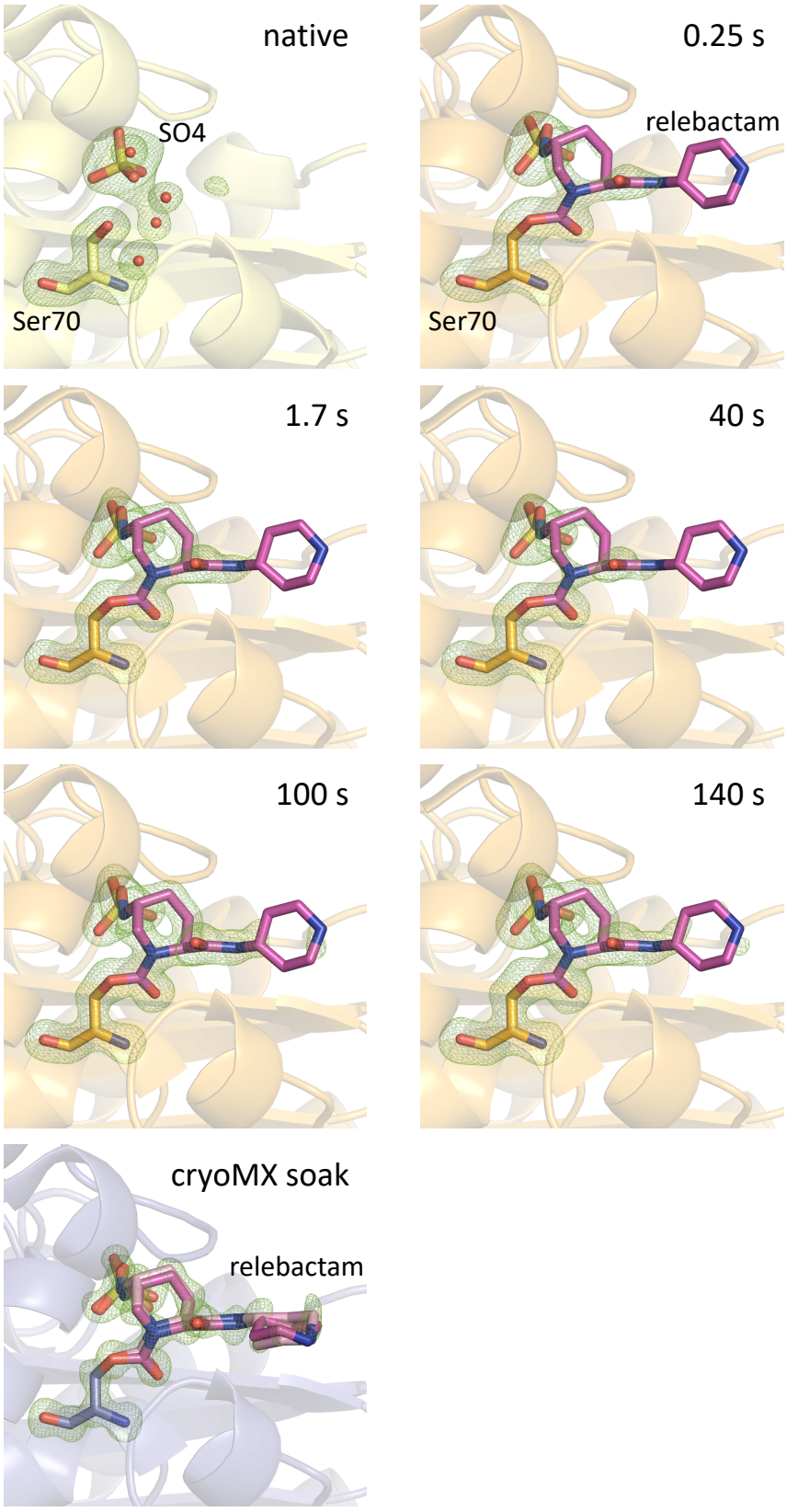

Figure 29: Timeline of CTX-M-14 mixed with relebactam (orange ribbon) using the TapeDrive at delay times of 0.25 s – 140 s showing the active site. The structure of the native enzyme (PDB 7zpv, yellow) and the cryoMX CTX-M-14 with soaked relebactam (purple) are shown for comparison. Even at the shortest delay time of 0.25 s, a clear polder electron density contoured at 5 σ is visible for relebactam. As the delay time increases, relebactam shows a clear increase in polder electron density (green mesh), covering parts of the piperidine ring.

Table 17. Data collection and refinement statistics for CTX-M-14 β-lactamase native enzyme and CTX-M-14 mixed with relebactam using the CFEL TapeDrive.

	CTX-M-14 native	CTX-M-14 relebactam 140 s	CTX-M-14 relebactam 100 s	CTX-M-14 relebactam 40 s	CTX-M-14 relebactam 1.7 s	CTX-M-14 relebactam 0.25 s
PDB entry	7zpv	n.a.	n.a.	n.a.	n.a.	n.a.
Temperature (K)	293	293	293	293	293	293
Crystal size (µm)	10-20µm	10-20µm	10-20µm	10-20µm	10-20µm	10-20µm
No. of collected images	127170	120000	200000	160000	268202	120000
Total measuring time (s)	5086	4800	8000	6400	10728	4800
Average acquisition rate (frames s^{-1})	25	25	25	25	25	25
Indexed patterns	61331	29861	107066	13996	108656	35897
Indexed per second	12.1	6.22	13.38	2.19	10.13	7.47
Space group	$P3_221$	$P3_221$	$P3_221$	$P3_221$	$P3_221$	$P3_221$
a, *b*, c (Å)	42.2, 42.2, 234.4	42.2, 42.2, 234.9	42.2, 42.2, 234.8	42.2, 42.2, 234.7	42.1, 42.1, 234.5	43.3, 43.3, 238.7
α, β, γ (°)	90, 90, 120	90, 90, 120	90, 90, 120	90, 90, 120	90, 90, 120	90, 90, 120
Resolution range (Å)	1.40-17.77 (1.40-1.42)	1.52-17.77 (1.52-1.55)	1.52-17.77 (1.52-1.55)	1.52-17.77 (1.52-1.55)	1.52-17.77 (1.52-1.55)	1.72-17.29 (1.72-1.76)
Unique reflections	49225 (4733)	36665 (3546)	37167 (3662)	36623 (3541)	36424 (3545)	29551 (2858)
$\langle I/\sigma(I)\rangle$	9.11(0.69)	6.64(0.83)	12.29(1.48)	4.46(0.55)	10.72(0.61)	6.39(0.54)
Completeness (%)	100 (100)	100 (99.35)	100 (100)	100 (98.62)	100 (98.47)	100 (100)
Multiplicity	2217 (1400)	867 (86)	3091 (314.7)	381 (52.5)	3453 (120.4)	1057 (614.3)
R_{split}	7.2 (165.91)	9.14 (168.53)	5.21 (96.76)	13.90 (218.83)	6.31 (280.19)	9.10 (204.21)
$CC_{1/2}$	0.991 (0.266)	0.993 (0.177)	0.998 (0.363)	0.966 (0.173)	0.997 (0.080)	0.994 (0.111)
CC*	0.998 (0.648)	0.999 (0.549)	0.999 (0.730)	0.992 (0.544)	0.999 (0.385)	0.999 (0.447)
Wilson *B* factor ($Å^2$)	24.22	19.94	19.63	20.01	19.63	30.97
Resolution range in refinement (Å)	1.40-17.78 (1.40-1.47)	1.55-17.45 (1.55-1.61)	1.54-17.41 (1.54-1.60)	1.55-17.45 (1.55-1.61)	1.55-17.41 (1.55-1.61)	1.72-17.29 (1.72-1.78)
Reflections used in refinement	49225 (4832)	36665 (3544)	37167 (3645)	36623 (3534)	36424 (3544)	29551 (2712)
Reflections used for R_{free}	1033 (100)	934 (186)	1932 (189)	1951 (185)	1895 (186)	1465 (133)
R_{work}	0.1410 (0.3338)	0.1551 (0.3282)	0.1449 (0.3009)	0.1630 (0.3509)	0.1529 (0.3413)	0.2064 (0.4140)
R_{free}	0.1561 (0.3827)	0.1700 (0.3545)	0.1661 (0.3262)	0.1862 (0.3642)	0.1745 (0.3524)	0.2562 (0.4575)
RMS (bonds)	0.009	0.003	0.004	0.003	0.004	0.013
RMS (angles)	1.01	0.70	0.73	0.69	0.70	1.19
Ramachandran favored (%)	97.68	97.68	97.68	98.08	97.68	98.08
Ramachandran allowed (%)	1.93	1.93	1.93	1.53	1.93	1.53
Ramachandran outliers (%)	0.39	0.39	0.39	0.39	0.39	0.39
Rotamer outliers (%)	1.87	0.93	0.93	1.40	0.93	0.90
Clashscore	2.19	0.49	0.73	0.73	0.97	0.71
Average *B*-factor	34.26	30.24	30.59	30.40	31.17	45.50
macromolecules	33.23	29.41	29.77	29.44	30.27	45.55
ligands	45.06	9.85	28.02	43.92	37.74	39.47
solvent	78.08	41.01	41.60	40.84	41.78	45.96
MolProbity score	1.27	0.80	0.74	0.68	0.80	0.73

Statistics for the highest-resolution shell are shown in parentheses.

Table 18. Data collection and refinement statistics for cryoMX structure of CTX-M-14 in complex with relebactam.

	CTX-M-14 Relebactam cryoMX
Temperature (K)	100
Space group	$P2_12_12_1$
a, *b*, c (Å)	41.56 62.94 85.82
α, β, γ (°)	90, 90, 90
Resolution range (Å)	1.14-34.68 (1.14-1.18)
Unique reflections	76602 (6972)
$\langle I/\sigma(I)\rangle$	17.32 (7.39)
Completeness (%)	92.14 (84.71)
Multiplicity	4.1 (3.5)
R_{merge}	0.04705 (0.1301)
R_{meas}	0.05349 (0.152)
$CC_{1/2}$	0.998 (0.977)
CC*	0.999 (0.994)
Wilson *B* factor (Å^2)	8.92
Resolution range in refinement (Å)	1.40-17.78 (1.40-1.47)
Reflections used in refinement	76519 (6971)
Reflections used for R_{free}	1986 (180)
R_{work}	0.1019 (0.1228)
R_{free}	0.1315 (0.1553)
RMS (bonds)	0.009
RMS (angles)	1.22
Ramachandran favored (%)	98.08
Ramachandran allowed (%)	1.53
Ramachandran outliers (%)	0.38
Rotamer outliers (%)	0.44
Clashscore	3.69
Average *B*-factor	14.77
macromolecules	11.26
ligands	19.24
solvent	28.84
MolProbity score	1.16

Statistics for the highest-resolution shell are shown in parentheses.

4.6.1.5. Time-resolved analysis of boric acid binding to Ser70 in the active site of CTX-M-14

Previously, it was shown that the buildup of electron density of relebactam is coupled with increasing delay time and lead to increased occupancy of the inhibitor. However, the inhibitor was already bound at the fastest time point. Therefore, the TapeDrive was improved and could thus achieve even shorter delay times of up to 50 ms. An in-line microscope was installed to measure the distance between the sample nozzle and the X-ray interaction region more accurately to obtain a more precise delay time. To observe the binding process even better, a small molecule with faster diffusion was needed. This could give better uniformity of the active sites of the enzymes in the crystal, as the ligand would distribute faster to all active sites. Recently approved inhibitors based on boric acid derivatives, such as vaborbactam (Lomovskaya et al., 2017) and taniborbactam (Liu et al., 2019), for the treatment of multidrug-resistant bacteria, represent a promising new inhibitor class to overcome emerging antibiotic resistance. Boric acid was utilized as a simplified inhibitor model of this class to gain mechanistic insights into binding to the serine in the active site of β-lactamase CTX-M-14 employing time-resolved serial crystallography. For this purpose, the CFEL TapeDrive was used for mix-and-diffuse experiments collecting time-resolved datasets for CTX-M-14 microcrystals with boric acid at various delay times from 50 ms to 10000 ms. Based on relevant electron densities and calculated occupancies, a reaction time frame of 80 ms – 100 ms was identified for boric acid binding. Data collection and structure determination were performed as described in sections 3.6.2.1 and 3.6.3 with the corresponding statistics shown in Table 19. The structures with a delay time of 100 ms and 150 ms reached a resolution of 2.04 Å and 1.97 Å, respectively. All other structures of this experiment achieved a resolution of 1.40 – 1.69 Å using a cutoff at CC* = 0.5. The calculated *R* factors of the final models reached values of R_{work} = 0.135 – 0.188 and R_{free} = 0.161 – 0.231, resulting in qualitatively very good structures that allowed a reliable interpretation of the time-resolved processes of boric acid binding. Boric acid was placed in the active site of the β-lactamase once the corresponding Fo-Fc difference electron density was apparent. The boron atom of the bound boric acid (BAB) is in a tetrahedral configuration, and no longer in a trigonal planar configuration as in native boric acid. As before, polder maps were generated to verify the presence of molecules in the active site and to show the build up of polder electron density of bound boric acid (Figure 30).

Table 19. Data collection and refinement statistics for CTX-M-14 mixing with boric acid (BAB) using the TapeDrive. (Prester et al., 2023)

	CTX-M-14 native 0 ms	CTX-M-14 BAB 50 ms	CTX-M-14 BAB 80 ms	CTX-M-14 BAB 100 ms	CTX-M-14 BAB 150 ms	CTX-M-14 BAB 250 ms	CTX-M-14 BAB 500 ms	CTX-M-14 BAB 2000 ms	CTX-M-14 BAB 5000 ms	CTX-M-14 BAB 10000 ms
PDB entry	8pc9	8pca	8pcb	8pcc	8pcd	8pce	8pcf	8pcg	8pci	8pcj
Resolution range (Å)	17.64-1.40 (1.42-1.40)	38.88-1.58 (1.60-1.58)	38.88-1.69 (1.71-1.69)	38.88-2.04 (2.06-2.04)	38.88-1.97 (1.99-1.97)	38.88-1.65 (1.67-1.65)	38.88-1.50 (1.52-1.50)	38.88-1.51 (1.53-1.51)	38.88-1.48 (1.50-1.48)	38.88-1.65 (1.67-1.65)
Space group	P3221	P3221	P3221	P3221	P3221	P3221	P3221	P3221	P3221	P3221
a=b, c (Å)	42.10, 234.47	41.84, 233.28	41.84, 233.28	41.84, 233.28	41.84, 233.28	41.84, 233.28	41.84, 233.28	41.84, 233.28	41.84, 233.28	41.84, 233.28
α, β, γ (°)	90, 90, 120	90, 90, 120	90, 90, 120	90, 90, 120	90, 90, 120	90, 90, 120	90, 90, 120	90, 90, 120	90, 90, 120	90, 90, 120
Unique reflections	48378 (3119)	33953 (2151)	27958 (1837)	16186 (1063)	17902 (1167)	29970 (1934)	39474 (2460)	38753 (2453)	40899 (2400)	29963 (1928)
⟨I/σ(I)⟩	9.09 (0.72)	30.27 (0.26)	16.44 (0.46)	7.17 (1.11)	9.17 (0.44)	18.97 (0.57)	26.93 (0.55)	24.60 (0.38)	23.33 (0.09)	26.86 (0.48)
Completeness (%)	100 (100)	99.77 (96.54)	100 (100)	100 (100)	100 (100)	100 (100)	99.74 (95.98)	99.91 (98.63)	99.36 (90.09)	99.98 (99.69)
Multiplicity	2214 (1363)	13328 (8.7)	7241 (1889.0)	3032 (1596.0)	3925 (1855.9)	15231 (26.9)	7186 (10.3)	7160 (11.2)	5842 (5.9)	8047 (13.2)
Rsplit	7.20 (157.58)	3.70 (272.32)	3.83 (225.30)	9.99 (104.11)	7.44 (250.08)	5.60 (188.20)	3.13 (232.82)	3.97 (241.59)	4.10 (225.50)	4.39 (243.74)
CC1/2	0.991 (0.273)	0.999 (0.171)	0.999 (0.154)	0.995 (0.188)	0.996 (0.170)	0.998 (0.227)	0.999 (0.191)	0.999 (0.158)	0.999 (0.155)	1.000 (0.164)
CC*	0.998 (0.655)	1.000 (0.541)	1.000 (0.516)	0.999 (0.563)	0.999 (0.539)	1.000 (0.609)	1.000 (0.567)	1.000 (0.522)	1.000 (0.518)	1.000 (0.531)
Wilson *B*-factor (Å^2)	23.58	19.96	32.20	38.85	41.93	18.36	20.03	17.91	16.98	21.34
Resolution range in refinement (Å)	17.64-1.40 (1.45-1.40)	38.88-1.58 (1.64-1.58)	38.88-1.69 (1.75-1.69)	38.88-2.04 (2.11-2.04)	38.88-1.97 (2.04-1.97)	38.88-1.65 (1.71-1.65)	38.88-1.53 (1.59-1.53)	38.88-1.52 (1.56-1.52)	38.88-1.50 (1.55-1.50)	38.88-1.65 (1.71-1.65)
Reflections used in refinement	48059 (4652)	33822 (3036)	27707 (2665)	16067 (1562)	17763 (1706)	29817 (2887)	37250 (3656)	38607 (3539)	39413 (3784)	29844 (2830)
Reflections used for R_{free}	2790 (271)	1956 (183)	1602 (150)	937(89)	1027(97)	1728 (165)	2159 (213)	2221 (202)	2284 (221)	1726 (162)
R_{work}	0.1446 (0.3926)	0.1437 (0.4033)	0.1521 (0.4683)	0.1882 (0.4664)	0.1711 (0.3819)	0.1588 (0.3985)	0.1350 (0.3027)	0.1423 (0.3943)	0.1433 (0.3582)	0.1424 (0.3910)
R_{free}	0.1702 (0.3989)	0.1700 (0.3982)	0.1875 (0.4547)	0.2309 (0.4978)	0.2153 (0.4554)	0.1962 (0.4398)	0.1607 (0.2992)	0.1662 (0.4177)	0.1651 (0.3588)	0.1768 (0.4327)
RMS (bonds)	0.009	0.008	0.005	0.003	0.004	0.007	0.009	0.010	0.017	0.012
RMS (angles)	0.96	1.01	0.81	0.56	0.71	0.93	1.03	1.05	1.40	1.15
Ramachandran favored (%)	98.46	97.30	96.91	97.68	97.68	97.30	97.68	97.68	97.68	96.91
Ramachandran allowed (%)	1.16	2.32	2.70	1.93	1.93	2.32	1.93	1.93	1.93	2.70
Ramachandran outliers (%)	0.39	0.39	0.39	0.39	0.39	0.39	0.39	0.39	0.39	0.39
Rotamer outliers (%)	0.92	0.93	0.93	0.93	0.93	0.93	0.93	0.93	0.93	0.93
Clashscore	1.45	3.88	1.71	1.71	2.67	2.20	3.42	2.19	2.19	3.40
Average *B*-factor	34.37	30.90	41.12	51.22	49.15	28.52	30.93	29.23	26.46	31.52
macromolecules	32.65	29.21	39.71	50.70	48.32	26.69	29.05	27.42	25.69	29.74
ligands	35.25	34.87	43.96	53.23	47.55	34.67	37.17	37.47	31.14	39.96
solvent	49.23	44.92	53.03	56.68	56.20	43.02	45.62	43.44	35.61	45.57
MolProbity score	0.88	1.13	1.02	0.86	0.91	1.02	1.13	0.99	0.99	1.14

Statistics for the highest-resolution shell are shown in parentheses.

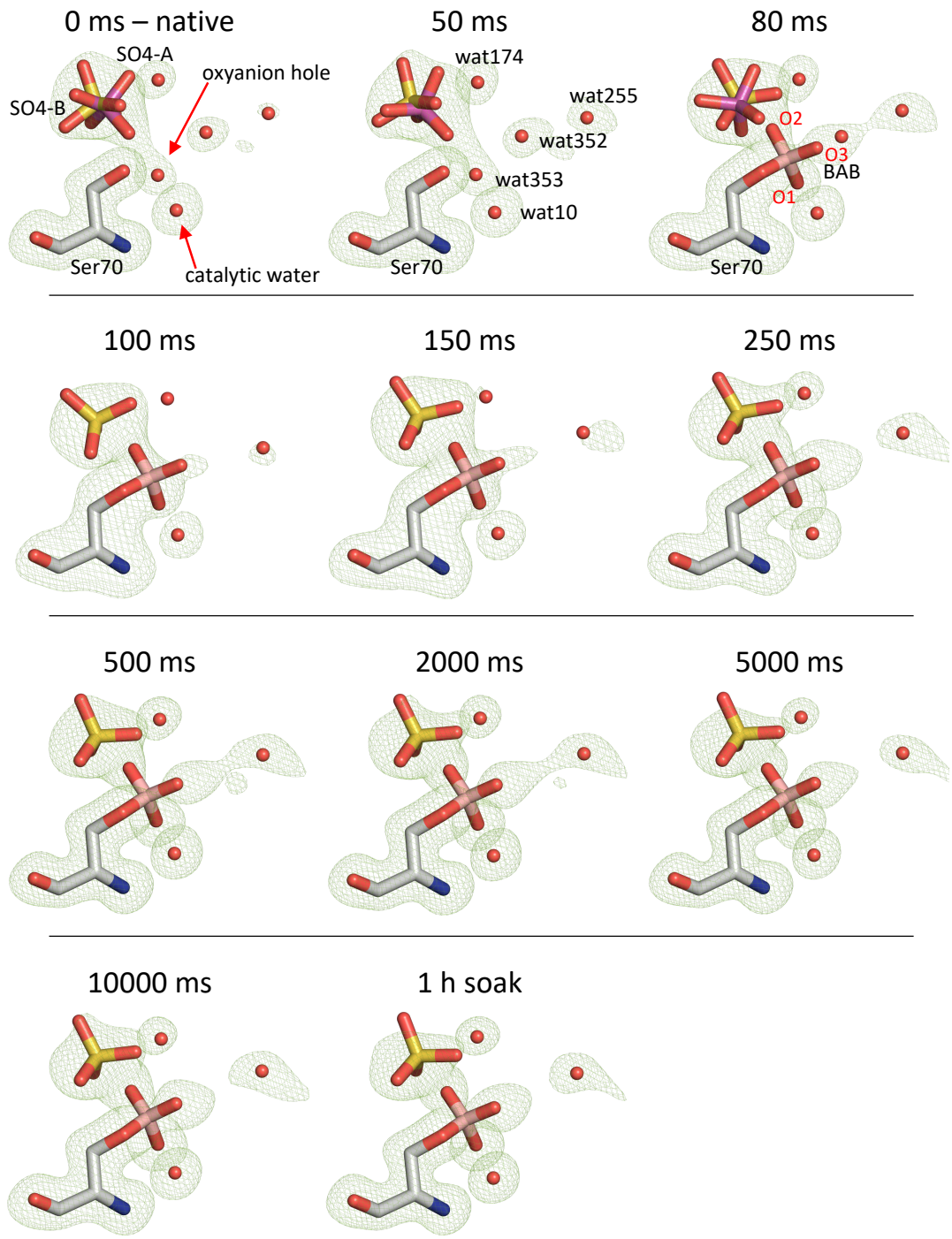

Figure 30: Timeline of the active site of CTX-M-14 mixed with boric acid at delay times of 50 ms – 10000 ms. The active site residue Ser70 as well as nearby water molecules, e.g. the catalytic water or the water in the oxyanion hole, as well as the rotationally disordered sulfate (SO4-A magenta; SO4-B yellow) and, if present, the bound boric acid (BAB) are shown as stick representation. Polder map electron density (green mesh) was generated for all shown molecules and is contoured at 5 σ. Structures of the native enzyme and of CTX-M-14 soaked with boric acid (1 h) are shown for comparison. A clear buildup of the polder electron density for boric acid is observed over the time period studied, indicating that boric acid binds to the active site of CTX-M-14 within 80 – 100 ms. As boric acid is not fully occupied at any time, mixed states of native enzyme and enzyme with bound boric acid are shown. (Prester et al., 2023)

Alignment of the structures of different delay time points against the structure of the native enzyme yielded RMSD values of 0.118 – 1.154 Å (Table 20). Due to these minor deviations of the different time points compared to the native enzyme, a large conformational change of the whole enzyme due to boric acid binding can be excluded.

Table 20. Root-mean-square deviation (RMSD) calculations and alignments of TapeDrive CTX-M-14 β-lactamase structures mixed with boric acid against the native enzyme.

CTX-M-14 TapeDrive structures	RMSD [Å]
50 ms versus native	0.122
80 ms versus native	0.128
100 ms versus native	0.145
150 ms versus native	0.154
250 ms versus native	0.133
500 ms versus native	0.118
2000 ms versus native	0.118
5000 ms versus native	0.121
10000 ms versus native	0.127
1 h soak versus native	0.119

The time course of boric acid binding is described by the build-up of the polder electron density for the boric acid molecule and by the shift of the polder electron density for the sulfate ion and water molecules (Figure 30). Boric acid reached a maximum occupancy of 53 % after a delay time of 10 s in the mixing experiments. Even soaking the microcrystals with boric acid for 1 h resulted in a maximum occupancy of only 57 %. This comparatively low occupancy led to the inevitable presence of mixed states of native enzyme and enzyme with bound boric acid in all delay time points. These two equilibrium states could be observed side by side because the ligand was not uniformly distributed within the crystal. However, the total occupancy of the molecules in both equilibrium states combined never exceeded 100 %. The individual equilibrium states are represented and analyzed independently in section 4.6.1.7.

The active site of the native enzyme is characterized by the sulfate ion in the anion binding site, the water in the oxyanion hole (wat353), and the catalytic water (wat10). Notably, the rotationally disordered sulfate ion was found in two slightly displaced alternative positions (SO4-A and SO4-B, Figure 30). Upon mixing the microcrystals with boric acid, no immediate electron density corresponding to boric acid was observed at a delay time of 50 ms. However,

the electron density of the sulfate ion changed, indicating a slight shift between the two alternative locations. In the native enzyme, the sulfate ions in the alternative positions originally refined to occupancies of 47 % and 44 % for SO4-A and SO4-B, respectively. At a delay time of 50 ms, these occupancies shifted to 54 % for SO4-A and 41 % for SO4-B, indicating a preference for the position closer to Ser70 before the covalent binding of boric acid to Ser70 OG. Subsequently, at a delay time of 80 ms, weak electron density corresponding to the bound boric acid (BAB) was observed in the calculated polder map, with a BAB occupancy of 35 % (Figure 30). Concurrently, the sulfate ion in the SO4-B position underwent slight translation and rotation, causing one oxygen atom of the sulfate to be at a distance of 2.6 Å to the O2 hydroxyl group of BAB. After a delay time of only 100 ms, boric acid reached an occupancy of 51 %, which was almost the maximum observed occupancy. This indicated that the binding of boric acid proceeded within a time frame of 80 – 100 ms. The evaluation of the polder electron density maps revealed that the hydroxyl groups of the bound boric acid occupied a position similar to that previously occupied by an oxygen of SO4-A and the two water molecules wat352 and wat353. Consequently, these had to be displaced during boric acid binding. Nevertheless, the calculated occupancy for BAB (Figure 31) and its corresponding electron density progressively increased with longer delay times after mixing (Figure 30). After only 250 ms delay time, this resulted in a well-defined electron density for BAB in the calculated polder map. At this delay time, the occupancy of bound boric acid reached 49 %, while the occupancy of SO4-A, which was originally present in the equilibrium state of the native structure, decreased to 33 %. In the remaining time course investigated, the occupancy of the bound boric acid increased only slightly until it reached the maximum of 53 % after 10 seconds. At this time, the occupancy of the molecules of the native equilibrium state SO4-A and the two water molecules wat352 and wat353 (oxyanion hole) were only 35 %. Thus, a total calculated occupancy of the active site of 88 % was observed in the mixing experiments. Even after the CTX-M-14 microcrystals were soaked in boric acid for 1 h, the occupancy of the bound boric acid could only reach 57 %. This indicated that the equilibrium of BAB formation was reached under these conditions. (Prester et al., 2023)

Note the outliers of the occupancy at 150 ms and 500 ms. The BAB occupancy at these delay times dropped to 42 % and 36 %, respectively. A clear explanation for this cannot be found in the diffraction data. Nevertheless, a clear trend can be seen, as the occupancy fluctuated very well around the 50 % value besides these outliers (Figure 31).

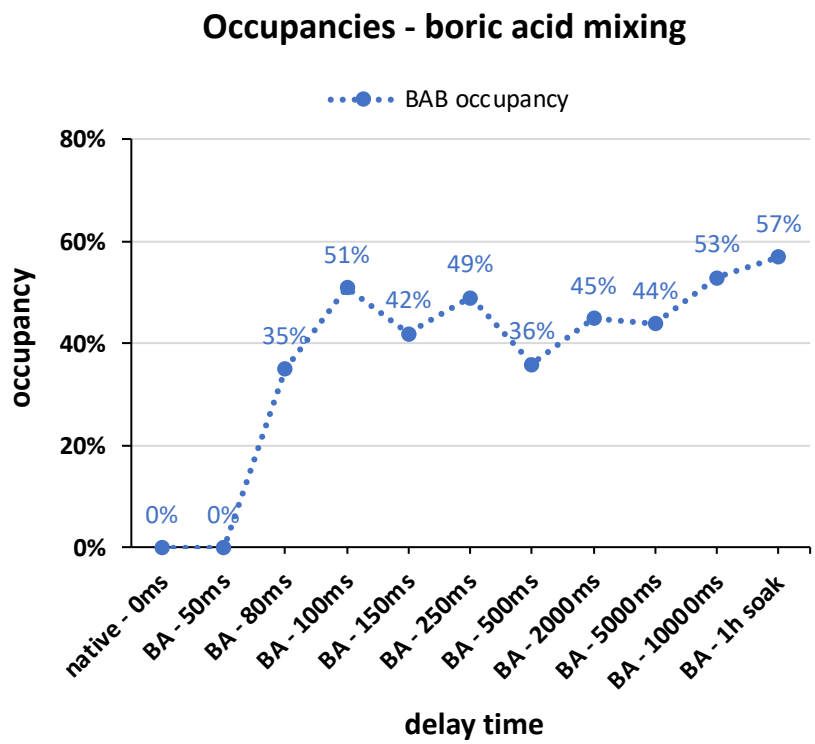

Figure 31: Plot of bound boric acid (BAB) occupancies against the respective delay times (not displayed linearly) when mixing with boric acid (BA). The BAB occupancy increased with longer delay times after mixing with boric acid and reached a maximum at 57 %. (Prester et al., 2023)

4.6.1.6. Time-resolved analysis of glycerol esterification to bound boric acid in the active site of CTX-M-14

After monitoring the time-resolved structure and dynamics of boric acid binding in the active site of CTX-M-14, another subsequent reaction, the esterification of the bound boric acid with glycerol, was additionally explored (Prester et al., 2023). The TapeDrive setup was employed again to mix glycerol with CTX-M-14 microcrystals that had previously been complexed with boric acid. It was shown that the esterification of boric acid with two diol groups of glycerol takes place within 100 – 150 ms, forming a glycerol boric acid diester (GBE).

Data collection and structure determination were performed as described in sections 3.6.2.1 and 3.6.3. Corresponding data collection and refinement statistics are shown in Table 22. The high-resolution limit of the collected datasets was set to 1.50 – 1.90 Å according to a cutoff at CC* = 0.5. All structures showed completeness values of >99 % for the full resolution range. Wilson *B*-factor values ranged from 17.55 to 24.15 Å^2, except for the datasets for the 80 ms and 100 ms delay times, which had Wilson *B*-factors of 36.86 Å^2 and 42.53 Å^2, respectively. The calculated *R* factors of the final models reached values of R_{work} = 0.137 – 0.167 and R_{free} = 0.160 – 0.210. Thus, the collected datasets and refined models were of good quality and ideally suited for the interpretation of the time-resolved esterification process. As before, polder maps were used to verify the presence of glycerol-boric acid ester (GBE) in the active site of CTX-M-14 (Figure 32).

As in section 4.6.1.5, the different equilibrium states overlap. Thus, the state with bound boric acid and the state with bound glycerol-boric acid ester are shown together as an overlapping mixed state.

CTX-M-14 microcrystals saturated with boric acid for 1 h were used as the initial condition. Thus, the time point 0 ms is equivalent with the 1 h soak time point from the boric acid time series. No glycerol has been added at this time point. The occupancy of bound boric acid was at 57 % for the 0 ms delay time. The initial change in the polder electron density map was already evident at the 50 ms mixing/delay point. In the region where the bound boric acid hydroxyl groups were located, an extension of electron density was observed, indicating the formation of a glycerol diester.

This allowed the insertion and refinement of the glycerol-boric acid ester (GBE), resulting in a calculated GBE occupancy of 26 %, while the BAB occupancy remained nearly constant at 55 % (Figure 33). Furthermore, the electron density for the sulfate decreased, leaving no space for the SO4-A position, which was then occupied by the newly formed glycerol diester. At the 80 ms and 100 ms delay times, there was only a slight increase in GBE occupancy. (Prester et al., 2023)

However, at the 150 ms time point, a significant increase in GBE occupancy to 51 % was observed and refined, while the BAB occupancy dropped to 35 % (Figure 32). This was the first time that the occupancy of GBE exceeded that of the BAB state, indicating that the esterification of boric acid bound to CTX-M-14 with glycerol occurred within a time frame of 100 – 150 ms. After a delay time of 750 ms the entire glycerol boric acid ester was well covered by the calculated polder electron density map, resulting in an occupancy of 65 %.

Due to the lack of hydrogens at GBE O2, the GBE could no longer act as a hydrogen bond donor for SO4-B, leading to the displacement of the sulfate ion by the water molecule wat357. This was accompanied by an increase in the occupancy of the GBE state and a decrease in the BAB state, as reflected by the lower electron density at the SO4 binding site.

Notably, the GBE reached 67 % occupancy within only 10 s delay time, in contrast to the BAB occupancy which dropped to 21 %. However, it is important to note that the overall occupancy of the ligands (BAB and GBE) bound to Ser70 increased with prolonged mixing, which was observed with the increase in the polder electron density obtained and refined for the cyclic ester (Figure 33). Consequently, the total boron occupancy in the binding site increased from 57 %, observed for only soaking/mixing with boric acid, up to 88 % when additionally mixed with glycerol up to a delay time of 10 s (Figure 33). (Prester et al., 2023)

As before, esterification of glycerol with boric acid in the active site did not induce major conformational changes in the enzyme, as indicated by the low RMSD values of 0.127 – 0.148 Å for the alignment of the structures against the native structure (Table 21). (Prester et al., 2023)

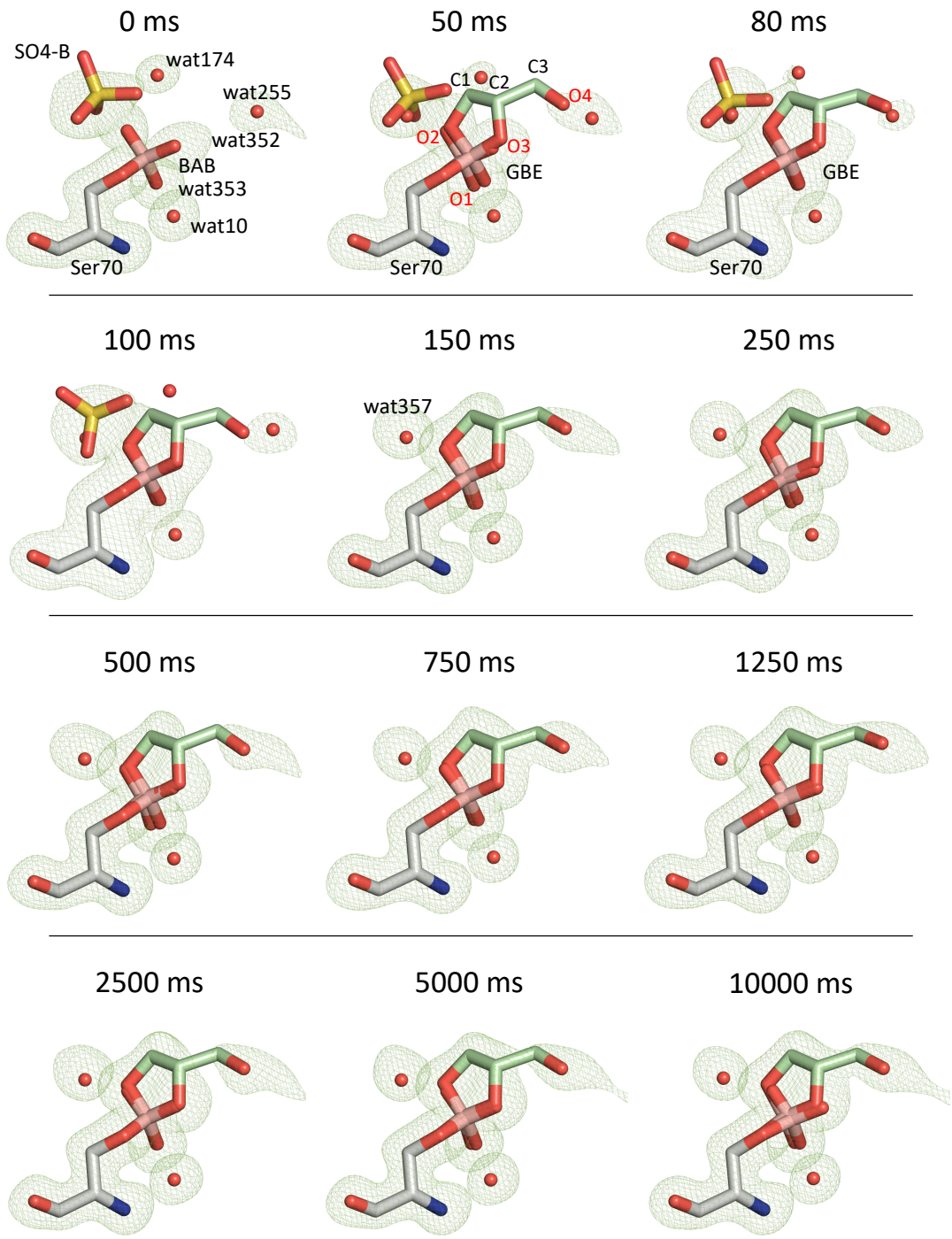

Figure 32: Timeline of the active site of CTX-M-14 presoaked with boric acid and subsequently mixed with glycerol at delay times of 50 ms – 10000 ms. The active site residue Ser70 as well as nearby water molecules, the rotationally disordered sulfate, bound boric acid (BAB) and, if present, the bound glycerol boric acid ester (GBE) are shown as stick representation. Polder map electron density (green mesh) was generated for all shown molecules and is contoured at 5 σ. A clear buildup of the polder electron density for the glycerol boric acid ester was observed over the time period studied, indicating that esterification with glycerol and the boric acid in the active site of CTX-M-14 occurs within 50 – 150 ms. Moreover, the sulfate ion was displaced by the limited space due to the binding of GBE and replaced by the wat357. As GBE was not fully occupied at any time, mixed states with overlapping of BAB and GBE states are shown. (Prester et al., 2023)

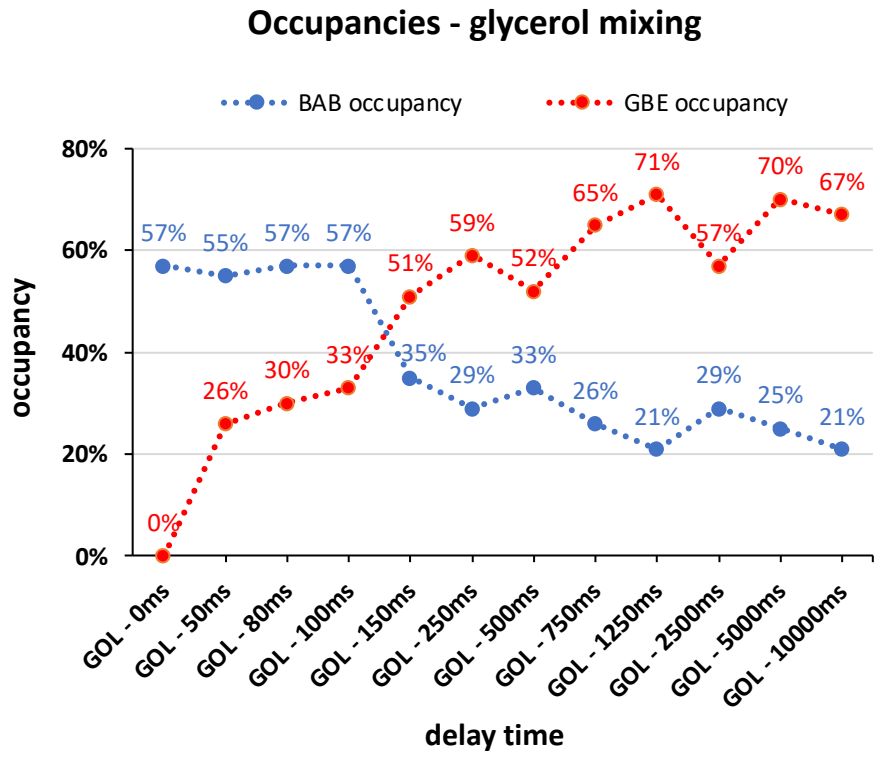

Figure 33: Plot of glycerol boric acid ester (GBE) occupancies against the respective delay times (not displayed linearly) when mixing with glycerol (GOL). Microcrystals have been presoaked with boric acid. The bound boric acid (BAB) occupancy decreased when mixing with glycerol, while occupancy of GBE increased as esterification progressed. Nevertheless, the total boron content continued to increase when mixing with glycerol. (Prester et al., 2023)

Table 21. Root-mean-square deviation (RMSD) calculations and alignments of TapeDrive CTX-M-14 β-lactamase structures presoaked with boric acid and mixed with glycerol.

CTX-M-14 TapeDrive structures	RMSD [Å]
0 ms versus native	0.119
50 ms versus native	0.131
80 ms versus native	0.141
100 ms versus native	0.148
150 ms versus native	0.132
250 ms versus native	0.132
500 ms versus native	0.127
750 ms versus native	0.128
1250 ms versus native	0.130
2500 ms versus native	0.131
5000 ms versus native	0.130
10000 ms versus native	0.133

Table 22. Data collection and refinement statistics for CTX-M-14 β-lactamase mixing with glycerol (GBE) using the TapeDrive. (Prester et al., 2023)

	CTX-M-14 GBE 0 ms	CTX-M-14 GBE 50 ms	CTX-M-14 GBE 80 ms	CTX-M-14 GBE 100 ms	CTX-M-14 GBE 150 ms	CTX-M-14 GBE 250 ms	CTX-M-14 GBE 500 ms	CTX-M-14 GBE 750 ms	CTX-M-14 GBE 1250 ms	CTX-M-14 GBE 2500 ms	CTX-M-14 GBE 5000 ms	CTX-M-14 GBE 10000 ms
PDB entry	8pck	8pcl	8pcm	8pcn	8pco	8pcp	8pcq	8pcr	8pcs	8pct	8pcu	8pcv
Resolution range (Å)	35.81-1.51 (1.53-1.51)	38.88-1.60 (1.62-1.60)	38.88-1.84 (1.86-1.84)	38.88-1.90 (1.92-1.90)	38.88-1.55 (1.57-1.55)	36.23-1.76 (1.78-1.76)	38.88-1.52 (1.54-1.52)	35.81-1.70 (1.72-1.70)	35.81-1.67 (1.69-1.67)	38.88-1.53 (1.55-1.53)	38.88-1.50 (1.52-1.50)	38.88-1.58 (1.60-1.58)
Space group	$P3_221$	$P3_221$	$P3_221$	$P3_221$	$P3_221$	$P3_221$	$P3_221$	$P3_221$	$P3_221$	$P3_221$	$P3_221$	$P3_221$
a=b, c (Å)	41.84, 233.28	41.84, 233.28	41.84, 233.28	41.84, 233.28	41.84, 233.28	41.84, 233.28	41.84, 233.28	41.84, 233.28	41.84, 233.28	41.84, 233.28	41.84, 233.28	41.84, 233.28
α, β, γ (°)	90, 90, 120	90, 90, 120	90, 90, 120	90, 90, 120	90, 90, 120	90, 90, 120	90, 90, 120	90, 90, 120	90, 90, 120	90, 90, 120	90, 90, 120	90, 90, 120
Unique reflections	38700 (2403)	32725 (2042)	21824 (1402)	19841 (1230)	35926 (2309)	24839 (1602)	38024 (2425)	27494 (1819)	28920 (1854)	37341 (2393)	39560 (2546)	34013 (2210)
⟨I/σ(I)⟩	10.43 (0.48)	23.76 (0.44)	10.73 (0.59)	10.65 (0.57)	26.85 (0.67)	10.52 (0.53)	18.55 (0.47)	10.72 (0.47)	11.29 (0.48)	16.31 (0.49)	27.45 (0.50)	17.47 (0.43)
Completeness (%)	99.79 (96.62)	99.88 (98.13)	100 (100)	100 (100)	99.93 (98.89)	100 (100)	99.80 (96.88)	100 (99.95)	100 (100)	99.86 (97.91)	99.96 (99.34)	99.95 (99.19)
Multiplicity	841 (7.0)	6417 (9.7)	3113 (1188.3)	3905 (1428.6)	10849 (11.8)	1411 (20.5)	3101 (8.8)	1182 (24.6)	1149 (22.3)	2558 (9.5)	7437 (15.2)	3311 (10.1)
Rsplit	8.37 (221.50)	4.79 (295.84)	5.64 (178.63)	6.30 (189.92)	4.00 (229.50)	9.17 (204.95)	4.78 (235.48)	8.19 (234.06)	8.11 (235.34)	5.75 (225.93)	3.50 (216.25)	5.75 (239.54)
CC1/2	0.995 (0.175)	0.999 (0.187)	0.998 (0.195)	0.996 (0.199)	0.999 (0.181)	0.997 (0.225)	0.998 (0.218)	0.995 (0.161)	0.997 (0.150)	0.998 (0.161)	0.999 (0.174)	0.999 (0.200)
CC*	0.999 (0.546)	1.000 (0.561)	0.999 (0.572)	0.999 (0.577)	1.000 (0.553)	0.999 (0.606)	1.000 (0.598)	0.999 (0.526)	0.999 (0.510)	1.000 (0.527)	1.000 (0.544)	1.000 (0.577)
Wilson *B*-factor (Å^2)	16.34	19.08	38.38	41.48	18.41	21.22	19.45	21.16	20.36	17.97	17.54	18.29
Resolution range in refinement (Å)	35.81-1.53 (1.59-1.53)	38.88-1.60 (1.66-1.60)	38.88-1.84 (1.91-1.84)	38.88-1.90 (1.97-1.90)	38.88-1.55 (1.61-1.55)	36.23-1.76 (1.82-1.76)	38.88-1.55 (1.61-1.55)	35.81-1.70 (1.76-1.70)	35.81-1.67 (1.73-1.67)	38.88-1.55 (1.61-1.55)	38.88-1.50 (1.55-1.50)	38.88-1.58 (1.63-1.58)
Reflections used in refinement	37258 (3616)	32612 (2965)	21655 (2123)	19688 (1843)	35787 (3360)	24717 (2419)	35817 (3501)	27370 (2672)	28807 (2791)	35828 (3497)	39421 (3757)	33900 (3184)
Reflections used for R_{free}	2166 (219)	1877 (170)	1251 (119)	1142 (107)	2067 (198)	1435 (142)	2078 (207)	1590 (154)	1669 (160)	2077 (207)	2286 (223)	1959 (186)
R_{work}	0.1430 (0.3589)	0.1446 (0.3935)	0.1647 (0.3688)	0.1639 (0.4202)	0.1435 (0.3802)	0.1585 (0.3600)	0.1389 (0.3449)	0.1502 (0.3531)	0.1460 (0.3665)	0.1406 (0.3523)	0.1411 (0.3681)	0.1498 (0.3767)
R_{free}	0.1697 (0.3608)	0.1748 (0.4038)	0.2096 (0.3717)	0.2061 (0.4680)	0.1692 (0.3752)	0.1922 (0.3268)	0.1664 (0.3625)	0.1832 (0.3952)	0.1784 (0.3910)	0.1656 (0.3594)	0.1626 (0.3829)	0.1740 (0.3482)
RMS (bonds)	0.013	0.007	0.003	0.004	0.012	0.005	0.008	0.004	0.006	0.017	0.014	0.008
RMS (angles)	1.23	0.90	0.62	0.64	1.24	0.84	1.07	0.768	0.96	1.45	1.24	0.99
Ramachandran favored (%)	98.08	97.70	97.32	98.47	97.32	98.08	97.70	98.08	98.08	97.70	98.08	98.08
Ramachandran allowed (%)	1.53	1.92	2.30	1.15	2.30	1.53	1.92	1.53	1.53	1.92	1.53	1.53
Ramachandran outliers (%)	0.38	0.38	0.38	0.38	0.38	0.38	0.38	0.38	0.38	0.38	0.38	0.38
Rotamer outliers (%)	0.93	0.93	0.93	0.93	0.93	0.93	0.93	0.93	0.93	0.93	0.93	0.93
Clashscore	2.18	2.19	1.94	2.19	2.90	2.40	1.93	2.66	2.66	3.13	3.13	2.16
Average *B*-factor	25.33	30.86	46.13	48.68	29.57	29.89	29.35	30.82	29.80	28.12	28.39	29.73
macromolecules	23.52	29.06	45.40	48.21	28.19	28.71	27.93	29.50	28.56	26.78	27.14	28.49
ligands	35.25	31.64	44.36	48.68	26.30	23.59	23.89	25.53	23.36	23.09	22.97	22.17
solvent	39.30	45.23	53.37	53.39	41.83	40.44	41.83	42.99	41.18	40.51	39.99	41.24
MolProbity score	0.84	0.91	0.87	0.88	1.09	0.67	0.86	0.92	0.99	1.06	0.92	0.96

Statistics for the highest-resolution shell are shown in parentheses.

4.6.1.7. Detailed analysis of the steady-state equilibria of boric acid binding and subsequent glycerol esterification in the active site of CTX-M-14

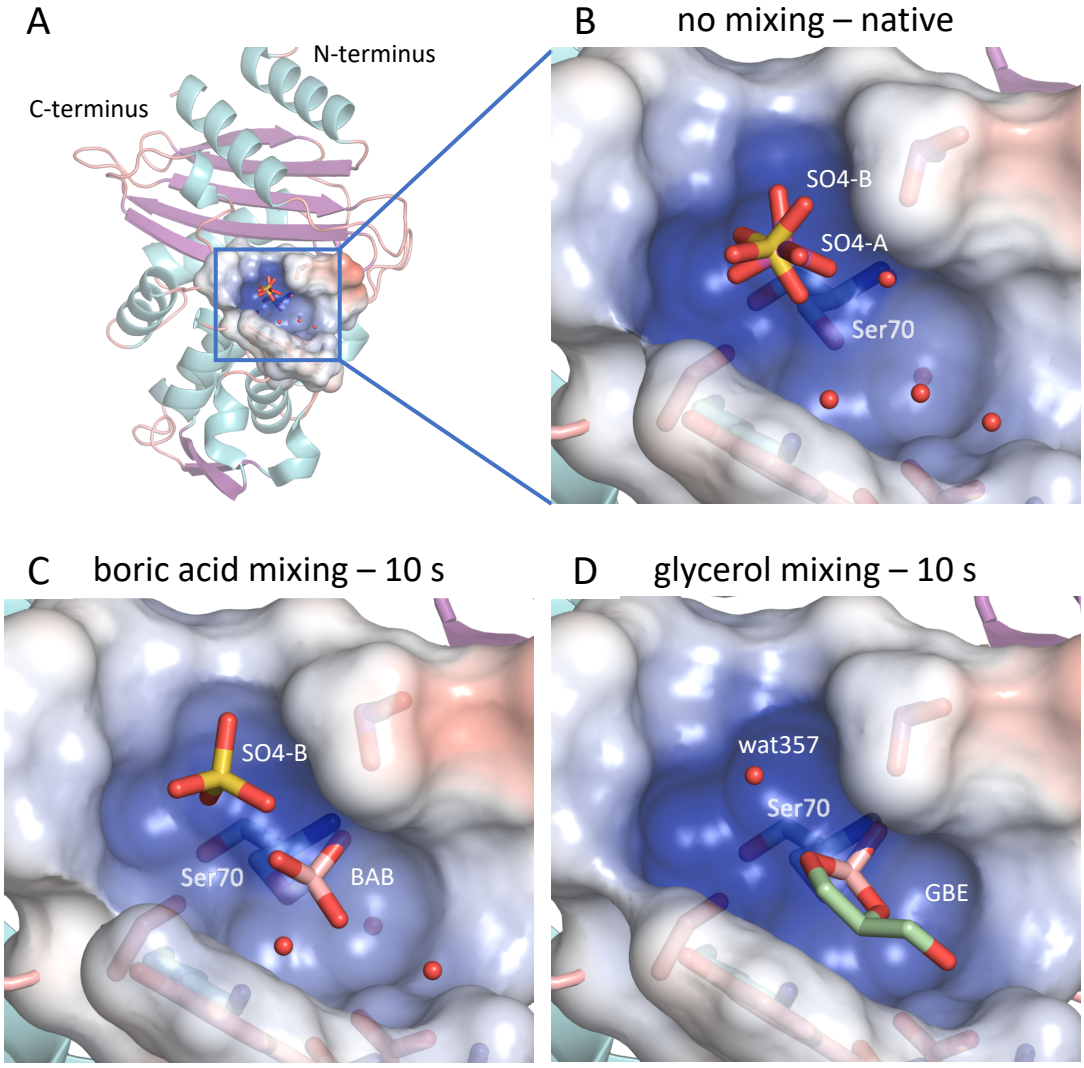

Figure 34: (A) Overview of CTX-M-14 β-lactamase and a close-up view of the active site of the three equilibrium states - (B) the native form, (C) the bound boric acid, and (D) the bound glycerol boric acid ester. Ribbon diagram of the overall structure of CTX-M-14 with the active site region highlighted by a surface representation (A). The close up shows the amino acid residues of the active site as well as the sulfate ions (SO4-A magenta; SO4-B yellow) in the native form (B) and covalently bound boric acid (C; BAB, pink) or covalently bound glycerol boric acid ester (D; GBE, palegreen) as a stick representation. The CTX-M-14 crystals were mixed with boric acid (C) or soaked with boric acid and subsequently mixed with glycerol (D) in order to collect data at a delay time of 10 s, which corresponds to the latest time point measured and thus resulted in the high BAB and GBE occupancies of 53 % and 67 %, respectively. (Prester et al., 2023)

Based on the time-resolved structures shown in section 4.6.1.5 and 4.6.1.6, two equilibrium reactions could be derived with the three equilibrium states: native enzyme, bound boric acid and bound glycerol-boric acid ester (Figure 34). Although these equilibrium states exist as mixed overlapping states in mix-and-diffuse serial crystallography experiments due to the unequal distribution within the crystal, they were considered separately here to highlight relevant interactions between ligand and enzyme (Figure 35).

The structure and possible interactions in the active site of the native enzyme have already been described in detail in section 4.6.1.1. However, the polar contacts of the rotationally disordered sulfate in the anion binding site have not yet been addressed in detail. This sulfate ion is represented in two slightly displaced alternative positions (SO4-A and SO4-B, Figure 34 B). SO4-A is strongly coordinated by possible hydrogen bonds with the side chain groups of Ser70 (3.1 Å), Ser130 (2.6 Å), Lys234 (3.5 Å; weak), Thr235 (3.1 Å) and Ser237 (3.3 Å) as well as the main chain nitrogen of Ser237 (3.1 Å). SO4-B is coordinated by hydrogen bonds with the same side chain groups of Ser70 (3.4 Å), Ser130 (2.9 Å), Lys234 (3.2 Å), Thr235 (3.3 Å) and Ser237 (2.8 Å) as well as the main chain nitrogen of Ser237 (3.2 Å) and additionally the main chain carbonyl group of Thr235 (2.8 Å) (Figure 35 A).

Boric acid binds to the active site of CTX-M-14 forming an ester with the catalytic side chain hydroxyl group of Ser70 (Figure 34). The stabilization of the tetrahedral transition state during initial binding involves hydrogen bonding interactions facilitated by the oxyanion hole, consisting of Ser70 and Ser237 main chain amide groups. Similar to the binding mechanism observed in typical substrates, the nucleophilic attack of Ser70 on the boron atom is facilitated via activation of the Ser70 hydroxyl oxygen by the general base Lys73 or Glu166 (Fisher et al., 2005; Strynadka et al., 1992; Tooke et al., 2019a). The Glu166 via a catalytic water molecule or the unprotonated Lys73 assist in the nucleophilic attack by acting as a general base, thereby accepting the proton from the Ser70 side chain, when the tetrahedral intermediate is formed (Prester et al., 2023).

Similar to the carboxylate of the acyl-enzyme intermediate, a hydroxyl group of boric acid (O1) establishes hydrogen bonds with the main chain nitrogen atoms of Ser70 (2.8 Å) and Ser237 (2.8 Å), which form the oxyanion hole. Additionally, BAB O1 forms a hydrogen bond with the main chain carbonyl oxygen of Ser237 (2.8 Å) (Figure 35 B). Unlike bortezomib, ixazomib or other boronate based inhibitors, the two remaining hydroxyl groups of bound boric acid do not engage in hydrogen bonding interactions with Asn170 and Glu166 (Perbandt

et al., 2022). Instead, the boric acid is shifted in the opposite direction within the anion binding site, forcing a reorientation of the sulfate ion from SO4-A to SO4-B position (Figure 35 B), to avoid too close atomic contacts. In this particular position, boric acid receives additional stabilization via hydrogen bonding interactions of the BAB hydroxyl group (O2) with the Ser130 (3.0 Å) side chain hydroxyl group and the sulfate ion (SO4-B, 2.6 Å). Additionally, the third BAB hydroxyl group (O3) forms hydrogen bonds with the water molecule wat10 (2.8 Å). Collectively, these intermolecular interactions result in a highly coordinated bound boric acid, with no rotational disorder observed around the Ser70 borate ester bond. (Prester et al., 2023)

Boric and boronic acids are known to form esters with polyalcohols forming five- or six-membered ring systems (Turker, 2006). In the case of the triol glycerol, both ring systems can be formed, but the formation of a six-membered ring is energetically favored over the five-membered ring (Turker, 2006). However, within the active site of an enzyme, steric constraints and other intermolecular interactions play a crucial role in guiding the esterification process of boric acid with glycerol, determining the preferential formation of one of these cyclic diesters (Lei et al., 2016; Nitsche et al., 2017). In the CTX-M-14 active site, glycerol forms a five-membered cyclic diester with two hydroxyl groups (O2, O3) of bound boric acid (Figure 35 C) (Prester et al., 2023). The remaining hydroxyl group (O1) of the boric acid is critical for maintaining the stabilizing hydrogen bonds with the main chain nitrogen atoms of Ser70 (2.9 Å) and Ser237 (3.0 Å) in the oxyanion hole. The remaining free hydroxyl group of glycerol (O4) also forms an additional hydrogen bond with the amide group of Asn132 (3.0 Å) and a weak hydrogen bond with Asn104 (3.5 Å) to stabilize the GBE. (Prester et al., 2023)

As the esterification proceeds, the electron density for the sulfate ion is substantially reduced (Figure 32). This is probably because the resulting cyclic ester lacks a proton at the O2 (GBE) and thus, in contrast to BAB, cannot act as a hydrogen bond donor for the sulfate ion. The sulfate ion is then completely displaced from the anion binding site by a water molecule wat357, which forms hydrogen bonds with the GBE (O2, 2.7 Å) and the hydroxyl group of Thr235 (2.8 Å).

The central carbon atom (C2) of glycerol becomes a stereo center with (*S*)-configuration in the glycerol – boric acid diester. During esterification, the boron atom in GBE also becomes a

stereo center with (*S*)-configuration. The absence of any racemic disorder in both stereocenters emphasizes the unique and specific environment of the β-lactamase active site.

Throughout all observed time steps, wat10 remained consistently well-defined in the same position. This particular water molecule is considered the catalytic water molecule essential for the deacylating step in β-lactam hydrolysis (Tooke et al., 2019a). It has a crucial role in the initiation of the nucleophilic attack on the carbonyl carbon atom of the acyl-enzyme complex, resulting in the hydrolysis of the acyl bond. Wat10 is highly coordinated through short hydrogen bonds with the side chains of Ser70 (2.6 Å), Glu166 (2.6 Å), Asn170 (2.5 Å) and BAB (O3, 2.8 Å). Such particularly short hydrogen bonds of a serine-β-lactamase with the catalytic water have been previously reported by other researchers (Nichols et al., 2015). (Prester et al., 2023)

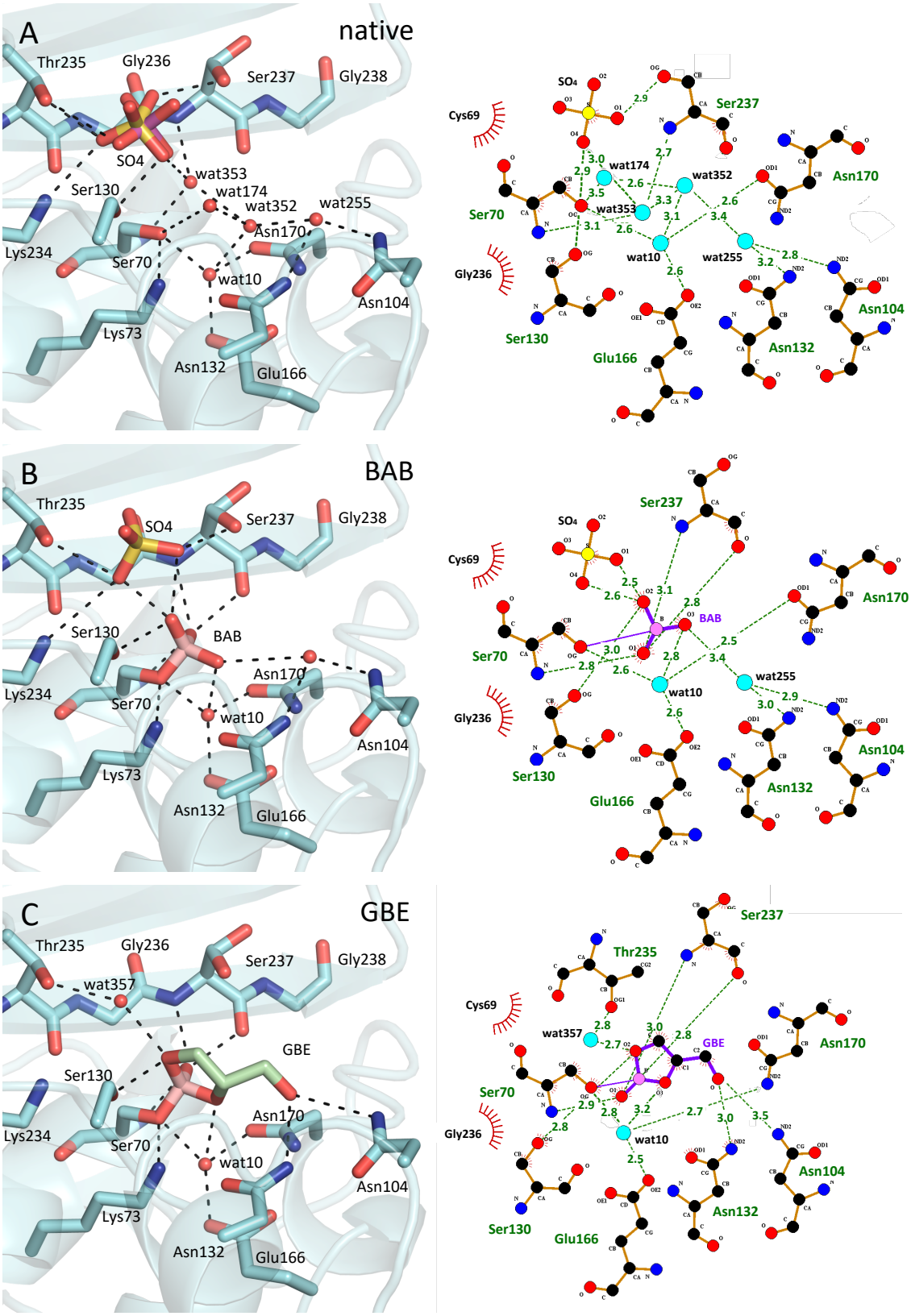

Figure 35: Visualization of polar contacts between the active site of CTX-M-14 and ambient sulfate ions and water molecules (A), bound boric acid (B) and glycerol boric acid ester (C) in 3D (left) and 2D (right) view. Potential hydrogen bonds are depicted as black dashes (left) or green dashes (right) with the atomic distance in Ångström. (Prester et al., 2023)

4.6.2. Serial synchrotron crystallography using the HARE Chip

4.6.2.1. Time-resolved analysis of piperacillin hydrolysis by CTX-M-14 revealing four states including distinct intermediates

To fully exploit the potential of time-resolved serial synchrotron X-ray crystallography, a fixed target - based approach was used in addition to the CFEL TapeDrive to generate time-resolved structural data and obtain insights into enzymatic function and dynamics. The LAMA method (Mehrabi et al., 2020) was used in combination with HARE (Schulz et al., 2018), as described in section 3.6.2.2. The CTX-M-14 microcrystals were loaded onto a chip and the reaction was then initiated by applying a picoliter sized drop of the substrate piperacillin directly to each crystal well of the chip before collecting diffraction data. The delay time is defined as the time between droplet deposition and X-ray diffraction collection of each individual crystal well. These time-resolved experiments were performed at 30 °C at various delay times ranging from 2 s – 12 s in order to analyze the hydrolysis of the broad spectrum β-lactam antibiotic piperacillin by CTX-M-14.

Data collection and structure determination were performed as described in sections 3.6.2.2 and 3.6.3. Corresponding data collection and refinement statistics are shown in Table 23. The native structure diffracted to a resolution of 1.65 Å. All other structures of this experiment achieved a resolution of about 1.70 Å. Diffraction data showed good quality with a CC* of at least 0.97 overall and at least 0.73 for the highest resolution shells. The Matthews coefficient of the crystals is 2.15 $Å^3$/Da, corresponding to a solvent content of 43 %. According to Matthews Cell Content Analysis (CCP4i; Winn et al., 2011) the asymmetric unit contains one molecule of the protein, as in the crystals in previous chapters. The calculated *R* factors of the final refined models reached values of R_{work} = 0.163 – 0.185 and R_{free} = 0.190 – 0.208.

Table 23. Data collection and refinement statistics for CTX-M-14 β-lactamase mixing with piperacillin using the LAMA approach and HARE data collection on a chip.

	CTX-M-14 native 0 s	CTX-M-14 piperacillin 2 s	CTX-M-14 piperacillin 2.4 s	CTX-M-14 piperacillin 3 s	CTX-M-14 piperacillin 4.5 s	CTX-M-14 piperacillin 6 s	CTX-M-14 piperacillin 12 s
PDB entry	n.a.	n.a.	n.a.	n.a.	n.a.	n.a.	n.a.
Resolution range (Å)	117.65-1.65 (1.71-1.65)	117.65-1.70 (1.76-1.70)	117.65-1.70 (1.76-1.70)	116.28-1.70 (1.76-1.70)	116.28-1.70 (1.76-1.70)	117.65-1.70 (1.76-1.70)	117.65-1.70 (1.76-1.70)
Space group	P3221	P3221	P3221	P3221	P3221	P3221	P3221
a, b, c, (Å)	42.15, 42.15, 234.2	42.15, 42.15, 234.2	42.15, 42.15, 234.2	42.15, 42.15, 234.2	42.15, 42.15, 234.2	42.15, 42.15, 234.2	42.15, 42.15, 234.2
α, β, γ (°)	90, 90, 120	90, 90, 120	90, 90, 120	90, 90, 120	90, 90, 120	90, 90, 120	90, 90, 120
Unique reflections	30415 (2968)	27863 (2729)	27878 (2732)	27314 (2582)	27300 (2578)	27883 (2733)	27878 (2731)
⟨I/σ(I)⟩	5.94 (1.83)	3.6 (1.05)	5.74 (1.47)	4.46 (1.04)	4.37 (0.92)	4.85 (1.38)	4.35 (1.17)
Completeness (%)	99.90 (99.73)	99.90 (99.71)	99.95 (99.85)	99.60 (96.20)	99.54 (96.05)	99.97 (99.89)	99.95 (99.82)
Multiplicity	287 (155)	102 (62)	173 (105)	131 (81)	116 (72)	122 (74)	103 (63)
Rsplit	13.85 (54.03)	26.02 (96.41)	14.92 (96.68)	18.16 (99.47)	18.13 (118.56)	18.77 (71.00)	20.57 (88.30)
CC	0.970 (0.727)	0.898 (0.432)	0.962 (0.621)	0.952 (0.446)	0.959 (0.361)	0.944 (0.599)	0.927 (0.530)
CC*	0.992 (0.918)	0.973 (0.777)	0.990 (0.875)	0.988 (0.786)	0.990 (0.729)	0.986 (0.866)	0.981 (0.832)
Wilson *B*-factor (Å^2)	20.18	21.71	22.42	22.27	22.24	20.54	21.24
Resolution range in refinement (Å)	78.07-1.65 (1.71-1.65)	78.07-1.70 (1.76-1.70)	78.07-1.70 (1.76-1.70)	78.07-1.71 (1.77-1.71)	78.07-1.71 (1.77-1.71)	78.07-1.70 (1.76-1.70)	78.07-1.70 (1.76-1.70)
Reflections used in refinement	30415 (2964)	27863 (2728)	27878 (2732)	27314 (2582)	27300 (2578)	27883 (2733)	27878 (2731)
Reflections used for *R*free	1526 (165)	1377 (154)	1378 (154)	1352 (145)	1351 (144)	1378 (154)	1378 (154)
*R*work	0.1626 (0.2318)	0.1846 (0.3145)	0.1626 (0.2783)	0.1663 (0.3014)	0.1704 (0.3233)	0.1662 (0.2704)	0.1696 (0.2959)
*R*free	0.1907 (0.2914)	0.2083 (0.3378)	0.1903 (0.3190)	0.1992 (0.3093)	0.2048 (0.3624)	0.2000 (0.2807)	0.2038 (0.3222)
RMS (bonds)	0.005	0.005	0.005	0.007	0.006	0.007	0.007
RMS (angles)	0.76	1.04	1.06	1.11	1.08	1.16	1.13
Ramachandran favored (%)	98.45	98.06	98.06	98.06	97.67	98.45	97.67
allowed (%)	1.16	1.55	1.55	1.55	1.94	1.16	1.94
outliers (%)	0.39	0.39	0.39	0.39	0.39	0.39	0.39
Rotamer outliers (%)	0.89	0.89	0.89	1.33	1.33	1.33	1.33
Clashscore	0.70	0.90	1.12	0.89	1.56	1.56	0.67
Average *B*-factor	27.10	30.16	31.35	29.97	29.99	28.03	28.52
macromolecules	26.03	27.89	29.41	28.68	28.50	26.78	27.58
ligands	34.73	55.07	48.38	35.20	41.09	34.87	28.60
solvent	40.35	41.91	44.26	42.80	41.35	39.31	40.37
MolProbity score	0.73	0.77	0.82	0.87	1.06	0.99	0.88

Statistics for the highest-resolution shell are shown in parentheses.

The study of the molecular reaction pathway of the enzymatic hydrolysis of β-lactam antibiotics by a β-lactamase is complex, not only because of the many potential antibiotics. However, the results of the kinetic assays (see 4.6.1.3) served as a reference for the choice of antibiotics to be investigated. Slowly hydrolyzed antibiotics were selected to allow the observation of the reaction with the available time-resolved crystallography methods. Nevertheless, many antibiotics and inhibitors had to be screened until finally piperacillin (Figure 36) was found to be the ideal substrate for time-resolved studies. Piperacillin is a β-lactam antibiotic that is often used in combination with the β-lactamase inhibitor

tazobactam and offers broad spectrum activity against Gram-positive and Gram-negative aerobic and anaerobic bacteria, including some ESBL producers (Gin et al., 2007; Paterson & Bonomo, 2005). This allowed the first time-resolved protein structure of the enzyme-substrate/product complex of a functional wild-type serine-β-lactamase with a medically relevant antibiotic to be determined. In addition, information on intermediate states during hydrolysis was obtained.

The kinetic mechanism of β-lactamases can be represented in a flow diagram (Equation 6) as already mentioned in section 1.6.5. The enzyme and substrate are initially free in solution until they form a non-covalent Michaelis-Menten complex. During hydrolysis, an acyl-enzyme intermediate is then formed, which is finally converted to the product. Initially, the product is still located in the active site forming the enzyme product complex but is then released so that enzyme and product are free in solution. A corresponding reaction scheme is shown in the introduction (section 1.4; Scheme 1).

Michaelis -Menten | acyl-enzyme intermediate | product complex

$$E + S \underset{k_{-1}}{\overset{k_1}{\rightleftarrows}} [ES] \xrightarrow{k_2} [E-S] \xrightarrow{k_3} [EP] \xrightarrow{k_4} E + P$$

Equation 6: Kinetic mechanism of enzymatic hydrolysis of β-lactam antibiotics by a β-lactamase. Where $E + S$ is the free enzyme and the substrate, $[ES]$ the non-covalent Michaelis-Menten complex, $[E - S]$ the covalent bound acyl-enzyme intermediate, $[EP]$ the enzyme product complex, $[E + P]$ the free enzyme and product, and k_n as the respective rate.

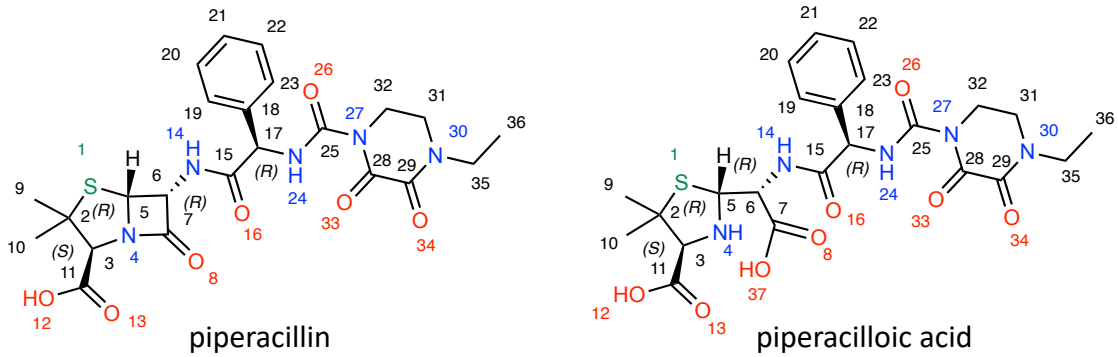

Figure 36: Chemical structure of the β-lactam antibiotic piperacillin and the hydrolyzed product piperacilloic acid.

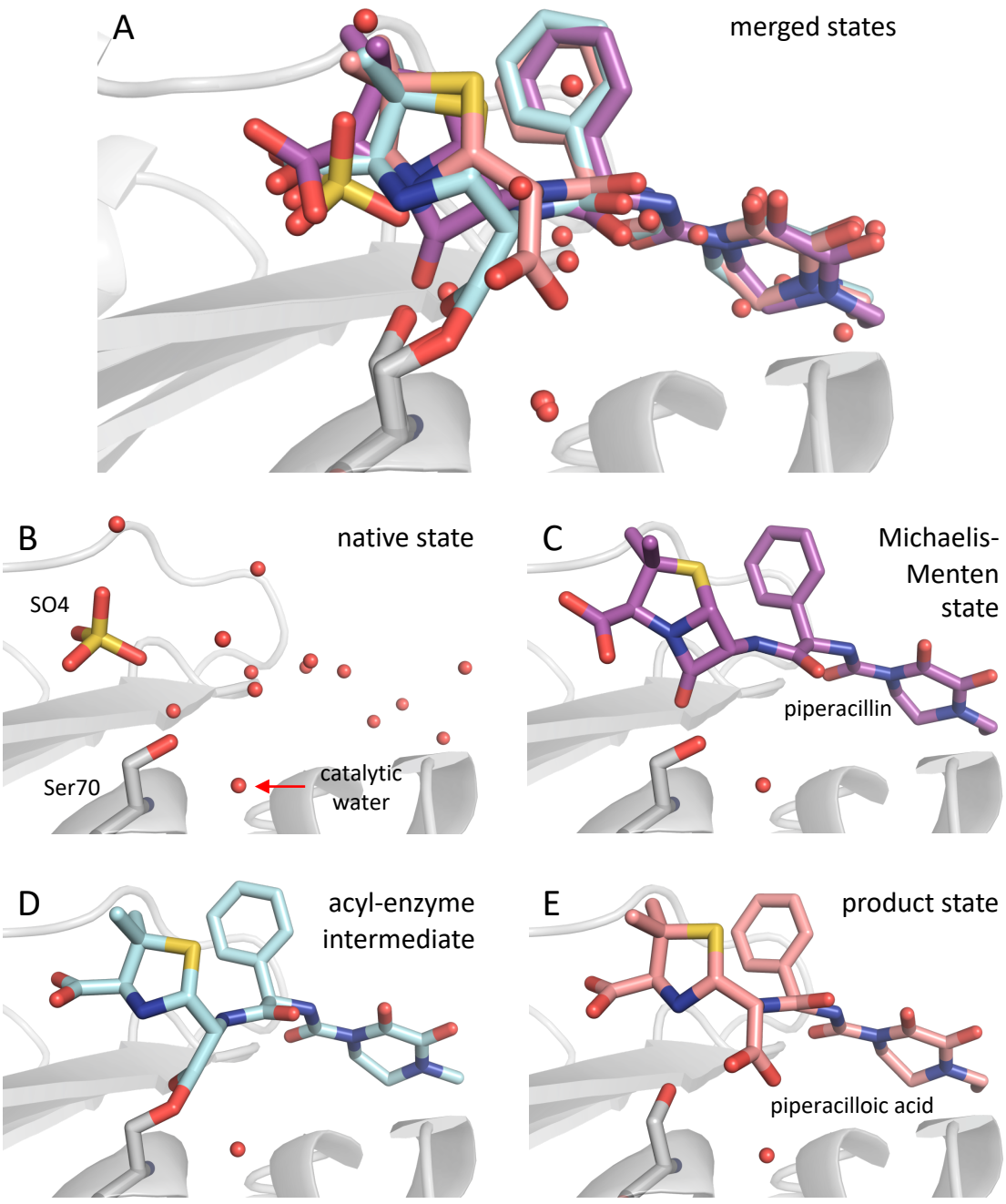

Figure 37: Close-up view of the CTX-M-14 β-lactamase active site of the piperacillin hydrolysis reaction states – (A) all states merged, (B) the native state, (C) the Michaelis-Menten state with non-covalent piperacillin in the active site, (D) the covalently bound piperacilloic acid forming the acyl-enzyme intermediate, and (E) the product state with hydrolyzed piperacilloic acid still present in the active site.

The four reaction states obtained by time-resolved crystallography are summarized and merged in Figure 37 A, and shown individually in Figure 37 B-E. In principle, they accurately reveal the protein coordinates of the reaction states described in Equation 6. This demonstrates that the active site in the native state is already occupied by some water molecules and the sulfate already discussed (Figure 37 B). Then, the piperacillin converges to

the active site and forms the Michaels-Menten complex with the enzyme. This is followed by the nucleophilic attack of Ser70 on the C7 of piperacillin, resulting in cleavage of the β-lactam ring and formation of an acyl-enzyme intermediate. This intermediate is deacylated by the catalytic water molecule, leaving a temporary enzyme product complex that subsequently dissociates.

The time course of this reaction can be observed in Figure 38 and Figure 39 based on the change in the polder electron density maps of the time-resolved crystallography structures, leading to the various occupancies of the distinct reaction states (Table 24). Some of the water molecules present in the native state and the sulfate are displaced upon binding of piperacillin, as has already been observed with the binding of other inhibitors (sections 4.6.1.4 – 4.6.1.6). It is particularly noticeable that some of the oxygen atoms of the carbonyl and carboxyl groups of piperacillin occupy exactly the positions previously occupied by water molecules. This includes the oxyanion hole, which is occupied by the O8 of the β-lactam ring of piperacillin (Figure 38, 2 s). Furthermore, the anion binding site is occupied by a carboxylate group of the piperacillin and thus enhances the interactions with the enzyme. Admittedly, the polder electron density for the piperacillin substrate is relatively weak at the 2 s time point, yet the refinement calculated an occupancy of 15 %. At the same time, the occupancy of the native state is 74 %. Nevertheless, it is the time point with the highest occupancy for the piperacillin in the Michaelis-Menten state (Table 24). This indicates that this state is relatively short-lived and is removed from the equilibrium by the formation of the products.

The β-lactam ring of piperacillin is perfectly positioned for nucleophilic attack by the hydroxyl group of Ser70 mainly due to the coordination of O8 in the oxyanion hole. In this position, the distance between the Ser70 hydroxyl and the C7 carbon atom of piperacillin is 3.0 Å. After nucleophilic attack and cleavage of the β-lactam ring, the acyl-enzyme intermediate can first be observed at 2.4 s with an occupancy of 12 % (Figure 38). In particular, the polder electron density for the dioxopiperazine ring of piperacillin is the first moiety to be well defined, suggesting that it plays an important role in the binding and recognition of piperacillin. At the same time, it is apparent that only little polder electron density is observed in the region of the acyl bond or in the vicinity of the β-lactam ring, the region of particular interest for the observation of the hydrolysis reaction. However, this could also be the reason why the polder electron density is very weak at this region, since the reaction occurs at this area but is not uniformly in sync throughout the protein crystal. After 3 s, polder electron density can be

observed for the first time for the state with the product complex with an occupancy of 33 %. It is particularly notable that the newly formed carboxylate group (at C7) of piperacilloic acid is rotated away from the oxyanion hole (Figure 39, 3 s). This simultaneously caused the Ser70 to rotate in the opposite direction to the oxyanion hole to avoid steric clashes, leaving sufficient space for both moieties. These movements are evidenced by the emergence of additional polder electron density (Figure 38 and Figure 39; 3 s) and corresponding difference electron density (not shown). Moreover, at the 3 s time point, the ligand is increasingly better represented with polder electron density, resulting in increasingly better representation of the phenyl ring. At 4.5 s, the entire piperacilloic acid molecule is fully covered in polder electron density and reaches an occupancy of 49 %, which is for the first time higher than the occupancy of the native state (35 %). In the further observed course of the reaction, the polder electron density becomes even better defined and the occupancy of the product complex increases to 63 %. It should be noted that at this point, according to the refinement, the acyl-enzyme intermediate state is also present with 20 % and the native state with 15 %. It is particularly noteworthy that the catalytic water is always completely covered in polder electron density over the entire time course. This indicates that it is likely to be quickly repopulated after hydrolysis. Nevertheless, some dynamics can be determined for the catalytic water over the observed time period. The difference in the position of the catalytic water molecule at 2 s versus 12 s is 0.5 Å (Figure 37 A).

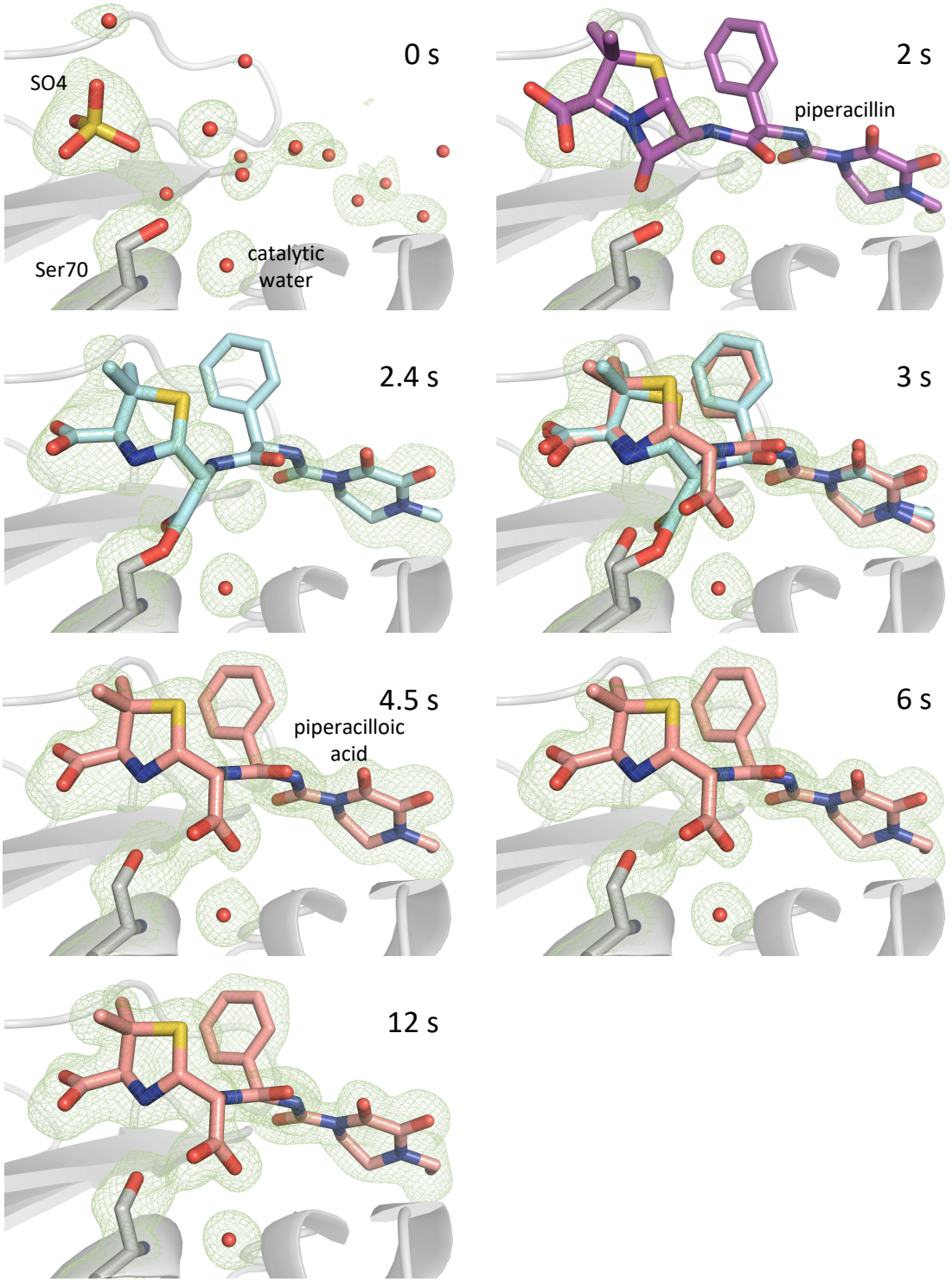

Figure 38: Timeline of enzymatic piperacillin hydrolysis in the active site of CTX-M-14 at delay times of 0 s – 12 s. The active site residue Ser70 as well as nearby water molecules, the sulfate (rotational disorder omitted for clarity), piperacillin and, the hydrolyzed piperacilloic acid are shown as stick representation. Generated polder electron density maps (green mesh) are contoured at 3 σ. A clear buildup of the polder electron density for the piperacillin is observed over the time period studied. In addition, hydrolysis of piperacillin is observed by the formation of the product, piperacilloic acid, after 3 s. This shows that the hydrolysis reaction occurs within 2 – 3 s and leads to an increased occupancy of the product state at subsequent time points. As observed previously, the sulfate ion is displaced by the carboxylate group of the piperacillin substrate, which utilizes the anion binding site.

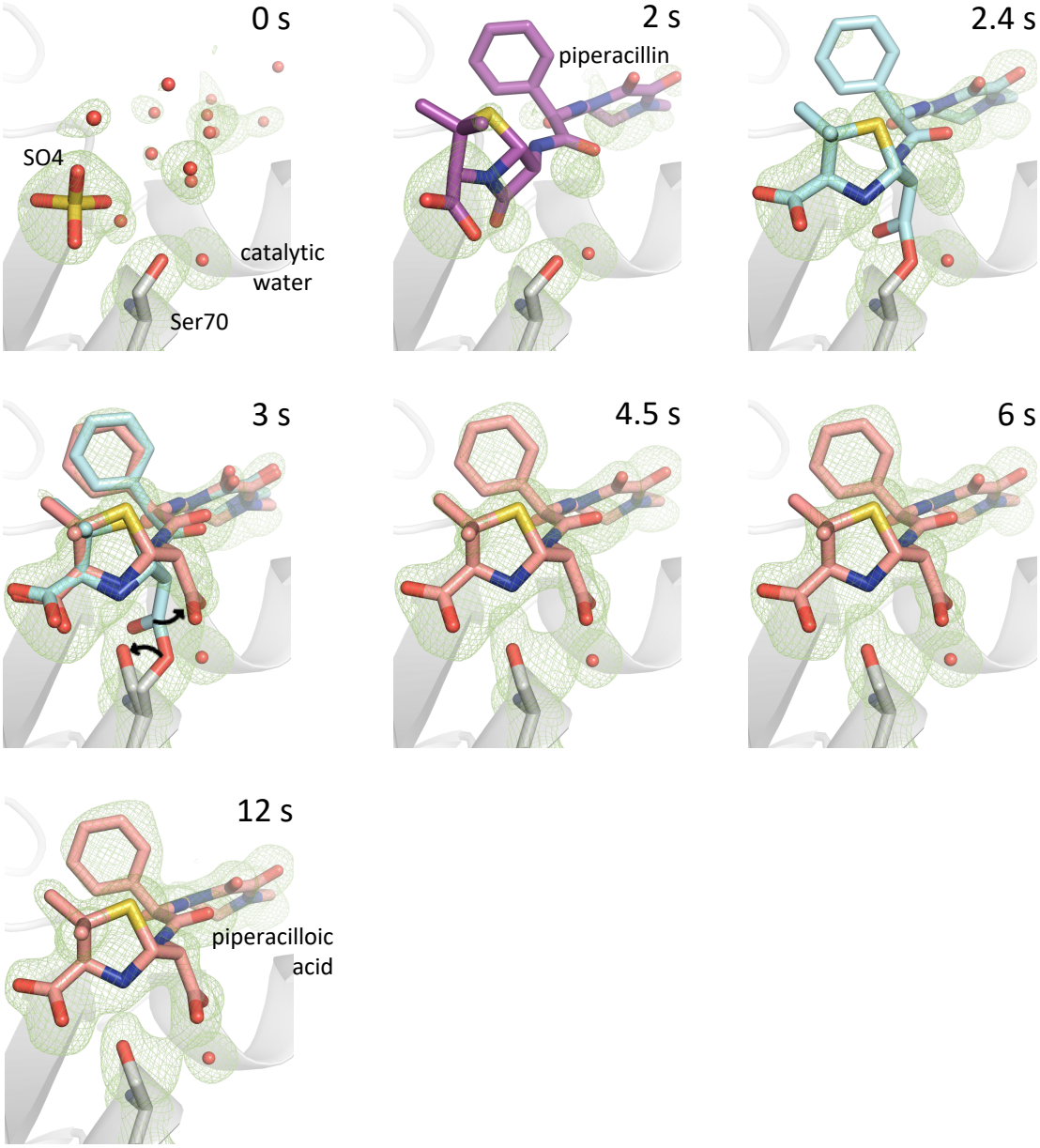

Figure 39: Timeline of enzymatic piperacillin hydrolysis in the active site of CTX-M-14 at delay times of 0 s – 12 s with special focus on Ser70 conformational changes. The active site residue Ser70 as well as nearby water molecules, the sulfate (rotational disorder omitted for clarity), piperacillin and, the hydrolyzed piperacilloic acid are shown as stick representation. Generated polder electron density maps (green mesh) are contoured at 3 σ. This perspective allows to observe the function of Ser70. It is in an identical position to the native state until the piperacillin binds, forming the acyl-enzyme. After hydrolysis and the formation of the product, piperacilloic acid, the carboxylate group is too close to Ser70. This favors a rotation of the Ser70 in the direction of the oxyanion hole and a rotation of the carboxylate of piperacilloic acid in the opposite direction as indicated by black arrows.

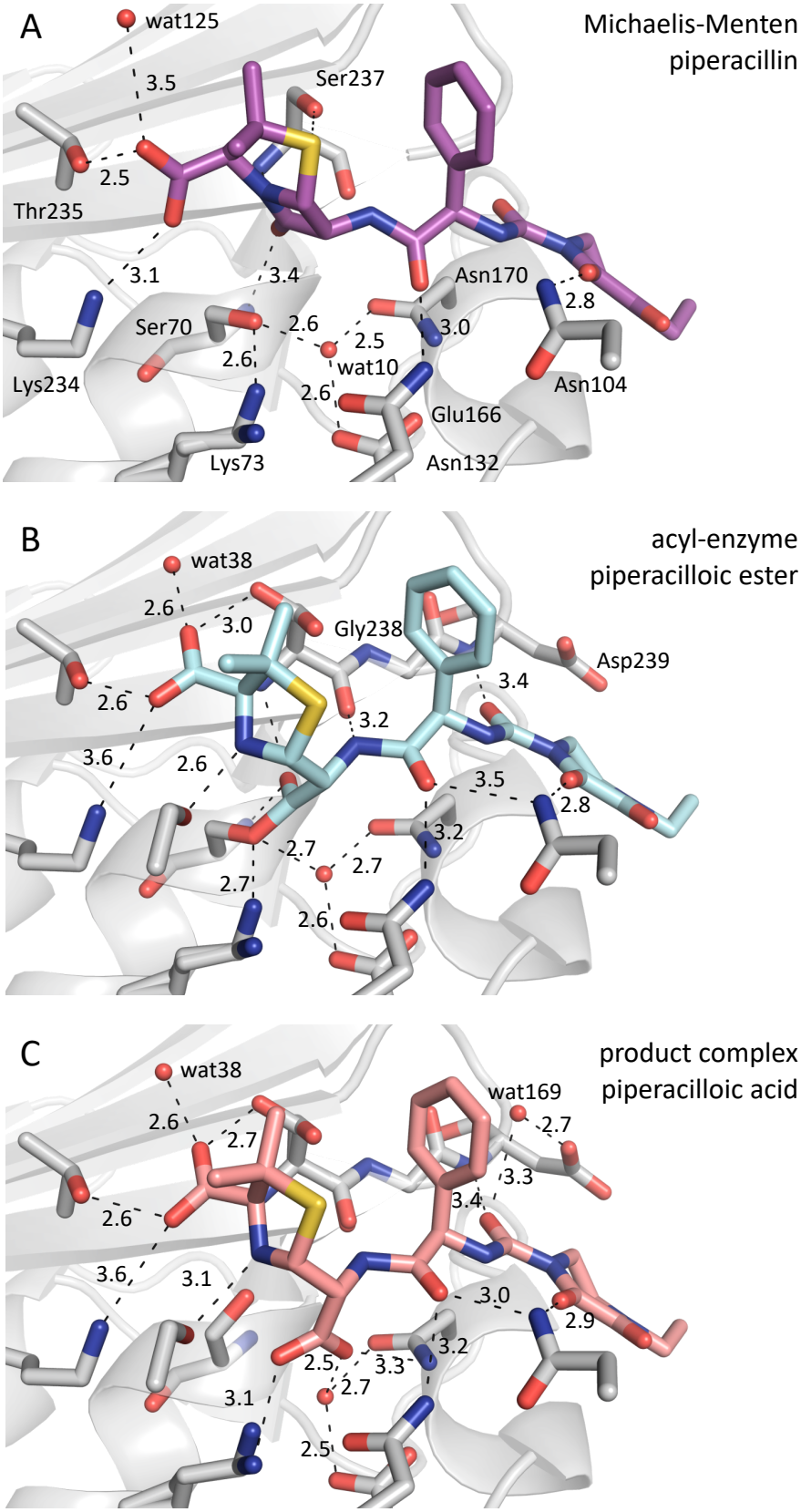

Figure 40: Visualization of polar contacts in the active site of CTX-M-14 with reaction states during hydrolysis of piperacillin showing the (A) Michaelis-Menten state with intact piperacillin, (B) the acyl-enzyme intermediate with a covalent bonded piperacilloic ester and (C) the product complex of CTX-M-14 and the piperacilloic acid. Potential hydrogen bonds are depicted as black dashes with the atomic distance in Ångström.

The polar contacts of piperacillin and its hydrolysis product with the active site residues of CTX-M-14 are visualized in Figure 40. As mentioned previously, the O8 of the β-lactam ring of piperacillin is located in the oxyanion hole and thus forms hydrogen bonds with the main chain nitrogen atoms of Ser70 (3.4 Å) and Ser237 (2.5 Å). These hydrogen bonds are preserved in the acyl-enzyme state until they are disrupted in the product complex as the newly formed carboxylate group of piperacilloic acid rotates aside and is subsequently coordinated by hydrogen bonds with Lys73 (3.1 Å), Asn170 (3.3 Å), and wat10 (2.5 Å). The catalytic water is coordinated throughout all states by hydrogen bonds with Glu166 (2.5 – 2.6 Å) and Asn170 (2.5 – 2.7 Å). In addition, it forms a hydrogen bond with the Ser70 hydroxyl in the Michaelis-Menten (2.6 Å) and acyl-enzyme (2.7 Å) states until this interaction is replaced by a weak hydrogen bond with the carboxylate O8 atom (3.3 Å) in the product complex. It should be mentioned that these particularly short hydrogen bonds of a serine β-lactamase with the catalytic water have already been reported by other researchers (Nichols et al., 2015). Lys73 forms a hydrogen bond with the Ser70 hydroxyl group in the Michaelis-Menten (2.6 Å) and acyl-enzyme (2.7 Å) states. This hydroxyl bond is proposed to remove a proton from Ser70 and thus increase the nucleophilicity, allowing the acylation process to take place. However, in the product complex, the Lys73 side chain adopts a different alternative position and can no longer form a hydrogen bond with the Ser70 side chain, due to Ser70 rotation in the oxyanion hole (Figure 40 C). Therefore, the Lys73 side chain in the product complex forms a hydrogen bond to the newly formed carboxylate O37 (3.1 Å) if the piperacilloic acid.

The carboxylate group of piperacillin at C3 forms hydrogen bonds in the Michaelis-Menten complex with the side chains of Lys234 (3.1 Å) and Thr235 (2.5 Å), as well as a weak hydrogen bond with wat125 (3.5 Å). In the acyl-enzyme and product state, the hydrogen bond with Thr235 (2.6 Å) is preserved, whereas that with Lys234 is likely to be omitted due to the too-long distance of 3.6 Å. In addition, a hydrogen bond is formed with a different water molecule wat38 (2.6 Å). Particularly noticeable is the adoption of an alternative position of the Ser237 side chain in a different rotamer configuration (Figure 40 B and C). In this position, Ser237 (2.7 – 3.0 Å) can form a hydrogen bond with the C3 carboxylate group of piperacilloic acid in the acyl-enzyme and product state.

The carbonyl O16 of piperacillin forms hydrogen bonds with Asn132 (3.0 – 3.2 Å) and in the acyl-enzyme and product state additionally weak hydrogen bonds with Asn104 (3.0 – 3.5 Å). Moreover, the O33 of the dioxopiperazine moiety also forms hydrogen bonds with

Asn104 (2.8 – 2.9 Å) in all states. In the acyl-enzyme and product states, the piperacilloic acid carbonyl O26 can form a weak hydrogen bond with Gly238 (3.4 Å). Furthermore, in the product complex, a water bridge is also formed by the O26 via wat169 (3.3 Å) to the Asp239 side chain (2.7 Å).

For the calculation of the occupancies, all possible reaction states (native, Michaelis-Menten, acyl-enzyme, product complex; see Figure 37 A) were incorporated into the pdb model files at each time point and refined. Thus, a rough time course of the reaction can be observed over the calculated occupancy values.

The molecules of the different states were assigned their own alternative location groups so that they did not influence each other except for the occupancies. It should be noted that the default restraint that alternative locations should add up to 100 % was removed in the refinement program. Nevertheless, the total occupancy of all states of a delay time point should theoretically still add up to 100 %. Thus, there is a control for the calculated occupancy numbers. With a maximum deviation of ± 5 %, this value is maintained for all delay times (Table 24).

Table 24. Occupancies of the four reaction states at the respective delay times during piperacillin hydrolysis by CTX-M-14 obtained by time-resolved crystallography. In addition, and as a control, the occupancies of the individual states were summed to provide an overview of the total occupancy of the active site.

delay time	native	Michaelis-Menten	acyl-enzyme	product	sum
0 s	100 %	0 %	0 %	0 %	100 %
2 s	74 %	15 %	9 %	6 %	104 %
2.4 s	52 %	9 %	12 %	30 %	103 %
3 s	43 %	5 %	14 %	33 %	95 %
4.5 s	35 %	5 %	16 %	49 %	105 %
6 s	28 %	0 %	23 %	54 %	105 %
12 s	16 %	1 %	20 %	63 %	100 %

5. Discussion

5.1. Kinetic parameters of CTX-M-14

Synchrotron beamtimes are very limited and therefore precious, and the production of crystals consumes a lot of time and resources as well. Especially the SSX methods, which are not yet permanently available, require a lot of time to set up and are therefore not (yet) usable at every beamtime.

Therefore, it is particularly important to carefully plan the beamtimes in advance and to perform as many experiments as possible, in order to provide initial recommendations for the experimental setup and procedure.

Since β-lactamases have many substrates and substrate classes that are hydrolyzed at very different rates, it is particularly important to choose a good candidate for time-resolved studies beforehand. Assays for the determination of kinetic parameters can be used to assist in the selection process, as they can be performed quickly on a daily basis and provide fast results. These kinetic parameters are commonly used for the characterization of newly discovered β-lactamase variants in order to classify them by substrate profile. However, in this case, the kinetic parameters were used to identify the most suitable substrates for time-resolved crystallography studies. Less suitable antibiotics were also identified and excluded for further TRX studies.

A very big advantage of these assays is that the influence of different reaction parameters can also be determined quickly. Having determined that the observed reaction had been too fast for current TRX methods, it was thus possible to find conditions where the reaction rate was slower. For ampicillin, for example, a reduction in the turnover rate k_{cat} by a factor of 5 was determined with a pH reduction from pH 7.4 to pH 3 (section 4.5.1). Furthermore, the turnover rate decreased by a factor of 2.5 when the temperature was reduced from 28 °C to 4 °C (section 4.5.2.).

Investigation of various antibiotics as potential substrates CTX-M-14 in TRX experiments revealed that ceftazidime was the slowest hydrolyzed antibiotic with a $k_{cat} = 0.9 \pm 0.2\ s^{-1}$. However, ceftazidime had the highest value for $K_m = 676 \pm 177$ µM among all antibiotics tested, which may imply a lower affinity for the enzyme. The K_m value is inversely related to the affinity of the enzyme for its substrate, as high K_m values result in the need for a higher

substrate concentration to achieve half v_{max}. Based on these findings, not only ceftazidime but also other antibiotics such as piperacillin (k_{cat} = 45 ± 2.0 s^{-1}; K_m = 10 ± 6.5 µM) were used for TRX experiments.

It has been shown that ceftazidime was indeed not suitable for TRX studies despite the low turnover rate. Even after lowering the pH, no electron density could be observed for ceftazidime in the active site of CTX-M-14 (section 4.6.1.3). With piperacillin, it has been possible for the first time to capture a time-resolved structure of the complex of a medically relevant antibiotic and functional wild-type serine β-lactamase (section 4.6.2.1).

Table 25: Kinetic parameter k_{cat} of CTX-M-14 with various substrates determined in this study compared with literature values.

Antibiotic	k_{cat} [s^{-1}] (this work)	k_{cat} [s^{-1}] (Dutour et al., 2002)	k_{cat} [s^{-1}] (Ishii et al., 2007)	k_{cat} [s^{-1}] (He et al., 2015)	k_{cat} [s^{-1}] (Tian et al., 2016)
ampicillin	49 ± 0.9	–	–	25 ± 2	197 ± 18
benzylpenicillin	254 ± 5.7	290	48 ± 3	–	–
cefalotin	565 ± 13.2	2700	510 ± 30	357 ± 18	1117 ± 254
cefdinir	2 ± 0.1	–	83 ± 3	–	–
cefepime	129 ± 13.1	–	N.D.	–	13 ± 1
cefotaxime	75 ± 2.6	415	1400 ± 180	37 ± 2	761 ± 149
ceftazidime	0.9 ± 0.2	3	n.d.	N.D.	0.9 ± 0.15
ceftriaxone	25 ± 0.8	–	–	42 ± 4	–
cefuroxime	96 ± 3.1	320	–	56 ± 3	–
piperacillin	45 ± 2.0	200	39 ± 3	–	–

N.D., not determined; n.d., not detectable

For the literature comparison of the kinetic parameters of this study with the values from 4 research articles, the focus was placed on k_{cat} as the crucial parameter for the reaction rate. Some of the values measured here differ greatly from those in some research articles. However, the k_{cat} values also differ greatly among those research articles referred to. For example, CTX-M-14 with cefotaxime showed k_{cat} values in the range of 37 – 1400 s^{-1}. Overall, the values measured here agree well with those from at least one article. For example, a k_{cat}

of 0.9 s^{-1} for ceftazidime was determined in this work. Exactly the same value was also determined in another article (He et al., 2015).

Nevertheless, the data obtained should be handled with care. The sometimes large differences in the kinetic parameters are probably due to different expression and purification methods of CTX-M-14 as well as different measurement methods. For example, Dutour et al. performed a pH titration measurement, while all others performed UV absorbance measurements to determine the kinetic parameters. UV absorbance measurements were performed in 50 mM phosphate buffer at pH 7 and 25 °C (He et al., 2015) or 30 °C (Ishii et al., 2007), whereas 20 mM MES buffer at pH 6 and 28 °C was used in this study.

Overall, it can be said that these measurements for determination of kinetic parameters can be performed in a variety of experimental setups. Therefore, it was even more important that the k_{cat} values were determined according to the conditions given in this study. In this way, protein expression and purification could be taken into account. Ultimately, the most important thing was to determine the differences between the various antibiotics, which was accomplished.

One of the reasons why a time-resolved crystallography analysis with ceftazidime was not possible despite the low k_{cat} could be the high K_m value. If the high K_m is due to a low affinity of ceftazidime to the active site of CTX-M-14, then it could mean that ceftazidime binds only slowly or at high concentrations to the β-lactamase but is then hydrolyzed very quickly. This would make a uniform distribution of ceftazidime in the active sites of the crystal nearly impossible.

However, the determined kinetic parameters served only as a reference, because in the crystalline environment the reactions may exhibit different reaction rates. Nevertheless, it could be shown how the determined kinetic parameters can be used to select suitable candidates for time-resolved crystallography studies. Adjusting the reaction rate by changing the environmental conditions did yield expected results and gave a better insight into the extent of the effects.

In addition, the proteasome inhibitors bortezomib and ixazomib were studied as part of a drug repurposing approach in search of new opportunities for the development of β-lactamase

inhibitors. Both drugs are used to treat multiple myeloma, a type of cancer of the white blood cells (Adams & Kauffman, 2004; Mina et al., 2021). Using cryo X-ray crystallography, it was demonstrated that bortezomib and ixazomib also bind to the catalytic Ser70 in the active site of CTX-M-14 β-lactamase (Perbandt et al., 2022). These findings suggest a possible inhibition of the β-lactamase. Therefore, the inhibitory effect of these proteasome inhibitors on CTX-M-14 was investigated by determination of IC_{50}. This revealed that bortezomib (68 ± 19 µM) and ixazomib (13 ± 2.4 µM) had an inhibitory effect, albeit much weaker compared with β-lactamase specific inhibitors such as avibactam (0.0034 ± 0.0003 µM).

The dual inhibition mode is not unexpected, as protease and β-lactamase enzymes share important key features in their catalytic mechanism. Although the proteasome inhibitors investigated here would have to be used at relatively high concentrations to achieve an inhibitory effect. In this case, however, the particularly strong side effects of the drugs would have to be taken into account. The already approved β-lactamase inhibitors have been developed in such a way that they achieve a higher affinity to the active site of the β-lactamase through various chemical groups and thus also exhibit better effects. For example, the anion binding site has been utilized, with many inhibitors having sulfate or carboxyl groups occupying this very site. Nevertheless, the boronic acid-based protease inhibitors discussed here are suitable as promising lead compounds.

5.2. Significance of the anion binding site

β-lactamases like CTX-M-14 have a crucial anion binding site adjacent to the active site as clearly indicated by a positive charged pocket (blue, Figure 41 A and B). In the native enzyme, this anion binding site is usually occupied by a tetrahedral anion, such as a phosphate (PDB 4ua6, Nichols et al. (2015)) or a sulfate (PDB 7q0z, Perbandt et al. (2022)). The anion binding site is always occupied in both cryoMX and SSX structures to balance the electrostatic requirements of the side chains of Lys73 and Lys234.

During the catalytic hydrolysis of β-lactam antibiotics, their carboxylate moiety is located in the anion binding site (Brown et al., 2020) as shown by the mutant variant CTX-M-14 E166A acyl-enzyme complex with ceftazidime (Figure 41 F, PDB 5u53, Patel et al. (2017)).

However, time-resolved experiments of this study have shown that the anion binding site is very important during the binding process. For example, when boric acid was bound, the sulfate was reoriented at this point to avoid steric conflicts. During the esterification process,

the sulfate was replaced by a water molecule because hydrogen bonding with GBE was not possible. GBE lacks the proton at O2 and cannot act as a hydrogen bond donor for the sulfate ion, while the water at this position is able to act as hydrogen bond donor for GBE. Thus, the possible hydrogen bonds in the anion binding site are an additional feature that can be used especially for ligand stability. Comparison of the surface charge of several inhibitors in the binding pocket of CTX-M-14 or related β-lactamases confirms this (Figure 41). Similar to BAB and GBE, the proteasome inhibitors bortezomib (PDB 7q0y) and ixazomib (PDB 7q11), which were investigated in a drug repurposing approach (Perbandt et al., 2022), do not have a moiety that occupies the anion binding site. However, a chloride ion is located there to balance the charge, as the sulfate ion would be too large to bind in presence of the covalently bound bortezomib and ixazomib. As mentioned in the previous section, the observed lower inhibitory effect on β-lactamases is probably due to the fact that the anion binding site is not utilized by bortezomib and ixazomib.

In contrast, in the recently approved diazabicyclooctane (DBO) inhibitors avibactam and relebactam, the sulfonate groups occupy the mentioned anion binding site (King et al., 2015; Perbandt et al., 2022). This characteristic molecular mimicry was also used for vaborbactam (PDB 6v7h, Pemberton et al. (2020)) and taniborbactam (PDB 6sp6, Liu et al. (2019)), as the carboxylate appendage occupies the same position (Figure 41 G and H). These groups were introduced during drug development to increase the stability and activity of inhibitors.

In summary, the displacement of the anion of the native enzyme (e.g., sulfate ion) is important for enzymatic hydrolysis, as it creates space for the carboxylate appendage of antibiotics. At the same time, this anion binding site can also be used for enhanced binding of inhibitors with a suitable group at the site.

This anion binding site thus represents an important property of the enzyme to be considered in drug development. In addition, the time course of the displacement of the sulfate ion was shown (section 4.6.1.5 and 4.6.1.6).

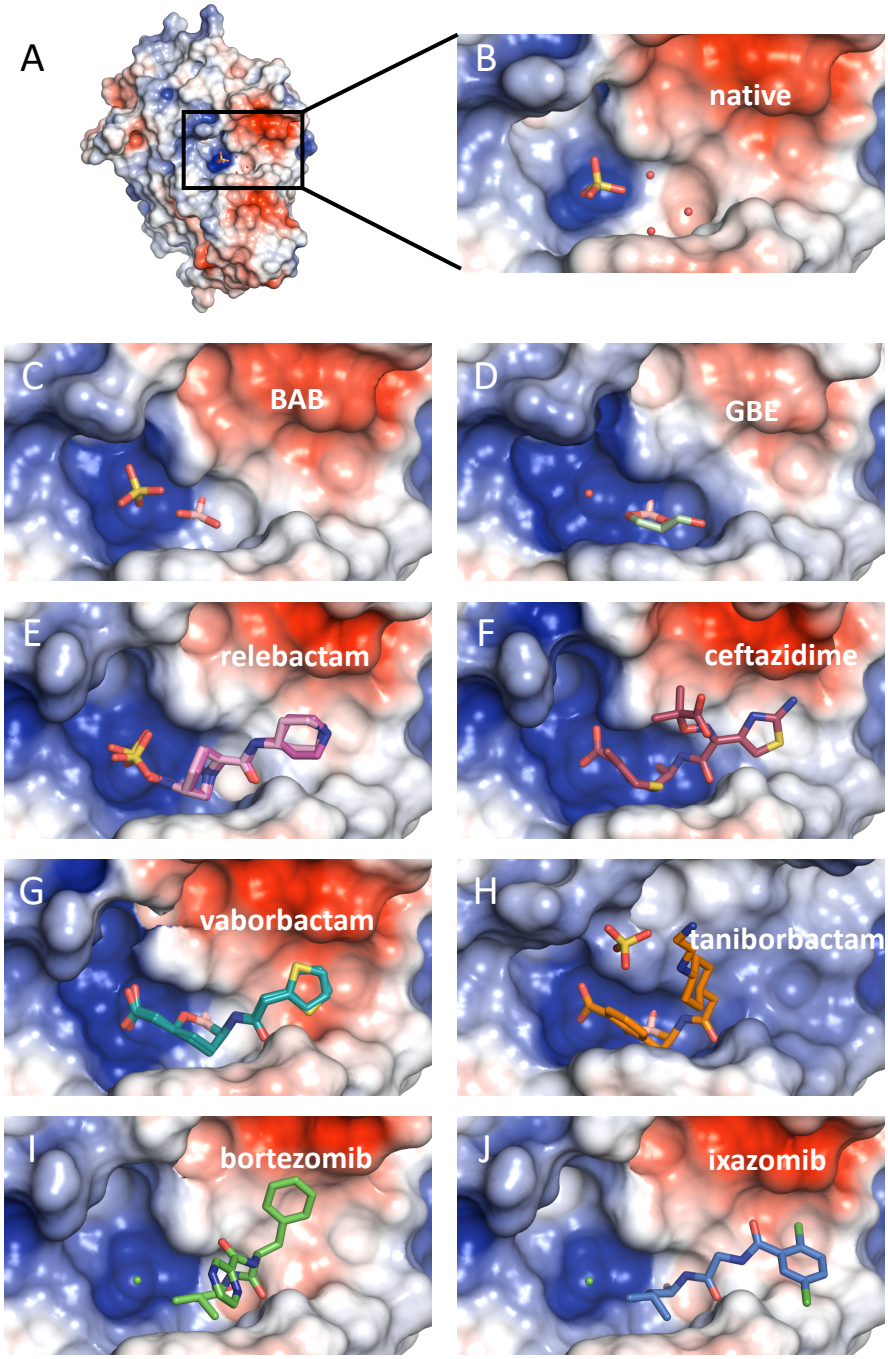

Figure 41: Electrostatic surface representation of β-lactamase active site with various inhibitors and substrates. (A) CTX-M-14 native enzyme overview**, (B)** CTX-M-14 native enzyme, **(C)** CTX-M-14 in complex with bound boric acid (BAB, pink/red), **(D)** CTX-M-14 in complex with bound glycerol boric acid ester (GBE, palegreen), **(E)** CTX-M-14 in complex with bound relebactam (pink), **(F)** CTX-M-14 E166A mutant variant in complex with bound ceftazidime (5u53, raspberry), **(G)** CTX-M-14 in complex with bound vaborbactam (6v7h, teal), **(H)** CTX-M-15 in complex with bound taniborbactam (6sp6, orange), **(I)** CTX-M-14 in complex with bound bortezomib (7q0y, green), **(J)** CTX-M-14 in complex with bound ixazomib (7q11, blue). Positively charged areas of the enzyme surface are displayed in blue and negatively charged areas in red. The binding pocket of CTX-M-14 forms a strong positively charged region which is used by negative charged groups of several inhibitors for stronger binding. The electrostatic surface representation is calculated and visualized by the APBS Electrostatics plugin in Pymol (Jurrus et al., 2018; Lerner & Carlson, 2006).

5.3. Relebactam binding modes in CTX-M β-lactamases

The first crystal structures of CTX-M-14 in complex with relebactam at room temperature and at cryogenic temperature were successfully solved and refined. In addition, the analysis of the time-resolved structures obtained with the CFEL TapeDrive showed the buildup of the polder electron density for the relebactam molecule. The DBO inhibitor was covalently bound in the active site after only 0.25 s with an occupancy of 77 %. To investigate the molecular basis for the inhibition of class A β-lactamases by relebactam, further analysis of the binding process by comparison with other relebactam structures is appropriate. Especially the CTX-M-15 structure in complex with relebactam (PDB 6qw8, Tooke et al. (2019b)) is very suitable for this purpose. The high sequence identity of 83 % (Figure S5) between CTX-M-15 and CTX-M-14 allows the comparison of the structures of these two enzymes (Figure 42).

All three studied structures reveal relebactam covalently attached to the nucleophilic Ser70. Binding to C7 of relebactam opens the ring and forms a carbamoyl enzyme complex as seen in previous DBO inhibitors (Blizzard et al., 2014; Ehmann et al., 2012). The remaining six-membered ring of the DBO scaffold adopts a chair conformation, as does the terminal piperidine ring. Most of the interactions of relebactam with the enzyme are similar in all three structures. Relebactam is positioned to form hydrogen bonds with Ser70 and Thr237 backbone amide groups (oxyanion hole), Asn132, Ser130 and with the anion binding site. In the anion binding site, differences in the binding mode of CTX-M-14 and CTX-M-15 are apparent. While the sulfate moieties of relebactam form hydrogen bonds with the side chains of Lys234, Thr235 and Ser237 in the CTX-M-14 structures, only Lys234 and Thr235 can form hydrogen bonds in CTX-M-15. In CTX-M-15, the distance of Ser237 side chain hydroxyl to relebactams sulfate moiety is too large, resulting in an indirect hydrogen bond via a water molecule (Figure 42 C).

The active sites of CTX-M-14 and CTX-M-15 differ significantly in the position of Asn104. Asn104, together with Asn132, coordinate the carbamide group of relebactam in the CTX-M-14 active site via hydrogen bonds. In CTX-M-15, only Asn132 forms such a hydrogen bond, as Asn104 is strongly rotated outward from the active site to avoid steric hindrance with relebactam (Figure 42 C). Tooke et al. (2019b) proposed that the flexibility of Asn104 is important for relebactam binding. However, it is shown here that this is not the case, as the identified CTX-M-14 structures (cryoMX and TapeDrive) do not show displacement of the Asn104 in any way compared to the native enzyme (Figure 18). One reason for these different

binding modes of CTX-M-14 and CTX-M-15 could be the interactions of the enzyme with the piperidine ring linked to C2 of relebactam. On the one hand, the Asn104 residue displaced in CTX-M-15 prevents steric conflicts, but on the other hand, it can act as a hydrogen bond acceptor to the piperidine amino group. However, both CTX-M-14 structures show completely different hydrogen bonds with the piperidine amino group. The amino acid residue 239 of CTX-M-14 is an aspartate (Gly239 in CTX-M-15) that forms indirect hydrogen bonds with the piperidine NH via a water molecule (Figure 42 A and E).

Piperidine prefers a chair conformation, of which there are two distinguishable chair conformations, one with the N-H bond in the axial position and the other in the equatorial position. The distinct conformations can be switched by ring or NH inversion (Anet & Yavari, 1977; Blackburne et al., 1975; Eom et al., 2020). However, the conformation with equatorial NH position is energetically preferred as measured by IR spectroscopy (Baldock & Katritzky, 1968). Thus, there is a free electron pair in axial position at the piperidine NH. This provides an ideal geometry to serve as a hydrogen bond acceptor for the respective water molecule. This water molecule is then in turn coordinated with the Asp239 via a hydrogen bond. Since the water molecules in the CTX-M-14 cryo and RT structures are in different positions, this also explains the twisted orientation of the piperidine ring in these two structures. Since CTX-M-15 has a Gly239 at the comparable position, it cannot form indirect hydrogen bonds to the relebactam. This probably makes it necessary for relebactam to displace Asn104 and form hydrogen bonds with it in CTX-M-15. Importantly, the positioning of the deacylating water appears to be little affected, although the relebactam binds somewhat differently. In all 3 structures, the hydrogen bonds of the deacylating water are preserved, and the distance for decarbamoylation is also almost unchanged (Figure 27 B,D,F). The deacylating water is activated by Glu166 as in the catalytic hydrolysis of β-lactam antibiotics and performs a nucleophilic attack on the carbamoyl carbon C7. However, as reported for other DBO inhibitors, there is another pathway for de-carbamoylation. It has been proposed that Lys73 serves as a general base for activation of Ser130 for avibactam recyclization (Lahiri et al., 2013). This may also apply here as Ser130 is in short hydrogen bond distance (2.8 – 3.0 Å) to N6 of relebactam and N6 in turn interacts closely with the carbamoyl carbon C7 (2.9 – 3.0 Å). In this position, relebactam is in a recyclization primed state that is in favor for recyclization of relebactam followed by release of the intact inhibitor. This results in the reversible inhibition mode of relebactam and other DBO inhibitors (Tooke et al., 2019b).

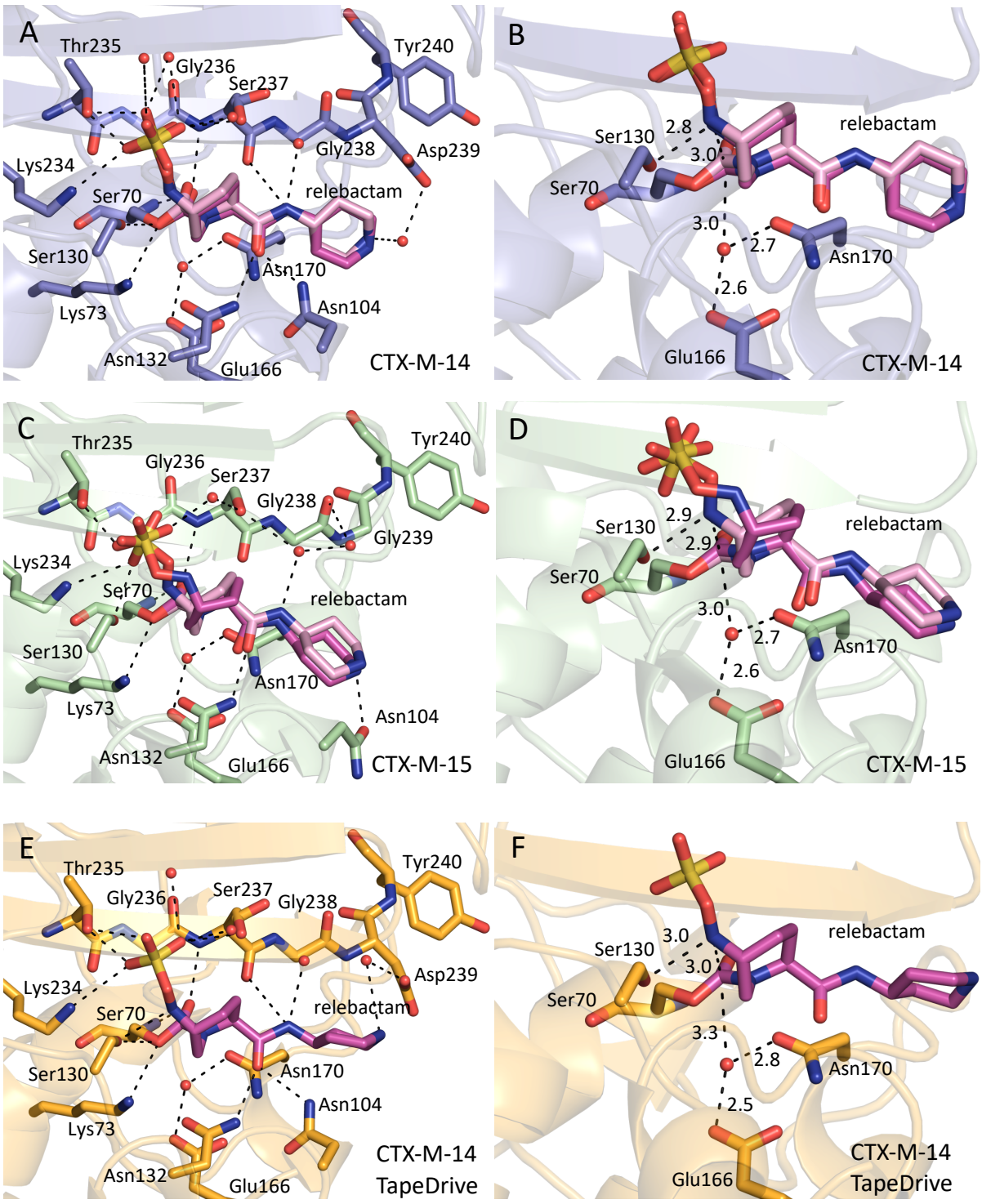

Figure 42: Comparison of CTX-M-14 (blue) and CTX-M-15 (green, PDB 6qw8, Tooke et al. (2019b)) active sites with covalently bound relebactam (magenta). Also shown is the RT structure of CTX-M-14 collected with the TapeDrive for comparison (orange, E and F). The polar contacts and the residue positions of CTX-M-14 (A), CTX-M-15 (C) and CTX-M-14 at room temperature (E) reveal differences in the binding mode of relebactam. Nevertheless, the position of the deacylating water molecule is the same in CTX-M-14 (B) and CTX-M-15 (D) cryoMX structures. Potential hydrogen bonds are depicted as black dashes with the atomic distance in Ångström.

5.4. Time-resolved boric acid binding and subsequent esterification

Boronate-based inhibitors are of particular interest as boron has the ability to mimic the tetrahedral transition state of the catalytic reaction mechanism of SBLs (Scheme 3) and can also inhibit some clinically important metallo-β-lactamases. In addition, the boronate-based inhibitors lack the β-lactam recognition motif and are chemically distinct enough to circumvent the resistance mechanisms that have already evolved (Eidam et al., 2010). In this study, It was observed that boric acid itself can play a versatile role for inhibition of β-lactamases, which also explains why boric acid-based compounds are currently of great interest in drug discovery (Hecker et al., 2015; Krajnc et al., 2019; Perbandt et al., 2022; Tooke et al., 2020).

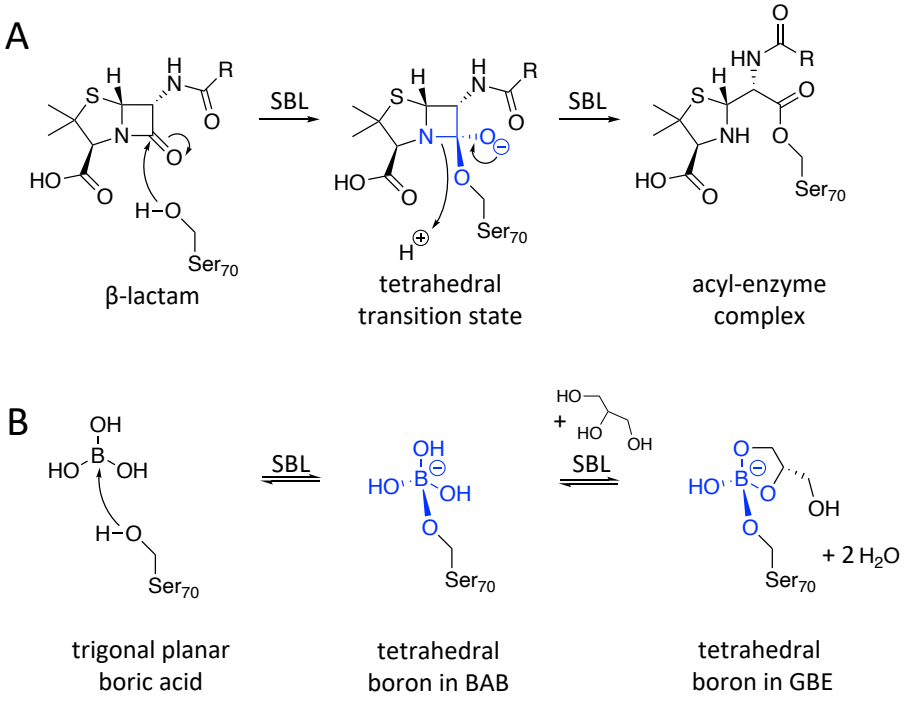

Scheme 3: Comparison of (A) the common tetrahedral transition state (colored blue) during β-lactam hydrolysis by serine β-lactamase and (B) the tetrahedral mimicry of bound boric acid and glycerol boronic acid ester. Boric acid is covalently bound to the catalytic serine resulting in the formation of a tetrahedral boronate, that mimics the tetrahedral transition state of a β-lactam. (Prester et al., 2023)

The inhibition of CTX-M-14 by boric acid was characterized by determining values for half maximal inhibitory concentration (IC_{50}) of 913 ± 324 µM. Compared to approved inhibitors such as avibactam (IC_{50} = 3.4 ± 0.3 nM), this value is too high to have an inhibitory effect in a practical use case. Effective inhibition can therefore only be achieved at very high boric acid

concentrations. This in turn would increase the likelihood of further undesirable side effects. Thus, boric acid must be modified to provide more potent inhibition. In addition to inhibition, it is essential that the inhibitor can also reach its target site. For example, development must consider the need to cross the outer membrane of Gram-negative bacteria. The already approved inhibitors vaborbactam (CTX-M-14 : IC_{50} = 0.11 ± 0.04 µM, Tsivkovski et al. (2020)) and taniborbactam (CTX-M-15 : IC_{50} = 0.01 µM, Liu et al. (2019)) show that it is possible to transform boric acid derivatives into a very effective inhibitor.

Even more impressive is that the active site of CTX-M-14 is nevertheless occupied by up to 53 % bound boric acid (BAB) in TapeDrive mix-and-diffuse experiments (see section 4.6.1.5). This is probably due to the very high final concentrations of 100 mM boric acid that were used. However, the concentration had to be so high to accelerate the diffusion into the crystal by a higher concentration gradient to achieve a more uniform distribution within the crystals.

A glycerol-boric acid ester (GBE) was formed by mixing glycerol to the boric acid-soaked CTX-M-14 microcrystals. As a result, a mixed state of bound BAB (21 %) and bound GBE (67 %) has formed. Taken together, the total occupancy of ligands covalently bound to the enzyme has increased from 53 % (mixing boric acid) to 88 % (Figure 33). Hence, the total occupancy of the active site has increased due to esterification. The addition of glycerol, which led to the formation of GBE, increased the affinity of the boric acid compound to the active site Ser70. While BAB alone only achieved a maximum occupancy of 53 %, GBE was able to reach 67 % after a mixing delay time of 10 s.

Since the binding of boric acid is an equilibrium reaction, it can also proceed in reverse. Unfortunately, the process of deacylation cannot be observed in the time-resolved structures of BAB or GBE, so only a hypothesis is possible. Similar to the deacylation of other β-lactam antibiotics, the deacylating wat10 is probably activated by Glu166 and performs a nucleophilic attack on the boron atom. Subsequently, the boric acid is released again.

The formed GBE was bonded to the already bound boric acid in two esterification steps. In the time-resolved structural analyses (Figure 32, section 4.6.1.6), it is unfortunately not possible to show unambiguously which ester bond is formed first on the basis of the observed electron density. The first sign of increased electron density in the polder map is at BAB O2 (nomenclature – Figure 43), but this does not necessarily mean that ester bonding occurs there first.

However, the probability of the first ester bond occurring at O2 is slightly higher, because the hydroxyl group of O2 is strongly stabilized by donating hydrogen bonds to the sulfate ion in the anion binding site. The second ester bond to form the cyclic ester then probably develops very quickly. The first ester bond greatly shortens the distance between the second hydroxyl group of glycerol and the boron atom. In addition, the glycerol molecule has less degrees of freedom.

Based on the time-resolved data, an equilibrium reaction equation (Scheme 4) for the binding of boric acid can be derived. The amino group of Lys73 is in hydrogen bond distance with Asn132 (2.5 Å) and Ser130 (3.2 Å) and possibly acts as hydrogen bond donor. Thus, it is possible to be hydrogen bond acceptor to the Ser70 (2.9 Å). At the same time, the catalytic water wat10 (coordinated by Glu166 and Asn170) is in a distance of 2.7 Å to the Ser70 OG and thus also suitable as a potential hydrogen bond acceptor. Unfortunately, the time-resolved structures cannot provide any conclusions about the protonation of the residues involved, so no more precise statement about the mechanism can be made.
However, one of these interactions makes Ser70 OG more nucleophilic. Catalysis is initiated by a nucleophilic attack of Ser70 OG on the boron atom. The nucleophilic attack is assisted by either Lys73 or Glu166 via wat10 acting as a general base and accepting the proton of the Ser70 hydroxyl group. This nucleophilic attack on the boron atom results in the formation of covalent bound boric acid (BAB).
The reaction sequence of boronic acid with a diol system is concluded from Furikado et al. (2014). Accordingly, the bound boric acid is present as a borate ion in the active site, which can also be observed by the electron density from time-resolved experiments (Figure 32). The glycerol can initiate the esterification with a nucleophilic attack on the boron atom and take the position of the O2 with the ester bond. The O2 of BAB is probably the first hydroxyl group to be subtracted, as it acts as a hydrogen bond donor for the sulfate ion in the anion binding site. During esterification a water molecule is released. Due to the resulting proximity of boric acid and glycerol, the second esterification step to cyclization likely occurs very rapidly. Basically, this second esterification step proceeds in the same way as the first.

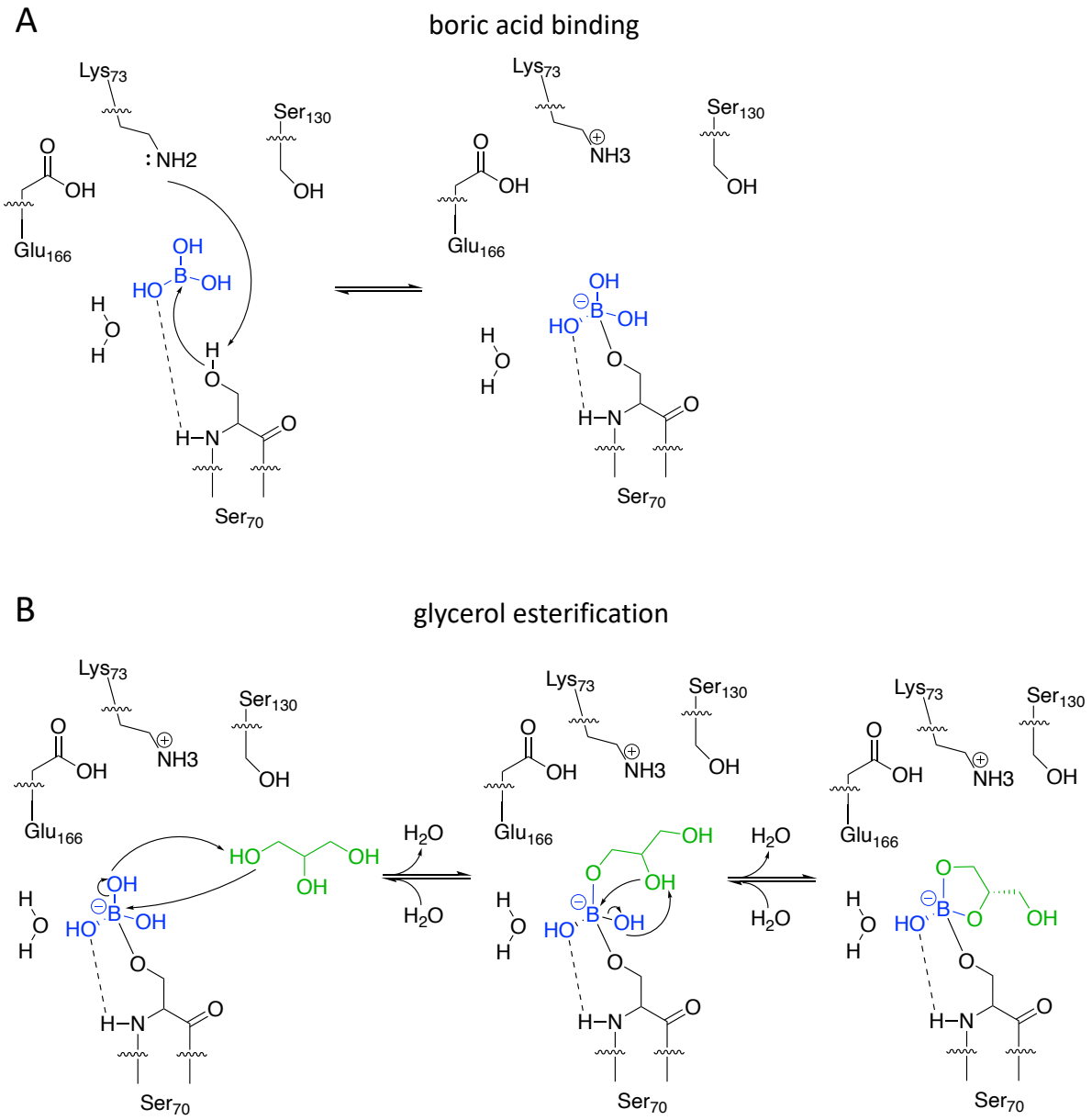

Scheme 4: Proposed reaction mechanism of (A) the binding process of boric acid (blue) to the active site serine of CTX-M-14 and (B) subsequent esterification of glycerol (green) to boric acid bound to CTX-M-14. (Prester et al., 2023)

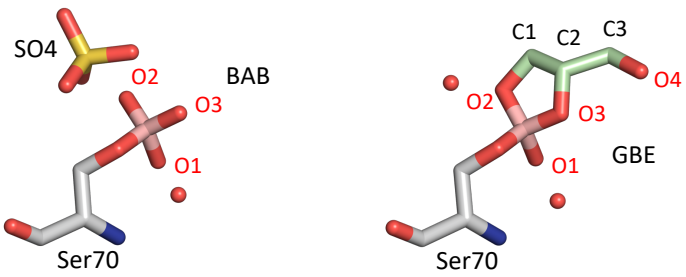

Figure 43: Nomenclature of BAB hydroxyl groups (left) and GBE hydroxyl groups and C-atoms (right).

The esterification of boric acid and glycerol to form a cyclic ester resulted in two new stereo centers at the C2 atom and the boron atom of GBE. According to the Cahn-Ingold-Prelog priority convention, both have (*S*)-configuration. The (*S*)-configuration of the boron atom is determined by the position of the initially bound boric acid. For C2, the (*S*)-enantiomer appears to be preferably formed due to the environment in the active site of the β-lactamase, as clearly indicated by the polder electron density (Figure 32). No electron density was observed for the position of a potential (*R*)-enantiomer.
It seems reasonable that no (*R*)-enantiomer is observed, since the (*R*)-configuration would lead to a collision of O4 with the Asn132 side chain (~ 1.6 Å) if the GBE position was otherwise unchanged. The GBE cannot circumvent this steric hindrance because it has too many constraints due to the strong coordination with hydrogen bonds in the anion binding site and the oxyanion hole. Moreover, the Asn132 acts as a hydrogen bond partner for the glycerol O4 and presumably provides the appropriate orientation already when the glycerol is approaching the active site. Therefore, it is likely that the Asn132 side chain forces the glycerol into the GBE (*S*)-configuration during the binding process.

Theoretically, the glycerol could also bind to the boric acid in such a way that the free hydroxyl group of the GBE would point to the anion binding site. In practice, however, this does not seem to be the case. On the one hand, the glycerol would then have to displace the sulfate/water from the anion binding site during the binding process, and on the other hand, the hydroxyl group of GBE in the anion binding site could only be stabilized by hydrogen bonds with the side chain of Ser237. This would result in the loss of interactions with the side chains of Asn104 and Asn132. Overall, fewer hydrogen bonds would be obtained with the active site of CTX-M-14. In contrast, in the observed position of the GBE, the free hydroxyl of GBE O4 can form hydrogen bonds with two side chains Asn104 and Asn132 and at the same time there is the possibility of stabilization via the water bridge of GBE O2 with wat357 in the anion binding site.

To prevent correlation between occupancies and *B*-factors during refinement, precautions were taken to ensure that the individual *B*-factors of each ligand in datasets of consecutive time points did not differ more than their Wilson *B*-factors or their average *B*-factors. The *B*-factors of the boron atoms are not unusually high even for the delay times with low

occupancies of the ligands (Figure 44). Variations in the boron atom *B*-factors at different delay times roughly correspond to the deviations of the average *B*-factors and Wilson *B*-factors. The *B*-factors of the boron atom at short delay times are slightly increased. However, the average *B*-factors are also elevated at exactly these times. Consequently, it can be assumed that the occupancy of the boron atom was calculated correctly. If the occupancy was calculated too high, the individual *B*-factors would increase to a greater extent than the average *B*-factors. Overall, the *B*-factors are in an acceptable range for room temperature protein structures and do not show any anomalies. However, they might indicate dynamic movement during binding processes, as they are increased at exactly the delay times when the binding occurs.

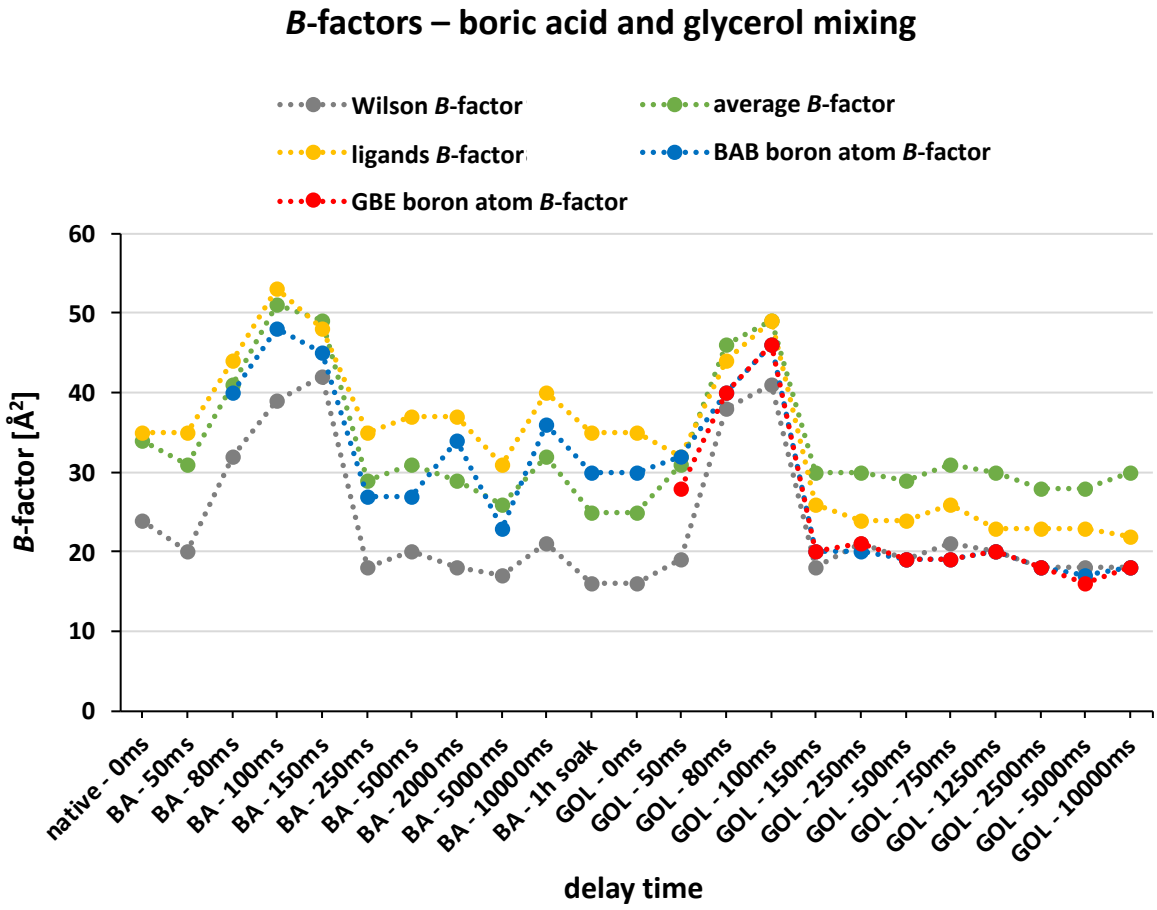

Figure 44: Diagram of various *B*-factors of bound boric acid (BAB) and glycerol boric acid ester (GBE) protein structures at the respective mixing delay times with boric acid (BA) or glycerol (GOL). The Wilson *B*-factor (gray), based on the collected data, and the average *B*-factor (green), based on the refined protein coordinates, show an equal trend as a function of the delay times. The ligands *B*-factors show the refined *B*-factors of all ligands, including the sulfates, whereas the BAB and GBE boron atom *B*-factors are intended to highlight only the boron atoms. Overall, it can be observed that all *B*-factors show a similar pattern and decent values for room temperature X-ray protein structures. Adapted from Prester et al., (2023).

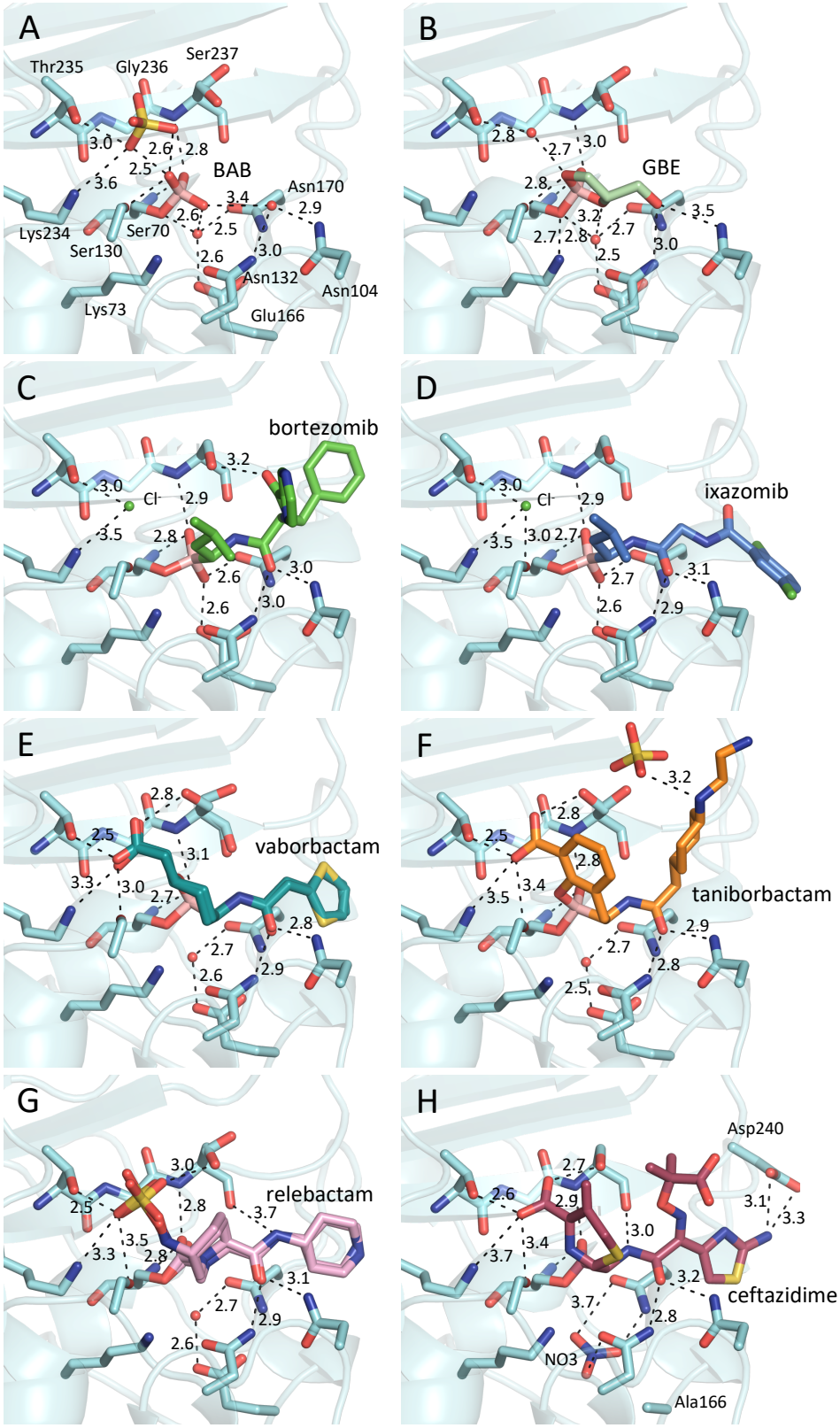

Figure 45: Comparison of β-lactamase active sites with various inhibitors and substrates for the analysis of advantageous features for consideration in the development of β-lactamase inhibitors. CTX-M-14 in complex with **(A)** bound boric acid (8pcj, BAB, pink/red), **(B)** bound glycerol boric acid ester (8pcv, GBE, palegreen), **(C)** bound bortezomib (7q0y, green), **(D)** bound ixazomib (7q11, blue), **(E)** bound vaborbactam (6v7h, teal). **(F)** CTX-M-15 in complex with bound taniborbactam (6sp6, orange), **(G)** CTX-M-14 in complex with bound relebactam (pink), **(H)** CTX-M-14 E166A mutant in complex with bound ceftazidime (5u53, raspberry).

In addition to the temporal analysis of binding events, the comparison of multiple inhibitors and substrates can be utilized for the development of new pharmaceutical substances. For example, beneficial properties can emerge from the analysis of multiple structures with various compounds. The following structures were used for this analysis: CTX-M-14 in complex with BAB (PDB 8pcj, Prester et al. (2023)), GBE (PDB 8pcv, Prester et al. (2023)), relebactam (this study), bortezomib (PDB 7q0y, Perbandt et al. (2022)), ixazomib (PDB 7q11, Perbandt et al. (2022)), vaborbactam (PDB 6v7h, Pemberton et al. (2020)), CTX-M-14 E166A mutant variant in complex with ceftazidime (PDB 5u53, Patel et al. (2017)) and CTX-M-15 in complex with taniborbactam (PDB 6sp6, Liu et al. (2019)). This includes simple boric acid compounds, cyclic boronate-based BLIs, diazabicyclooctane BLIs, boric acid-based proteasome inhibitors, and a β-lactamase substrate for analysis (Figure 45).

The structures are all very similar and have an RMSD value of only 0.27 – 0.31 Å when aligned against the CTX-M-14 native enzyme. Although CTX-M-15 belongs to the CTX-M-1 lineage group, it can still be compared to CTX-M-14 (CTX-M-9 lineage group) because they share a protein sequence identity of 83 % (Figure S5). The active sites of the β-lactamases contain highly conserved amino acids. However, it is striking that even the positional coordinates of these amino acids differ little in the various structures, although the ligands are very different (Figure 45). Only the side chain hydroxyl group of Ser237 adopts different rotamer configurations. In the structures with bortezomib, ixazomib and ceftazidime, Ser237 has only one position, whereas in the other structures it has two alternative positions. In most cases, this is one alternative position pointing towards the ligand to allow for possible hydrogen bond interactions and one alternative position pointing away from the ligand.

Analysis of the different inhibitors revealed that the following 4 features of the β-lactamase active site are particularly commonly used and therefore very important for binding in the active site of β-lactamases: the anion binding site, the oxyanion hole, the position of the deacylating water, and the coordination of a carbonyl oxygen by Asn104 and Asn132.

The oxyanion hole is a feature utilized by every compound studied here and is therefore one of the most important requirements to be considered in future drug development. In boric acid derivatives, it is occupied by a hydroxyl group of boric acid. In the case of relebactam, it is occupied by the carbamoyl group, and in the case of ceftazidime by the carbonyl group of

the ester bond. In the oxyanion hole, the inhibitors and substrates are stabilized by hydrogen bonds with the main chain amide groups of Ser70 (2.7 – 2.9 Å) and Ser237 (2.8 – 3.1 Å) (Figure 45). The stabilization in the oxyanion hole is so strong that the atoms coordinated in it are always at the same position with only 0.2 – 0.5 Å variance. In addition, the oxyanion hole is assumed to provide electrophilic assistance for the nucleophilic attack of Ser70 hydroxyl by stabilizing the carbonyl oxygen of, for example, β-lactam antibiotics in the oxyanion hole prior to acylation (Strynadka et al., 1992).

All approved β-lactamase inhibitors, relebactam, vaborbactam and taniborbactam, as well as the antibiotic ceftazidime utilize the anion binding site. They occupy the anion binding site with a sulfate or carboxylate group. Hydrogen bonds can then be formed with the side chains of Ser130, Lys234, Thr235 and Ser237. The strongest interactions involve Thr235 (2.5 – 3.0 Å) and Ser237 (2.7 – 3.0 Å) due to their relatively short hydrogen bond distance.
In the other structures, the anion binding site is also occupied, but not by the inhibitor itself. In bortezomib and ixazomib structures, it is occupied by a chloride ion from the buffer. The boric acid and glycerol boric acid ester structures studied in this work have a sulfate ion or a water molecule occupying this anion binding site. However, the compounds with a suitable moiety in the anion binding site develop much higher IC_{50} values and thus stronger inhibitory effects. It can be assumed that there is a clear advantage if the inhibitor compound itself can use this anion binding site for stabilization and displaces the previous anion. Indeed, if the anion cannot be displaced, then steric hindrance with this anion may occur and the position of the drug candidate might be altered. This important point could also be demonstrated in the time-resolved experiments of this work, as it was shown that the sulfate had to be reoriented during binding of boric acid. During the subsequent esterification with glycerol, the sulfate was finally displaced by a water molecule. Nevertheless, the glycerol boric acid ester could be stabilized via a hydrogen bond to this water molecule (wat 357, 2.7 Å) and another hydrogen bond from the water to Thr235 (2.8 Å) (Figure 45 B).

The catalytic water is coordinated by the side chains of Glu166 and Asn170 and occupies a position approximately 3.0 – 3.5 Å away from the boron atom or carbonyl carbon of the acyl-enzyme (Figure 45). The catalytic water is then activated by Glu166 and can perform a nucleophilic attack on the boron atom or carbonyl carbon of the acyl-enzyme and thus release

the hydrolyzed ligand. This process cannot occur in the CTX-M-14 E166A mutant variant, where Glu166 is not present for coordination of the deacylating water. Bortezomib and ixazomib are the only inhibitors that displace this deacylating water, since a hydroxyl group of the conjugated boric acid occupies exactly this position (Figure 45 C and D).
The boric acid moiety of bortezomib and ixazomib takes a slightly more downward position than the other boric acid compounds. These two proteasome inhibitors thus use the position of the deacylating water to get the stabilizing interactions with Glu166 and Asn170 and displace the deacylating water. All other inhibitors hardly changed the position of the deacylating water. Therefore, the question arises why bortezomib and ixazomib are not much more potent inhibitors since they are not hydrolyzed or are hydrolyzed by a different pathway. For the efficacy of an inhibitor, not only the stability in the active site of the target is crucial, but also the affinity and many more factors.

The side chain amide groups of Asn104 (2.8 – 3.2 Å) and Asn132 (2.8 – 3.0 Å) act as hydrogen bond donors for specific carbonyl groups of all inhibitors and substrates (Figure 45 C – H). Thus, they are among the few stabilizing interactions used by all inhibitors. In the case of the GBE, these hydrogen bonds are formed with the terminal hydroxyl group at O4 (weak 3.5 Å and 3.0 Å) (Figure 45 B). BAB is not directly stabilized by these asparagine residues, but via a water bridge to the BAB O3 hydroxyl group (2.9 Å and 3.4 Å) (Figure 45 A). In the development of new drugs, a potential hydrogen bond acceptor should be considered at this point.

Asp239, located at the exit of the active site, also appears to be important for large ligands. For example, the Asp239 carboxyl group can form hydrogen bonds with the amino thiazole moiety of ceftazidime (3.1 Å and 3.3 Å). However, it cannot be conclusively said how crucial this interaction is, since this direct interaction is only adapted by one of the ligands studied. However, relebactam also forms an interaction via a water bridge to Asp239 in CTX-M-14.

In summary, the following features should be considered in future drug design: A hydrogen bond acceptor such as a carbonyl oxygen adjacent to the atom to be acylated so that it can utilize the oxyanion hole, a negatively charged group that can be coordinated in the anion binding site, a polar group that displaces the deacylating water, and a hydrogen bond acceptor coordinated by hydrogen bonds with Asn104 and Asn132.

It should be noted that all these predictions are based on inhibitors that are already working. Of course, it is also possible that other very important features remain undiscovered and may be even stronger. For further development of β-lactamase inhibitors, it is exactly these features that have not yet been exploited that would be very important.
However, it would be important to look at even more β-lactamase substrates in the wild type active site in order to derive important key features from them as well. Time-resolved SSX is particularly well suited for this purpose.

5.5. Ceftazidime binding mode in CTX-M-14

Unfortunately, the SSX mixing experiments with CTX-M-14 and ceftazidime (CAZ) did not lead to the formation of a corresponding complex structure. Until recently, it was only possible to capture antibiotic complexes with CTX-M-14 mutant variants in which deacylation and thus catalytic hydrolysis was prevented by specific mutation of catalytic key residues Ser70, Lys73 or Glu166 (Adamski et al., 2015; Brown et al., 2020; Patel et al., 2018; Patel et al., 2017; Soeung et al., 2020).
As already shown in section 4.6.1.3, there are no differences between the CTX-M-14 native structure and structures mixed with ceftazidime. Fortunately, there is already a CTX-M-14 E166A mutant variant structure in complex with ceftazidime (PDB 5u53, Patel et al. (2017)) that can be used for structural comparison (Figure 46 A). This mutant variant lacks Glu166, which positions the deacylating water for nucleophilic attack and subsequent deacylation. The structure indicates that ceftazidime could in principle bind in the active site of CTX-M-14. However, the electron density for the pyridinium moiety at the C3 position of ceftazidime is absent even in the mutant variant (PDB 5u53, Patel et al. (2017)), indicating elimination of this group, which is consistent with the observations in other mutant variant acyl-enzyme complexes with serine-β-lactamases (Powers et al., 2001; Tooke et al., 2021).
If the CAZ in the CTX-M-14 WT structures is bound with only a very small occupancy, interpretation of the electron density would be difficult. To be sure that CAZ did not bind, the CAZ molecule was modeled into the TapeDrive CTX-M-14 WT mixed with ceftazidime structure (Figure 46 C) and compared with the water molecules (Figure 46 D). The corresponding polder electron density of the CAZ molecule of 5u53 and the CTX-M-14 WT structure differ significantly. In CTX-M-14 there is almost no coverage of the CAZ. In contrast, the modeled water molecules indicate a very good representation of the native active site (Figure 46 D).

Thus, it can be further clarified that ceftazidime did not bind to CTX-M-14 WT in the mix-and-diffuse SSX experiments.

It can be assumed that ceftazidime indeed binds poorly to CTX-M-14. As a result, it cannot accumulate in the intact WT enzyme and dissociates from the active site immediately after hydrolysis. Crystals of the 5u53 structure were soaked in 50 mM ceftazidime overnight. The high ceftazidime concentration and the fact that ceftazidime can accumulate in the active site due to the deacylation defective enzyme have ensured that such a complex could be acquired. This advantage, of course, does not exist with the WT enzymes in the SSX experiments. The aim was to observe the catalytic mechanism in the intact enzyme.

Studies by Patel et al. (2017) have shown that ceftazidime binding in the E166A is not as good as in the E166A/P167S variant. This is due to fewer hydrogen bonds and van der Waals contacts between bound ceftazidime and the E166A enzyme. This is also believed to be the reason for the higher K_m value of WT versus P167S variants. Overall, the catalytic efficiency (k_{cat}/K_m) of the WT enzyme is 10-fold lower than that of the P167S variant (Patel et al., 2017). The P167S is a natural mutation that is located in the Ω-loop near the active site. Due to the exchange of the proline residue, this Ω-loop acquires increased flexibility, so that the ceftazidime molecule has more space in the active site and can form more hydrogen bond contacts (Patel et al., 2017). This is also believed to be the reason for the extended-spectrum activity of this CTX-M-14 P167S β-lactamase (Both et al., 2017).

For the time-resolved structures performed here, this means that, as already suspected, the affinity of ceftazidime for the CTX-M-14 WT active site is probably too low to perform these types of studies. A possible alternative would be to use the P167S mutant for time-resolved SSX experiments, which provides more space and hydrogen bond contacts for the ceftazidime due to the flexible Ω-loop. However, it should be noted that the turnover rate of the P167S mutant must not be too high, otherwise the current fastest delay times may not be sufficient to capture important intermediate states.

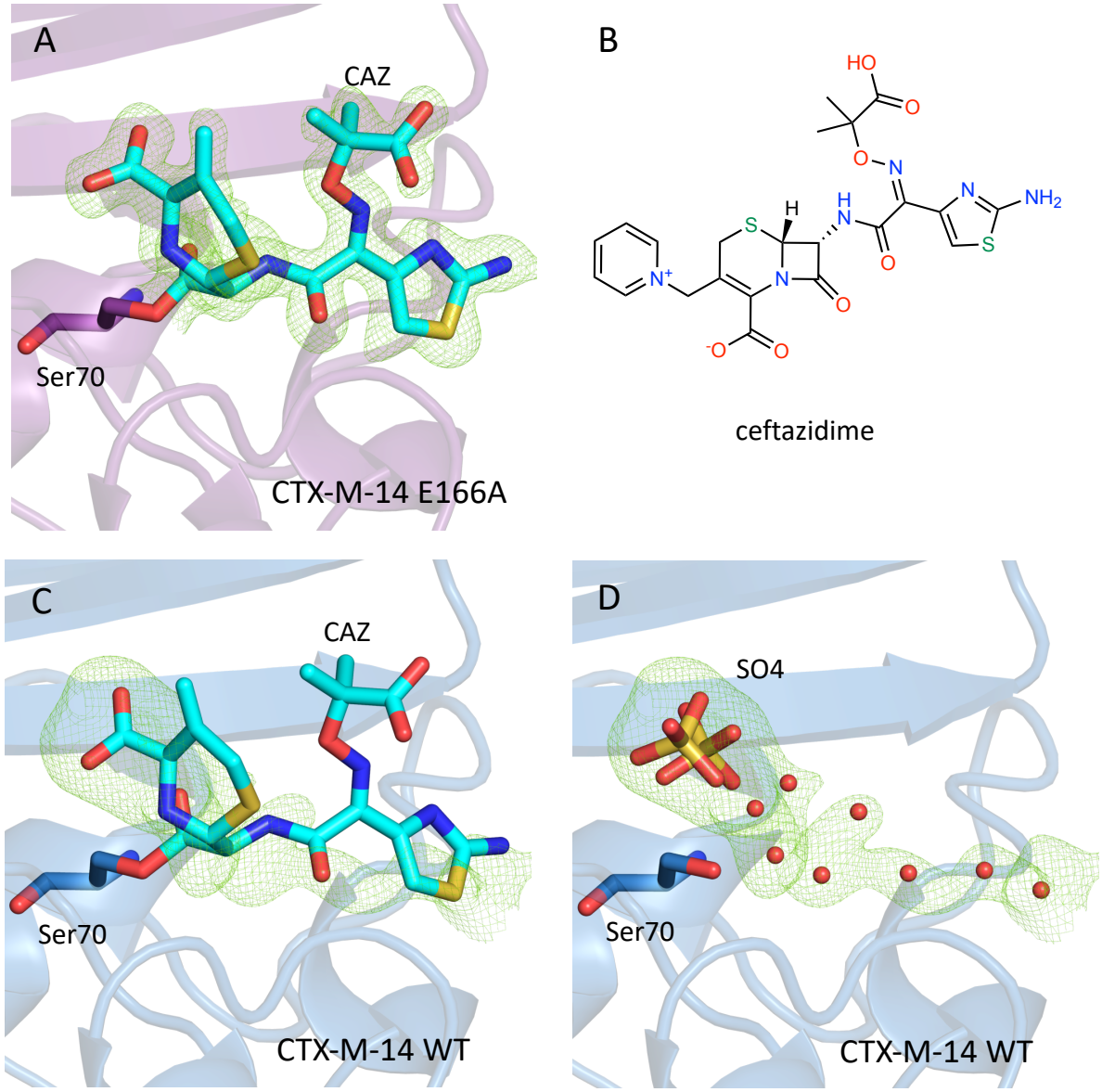

Figure 46: (A) CTX-M-14 E166A (PDB 5u53, Patel et al. (2017)) acyl-enzyme complex with ceftazidime (CAZ) compared to (C) TapeDrive CTX-M-14 WT structures mixed with ceftazidime with modeled CAZ or (D) water molecules in the active site. Corresponding polder electron density is contoured at 3 σ. The polder electron density clearly confirms the absence of CAZ in the active site of CTX-M-14 WT. Modeled water molecules fit better into the polder electron density. Chemical structure of the intact ceftazidime is shown for reference (B).

5.6. Time-resolved analysis of piperacillin hydrolysis by CTX-M-14

Time-resolved analysis of the hydrolysis of a β-lactam antibiotic like piperacillin, used in clinical contexts, by one of the most widely spread β-lactamases CTX-M-14 can provide important insight into antibiotic resistance mechanisms. Three main goals of any time-resolved crystallography experiment are to determine the physical properties such as the atomic structure of the intermediate states, the time-dependent concentration of these intermediate states and the rate coefficients of the kinetic reaction (Schmidt, 2013). In section 4.6.2.1, the time-resolved crystallography protein structures were already discussed and the main differences during the reaction were mentioned. However, the time-resolved analysis of this reaction can also help to better understand enzyme-catalyzed reactions in general.

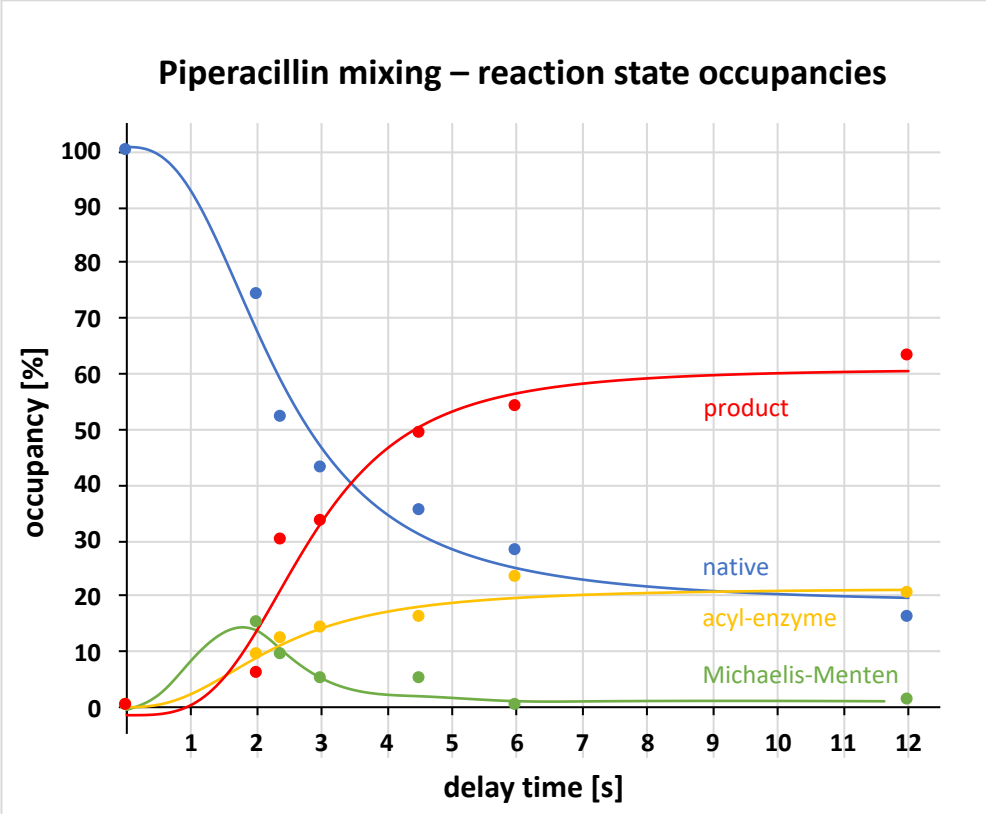

Figure 47: Diagram showing the occupancy of the individual states as a function of the delay times. Occupancies were refined using phenix.refine software with grouped molecules and alternative conformations that represent the individual states.

To generate an approximate overview of the relative concentrations of the reaction states, the occupancies of these states within the crystal can be extracted from the time-resolved protein structures. A plot of occupancies as a function of the delay time based on the values of Table 24 is shown in Figure 47. For the enzymatic reaction, the kinetic mechanism from

Equation 6 is again applied. In this reaction consideration, it must be taken into account that new substrate is supplied to the protein crystal by diffusion from the surrounding solution over a longer period of time. The native, the Michaelis-Menten, the acyl-enzyme and the product complex states are considered as possible observable states.

The reaction starts with a delay time of 0 s. At this point, no piperacillin state is present, only the native state with an occupancy of 100 %. Low occupancies of the other states are observed as early as 2 s, most notably the Michaelis-Menten state with non-covalently bound piperacillin with an occupancy of 15 %. At the same time, native state occupancy begins to decrease to 74 %. Subsequently, the occupancy of the product state increases the most and rises via 30 % at 2.4 s and via 49 % at 4.5 s to the maximum of 63 % at 12 s. The occupancy of the Michaelis-Menten state quickly decreases and from 6 s onwards has hardly any occupancy. This indicates that the acylation process (transition from Michaelis-Menten state to acyl-enzyme) is relatively fast and the rate k_3 (Equation 6) is high, while the binding of piperacillin is comparably slower. As a result, the piperacillin cannot accumulate in the Michaelis-Menten state but continues to be acylated directly. The acyl-enzyme state, on the other hand, can accumulate with an occupancy of 20 % at 12 s. This indicates that the deacylation process is somewhat slower than the acylation process.
A certain time after the start of the reaction, a quasi-steady state is established, as new piperacillin is added via diffusion from the solution and the hydrolyzed piperacilloic acid in the product complex is released from the enzyme at a constant rate. This point is approached at 6 s and is finally reached at 12 s. At this delay time, there is only a modest change in the occupancies observed.

The progression of the diagram is comparable to a diagram in a publication by Marius Schmidt (2013), in which a simulation was made of the enzymatic reaction of a kinetic mechanism with 3 observable states. It looks similar to a reaction whose turnover time is much faster than the diffusion time. Overall, however, it looks like the enzymatic reaction is relatively slow, especially compared to the kinetic parameters obtained in solution (section 4.5 and 5.1). In the crystal, a turnover seems to take place in seconds, whereas in solution only 22 ms (k_{cat} = 45 ± 2 s^{-1}) were determined. However, diffusion alone is unlikely to be the determining factor, since a diffusion time of approx. 15 ms was calculated for crystals of this size (Schmidt,

2013), which is in the same order of magnitude as the turnover time in solution. Apparently, enzymatic reactions in a crystal are much slower than in solution, possibly due to conformational space limitations, unfavorable buffer conditions, and to some extent slower diffusion times.

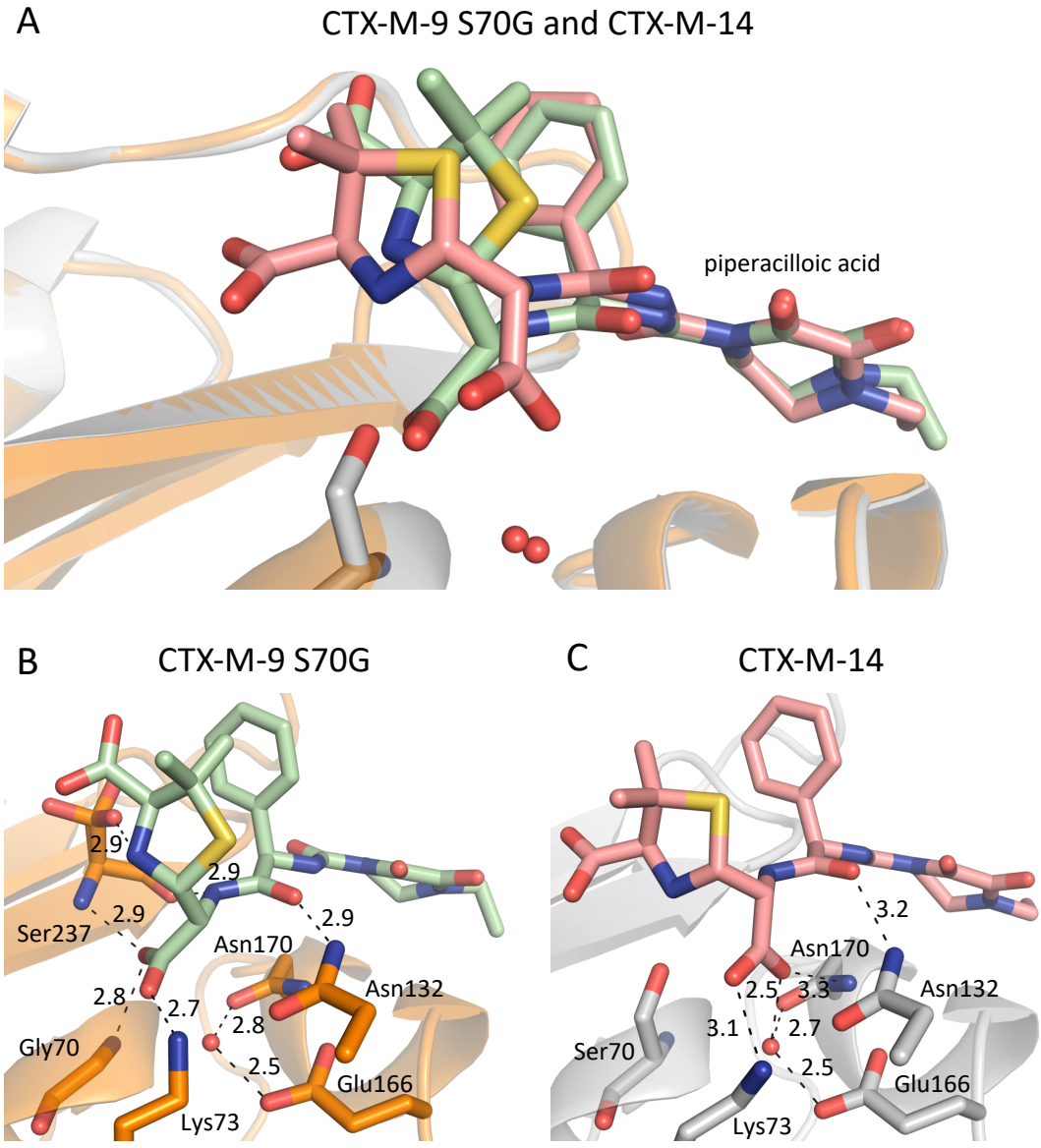

Figure 48: CTX-M-14 product complex with hydrolyzed piperacilloic acid and CTX-M-9 S70G (PDB 3q1f) mutant variant in complex with hydrolyzed piperacilloic acid (A) merged in one figure for comparison and separate with (B) only the CTX-M-9 S70G and (C) only CTX-M14 structures for detailed analysis of polar contacts. Potential hydrogen bonds are depicted as black dashes with the atomic distance in Ångström. Obviously, the carboxylate formed by hydrolysis of piperacillin at C7 and the five-membered thiazolidine ring occupy different positions. The carboxylate group of CTX-M-9 S70G occupies a position that is only possible with the S70G mutation and thus represents an engineered artifact. The mutant variant protein structure is therefore not very reliable for making conclusions about the wild type.

Usually, inactive mutant variants of β-lactamases were used to obtain a protein crystal structure in complex with a substrate. This is also the case with piperacillin. There are only two entries of a β-lactamase cryo structure in complex with piperacillin in the PDB. Both times it is an inactive CTX-M-9 S70G mutant variant. One protein crystal structure shows it in complex with the substrate piperacillin and the hydrolyzed product, piperacilloic acid (PDB 3q07), but with not very good electron density for the ligands. The second protein crystal structure shows the CTX-M-9 S70G mutant variant in complex only with the hydrolyzed product, piperacilloic acid (PDB 3q1f), which is well covered in difference electron density. Both structures are deposited in the PDB but without a corresponding publication. The latter is used for comparison with the CTX-M-14 piperacilloic acid protein structure (12 s time point) determined in this work to evaluate conclusions about the quality, reliability, and accuracy of the time-resolved structures. CTX-M-9 has very high sequence identity (99.62 %; Supplemental Figure S6) to CTX-M-14 and both enzymes belong to the same CTX-M-9 lineage group, therefore they can be compared with respect to piperacillin binding.
When merging the protein structures into one figure (Figure 48), it is immediately apparent that the ligands are positioned differently in the active site. This is especially the case for the carboxylate formed by hydrolysis of piperacillin at C7 and the five-membered thiazolidine ring.

It is particularly noticeable that the position of the carboxylate group of CTX-M-9 S70G (PDB 3q1f) would overlap with the Ser70 hydroxyl group in the wildtype enzyme. Therefore, the carboxylate group can only occupy this position in the S70G mutant variant and thus this represents an engineered artifact. The protein structure of the mutant variant is consequently not reliable for drawing conclusions about the enzymatic reaction mechanism or binding modes. In addition, the rotation of the carboxylate group out of the oxyanion and the rotation of the Ser70 in the direction of the oxyanion as described in section 4.6.2.1 is completely overlooked. This shows one of the biggest advantages of time-resolved crystallography, which allows the accurate observation of the wild type enzyme function and dynamics without the need of mutation variants. Therefore, these novel methods should be considered for complementation with existing mutation studies to avoid misinterpretation and thus incorrect depiction of the binding mode or reaction mechanism.

Furthermore, these different positions also result in different hydrogen bonding patterns, which represent a leaving group with a vastly different impact. The hydrogen bonding pattern of CTX-M-14 active site residues in complex with piperacilloic acid (12 s) has already been described in detail in section 4.6.2.1 (Figure 40). The major differences are that the C7 carboxylate group does not form a hydrogen bond with the catalytic water wat10 and the Asn170 side chain in CTX-M-9 S70G. Instead, this carboxylate group is located in the oxyanion hole with one of the oxygen atoms and therefore forms hydrogen bonds with main chain nitrogen atoms of Gly70 (2.8 Å) and Ser237 (2.9 Å) (Figure 48). Moreover, the hydrogen bonds of the C3 carboxylate group with Lys234, Thr235, Ser237 are lost due to the rotation of the thiazolidine ring and are not replaced by other hydrogen bonds. The nitrogen atom of the thiazolidine ring can form a hydrogen bond with the hydroxyl group of Ser237 (2.9 Å) in the CTX-M-9 S70G structure. In addition, the piperacilloic acid N14 forms a hydrogen bond with the main chain carbonyl oxygen of Ser237 (2.9 Å).

6. Conclusion and Outlook

6.1. Time-resolved crystallography

In this work, 4 novel methods were used for the determination of time-resolved protein structures. Mainly, the TapeDrive with mix-and-diffuse for the study of inhibitor and inhibitor model systems. This included contributing to the further development and testing of these methods for new end users (Zielinski et al., 2022). In addition, the fixed target approach using HARE chips and the liquid-application-method (LAMA) for reaction initiation was employed for the analysis of β-lactamase substrate hydrolysis. Two other methods applied have not been mentioned here so far:

Initial experiments with a liquid jet mix-and-inject approach were performed at the Linac Coherent Light Source (LCLS) using the X-ray free electron laser (XFEL). The aim was to investigate the binding and hydrolysis of ceftazidime by CTX-M-14 at fast time scales. Due to the pandemic-related travel restrictions in the USA in 2020, the experiments had to be performed remotely. In addition, due to difficulties with customs and transport of the microcrystals, antibiotics and injector nozzles, the experiments could not be performed

optimally. This resulted in data collection being limited to fewer time points than planned. Unfortunately, no electron density was observed for the substrate.

Furthermore, I collaborated on the development of a system to simplify time-resolved crystallography and make it more accessible to the large user base that already has access to standard macromolecular crystallography at synchrotron beamlines. This resulted in the creation of the spitrobot, a protein crystal plunger, enabling reaction quenching from physiological temperatures via cryo-trapping with millisecond time-resolution (Mehrabi et al., 2023). It uses micro meshes on SPINE standard sample holders suitable for automatic sample changing systems available at most modern beamlines. The protein crystals are placed on the micro meshes and sprayed with picoliter-sized droplets of the substrate using a LAMA nozzle to initiate the reaction. The crystals are then automatically immersed in liquid nitrogen with a specified delay time (up to 50 ms). Diffraction data for samples prepared in this way can be collected on standard cryoMX beamlines. In this case, CTX-M-14 was used as a model system to demonstrate that the system performs well.

With all the mentioned methods, time-resolved structures could be determined. What they all had in common was the overlapping of multiple states at a single time point. As in any time-resolved experiment, multiple states can mix at a single time point during the reaction (Schmidt et al., 2023; Steinfeld et al., 1999). This is due to the nature of diffusion, since not all active centers in the crystal can be reached simultaneously. This effect can be reduced by using small microcrystals (Schmidt, 2013). With the increasing accessibility of X-ray free-electron laser (XFEL) facilities with extremely brilliant and short pulsed radiation, smaller crystals can be used to obtain sufficient diffraction. This can further shorten the diffusion time and minimize the overlap of multiple states. Laser-triggered reactions with photocaged substrates are easier to handle in this respect, since the substrates can already be uniformly distributed in the crystal before reaction initiation. However, other factors such as the depth of penetration of the laser into the crystal must then be considered.

Nevertheless, reaction initiation by mix-and-diffuse is one of the methods suitable for most enzymatically catalyzed reactions, since photocaged compounds or photochemical reactions are rarely available.

The CFEL TapeDrive is also ideally suited for a rapid high-throughput screen of different compounds whose binding to a target enzyme is to be investigated on a crystallographic basis.

Mixtures with several compounds were investigated, demonstrating that only the best binding ligand is actually visible in the active site of the β-lactamase in the resulting model.
Substrates that have a high affinity for the active site but are slowly converted are beneficial. The hydrolysis of ceftazidime, for example, probably could not be observed because its K_m is relatively high and the affinity for the active site is probably relatively low. With piperacillin, on the other hand, it was possible to observe intermediates, although it has a higher turnover rate.
TRX is particularly important to observe interactions of ligands in the wild-type enzyme. Since mutations can be avoided, no artifacts introduced by these mutations will give a false representation of the protein-ligand interactions. For example, it was shown that the position of a carboxylate group of the hydrolyzed piperacillin in the wild type is quite different from that in the mutant variant. In this case, it was easy to observe that the position in the mutant variant was "wrong", as it could not be present in the wild type due to steric hindrance. Only the absence of the catalytic serine side chain due to the S70G mutation enabled this position. Essentially, the combination of room temperature TRX and cryoMX structures provides huge advantages. While cryoMX can currently achieve much higher resolutions, the room temperature TRX data can provide information about the dynamics and conformational space of the protein residues, as has been observed with the dynamic of the piperidine ring of relebactam (section 4.6.1.4).

The serial crystallography and macromolecular crystallography methods differ with respect to possible radiation damage during data collection. Since for the cryoMX method only a single macrocrystal is measured repeatedly in a rotation series, it is exposed to a higher radiation dose. Therefore, it is cooled to cryogenic temperatures to avoid this radiation damage. However, this decouples global and specific radiation damage. While the global radiation damage is reduced, the specific radiation damage affecting certain amino acid residues is not reduced by the same amount (Gotthard et al., 2019). In serial crystallography, on the other hand, the microcrystals are measured only once, so that protection against radiation damage can be omitted and experiments are performed at room temperature. For serial femtosecond crystallography using XFELs the principle of diffraction-before-destruction is applied. The microcrystals are exposed to a very intense and short X-ray pulse, allowing to collect diffraction data before the crystal is destroyed.

The accessibility of TRX measurements has greatly improved in recent years. However, evaluation is currently still very difficult, especially if no allosteric effects or large conformational changes are observed, because then very small differences have to be identified and interpreted. Evaluation can be facilitated, for example, by the use of specialized software such as Xtrapol8 (De Zitter et al., 2022), PanDAA (Pan-Dataset Density Analysis) (Pearce & Gros, 2021) or RoPe (Representation of Protein Entities) (Ginn, 2023). These software packages allow a better differentiation of ligands with very low occupancies or use the torsion angles to describe a proteins conformational space. However, it also requires training and was not suitable for the size of the dataset or not available at the time of the evaluations conducted in this thesis.

Finally, additional parameters such as temperature or the pH value can be varied to achieve more observables. In this way, five-dimensional crystallography is possible and the energetics of the reaction can be investigated. These include entropy and enthalpy values of the activation barriers in the chemical and kinetic mechanism, which enables the determination of free energy landscapes of the enzymatic reaction (Schmidt, 2013). Such experiments are already being conducted with the CTX-M-14 β-lactamase and piperacillin using the environmental control box (Mehrabi et al., 2021).

6.2. Important characteristics for β-lactamase inhibitors

Developing new antibiotics is difficult and expensive. On the one hand, they obviously must exhibit antibacterial activity against a broad spectrum of bacterial organisms, must not be susceptible to current resistance mechanisms, and must be tolerated by the patient. In the following, particular attention will be given to β-lactam antibiotics, as they are relevant to this thesis. Basically, a β-lactam antibiotic must bind as effectively as possible to penicillin binding proteins (PBP) and thus unfold its antibacterial effect, while at the same time being a poor substrate for β-lactamases. As mentioned in section 1.4, β-lactamases represent the most common resistance mechanism to β-lactam antibiotics. Therefore, it is reasonable to develop β-lactamase inhibitors that allow already approved antibiotics (to which resistance has already emerged) to be reused in a combined drug.

A comprehensive review of current inhibitors of serine β-lactamases and the observed time-resolved binding of inhibitors as well as inhibitor models revealed important characteristics for β-lactamase inhibitors. In summary, the following features should be considered in future

drug design: A hydrogen bond acceptor such as a carbonyl oxygen adjacent to the atom to be acylated so that it can utilize the oxyanion hole, a negatively charged group that can be coordinated in the anion binding site, a polar group that displaces the deacylating water, and a hydrogen bond acceptor coordinated by hydrogen bonds with Asn104 and Asn132.

This information could be used as it has been for other systems such as in "metallo-β-lactamase inhibitors inspired on snapshots from the catalytic mechanism" (Palacios et al., 2020). In this article, the potential of intermediates and product mimicking compounds for inhibition of metallo-β-lactamases was evaluated. Using the intermediates and tetrahedral transition state mimics described in this thesis, such a study can also be applied to serine β-lactamases.

There are already many approaches that use structure-based drug discovery (Fischer et al., 2021; S Ferreira & D Andricopulo, 2014; Shi et al., 2019; Staker et al., 2015). Accordingly, of course, all the available knowledge about the structural conditions is already used. Among other things, information about which conditions are necessary for binding, how large the binding pocket is, how polar/hydrophobic the binding pocket is, in which environment the target object is located and how to get there, and many more. This method already works, and many drugs have already been developed without the help of time-resolved protein structures. Nevertheless, this information, especially about the intermediate states, can generate additional value and thus make targeted drug development much more precise and thus more efficient.

The characteristics for in vitro inhibition are important, but then the potential drug candidates must also be able to reach their site of action. First, the antibiotic compound must reach the site of infection, but even more importantly, it must be able to cross the outer membrane of multiple clinically relevant Gram-negative pathogens (Liu et al., 2019). Typically, the transport of nutrients through the outer membrane is facilitated by porins and is strongly regulated. These are transmembrane proteins forming hydrophilic channels that enable the passive transport of molecules into the periplasm. For example, polar groups can be attached to the compounds to increase the permeability with the help of porins (Liu et al., 2019). In order to obtain an effective β-lactam inhibitor, all these aspects must be considered, and in the end, many potential drug candidates have to be screened for their activity.

Since enzymes have distinct binding pockets and perform unique chemical reactions, understanding the structure and molecular mechanisms of these enzymes provides a path for rational design and improvement of inhibitors that can, for example, restore susceptibility to β-lactams (Schaenzer & Wright, 2020).

6.3. Unraveling the mechanism of action of β-lactamases

Research in the field of time-resolved crystallography is becoming increasingly popular. At the same time, the research field of β-lactamases is gaining importance in the face of the ever-increasing threat of emerging antibiotic resistance. Since the beginning of this thesis project, more and more scientific articles have been published in this field. This emphasizes the importance and brisance of the topic and shows that it is absolutely up-to-date.

In 2018, mix and inject serial crystallography (MISC) experiments were performed using the *Mycobacterium tuberculosis* BlaC β-lactamase and the third-generation cephalosporin antibiotic ceftriaxone (Olmos et al., 2018). The determined time-resolved protein structures with delay times of 30 ms, 100 ms, 500 ms and 2 s enabled the observation of the binding and formation of the acyl-enzyme, but not that of the product complex.

A more recent preprint addresses the heterogeneity in the same BlaC β-lactamase inhibition by sulbactam by using serial mix-and-inject crystallography (MISC) at X-ray free-electron laser systems (Schmidt et al., 2023). According to the authors, the binding process and the formation of the covalent bound inhibitor sulbactam (equivalent to the acyl-enzyme state) could be observed. The utilized crystals have 4 subunits in the asymmetric unit. It was observed that the acyl-enzyme intermediate is coordinated differently in the subunits. While in one subunit pair the carbonyl oxygen of the cleaved β-lactam ring seems to be coordinated in the oxyanion hole, in the other subunit pair it is rotated to the other side and coordinated by Lys73 and Glu168 (equivalent to CTX-M-14 Glu166). The latter is not consistent with the observations reported in this thesis, regarding the acyl-enzyme state in CTX-M-14.

Another research article describes the binding and cleavage of a β-lactam antibiotic moxalactam by L1 metallo-β-lactamase from *Stenotrophomonas maltophilia* (M. Wilamowski et al., 2022). Since metallo-β-lactamases require zinc ions for hydrolysis, a caged compound for zinc ions was used for light induced reaction initiation. In this way, diffusion effects were completely minimized. Time-resolved serial synchrotron crystallography structures (2.20 Å resolution) revealed binding of moxalactam at 100 ms and cleavage of the same at 150 ms.

However, metallo-β-lactamases function mechanistically completely different than serine-β-lactamases, therefore no conclusion about mechanistic details of serine-β-lactamases can be drawn from these results. In addition, most protein structures of this thesis were determined at a higher resolution, which allows a better definition of the individual atomic positions.

In this study, CTX-M-14 was investigated with both hydrolysable substrates and non-hydrolysable inhibitors. In the former, the 4 states mentioned in section 4.6.2.1 were observed: native state, Michaelis-Menten complex, acyl-enzyme intermediate, and the product complex. All of them were observed in time-resolved experiments, although some of them had low occupancies. In addition, the temporal change of occupancies of the individual states could be observed. However, this allowed to determine the time course of the increase in calculated occupancy for each state. This represents a significant extension of the findings from the previously mentioned research articles.
In the case of the non-hydrolysable inhibitors, only two states were observed for CTX-M-14, the native state without inhibitor and the covalently bound inhibitor. The TapeDrive experiments showed that the inhibitor relebactam was bound to CTX-M-14 with 77 % occupancy after a very short delay time of only 250 ms. The inhibitor model with boric acid and the subsequent glycerol esterification showed even shorter delay times until the ligands were observed in the active site of the enzyme. This clearly confirms that diffusion limitations can be reduced by using small microcrystals for time-resolved studies (Schmidt, 2013, 2020).

Despite the high enzyme activity of CTX-M-14, it was possible to perform time-resolved data collections of the wild-type protein at synchrotron sources and observe intermediates. In order to monitor the fast and short-lived transition states during binding, pulsed X-rays from XFELs could be used. Initial experiments on this have been conducted at the Linac Coherent Light Source (LCLS) but have so far been unsuccessful.

Hydrogen bonds are one of the most fundamental inter- and intramolecular interactions and form important linkages between ligands and proteins, defining the stability and affinity of their complexes (Chen & Unkefer, 2017). In order to elucidate the reaction mechanism, it is important to be able to determine not only the temporal processes but also the present

protonation states of the active site residues. They are crucial for a statement about where a proton migrates to and where it comes from. After all, the observed reaction is a hydrolysis. However, despite their significance, hydrogen atom positions are very difficult to determine by X-ray crystallography. Hydrogen atoms have only one electron, which only weakly diffracts X-rays. Therefore, the determination of the position of hydrogen atoms is only possible at sub Ångström resolution below 1.0 Å, which could not be achieved with the used time-resolved crystallography methods. It is known that the CTX-M-14 macrocrystals diffract very well and resolutions of 0.8 Å can be achieved. In fact, we have already collected native CTX-M-14 datasets with 0.8 Å resolution. The aim is now to reproduce the intermediate states observed in the time-resolved studies with macrocrystals and conventional cryoMX revealing ultra high resolution structures. Of course, this is not trivial either, since the substrates could simply be unevenly distributed in the crystal due to the long diffusion times. In an extreme case, this would result in no substrate being observed in the active site by X-ray crystallography. With the inhibitors, on the other hand, it should work because the covalent bond is relatively stable, allowing the inhibitor to accumulate in the active site and thus achieve sufficient occupancy. This could provide a better understanding of the hydrogen bond interactions of active site residues with the inhibitors.

Species such as H+ or mobile hydrogen atoms with relatively high *B*-factors, which are often found in the active sites of enzymes, can hardly be determined by X-ray crystallography (Chen & Unkefer, 2017). In this case, neutron diffraction could be used for determination. Neutron crystallography is another method that allows to directly determine the position of hydrogen atoms (Kono & Tamada, 2021). The neutrons are diffracted by the protons of the hydrogen atoms. Often the protein crystals are deuterated beforehand to reduce the background of the measurement and to improve the signal-to-noise ratio. The exact position of the hydrogen atoms can provide further insight into the hydrolysis mechanism of β-lactamases, since, for example, the exact orientation of the catalytic water can be determined.

The functional and structural mutagenesis studies of previous efforts to elucidate the hydrolysis mechanism are clearly valuable and have contributed to great progress in the understanding of the same. However, the results obtained should always be treated with caution, as the modification of single amino acid residues in the active site can have a great effect on the structure and function of enzymes. Especially in reaction mechanisms such as

the hydrolysis mechanisms of β-lactamases, in which protons are transferred, the environment of the active site is very important. This is because specific mutations of amino acids in the active site can change the protonation states of the surrounding amino acid residues involved in the reaction, leading to a possibly incorrect interpretation of the reaction mechanism. Therefore, studies with the wild-type enzyme, as conducted here, are always more representative than those with hydrolysis defect mutant variants. The time-resolved data provide a better understanding of antibiotic resistance mechanisms, thus contributing to the future development of new drugs.

In summary, the mechanism of serine β-lactamases is far from being fully elucidated. This is not surprising, since research on this very topic has been conducted for decades and represents a serious challenge. Nevertheless, the current development and technology makes it possible to finally come very close to the goal. To unravel the mechanism of β-lactamases, the data obtained from the time-resolved studies must now be combined with high resolution X-ray structures and possibly even neutron structures to gain a comprehensive overview. The results would both finally unravel the mechanism that has been studied for decades and provide important information for the fight against antibiotic resistance.

7. References

Abedon, S. T., Kuhl, S. J., Blasdel, B. G., & Kutter, E. M. (2011). Phage treatment of human infections. *Bacteriophage*, *1*(2), 66-85.

Abraham, E. P., & Chain, E. (1940). An enzyme from bacteria able to destroy penicillin. *Nature*, *146*(3713), 837-837.

Adachi, H., Ohta, T., & Matsuzawa, H. (1991). Site-directed mutants, at position 166, of RTEM-1 beta-lactamase that form a stable acyl-enzyme intermediate with penicillin. *Journal of Biological Chemistry*, *266*(5), 3186-3191.

Adams, J., & Kauffman, M. (2004). Development of the proteasome inhibitor Velcade™(Bortezomib). *Cancer investigation*, *22*(2), 304-311.

Adams, P. D., Afonine, P. V., Bunkóczi, G., Chen, V. B., Davis, I. W., Echols, N., Headd, J. J., Hung, L.-W., Kapral, G. J., & Grosse-Kunstleve, R. W. (2010). PHENIX: a comprehensive Python-based system for macromolecular structure solution. *Acta Crystallographica Section D: Biological Crystallography*, *66*(2), 213-221.

Adams, P. D., Afonine, P. V., Bunkoczi, G., Chen, V. B., Davis, I. W., Echols, N., Headd, J. J., Hung, L. W., Kapral, G. J., Grosse-Kunstleve, R. W., McCoy, A. J., Moriarty, N. W., Oeffner, R., Read, R. J., Richardson, D. C., Richardson, J. S., Terwilliger, T. C., & Zwart, P. H. (2010). PHENIX: a comprehensive Python-based system for macromolecular structure solution. *Acta Crystallogr D Biol Crystallogr*, *66*(Pt 2), 213-221. https://doi.org/10.1107/S0907444909052925

Adamski, C. J., Cardenas, A. M., Brown, N. G., Horton, L. B., Sankaran, B., Prasad, B. V., Gilbert, H. F., & Palzkill, T. (2015). Molecular basis for the catalytic specificity of the CTX-M extended-spectrum β-lactamases. *Biochemistry*, *54*(2), 447-457.

Afonine, P. V., Grosse-Kunstleve, R. W., Echols, N., Headd, J. J., Moriarty, N. W., Mustyakimov, M., Terwilliger, T. C., Urzhumtsev, A., Zwart, P. H., & Adams, P. D. (2012). Towards automated crystallographic structure refinement with phenix.refine. *Acta Crystallogr D Biol Crystallogr*, *68*(Pt 4), 352-367. https://doi.org/10.1107/S0907444912001308

Aldred, K. J., Kerns, R. J., & Osheroff, N. (2014). Mechanism of quinolone action and resistance. *Biochemistry*, *53*(10), 1565-1574.

Alhede, M., Kragh, K. N., Qvortrup, K., Allesen-Holm, M., van Gennip, M., Christensen, L. D., Jensen, P. Ø., Nielsen, A. K., Parsek, M., & Wozniak, D. (2011). Phenotypes of non-attached Pseudomonas aeruginosa aggregates resemble surface attached biofilm. *PLoS One*, *6*(11), e27943.

Ambler, R. P., Coulson, A. F., Frère, J.-M., Ghuysen, J.-M., Joris, B., Forsman, M., Levesque, R. C., Tiraby, G., & Waley, S. G. (1991). A standard numbering scheme for the class A beta-lactamases. *Biochemical Journal*, *276*(Pt 1), 269.

Andrei, S., Droc, G., & Stefan, G. (2019). FDA approved antibacterial drugs: 2018-2019. *Discoveries*, *7*(4).

Anet, F., & Yavari, I. (1977). Nitrogen inversion in piperidine. *Journal of the American Chemical Society*, *99*(8), 2794-2796.

Baldock, R., & Katritzky, A. (1968). The conformational analysis of saturated heterocycles. Part XVIII. The orientation of NH-groups in piperidines and

morpholines from infrared spectroscopy. *Journal of the Chemical Society B: Physical Organic*, 1470-1477.

Baquero, F., & Levin, B. R. (2021). Proximate and ultimate causes of the bactericidal action of antibiotics. *Nature Reviews Microbiology*, *19*(2), 123-132.

Barends, T. R., Stauch, B., Cherezov, V., & Schlichting, I. (2022). Serial femtosecond crystallography. *Nature Reviews Methods Primers*, *2*(1), 59.

Barty, A., Caleman, C., Aquila, A., Timneanu, N., Lomb, L., White, T. A., Andreasson, J., Arnlund, D., Bajt, S., & Barends, T. R. (2012). Self-terminating diffraction gates femtosecond X-ray nanocrystallography measurements. *Nature photonics*, *6*(1), 35-40.

Bauernfeind, A., Schweighart, S., & Grimm, H. (1990). A new plasmidic cefotaximase in a clinical isolate of Escherichia coli. *Infection*, *18*(5), 294-298.

Beesley, T., Gascoyne, N., Knott-Hunziker, d. V., Petursson, S., Waley, S., Jaurin, B., & Grundström, T. (1983). The inhibition of class C β-lactamases by boronic acids. *Biochemical Journal*, *209*(1), 229-233.

Berman, H. M., Westbrook, J., Feng, Z., Gilliland, G., Bhat, T. N., Weissig, H., Shindyalov, I. N., & Bourne, P. E. (2000). The protein data bank. *Nucleic acids research*, *28*(1), 235-242.

Bevan, E. R., Jones, A. M., & Hawkey, P. M. (2017). Global epidemiology of CTX-M β-lactamases: temporal and geographical shifts in genotype. *Journal of Antimicrobial Chemotherapy*, *72*(8), 2145-2155.

Beyerlein, K. R., Dierksmeyer, D., Mariani, V., Kuhn, M., Sarrou, I., Ottaviano, A., Awel, S., Knoska, J., Fuglerud, S., Jönsson, O., Stern, S., Wiedorn, M. O., Yefanov, O., Adriano, L., Bean, R., Burkhardt, A., Fischer, P., Heymann, M., Horke, D. A., . . . Oberthuer, D. (2017). Mix-and-diffuse serial synchrotron crystallography. *IUCrJ*, *4*(6), 769. https://doi.org/10.1107/s2052252517013124

Bhujbalrao, R., & Anand, R. (2019). Deciphering determinants in ribosomal methyltransferases that confer antimicrobial resistance. *Journal of the American Chemical Society*, *141*(4), 1425-1429.

Blackburne, I. D., Katritzky, A. R., & Takeuchi, Y. (1975). Conformation of piperidine and of derivatives with additional ring hetero atoms. *Accounts of Chemical Research*, *8*(9), 300-306.

Blair, J. M., Webber, M. A., Baylay, A. J., Ogbolu, D. O., & Piddock, L. J. (2015). Molecular mechanisms of antibiotic resistance. *Nature Reviews Microbiology*, *13*(1), 42-51.

Blakeley, M. P., Langan, P., Niimura, N., & Podjarny, A. (2008). Neutron crystallography: opportunities, challenges, and limitations. *Current opinion in structural biology*, *18*(5), 593-600.

Blizzard, T. A., Chen, H., Kim, S., Wu, J., Bodner, R., Gude, C., Imbriglio, J., Young, K., Park, Y.-W., & Ogawa, A. (2014). Discovery of MK-7655, a β-lactamase inhibitor for combination with Primaxin®. *Bioorganic & medicinal chemistry letters*, *24*(3), 780-785.

Bonnet, R. (2004). Growing group of extended-spectrum β-lactamases: the CTX-M enzymes. *Antimicrobial agents and chemotherapy*, *48*(1), 1-14.

Bostedt, C., Boutet, S., Fritz, D. M., Huang, Z., Lee, H. J., Lemke, H. T., Robert, A., Schlotter, W. F., Turner, J. J., & Williams, G. J. (2016). Linac coherent light source: The first five years. *Reviews of Modern Physics*, *88*(1), 015007.

Both, A., Büttner, H., Huang, J., Perbandt, M., Belmar Campos, C., Christner, M., Maurer, F. P., Kluge, S., König, C., & Aepfelbacher, M. (2017). Emergence of ceftazidime/avibactam non-susceptibility in an MDR Klebsiella pneumoniae isolate. *Journal of Antimicrobial Chemotherapy*, *72*(9), 2483-2488.

Bragg, W. H., & Bragg, W. L. (1913). The reflection of X-rays by crystals. *Proceedings of the Royal Society of London. Series A, Containing Papers of a Mathematical and Physical Character*, *88*(605), 428-438.

Bragg, W. L. (1912). The Specular Reflection of X-rays. *Nature*, *90*(2250), 410-410.

Brändén, G., & Neutze, R. (2021). Advances and challenges in time-resolved macromolecular crystallography. *Science*, *373*(6558), eaba0954.

Brogden, R., Carmine, A., Heel, R., Speight, T., & Avery, G. (1982). Trimethoprim: a review of its antibacterial activity, pharmacokinetics and therapeutic use in urinary tract infections. *Drugs*, *23*(6), 405-430.

Brown, C. A., Hu, L., Sun, Z., Patel, M. P., Singh, S., Porter, J. R., Sankaran, B., Prasad, B. V., Bowman, G. R., & Palzkill, T. (2020). Antagonism between substitutions in β-lactamase explains a path not taken in the evolution of bacterial drug resistance. *Journal of Biological Chemistry*, *295*(21), 7376-7390.

Burkhardt, A., Pakendorf, T., Reime, B., Meyer, J., Fischer, P., Stübe, N., Panneerselvam, S., Lorbeer, O., Stachnik, K., & Warmer, M. (2016). Status of the crystallography beamlines at PETRA III. *The European Physical Journal Plus*, *131*(3), 1-9.

Burmeister, W. P. (2000). Structural changes in a cryo-cooled protein crystal owing to radiation damage. *Acta Crystallographica Section D: Biological Crystallography*, *56*(3), 328-341.

Bush, K. (2013). The ABCD's of β-lactamase nomenclature. *Journal of Infection and Chemotherapy*, *19*(4), 549-559.

Bush, K. (2015). A resurgence of β-lactamase inhibitor combinations effective against multidrug-resistant Gram-negative pathogens. *International journal of antimicrobial agents*, *46*(5), 483-493.

Bush, K., & Bradford, P. A. (2016). β-Lactams and β-lactamase inhibitors: an overview. *Cold Spring Harbor perspectives in medicine*, *6*(8), a025247.

Bush, K., & Jacoby, G. A. (2010). Updated functional classification of β-lactamases. *Antimicrobial agents and chemotherapy*, *54*(3), 969-976.

Calderón, C. B., & Sabundayo, B. P. (2007). Antimicrobial Classifications. In R. Schwalbe, L. Steele-Moore, & A. C. Goodwin (Eds.), *Antimicrobial susceptibility testing protocols* (Vol. 7, pp. 2356-2365). CRC Press.

Campbell, E. A., Korzheva, N., Mustaev, A., Murakami, K., Nair, S., Goldfarb, A., & Darst, S. A. (2001). Structural mechanism for rifampicin inhibition of bacterial RNA polymerase. *Cell*, *104*(6), 901-912.

Cantón, R., & Coque, T. M. (2006). The CTX-M β-lactamase pandemic. *Current opinion in microbiology*, *9*(5), 466-475.

Cantón, R., González-Alba, J. M., & Galán, J. C. (2012). CTX-M enzymes: origin and diffusion. *Frontiers in microbiology*, *3*, 110.

Cantón, R., Novais, A., Valverde, A., Machado, E., Peixe, L., Baquero, F., & Coque, T. M. (2008). Prevalence and spread of extended-spectrum β-lactamase-producing Enterobacteriaceae in Europe. *Clinical Microbiology and infection*, *14*, 144-153.

Cartwright, S., & Waley, S. (1984). Purification of β-lactamases by affinity chromatography on phenylboronic acid-agarose. *Biochemical Journal*, *221*(2), 505-512.

Casadevall, A., & Fang, F. C. (2020). The intracellular pathogen concept. *Molecular Microbiology*, *113*(3), 541-545.

Cavalli, A., Salvatella, X., Dobson, C. M., & Vendruscolo, M. (2007). Protein structure determination from NMR chemical shifts. *Proceedings of the National Academy of Sciences*, *104*(23), 9615-9620.

CDC, C. f. D. C. a. P. (2022). *Outpatient antibiotic prescriptions—United States, 2021* (CDC: Atlanta, GA, USA, Issue. https://www.cdc.gov/antibiotic-use/data/report-2021.html

Chapman, H. N., Caleman, C., & Timneanu, N. (2014). Diffraction before destruction. *Philosophical Transactions of the Royal Society B: Biological Sciences*, *369*(1647). https://doi.org/10.1098/rstb.2013.0313

Chapman, H. N., Fromme, P., Barty, A., White, T. A., Kirian, R. A., Aquila, A., Hunter, M. S., Schulz, J., DePonte, D. P., Weierstall, U., Doak, R. B., Maia, F. R. N. C., Martin, A. V., Schlichting, I., Lomb, L., Coppola, N., Shoeman, R. L., Epp, S. W., Hartmann, R., . . . Spence, J. C. H. (2011). Femtosecond X-ray protein nanocrystallography. *Nature*, *470*(7332), 73-77. https://doi.org/10.1038/nature09750

Chawla, M., Verma, J., Gupta, R., & Das, B. (2022). Antibiotic potentiators against multidrug-resistant bacteria: discovery, development, and clinical relevance. *Frontiers in microbiology*, *13*.

Chayen, N. E., & Saridakis, E. (2008). Protein crystallization: from purified protein to diffraction-quality crystal. *Nature methods*, *5*(2), 147-153.

Chen, C. C., Smith, T. J., Kapadia, G., Wäsch, S., Zawadzke, L. E., Coulson, A., & Herzberg, O. (1996). Structure and kinetics of the β-lactamase mutants S70A and K73H from Staphylococcus aureus PC1. *Biochemistry*, *35*(38), 12251-12258.

Chen, J.-H., & Unkefer, C. J. (2017). Fifteen years of the Protein Crystallography Station: the coming of age of macromolecular neutron crystallography. *IUCrJ*, *4*(1), 72-86.

Chen, V. B., Arendall, W. B., 3rd, Headd, J. J., Keedy, D. A., Immormino, R. M., Kapral, G. J., Murray, L. W., Richardson, J. S., & Richardson, D. C. (2010). MolProbity: all-atom structure validation for macromolecular crystallography. *Acta Crystallogr D Biol Crystallogr*, *66*(Pt 1), 12-21. https://doi.org/10.1107/S0907444909042073

Chen, Y., Bonnet, R., & Shoichet, B. K. (2007). The acylation mechanism of CTX-M β-lactamase at 0.88 Å resolution. *Journal of the American Chemical Society*, *129*(17), 5378-5380.

Chen, Y., Delmas, J., Sirot, J., Shoichet, B., & Bonnet, R. (2005a). Atomic resolution structures of CTX-M β-lactamases: extended spectrum activities from increased mobility and decreased stability. *Journal of molecular biology*, *348*(2), 349-362.

Chen, Y., Shoichet, B., & Bonnet, R. (2005b). Structure, function, and inhibition along the reaction coordinate of CTX-M β-lactamases. *Journal of the American Chemical Society*, *127*(15), 5423-5434.

Coelho, A., González-López, J. J., Miró, E., Alonso-Tarrés, C., Mirelis, B., Larrosa, M. N., Bartolomé, R. M., Andreu, A., Navarro, F., & Johnson, J. R. (2010). Characterisation of the CTX-M-15-encoding gene in Klebsiella pneumoniae strains from the Barcelona metropolitan area: plasmid diversity and chromosomal integration. *International journal of antimicrobial agents*, *36*(1), 73-78.

Cook, M. A., & Wright, G. D. (2022). The past, present, and future of antibiotics. *Science Translational Medicine*, *14*(657), eabo7793.

Coolidge, W. D. (1913). A powerful Röntgen ray tube with a pure electron discharge. *Physical Review*, *2*(6), 409.

Craft, K. M., Nguyen, J. M., Berg, L. J., & Townsend, S. D. (2019). Methicillin-resistant Staphylococcus aureus (MRSA): antibiotic-resistance and the biofilm phenotype. *MedChemComm*, *10*(8), 1231-1241.

Craig, W., & Andes, D. (2013). In vivo activities of ceftolozane, a new cephalosporin, with and without tazobactam against Pseudomonas aeruginosa and Enterobacteriaceae, including strains with extended-spectrum β-lactamases, in the thighs of neutropenic mice. *Antimicrobial agents and chemotherapy*, *57*(4), 1577-1582.

D'Arcy, A. (1994). Crystallizing proteins–a rational approach? *Acta Crystallographica Section D: Biological Crystallography*, *50*(4), 469-471.

D'Andrea, M. M., Arena, F., Pallecchi, L., & Rossolini, G. M. (2013). CTX-M-type β-lactamases: a successful story of antibiotic resistance. *International Journal of Medical Microbiology*, *303*(6-7), 305-317.

Danev, R., Yanagisawa, H., & Kikkawa, M. (2019). Cryo-electron microscopy methodology: current aspects and future directions. *Trends in biochemical sciences*, *44*(10), 837-848.

Darby, E. M., Trampari, E., Siasat, P., Gaya, M. S., Alav, I., Webber, M. A., & Blair, J. M. (2022). Molecular mechanisms of antibiotic resistance revisited. *Nature Reviews Microbiology*, 1-16.

Davies, J. (2006). Where have all the antibiotics gone? *Canadian Journal of Infectious Diseases and Medical Microbiology*, *17*(5), 287-290.

De Zitter, E., Coquelle, N., Oeser, P., Barends, T. R. M., & Colletier, J.-P. (2022). Xtrapol8 enables automatic elucidation of low-occupancy intermediate-states in crystallographic studies. *Communications Biology*, *5*(1), 640. https://doi.org/10.1038/s42003-022-03575-7

DeLano, W. L. (2002). Pymol: An open-source molecular graphics tool. *CCP4 Newsl. Protein Crystallogr*, *40*(1), 82-92.

Doi, Y., Potoski, B. A., Adams-Haduch, J. M., Sidjabat, H. E., Pasculle, A. W., & Paterson, D. L. (2008). Simple disk-based method for detection of Klebsiella pneumoniae carbapenemase-type β-lactamase by use of a boronic acid compound. *Journal of clinical microbiology*, *46*(12), 4083-4086.

Drawz, S. M., & Bonomo, R. A. (2010). Three decades of β-lactamase inhibitors. *Clinical microbiology reviews*, *23*(1), 160-201.

Dutour, C., Bonnet, R., Marchandin, H., Boyer, M., Chanal, C., Sirot, D., & Sirot, J. (2002). CTX-M-1, CTX-M-3, and CTX-M-14 β-lactamases from Enterobacteriaceae isolated in France. *Antimicrobial agents and chemotherapy*, *46*(2), 534-537.

Ehmann, D. E., Jahić, H., Ross, P. L., Gu, R.-F., Hu, J., Kern, G., Walkup, G. K., & Fisher, S. L. (2012). Avibactam is a covalent, reversible, non–β-lactam β-lactamase inhibitor. *Proceedings of the National Academy of Sciences*, *109*(29), 11663-11668.

Eidam, O., Romagnoli, C., Caselli, E., Babaoglu, K., Pohlhaus, D. T., Karpiak, J., Bonnet, R., Shoichet, B. K., & Prati, F. (2010). Design, synthesis, crystal structures, and antimicrobial activity of sulfonamide boronic acids as β-lactamase inhibitors. *Journal of medicinal chemistry*, *53*(21), 7852-7863.

Emsley, P., Lohkamp, B., Scott, W. G., & Cowtan, K. (2010). Features and development of Coot. *Acta Crystallographica Section D: Biological Crystallography*, *66*(4), 486-501.

Engleberg, C., DiRita, V. J., & Dermody, T. (2007). *Schaechter's mechanisms of microbial disease*. Lippincott Williams & Wilkins.

Eom, S. Y., Lee, Y. R., & Kwon, C. H. (2020). Accurate conformational stability and cationic structure of piperidine determined by conformer-specific VUV-MATI spectroscopy. *Physical Chemistry Chemical Physics*, *22*(39), 22823-22832.

Evans, R., O'Neill, M., Pritzel, A., Antropova, N., Senior, A., Green, T., Žídek, A., Bates, R., Blackwell, S., Yim, J., Ronneberger, O., Bodenstein, S., Zielinski, M., Bridgland, A., Potapenko, A., Cowie, A., Tunyasuvunakool, K., Jain, R., Clancy, E., . . . Hassabis, D. (2022). Protein complex prediction with AlphaFold-Multimer. *bioRxiv*, 2021.2010.2004.463034. https://doi.org/10.1101/2021.10.04.463034

FDA.gov. (2018). *US Food & Drug Administration. Highlights of prescribing information. VabomereTM (meropenem and vaborbactam) for injection, for intravenous use.* FDA.gov. https://www.accessdata.fda.gov/drugsatfda_docs/label/2017/209776lbl.pdf

Fernández, L., & Hancock, R. E. (2012). Adaptive and mutational resistance: role of porins and efflux pumps in drug resistance. *Clinical microbiology reviews*, *25*(4), 661-681.

Ferreira, L. G., Dos Santos, R. N., Oliva, G., & Andricopulo, A. D. (2015). Molecular docking and structure-based drug design strategies. *Molecules*, *20*(7), 13384-13421.

Finch, R., Discovery, B. W. P. o. T. U. N. R. A. D., Development, Blaser, M., Carrs, O., Cassell, G., Fishman, N., Guidos, R., Levy, S., Powers, J., & Norrby, R. (2011). Regulatory opportunities to encourage technology solutions to antibacterial drug resistance. *Journal of Antimicrobial Chemotherapy*, *66*(9), 1945-1947.

Fischer, A., Smiesko, M., Sellner, M., & Lill, M. A. (2021). Decision making in structure-based drug discovery: visual inspection of docking results. *Journal of medicinal chemistry*, *64*(5), 2489-2500.

Fisher, J., Belasco, J. G., Khosla, S., & Knowles, J. R. (1980). . beta.-Lactamase proceeds via an acyl-enzyme intermediate. Interaction of the Escherichia coli RTEM enzyme with cefoxitin. *Biochemistry*, *19*(13), 2895-2901.

Fisher, J. F., Meroueh, S. O., & Mobashery, S. (2005). Bacterial resistance to β-lactam antibiotics: compelling opportunism, compelling opportunity. *Chemical reviews*, *105*(2), 395-424.

Flannagan, R. S., Heit, B., & Heinrichs, D. E. (2016). Intracellular replication of Staphylococcus aureus in mature phagolysosomes in macrophages precedes host cell death, and bacterial escape and dissemination. *Cellular Microbiology*, *18*(4), 514-535.

Fleming, A. (1929). On the antibacterial action of cultures of a penicillium, with special reference to their use in the isolation of B. influenzae. *British journal of experimental pathology*, *10*(3), 226.

Flemming, H.-C., & Wingender, J. (2010). The biofilm matrix. *Nature Reviews Microbiology*, *8*(9), 623-633.

Forsberg, K. J., Patel, S., Wencewicz, T. A., & Dantas, G. (2015). The tetracycline destructases: a novel family of tetracycline-inactivating enzymes. *Chemistry & biology*, *22*(7), 888-897.

Freeman, C. D., Klutman, N. E., & Lamp, K. C. (1997). Metronidazole. *Drugs*, *54*(5), 679-708.

Friedrich, W., Knipping, P., & Laue, M. (1913). Interferenzerscheinungen bei roentgenstrahlen. *Annalen der Physik*, *346*(10), 971-988.

Fuller, F. D., Gul, S., Chatterjee, R., Burgie, E. S., Young, I. D., Lebrette, H., Srinivas, V., Brewster, A. S., Michels-Clark, T., & Clinger, J. A. (2017). Drop-on-demand sample delivery for studying biocatalysts in action at X-ray free-electron lasers. *Nature methods*, *14*(4), 443-449.

Furikado, Y., Nagahata, T., Okamoto, T., Sugaya, T., Iwatsuki, S., Inamo, M., Takagi, H. D., Odani, A., & Ishihara, K. (2014). Universal reaction mechanism of boronic acids with diols in aqueous solution: kinetics and the basic concept of a conditional formation constant. *Chemistry–A European Journal*, *20*(41), 13194-13202.

Galleni, M., Lamotte-Brasseur, J., Raquet, X., Dubus, A., Monnaie, D., Knox, J. R., & Frère, J.-M. (1995). The enigmatic catalytic mechanism of active-site serine β-lactamases. *Biochemical pharmacology*, *49*(9), 1171-1178.

García-Nafría, J., & Tate, C. G. (2020). Cryo-electron microscopy: moving beyond X-ray crystal structures for drug receptors and drug development. *Annual review of pharmacology and toxicology*, *60*, 51-71.

Garman, E. F., & Schneider, T. R. (1997). Macromolecular cryocrystallography. *Journal of Applied Crystallography*, *30*(3), 211-237.

Gasteiger, E., Hoogland, C., Gattiker, A., Wilkins, M. R., Appel, R. D., & Bairoch, A. (2005). Protein identification and analysis tools on the ExPASy server. *The proteomics protocols handbook*, 571-607.

Gati, C., Bourenkov, G., Klinge, M., Rehders, D., Stellato, F., Oberthür, D., Yefanov, O., Sommer, B. P., Mogk, S., & Duszenko, M. (2014). Serial crystallography on in vivo grown microcrystals using synchrotron radiation. *IUCrJ*, *1*(2), 87-94.

Ghosh, C., Sarkar, P., Issa, R., & Haldar, J. (2019). Alternatives to conventional antibiotics in the era of antimicrobial resistance. *Trends in microbiology*, *27*(4), 323-338.

Gin, A., Dilay, L., Karlowsky, J. A., Walkty, A., Rubinstein, E., & Zhanel, G. G. (2007). Piperacillin–tazobactam: a β-lactam/β-lactamase inhibitor combination. *Expert review of anti-infective therapy*, *5*(3), 365-383.

Ginn, H. M. (2023). Torsion angles to map and visualize the conformational space of a protein. *Protein Science*, *32*(4), e4608.

González-Bello, C. n., Rodríguez, D., Pernas, M., Rodriguez, A., & Colchón, E. (2019). β-Lactamase inhibitors to restore the efficacy of antibiotics against superbugs. *Journal of medicinal chemistry*, *63*(5), 1859-1881.

Gotthard, G., Aumonier, S., De Sanctis, D., Leonard, G., von Stetten, D., & Royant, A. (2019). Specific radiation damage is a lesser concern at room temperature. *IUCrJ*, *6*(4), 665-680.

Guillaume, G., Vanhove, M., Lamotte-Brasseur, J., Ledent, P., Jamin, M., Joris, B., & Frere, J.-M. (1997). Site-directed mutagenesis of glutamate 166 in two β-lactamases: kinetic and molecular modeling studies. *Journal of Biological Chemistry*, *272*(9), 5438-5444.

Hall, B. G., & Barlow, M. (2005). Revised Ambler classification of β-lactamases. *Journal of Antimicrobial Chemotherapy*, *55*(6), 1050-1051.

Hall, C. W., & Mah, T.-F. (2017). Molecular mechanisms of biofilm-based antibiotic resistance and tolerance in pathogenic bacteria. *FEMS microbiology reviews*, *41*(3), 276-301.

Hamad, B. (2010). The antibiotics market. *Nature reviews Drug discovery*, *9*(9), 675.

Hawkey, P. (2015). Multidrug-resistant Gram-negative bacteria: a product of globalization. *Journal of Hospital Infection*, *89*(4), 241-247.

He, D., Chiou, J., Zeng, Z., Liu, L., Chen, X., Zeng, L., Chan, E. W. C., Liu, J.-H., & Chen, S. (2015). Residues distal to the active site contribute to enhanced catalytic activity of variant and hybrid β-lactamases derived from CTX-M-14 and CTX-M-15. *Antimicrobial agents and chemotherapy*, *59*(10), 5976-5983.

Hecker, S. J., Reddy, K. R., Totrov, M., Hirst, G. C., Lomovskaya, O., Griffith, D. C., King, P., Tsivkovski, R., Sun, D., & Sabet, M. (2015). Discovery of a cyclic boronic acid β-lactamase inhibitor (RPX7009) with utility vs class A serine carbapenemases. In: ACS Publications.

Heimer, S. R., Evans, D. J., Stern, M. E., Barbieri, J. T., Yahr, T., & Fleiszig, S. M. (2013). Pseudomonas aeruginosa utilizes the type III secreted toxin ExoS to avoid acidified compartments within epithelial cells. *PLoS One*, *8*(9), e73111.

Hekkelman, M. L., de Vries, I., Joosten, R. P., & Perrakis, A. (2023). AlphaFill: enriching AlphaFold models with ligands and cofactors. *Nature methods*, *20*(2), 205-213. https://doi.org/10.1038/s41592-022-01685-y

Hendrickson, W. A., Smith, J. L., & Sheriff, S. (1985). Direct phase determination based on anomalous scattering. In *Methods in enzymology* (Vol. 115, pp. 41-55). Elsevier.

Hendrickson, W. A., & Teeter, M. M. (1981). Structure of the hydrophobic protein crambin determined directly from the anomalous scattering of sulphur. *Nature*, *290*(5802), 107-113.

Hermann, J. C., Hensen, C., Ridder, L., Mulholland, A. J., & Höltje, H.-D. (2005). Mechanisms of antibiotic resistance: QM/MM modeling of the acylation reaction

of a class A β-lactamase with benzylpenicillin. *Journal of the American Chemical Society*, *127*(12), 4454-4465.

Hermann, J. C., Pradon, J., Harvey, J. N., & Mulholland, A. J. (2009). High level QM/MM modeling of the formation of the tetrahedral intermediate in the acylation of wild type and K73A mutant TEM-1 class A β-lactamase. *The Journal of Physical Chemistry A*, *113*(43), 11984-11994.

Hermann, J. C., Ridder, L., Mulholland, A. J., & Höltje, H.-D. (2003). Identification of Glu166 as the general base in the acylation reaction of class A β-lactamases through QM/MM modeling. *Journal of the American Chemical Society*, *125*(32), 9590-9591.

Höltje, J.-V. (1995). From growth to autolysis: the murein hydrolases inEscherichia coli. *Archives of microbiology*, *164*(4), 243-254.

Horn, J., Stelzner, K., Rudel, T., & Fraunholz, M. (2018). Inside job: Staphylococcus aureus host-pathogen interactions. *International Journal of Medical Microbiology*, *308*(6), 607-624.

Hunter, M. S., DePonte, D. P., Shapiro, D., Kirian, R. A., Wang, X., Starodub, D., Marchesini, S., Weierstall, U., Doak, R. B., & Spence, J. C. (2011). X-ray diffraction from membrane protein nanocrystals. *Biophysical journal*, *100*(1), 198-206.

Hutchings, M. I., Truman, A. W., & Wilkinson, B. (2019). Antibiotics: past, present and future. *Current opinion in microbiology*, *51*, 72-80.

Ishii, Y., Galleni, M., Ma, L., Frère, J.-M., & Yamaguchi, K. (2007). Biochemical characterisation of the CTX-M-14 β-lactamase. *International journal of antimicrobial agents*, *29*(2), 159-164.

Ito, A., Taniuchi, A., May, T., Kawata, K., & Okabe, S. (2009). Increased antibiotic resistance of Escherichia coli in mature biofilms. *Applied and environmental microbiology*, *75*(12), 4093-4100.

Jacoby, G., & Bush, K. (2005). β-Lactam Resistance in the 21st Century. *Frontiers in antimicrobial resistance: a tribute to Stuart B. Levy*, 53-65.

Juers, D. H., & Ruffin, J. (2014). MAP_CHANNELS: a computation tool to aid in the visualization and characterization of solvent channels in macromolecular crystals. *Journal of Applied Crystallography*, *47*(6), 2105-2108.

Jumper, J., Evans, R., Pritzel, A., Green, T., Figurnov, M., Ronneberger, O., Tunyasuvunakool, K., Bates, R., Žídek, A., Potapenko, A., Bridgland, A., Meyer, C., Kohl, S. A. A., Ballard, A. J., Cowie, A., Romera-Paredes, B., Nikolov, S., Jain, R., Adler, J., . . . Hassabis, D. (2021). Highly accurate protein structure prediction with AlphaFold. *Nature*, *596*(7873), 583-589. https://doi.org/10.1038/s41586-021-03819-2

Jurrus, E., Engel, D., Star, K., Monson, K., Brandi, J., Felberg, L. E., Brookes, D. H., Wilson, L., Chen, J., & Liles, K. (2018). Improvements to the APBS biomolecular solvation software suite. *Protein Science*, *27*(1), 112-128.

Kabsch, W. (2010a). Integration, scaling, space-group assignment and post-refinement. *Acta Crystallographica Section D: Biological Crystallography*, *66*(2), 133-144.

Kabsch, W. (2010b). Xds. *Acta Crystallographica Section D: Biological Crystallography*, *66*(2), 125-132.

Kay, L. E. (2011). NMR studies of protein structure and dynamics. *Journal of magnetic resonance*, *213*(2), 477-491.

Ke, H. (1997). [25] Overview of isomorphous replacement phasing. In *Methods in enzymology* (Vol. 276, pp. 448-461). Elsevier.

Kendrew, J. C., Bodo, G., Dintzis, H. M., Parrish, R., Wyckoff, H., & Phillips, D. C. (1958). A three-dimensional model of the myoglobin molecule obtained by x-ray analysis. *Nature*, *181*(4610), 662-666.

Kiener, P. A., & Waley, S. G. (1978). Reversible inhibitors of penicillinases. *Biochemical Journal*, *169*(1), 197-204. https://doi.org/https://doi.org/10.1042/bj1690197

King, D. T., King, A. M., Lal, S. M., Wright, G. D., & Strynadka, N. C. (2015). Molecular mechanism of avibactam-mediated β-lactamase inhibition. *ACS infectious diseases*, *1*(4), 175-184.

Kitano, K., & Tomasz, A. (1979). Triggering of autolytic cell wall degradation in Escherichia coli by beta-lactam antibiotics. *Antimicrobial agents and chemotherapy*, *16*(6), 838-848.

Kono, F., & Tamada, T. (2021). Neutron crystallography for the elucidation of enzyme catalysis. *Current opinion in structural biology*, *71*, 36-42.

Krajnc, A., Brem, J. r., Hinchliffe, P., Calvopiña, K., Panduwawala, T. D., Lang, P. A., Kamps, J. J., Tyrrell, J. M., Widlake, E., & Saward, B. G. (2019). Bicyclic boronate VNRX-5133 inhibits metallo-and serine-β-lactamases. *Journal of medicinal chemistry*, *62*(18), 8544-8556.

Krause, K. M., Serio, A. W., Kane, T. R., & Connolly, L. E. (2016). Aminoglycosides: an overview. *Cold Spring Harbor perspectives in medicine*, *6*(6), a027029.

Kupitz, C., Basu, S., Grotjohann, I., Fromme, R., Zatsepin, N. A., Rendek, K. N., Hunter, M. S., Shoeman, R. L., White, T. A., Wang, D., James, D., Yang, J.-H., Cobb, D. E., Reeder, B., Sierra, R. G., Liu, H., Barty, A., Aquila, A. L., Deponte, D., . . . Fromme, P. (2014). Serial time-resolved crystallography of photosystem II using a femtosecond X-ray laser. *Nature*, *513*(7517), 261-265. https://doi.org/10.1038/nature13453

Kupitz, C., OlmosJr., J. L., Holl, M., Tremblay, L., Pande, K., Pandey, S., Oberthür, D., Hunter, M., Liang, M., Aquila, A., Tenboer, J., Calvey, G., Katz, A., Chen, Y., Wiedorn, M. O., Knoska, J., Meents, A., Majriani, V., Norwood, T., . . . Schmidt, M. (2017). Structural enzymology using X-ray free electron lasers. *Structural Dynamics*, *4*(4), 044003.

Laemmli, U. K. (1970). Cleavage of structural proteins during the assembly of the head of bacteriophage T4. *Nature*, *227*(5259), 680-685.

Lahiri, S. D., Mangani, S., Durand-Reville, T., Benvenuti, M., De Luca, F., Sanyal, G., & Docquier, J.-D. (2013). Structural insight into potent broad-spectrum inhibition with reversible recyclization mechanism: avibactam in complex with CTX-M-15 and Pseudomonas aeruginosa AmpC β-lactamases. *Antimicrobial agents and chemotherapy*, *57*(6), 2496-2505.

Laminet, A. A., & Plückthun, A. (1989). The precursor of beta-lactamase: purification, properties and folding kinetics. *The EMBO Journal*, *8*(5), 1469-1477.

Laskowski, R. A., & Swindells, M. B. (2011). LigPlot+: multiple ligand–protein interaction diagrams for drug discovery. In: ACS Publications.

Laxminarayan, R., Duse, A., Wattal, C., Zaidi, A. K., Wertheim, H. F., Sumpradit, N., Vlieghe, E., Hara, G. L., Gould, I. M., & Goossens, H. (2013). Antibiotic resistance—the need for global solutions. *The Lancet infectious diseases*, *13*(12), 1057-1098.

Lee, Y., Kim, J., & Trinh, S. (2019). Meropenem–vaborbactam (Vabomere™): another option for carbapenem-resistant Enterobacteriaceae. *Pharmacy and Therapeutics*, *44*(3), 110.

Lei, J., Hansen, G., Nitsche, C., Klein, C. D., Zhang, L., & Hilgenfeld, R. (2016). Crystal structure of Zika virus NS2B-NS3 protease in complex with a boronate inhibitor. *Science*, *353*(6298), 503-505.

Lerner, M., & Carlson, H. (2006). APBS plugin for PyMOL. *Ann Arbor: University of Michigan*, *522*.

Lewis, K. (2013). Platforms for antibiotic discovery. *Nature reviews Drug discovery*, *12*(5), 371-387.

Liebschner, D., Afonine, P. V., Baker, M. L., Bunkóczi, G., Chen, V. B., Croll, T. I., Hintze, B., Hung, L.-W., Jain, S., & McCoy, A. J. (2019). Macromolecular structure determination using X-rays, neutrons and electrons: recent developments in Phenix. *Acta Crystallographica Section D: Structural Biology*, *75*(10), 861-877.

Liebschner, D., Afonine, P. V., Moriarty, N. W., Poon, B. K., Sobolev, O. V., Terwilliger, T. C., & Adams, P. D. (2017). Polder maps: improving OMIT maps by excluding bulk solvent. *Acta Crystallographica Section D: Structural Biology*, *73*(2), 148-157.

Lima, L. M., da Silva, B. N. M., Barbosa, G., & Barreiro, E. J. (2020). β-lactam antibiotics: An overview from a medicinal chemistry perspective. *European journal of medicinal chemistry*, *208*, 112829.

Lipfert, J., & Doniach, S. (2007). Small-angle X-ray scattering from RNA, proteins, and protein complexes. *Annu. Rev. Biophys. Biomol. Struct.*, *36*, 307-327.

Liscio, J. L., Mahoney, M. V., & Hirsch, E. B. (2015). Ceftolozane/tazobactam and ceftazidime/avibactam: two novel β-lactam/β-lactamase inhibitor combination agents for the treatment of resistant Gram-negative bacterial infections. *International journal of antimicrobial agents*, *46*(3), 266-271.

Liu, B., Trout, R. E. L., Chu, G.-H., McGarry, D., Jackson, R. W., Hamrick, J. C., Daigle, D. M., Cusick, S. M., Pozzi, C., & De Luca, F. (2019). Discovery of taniborbactam (VNRX-5133): a broad-spectrum serine-and metallo-β-lactamase inhibitor for carbapenem-resistant bacterial infections. In: ACS Publications.

Liu, H., & Lee, W. (2019). The XFEL protein crystallography: developments and perspectives. In (Vol. 20, pp. 3421): MDPI.

Livermore, D. M. (2012). Fourteen years in resistance. *International journal of antimicrobial agents*, *39*(4), 283-294.

Livermore, D. M., Canton, R., Gniadkowski, M., Nordmann, P., Rossolini, G. M., Arlet, G., Ayala, J., Coque, T. M., Kern-Zdanowicz, I., & Luzzaro, F. (2007). CTX-M: changing the face of ESBLs in Europe. *Journal of Antimicrobial Chemotherapy*, *59*(2), 165-174.

Livermore, D. M., Discovery, B. S. f. A. C. W. P. o. T. U. N. R. A. D., Development, Blaser, M., Carrs, O., Cassell, G., Fishman, N., Guidos, R., Levy, S., Powers, J., & Norrby,

R. (2011). Discovery research: the scientific challenge of finding new antibiotics. *Journal of Antimicrobial Chemotherapy*, *66*(9), 1941-1944.

Llarrull, L. I., Testero, S. A., Fisher, J. F., & Mobashery, S. (2010). The future of the β-lactams. *Current opinion in microbiology*, *13*(5), 551-557.

Lomovskaya, O., Sun, D., Rubio-Aparicio, D., Nelson, K., Tsivkovski, R., Griffith, D. C., & Dudley, M. N. (2017). Vaborbactam: spectrum of beta-lactamase inhibition and impact of resistance mechanisms on activity in Enterobacteriaceae. *Antimicrobial agents and chemotherapy*, *61*(11), e01443-01417.

Lowy, F. D. (2000). Is Staphylococcus aureus an intracellular pathogen? *Trends in microbiology*, *8*(8), 341-343.

Lynch III, J. P., Clark, N. M., & Zhanel, G. G. (2013). Evolution of antimicrobial resistance among Enterobacteriaceae (focus on extended spectrum β-lactamases and carbapenemases). *Expert opinion on pharmacotherapy*, *14*(2), 199-210.

Madeira, F., Pearce, M., Tivey, A. R., Basutkar, P., Lee, J., Edbali, O., Madhusoodanan, N., Kolesnikov, A., & Lopez, R. (2022). Search and sequence analysis tools services from EMBL-EBI in 2022. *Nucleic acids research*, *50*(W1), W276-W279.

Madey, J. M. (1971). Stimulated emission of bremsstrahlung in a periodic magnetic field. *Journal of Applied Physics*, *42*(5), 1906-1913.

Magiorakos, A.-P., Srinivasan, A., Carey, R. B., Carmeli, Y., Falagas, M., Giske, C., Harbarth, S., Hindler, J., Kahlmeter, G., & Olsson-Liljequist, B. (2012). Multidrug-resistant, extensively drug-resistant and pandrug-resistant bacteria: an international expert proposal for interim standard definitions for acquired resistance. *Clinical Microbiology and infection*, *18*(3), 268-281.

Majiduddin, F. K., Materon, I. C., & Palzkill, T. G. (2002). Molecular analysis of beta-lactamase structure and function. *International Journal of Medical Microbiology*, *292*(2), 127-137.

Mansell, T. J., Linderman, S. W., Fisher, A. C., & DeLisa, M. P. (2010). A rapid protein folding assay for the bacterial periplasm. *Protein Science*, *19*(5), 1079-1090.

Martiel, I., Müller-Werkmeister, H. M., & Cohen, A. E. (2019). Strategies for sample delivery for femtosecond crystallography. *Acta Crystallographica Section D: Structural Biology*, *75*(2), 160-177.

Martin-Garcia, J. M., Conrad, C. E., Coe, J., Roy-Chowdhury, S., & Fromme, P. (2016). Serial femtosecond crystallography: A revolution in structural biology. *Archives of biochemistry and biophysics*, *602*, 32-47.

McCoy, A. J., Grosse-Kunstleve, R. W., Adams, P. D., Winn, M. D., Storoni, L. C., & Read, R. J. (2007). Phaser crystallographic software. *Journal of Applied Crystallography*, *40*(4), 658-674.

McPHERSON, A. (1991). Review Current approaches to macromolecular crystallization. *EJB reviews 1990*, 49-71.

Meents, A., Wiedorn, M., Srajer, V., Henning, R., Sarrou, I., Bergtholdt, J., Barthelmess, M., Reinke, P., Dierksmeyer, D., & Tolstikova, A. (2017). Pink-beam serial crystallography. *Nature Communications*, *8*(1), 1281.

Mehrabi, P., Muller-Werkmeister, H. M., Leimkohl, J.-P., Schikora, H., Ninkovic, J., Krivokuca, S., Andricek, L., Epp, S. W., Sherrell, D., Owen, R. L., Pearson, A. R., Tellkamp, F., Schulz, E. C., & Miller, R. J. D. (2020). The HARE chip for efficient

time-resolved serial synchrotron crystallography. *Journal of Synchrotron Radiation*, *27*(2), 360-370. https://doi.org/doi:10.1107/S1600577520000685

Mehrabi, P., Schulz, E. C., Agthe, M., Horrell, S., Bourenkov, G., von Stetten, D., Leimkohl, J.-P., Schikora, H., Schneider, T. R., & Pearson, A. R. (2019a). Liquid application method for time-resolved analyses by serial synchrotron crystallography. *Nature methods*, *16*(10), 979-982.

Mehrabi, P., Schulz, E. C., Dsouza, R., Müller-Werkmeister, H. M., Tellkamp, F., Miller, R. D., & Pai, E. F. (2019b). Time-resolved crystallography reveals allosteric communication aligned with molecular breathing. *Science*, *365*(6458), 1167-1170.

Mehrabi, P., Sung, S., Stetten, D. v., Prester, A., Hatton, C. E., Kleine-Döpke, S., Berkes, A., Gore, G., Leimkohl, J.-P., Schikora, H., Kollewe, M., Rohde, H., Wilmanns, M., Tellkamp, F., & Schulz, E. C. (2022). Millisecond cryo-trapping by the spitrobot crystal plunger simplifies time-resolved crystallography. *bioRxiv*, 2022.2009.2020.508674. https://doi.org/10.1101/2022.09.20.508674

Mehrabi, P., Sung, S., von Stetten, D., Prester, A., Hatton, C. E., Kleine-Döpke, S., Berkes, A., Gore, G., Leimkohl, J.-P., Schikora, H., Kollewe, M., Rohde, H., Wilmanns, M., Tellkamp, F., & Schulz, E. C. (2023). Millisecond cryo-trapping by the spitrobot crystal plunger simplifies time-resolved crystallography. *Nature Communications*, *14*(1), 2365. https://doi.org/10.1038/s41467-023-37834-w

Mehrabi, P., von Stetten, D., Leimkohl, J.-P., Tellkamp, F., & Schulz, E. C. (2021). An environmental control box for serial crystallography enables multi-dimensional experiments. *bioRxiv*, 2021.2011. 2007.467596.

Meletis, G., Oustas, E., Botziori, C., Kakasi, E., & Koteli, A. (2015). Containment of carbapenem resistance rates of Klebsiella pneumoniae and Acinetobacter baumannii in a Greek hospital with a concomitant increase in colistin, gentamicin and tigecycline resistance. *New Microbiol*, *38*(3), 417-421.

Meroueh, S. O., Fisher, J. F., Schlegel, H. B., & Mobashery, S. (2005). Ab initio QM/MM study of class A β-lactamase acylation: dual participation of Glu166 and Lys73 in a concerted base promotion of Ser70. *Journal of the American Chemical Society*, *127*(44), 15397-15407.

Mertens, H. D., & Svergun, D. I. (2010). Structural characterization of proteins and complexes using small-angle X-ray solution scattering. *Journal of structural biology*, *172*(1), 128-141.

Mina, R., Falcone, A. P., Bringhen, S., Liberati, A. M., Pescosta, N., Petrucci, M. T., Ciccone, G., Capra, A., Patriarca, F., & Rota-Scalabrini, D. (2021). Ixazomib-based induction regimens plus ixazomib maintenance in transplant-ineligible, newly diagnosed multiple myeloma: the phase II, multi-arm, randomized UNITO-EMN10 trial. *Blood cancer journal*, *11*(12), 1-5.

Mishra, N. N., Bayer, A. S., Tran, T. T., Shamoo, Y., Mileykovskaya, E., Dowhan, W., Guan, Z., & Arias, C. A. (2012). Daptomycin resistance in enterococci is associated with distinct alterations of cell membrane phospholipid content.

Mohr, K. I. (2016). History of antibiotics research. *How to Overcome the Antibiotic Crisis*, 237-272.

Mojica, M. F., Rossi, M.-A., Vila, A. J., & Bonomo, R. A. (2022). The urgent need for metallo-β-lactamase inhibitors: an unattended global threat. *The Lancet infectious diseases*, *22*(1), e28-e34.

Moloney, M. G. (2016). Natural products as a source for novel antibiotics. *Trends in pharmacological sciences*, *37*(8), 689-701.

Monteiro, D. C., von Stetten, D., Stohrer, C., Sans, M., Pearson, A. R., Santoni, G., van der Linden, P., & Trebbin, M. (2020). 3D-MiXD: 3D-printed X-ray-compatible microfluidic devices for rapid, low-consumption serial synchrotron crystallography data collection in flow. *IUCrJ*, *7*(2), 207-219.

Munita, J. M., & Arias, C. A. (2016). Mechanisms of antibiotic resistance. *Virulence mechanisms of bacterial pathogens*, 481-511.

Munoz-Price, L. S., Poirel, L., Bonomo, R. A., Schwaber, M. J., Daikos, G. L., Cormican, M., Cornaglia, G., Garau, J., Gniadkowski, M., & Hayden, M. K. (2013). Clinical epidemiology of the global expansion of Klebsiella pneumoniae carbapenemases. *The Lancet infectious diseases*, *13*(9), 785-796.

Murphy, B. P., & Pratt, R. (1988). Evidence for an oxyanion hole in serine beta-lactamases and DD-peptidases. *Biochemical Journal*, *256*(2), 669.

Murray, C. J., Ikuta, K. S., Sharara, F., Swetschinski, L., Aguilar, G. R., Gray, A., Han, C., Bisignano, C., Rao, P., & Wool, E. (2022). Global burden of bacterial antimicrobial resistance in 2019: a systematic analysis. *The Lancet*, *399*(10325), 629-655.

Naas, T., Oueslati, S., Bonnin, R. A., Dabos, M. L., Zavala, A., Dortet, L., Retailleau, P., & Iorga, B. I. (2017). Beta-lactamase database (BLDB)–structure and function. *Journal of enzyme inhibition and medicinal chemistry*, *32*(1), 917-919.

Nakatani, H., HANAI, K., UEHARA, Y., & HIROMI, K. (1975). Temperature-jump Studies on Benzeneboronic Acid-Serine Protease Interactions: Subtilisin and α-Chymotrypsin. *The Journal of Biochemistry*, *77*(4), 905-908.

Nepal, K., Pant, N. D., Neupane, B., Belbase, A., Baidhya, R., Shrestha, R. K., Lekhak, B., Bhatta, D. R., & Jha, B. (2017). Extended spectrum beta-lactamase and metallo beta-lactamase production among Escherichia coli and Klebsiella pneumoniae isolated from different clinical samples in a tertiary care hospital in Kathmandu, Nepal. *Annals of clinical microbiology and antimicrobials*, *16*(1), 1-7.

Neutze, R., Wouts, R., van der Spoel, D., Weckert, E., & Hajdu, J. (2000). Potential for biomolecular imaging with femtosecond X-ray pulses. *Nature*, *406*(6797), 752-757. https://doi.org/10.1038/35021099

Newman, D. J., & Cragg, G. M. (2016). Natural products as sources of new drugs from 1981 to 2014. *Journal of natural products*, *79*(3), 629-661.

Nichols, D. A., Hargis, J. C., Sanishvili, R., Jaishankar, P., Defrees, K., Smith, E. W., Wang, K. K., Prati, F., Renslo, A. R., & Woodcock, H. L. (2015). Ligand-induced proton transfer and low-barrier hydrogen bond revealed by X-ray crystallography. *Journal of the American Chemical Society*, *137*(25), 8086-8095.

Niesen, F. H., Koch, A., Lenski, U., Harttig, U., Roske, Y., Heinemann, U., & Hofmann, K. P. (2008). An approach to quality management in structural biology: biophysical selection of proteins for successful crystallization. *Journal of structural biology*, *162*(3), 451-459.

Nitsche, C., Zhang, L., Weigel, L. F., Schilz, J., Graf, D., Bartenschlager, R., Hilgenfeld, R., & Klein, C. D. (2017). Peptide–boronic acid inhibitors of flaviviral proteases: medicinal chemistry and structural biology. *Journal of medicinal chemistry*, *60*(1), 511-516.

O'Dell, W. B., Bodenheimer, A. M., & Meilleur, F. (2016). Neutron protein crystallography: A complementary tool for locating hydrogens in proteins. *Archives of biochemistry and biophysics*, *602*, 48-60.

O'Neill, J. (2016). Tackling drug-resistant infections globally: final report and recommendations.

Oberthuer, D., Knoška, J., Wiedorn, M. O., Beyerlein, K. R., Bushnell, D. A., Kovaleva, E. G., Heymann, M., Gumprecht, L., Kirian, R. A., Barty, A., Mariani, V., Tolstikova, A., Adriano, L., Awel, S., Barthelmess, M., Dörner, K., Xavier, P. L., Yefanov, O., James, D. R., . . . Bajt, S. (2017). Double-flow focused liquid injector for efficient serial femtosecond crystallography. *Scientific Reports*, *7*(1). https://doi.org/10.1038/srep44628

Ocampo, P. S., Lázár, V., Papp, B., Arnoldini, M., Abel zur Wiesch, P., Busa-Fekete, R., Fekete, G., Pál, C., Ackermann, M., & Bonhoeffer, S. (2014). Antagonism between bacteriostatic and bactericidal antibiotics is prevalent. *Antimicrobial agents and chemotherapy*, *58*(8), 4573-4582.

Olmos, J. L., Pandey, S., Martin-Garcia, J. M., Calvey, G., Katz, A., Knoska, J., Kupitz, C., Hunter, M. S., Liang, M., Oberthuer, D., Yefanov, O., Wiedorn, M., Heyman, M., Holl, M., Pande, K., Barty, A., Miller, M. D., Stern, S., Roy-Chowdhury, S., . . . Schmidt, M. (2018). Enzyme intermediates captured “on the fly” by mix-and-inject serial crystallography. *BMC biology*, *16*(1), 59. https://doi.org/10.1186/s12915-018-0524-5

Otwinowski, Z. (1991). Isomorphous replacement and anomalous scattering. Proceedings of the CCP4 Study weekend,

Owen, R. L., Axford, D., Sherrell, D. A., Kuo, A., Ernst, O. P., Schulz, E. C., Miller, R. D., & Mueller-Werkmeister, H. M. (2017). Low-dose fixed-target serial synchrotron crystallography. *Acta Crystallographica Section D: Structural Biology*, *73*(4), 373-378.

Palacios, A. R., Rossi, M.-A., Mahler, G. S., & Vila, A. J. (2020). Metallo-β-lactamase inhibitors inspired on snapshots from the catalytic mechanism. *Biomolecules*, *10*(6), 854.

Pan, X., He, Y., Lei, J., Huang, X., & Zhao, Y. (2017). Crystallographic snapshots of class A β-lactamase catalysis reveal structural changes that facilitate β-lactam hydrolysis. *Journal of Biological Chemistry*, *292*(10), 4022-4033.

Pankey, G. A., & Sabath, L. (2004). Clinical relevance of bacteriostatic versus bactericidal mechanisms of action in the treatment of Gram-positive bacterial infections. *Clinical Infectious Diseases*, *38*(6), 864-870.

Patel, M. P., Hu, L., Brown, C. A., Sun, Z., Adamski, C. J., Stojanoski, V., Sankaran, B., Prasad, B. V., & Palzkill, T. (2018). Synergistic effects of functionally distinct substitutions in β-lactamase variants shed light on the evolution of bacterial drug resistance. *Journal of Biological Chemistry*, *293*(46), 17971-17984.

Patel, M. P., Hu, L., Stojanoski, V., Sankaran, B., Prasad, B. V., & Palzkill, T. (2017). The drug-resistant variant P167S expands the substrate profile of CTX-M β-lactamases for oxyimino-cephalosporin antibiotics by enlarging the active site upon acylation. *Biochemistry*, *56*(27), 3443-3453.

Paterson, D. (2000). Recommendation for treatment of severe infections caused by Enterobacteriaceae producing extended-spectrum β-lactamases (ESBLs). *Clinical Microbiology and infection*, *6*(9), 460-463.

Paterson, D. L., & Bonomo, R. A. (2005). Extended-spectrum β-lactamases: a clinical update. *Clinical microbiology reviews*, *18*(4), 657-686.

Pearce, N. M., & Gros, P. (2021). A method for intuitively extracting macromolecular dynamics from structural disorder. *Nature Communications*, *12*(1), 5493. https://doi.org/10.1038/s41467-021-25814-x

Pemberton, O. A., Tsivkovski, R., Totrov, M., Lomovskaya, O., & Chen, Y. (2020). Structural basis and binding kinetics of vaborbactam in class A β-lactamase inhibition. *Antimicrobial agents and chemotherapy*, *64*(10), e00398-00320.

Perbandt, M., Werner, N., Prester, A., Rohde, H., Aepfelbacher, M., Hinrichs, W., & Betzel, C. (2022). Structural basis to repurpose boron-based proteasome inhibitors Bortezomib and Ixazomib as β-lactamase inhibitors. *Scientific Reports*, *12*(1), 1-12.

Periasamy, H., Joshi, P., Palwe, S., Shrivastava, R., Bhagwat, S., & Patel, M. (2020). High prevalence of Escherichia coli clinical isolates in India harbouring four amino acid inserts in PBP3 adversely impacting activity of aztreonam/avibactam. *Journal of Antimicrobial Chemotherapy*, *75*(6), 1650-1651.

Petrova, O. E., & Sauer, K. (2016). Escaping the biofilm in more than one way: desorption, detachment or dispersion. *Current opinion in microbiology*, *30*, 67-78.

Pflugrath, J. (2015). Practical macromolecular cryocrystallography. *Acta Crystallographica Section F: Structural Biology Communications*, *71*(6), 622-642.

Pitout, J. D., & Laupland, K. B. (2008). Extended-spectrum β-lactamase-producing Enterobacteriaceae: an emerging public-health concern. *The Lancet infectious diseases*, *8*(3), 159-166.

Poirel, L., Naas, T., Le Thomas, I., Karim, A., Bingen, E., & Nordmann, P. (2001). CTX-M-type extended-spectrum β-lactamase that hydrolyzes ceftazidime through a single amino acid substitution in the omega loop. *Antimicrobial agents and chemotherapy*, *45*(12), 3355-3361.

Poole, K., Krebes, K., McNally, C., & Neshat, S. (1993). Multiple antibiotic resistance in Pseudomonas aeruginosa: evidence for involvement of an efflux operon. *Journal of bacteriology*, *175*(22), 7363-7372.

Powers, R. A., Caselli, E., Focia, P. J., Prati, F., & Shoichet, B. K. (2001). Structures of Ceftazidime and Its Transition-State Analogue in Complex with AmpC β-Lactamase: Implications for Resistance Mutations and Inhibitor Design. *Biochemistry*, *40*(31), 9207-9214. https://doi.org/10.1021/bi0109358

Prester, A., Perbandt, M., Galchenkova, M., Oberthuer, D., Werner, N., Henkel, A., Maracke, J., Yefanov, O., Hakanpää, J., Pompidor, G., Meyer, J., Chapman, H., Aepfelbacher, M., Hinrichs, W., Rohde, H., & Betzel, C. (2023). Time-resolved

crystallography of boric acid binding to the active site serine of the β-lactamase CTX-M-14 and subsequent 1,2-diol esterification. *PREPRINT (Version 1) Research Square (Manuscript submitted for publication, under review)*. https://doi.org/10.21203/rs.3.rs-3173899/v1

Price Ii, W. N., Chen, Y., Handelman, S. K., Neely, H., Manor, P., Karlin, R., Nair, R., Liu, J., Baran, M., & Everett, J. (2009). Understanding the physical properties that control protein crystallization by analysis of large-scale experimental data. *Nature biotechnology*, *27*(1), 51-57.

Pujol, C., & Bliska, J. B. (2003). The ability to replicate in macrophages is conserved between Yersinia pestis and Yersinia pseudotuberculosis. *Infection and immunity*, *71*(10), 5892-5899.

Queenan, A. M., & Bush, K. (2007). Carbapenemases: the versatile β-lactamases. *Clinical microbiology reviews*, *20*(3), 440-458.

Ravelli, R. B., & McSweeney, S. M. (2000). The 'fingerprint'that X-rays can leave on structures. *Structure*, *8*(3), 315-328.

Riekel, C., Burghammer, M., & Schertler, G. (2005). Protein crystallography microdiffraction. *Current opinion in structural biology*, *15*(5), 556-562.

Robert, X., & Gouet, P. (2014). Deciphering key features in protein structures with the new ENDscript server. *Nucleic acids research*, *42*(W1), W320-W324.

Roberts, M. C., & Schwarz, S. (2017). Tetracycline and Chloramphenicol Resistance Mechanisms. In D. L. Mayers, J. D. Sobel, M. Ouellette, K. S. Kaye, & D. Marchaim (Eds.), *Antimicrobial Drug Resistance: Mechanisms of Drug Resistance, Volume 1* (pp. 231-243). Springer International Publishing. https://doi.org/10.1007/978-3-319-46718-4_15

Rodkey, E. A., Drawz, S. M., Sampson, J. M., Bethel, C. R., Bonomo, R. A., & Van Den Akker, F. (2012). Crystal structure of a preacylation complex of the β-lactamase inhibitor sulbactam bound to a sulfenamide bond-containing thiol-β-lactamase. *Journal of the American Chemical Society*, *134*(40), 16798-16804.

Rodríguez-Baño, J., Gutiérrez-Gutiérrez, B., Machuca, I., & Pascual, A. (2018). Treatment of infections caused by extended-spectrum-beta-lactamase-, AmpC-, and carbapenemase-producing Enterobacteriaceae. *Clinical microbiology reviews*, *31*(2), e00079-00017.

Röntgen, W. C. (1895). Uber eine neue Art von Strahlen. *Sitzung Physikal-Medicin Gesellschaft*, *137*, 132-141.

Rossmann, M. G. (1990). The molecular replacement method. *Acta Crystallographica Section A: Foundations of Crystallography*, *46*(2), 73-82.

Rupp, B. (2009). *Biomolecular crystallography: principles, practice, and application to structural biology*. Garland Science.

S Ferreira, R., & D Andricopulo, A. (2014). Structure-based drug design to overcome drug resistance: challenges and opportunities. *Current pharmaceutical design*, *20*(5), 687-693.

Salehi, B., Ghalavand, Z., Yadegar, A., & Eslami, G. (2021). Characteristics and diversity of mutations in regulatory genes of resistance-nodulation-cell division efflux pumps in association with drug-resistant clinical isolates of Acinetobacter baumannii. *Antimicrobial Resistance & Infection Control*, *10*, 1-12.

Schaenzer, A. J., & Wright, G. D. (2020). Antibiotic resistance by enzymatic modification of antibiotic targets. *Trends in Molecular Medicine*, *26*(8), 768-782.

Schmidt, M. (2013). Mix and inject: Reaction initiation by diffusion for time-resolved macromolecular crystallography. *Advances in Condensed Matter Physics*, *2013*.

Schmidt, M. (2020). Reaction initiation in enzyme crystals by diffusion of substrate. *Crystals*, *10*(2), 116.

Schmidt, M., Malla, T. N., Zielinski, K., Aldama, L., Bajt, S., Feliz, D., Hayes, B., Hunter, M., Kupitz, C., Lisova, S., Knoska, J., Martin-Garcia, J., Mariani, V., Pandey, S., Poudyal, I., Sierra, R. G., Tolstikova, A., Yefanov, O., Yoon, C. H., . . . Pollack, L. (2023). Heterogeneity in the M. tuberculosis β-Lactamase Inhibition by Sulbactam. *Research Square (preprint)*. https://doi.org/https://doi.org/10.21203/rs.3.rs-2334665/v1

Schulz, E. C., Mehrabi, P., Müller-Werkmeister, H. M., Tellkamp, F., Jha, A., Stuart, W., Persch, E., De Gasparo, R., Diederich, F., & Pai, E. F. (2018). The hit-and-return system enables efficient time-resolved serial synchrotron crystallography. *Nature methods*, *15*(11), 901-904.

Schulz, E. C., Yorke, B. A., Pearson, A. R., & Mehrabi, P. (2022). Best practices for time-resolved serial synchrotron crystallography. *Acta Crystallographica Section D: Structural Biology*, *78*(1), 14-29.

Selas Castiñeiras, T., Williams, S. G., Hitchcock, A., Cole, J. A., Smith, D. C., & Overton, T. W. (2018). Development of a generic β-lactamase screening system for improved signal peptides for periplasmic targeting of recombinant proteins in Escherichia coli. *Scientific Reports*, *8*(1), 1-18.

Shi, C., Chen, J., Kang, X., Shen, X., Lao, X., & Zheng, H. (2019). Approaches for the discovery of metallo-β-lactamase inhibitors: A review. *Chemical biology & drug design*, *94*(2), 1427-1440.

Shi, D., Nannenga, B. L., Iadanza, M. G., & Gonen, T. (2013). Three-dimensional electron crystallography of protein microcrystals. *elife*, *2*, e01345.

Shi, Q., & Jackowski, G. (1998). One-dimensional polyacrylamide gel electrophoresis. *Gel electrophoresis of proteins: A practical approach*, *3*, 1-52.

Shi, Y. (2014). A glimpse of structural biology through X-ray crystallography. *Cell*, *159*(5), 995-1014.

Shurina, B. A., & Page, R. C. (2021). Structural Comparisons of Cefotaximase (CTX-M-ase) Sub Family 1. *Frontiers in microbiology*, *12*.

Sköld, O. (2000). Sulfonamide resistance: mechanisms and trends. *Drug resistance updates*, *3*(3), 155-160.

Smith, J. L., Fischetti, R. F., & Yamamoto, M. (2012). Micro-crystallography comes of age. *Current opinion in structural biology*, *22*(5), 602-612.

Smyth, M., & Martin, J. (2000). x Ray crystallography. *Molecular Pathology*, *53*(1), 8.

Soe, Y. M., Bedoui, S., Stinear, T. P., & Hachani, A. (2021). Intracellular Staphylococcus aureus and host cell death pathways. *Cellular Microbiology*, *23*(5), e13317.

Soeung, V., Lu, S., Hu, L., Judge, A., Sankaran, B., Prasad, B. V., & Palzkill, T. (2020). A drug-resistant β-lactamase variant changes the conformation of its active-site proton shuttle to alter substrate specificity and inhibitor potency. *Journal of Biological Chemistry*, *295*(52), 18239-18255.

Staker, B. L., Buchko, G. W., & Myler, P. J. (2015). Recent contributions of structure-based drug design to the development of antibacterial compounds. *Current opinion in microbiology*, *27*, 133-138.

Steinfeld, J. I., Francisco, J. S., & Hase, W. L. (1999). *Chemical kinetics and dynamics*. Prentice Hall Upper Saddle River, NJ.

Stewart, P. S. (2015). Antimicrobial tolerance in biofilms. *Microbiology spectrum*, *3*(3), 3.3. 07.

Stewart, P. S., & Costerton, J. W. (2001). Antibiotic resistance of bacteria in biofilms. *The Lancet*, *358*(9276), 135-138.

Straus, S. K., & Hancock, R. E. (2006). Mode of action of the new antibiotic for Gram-positive pathogens daptomycin: comparison with cationic antimicrobial peptides and lipopeptides. *Biochimica et Biophysica Acta (BBA)-Biomembranes*, *1758*(9), 1215-1223.

Strynadka, N. C., Adachi, H., Jensen, S. E., Johns, K., Sielecki, A., Betzel, C., Sutoh, K., & James, M. N. (1992). Molecular structure of the acyl-enzyme intermediate in β-lactam hydrolysis at 1.7 Å resolution. *Nature*, *359*(6397), 700-705.

Su, X.-D., Zhang, H., Terwilliger, T. C., Liljas, A., Xiao, J., & Dong, Y. (2015). Protein crystallography from the perspective of technology developments. *Crystallography reviews*, *21*(1-2), 122-153.

Subramanian, S., Roberts, C. L., Hart, C. A., Martin, H. M., Edwards, S. W., Rhodes, J. M., & Campbell, B. J. (2008). Replication of colonic Crohn's disease mucosal Escherichia coli isolates within macrophages and their susceptibility to antibiotics. *Antimicrobial agents and chemotherapy*, *52*(2), 427-434.

Tacconelli, E., Carrara, E., Savoldi, A., Harbarth, S., Mendelson, M., Monnet, D. L., Pulcini, C., Kahlmeter, G., Kluytmans, J., & Carmeli, Y. (2018). Discovery, research, and development of new antibiotics: the WHO priority list of antibiotic-resistant bacteria and tuberculosis. *The Lancet infectious diseases*, *18*(3), 318-327.

Takeda, S., Nakai, T., Wakai, Y., Ikeda, F., & Hatano, K. (2007). In vitro and in vivo activities of a new cephalosporin, FR264205, against Pseudomonas aeruginosa. *Antimicrobial agents and chemotherapy*, *51*(3), 826-830.

Teerawattanapong, N., Kengkla, K., Dilokthornsakul, P., Saokaew, S., Apisarnthanarak, A., & Chaiyakunapruk, N. (2017). Prevention and control of multidrug-resistant gram-negative bacteria in adult intensive care units: a systematic review and network meta-analysis. *Clinical Infectious Diseases*, *64*(suppl_2), S51-S60.

Ten Eyck, L. F. (1973). Crystallographic fast Fourier transforms. *Acta Crystallographica Section A: Crystal Physics, Diffraction, Theoretical and General Crystallography*, *29*(2), 183-191.

Tenboer, J., Basu, S., Zatsepin, N., Pande, K., Milathianaki, D., Frank, M., Hunter, M., Boutet, S., Williams, G. J., Koglin, J. E., Oberthuer, D., Heymann, M., Kupitz, C., Conrad, C., Coe, J., Roy-Chowdhury, S., Weierstall, U., James, D., Wang, D., . . . Schmidt, M. (2014). Time-resolved serial crystallography captures high-resolution intermediates of photoactive yellow protein. *Science*, *346*(6214), 1242-1246. https://doi.org/doi:10.1126/science.1259357

Tenson, T., Lovmar, M., & Ehrenberg, M. (2003). The mechanism of action of macrolides, lincosamides and streptogramin B reveals the nascent peptide exit path in the ribosome. *Journal of molecular biology*, *330*(5), 1005-1014.

Theuretzbacher, U., & Piddock, L. J. (2019). Non-traditional antibacterial therapeutic options and challenges. *Cell host & microbe*, *26*(1), 61-72.

Tian, G.-B., Jiang, Y.-Q., Huang, Y.-M., Qin, Y., Feng, L.-Q., Zhang, X.-F., Li, H.-Y., Zhong, L.-L., Zeng, K.-J., & Patil, S. (2016). Characterization of CTX-M-140, a variant of CTX-M-14 extended-spectrum β-lactamase with decreased cephalosporin hydrolytic activity, from cephalosporin-resistant Proteus mirabilis. *Antimicrobial agents and chemotherapy*, *60*(10), 6121-6126.

Tipper, D. J., & Strominger, J. L. (1965). Mechanism of action of penicillins: a proposal based on their structural similarity to acyl-D-alanyl-D-alanine. *Proc Natl Acad Sci U S A*, *54*(4), 1133-1141. https://doi.org/10.1073/pnas.54.4.1133

Tomanicek, S. J., Wang, K. K., Weiss, K. L., Blakeley, M. P., Cooper, J., Chen, Y., & Coates, L. (2011). The active site protonation states of perdeuterated Toho-1 β-lactamase determined by neutron diffraction support a role for Glu166 as the general base in acylation. *FEBS letters*, *585*(2), 364-368.

Tomasz, A. (1979). The mechanism of the irreversible antimicrobial effects of penicillins: how the beta-lactam antibiotics kill and lyse bacteria. *Annual Reviews in Microbiology*, *33*(1), 113-137.

Tooke, C. L., Hinchliffe, P., Bonomo, R. A., Schofield, C. J., Mulholland, A. J., & Spencer, J. (2021). Natural variants modify Klebsiella pneumoniae carbapenemase (KPC) acyl–enzyme conformational dynamics to extend antibiotic resistance. *Journal of Biological Chemistry*, *296*, 100126. https://doi.org/https://doi.org/10.1074/jbc.RA120.016461

Tooke, C. L., Hinchliffe, P., Bragginton, E. C., Colenso, C. K., Hirvonen, V. H., Takebayashi, Y., & Spencer, J. (2019a). β-Lactamases and β-Lactamase Inhibitors in the 21st Century. *Journal of molecular biology*, *431*(18), 3472-3500. https://doi.org/https://doi.org/10.1016/j.jmb.2019.04.002

Tooke, C. L., Hinchliffe, P., Krajnc, A., Mulholland, A. J., Brem, J., Schofield, C. J., & Spencer, J. (2020). Cyclic boronates as versatile scaffolds for KPC-2 β-lactamase inhibition. *RSC medicinal chemistry*, *11*(4), 491-496.

Tooke, C. L., Hinchliffe, P., Lang, P. A., Mulholland, A. J., Brem, J., Schofield, C. J., & Spencer, J. (2019b). Molecular basis of class A β-lactamase inhibition by relebactam. *Antimicrobial agents and chemotherapy*, *63*(10), e00564-00519.

Tremblay, L. W., Xu, H., & Blanchard, J. S. (2010). Structures of the Michaelis complex (1.2 Å) and the covalent acyl intermediate (2.0 Å) of cefamandole bound in the active sites of the Mycobacterium tuberculosis β-lactamase K73A and E166A mutants. *Biochemistry*, *49*(45), 9685-9687.

Trimble, M. J., Mlynárčik, P., Kolář, M., & Hancock, R. E. (2016). Polymyxin: alternative mechanisms of action and resistance. *Cold Spring Harbor perspectives in medicine*, *6*(10), a025288.

Tsivkovski, R., Totrov, M., & Lomovskaya, O. (2020). Biochemical characterization of QPX7728, a new ultrabroad-spectrum beta-lactamase inhibitor of serine and

metallo-beta-lactamases. *Antimicrobial agents and chemotherapy*, *64*(6), e00130-00120.

Turker, L. (2006). Some boric acid esters of glycerol-An ab initio treatment.

Tzouvelekis, L., Markogiannakis, A., Psichogiou, M., Tassios, P., & Daikos, G. (2012). Carbapenemases in Klebsiella pneumoniae and other Enterobacteriaceae: an evolving crisis of global dimensions. *Clinical microbiology reviews*, *25*(4), 682-707.

Uruén, C., Chopo-Escuin, G., Tommassen, J., Mainar-Jaime, R. C., & Arenas, J. (2020). Biofilms as promoters of bacterial antibiotic resistance and tolerance. *Antibiotics*, *10*(1), 3.

van Langevelde, P., Van Dissel, J., Meurs, C., Renz, J., & Groeneveld, P. (1997). Combination of flucloxacillin and gentamicin inhibits toxic shock syndrome toxin 1 production by Staphylococcus aureus in both logarithmic and stationary phases of growth. *Antimicrobial agents and chemotherapy*, *41*(8), 1682-1685.

Vandavasi, V. G., Langan, P. S., Weiss, K. L., Parks, J. M., Cooper, J. B., Ginell, S. L., & Coates, L. (2017). Active-site protonation states in an acyl-enzyme intermediate of a class A β-lactamase with a monobactam substrate. *Antimicrobial agents and chemotherapy*, *61*(1), e01636-01616.

Vandavasi, V. G., Weiss, K. L., Cooper, J. B., Erskine, P. T., Tomanicek, S. J., Ostermann, A., Schrader, T. E., Ginell, S. L., & Coates, L. (2016). Exploring the mechanism of β-lactam ring protonation in the class A β-lactamase acylation mechanism using neutron and X-ray crystallography. *Journal of medicinal chemistry*, *59*(1), 474-479.

Vena, A., Castaldo, N., & Bassetti, M. (2019). The role of new β-lactamase inhibitors in Gram-negative infections. *Current opinion in infectious diseases*, *32*(6), 638-646.

Vettoretti, L., Plésiat, P., Muller, C., El Garch, F., Phan, G., Attrée, I., Ducruix, A., & Llanes, C. (2009). Efflux unbalance in Pseudomonas aeruginosa isolates from cystic fibrosis patients. *Antimicrobial agents and chemotherapy*, *53*(5), 1987-1997.

Watkins, R., Papp-Wallace, K. M., Drawz, S. M., & Bonomo, R. A. (2013). Novel β-lactamase inhibitors: a therapeutic hope against the scourge of multidrug resistance. *Frontiers in microbiology*, *4*, 392.

Weierstall, U., Spence, J., & Doak, R. (2012). Injector for scattering measurements on fully solvated biospecies. *Review of Scientific Instruments*, *83*(3), 035108.

Werner, N. (2020). *Analyse von Struktur und Dynamik ausgewählter Enzyme und potenzieller Wirkstofftargets unter Anwendung gepulster Synchrotron-und X-FEL Strahlung* Staats-und Universitätsbibliothek Hamburg Carl von Ossietzky].

White, A. R., Discovery, B. W. P. o. T. U. N. R. A. D., Development, Blaser, M., Carrs, O., Cassell, G., Fishman, N., Guidos, R., Levy, S., Powers, J., & Norrby, R. (2011). Effective antibacterials: at what cost? The economics of antibacterial resistance and its control. *Journal of Antimicrobial Chemotherapy*, *66*(9), 1948-1953.

White, T. A., Kirian, R. A., Martin, A. V., Aquila, A., Nass, K., Barty, A., & Chapman, H. N. (2012). CrystFEL: a software suite for snapshot serial crystallography. *Journal of Applied Crystallography*, *45*(2), 335-341. https://doi.org/doi:10.1107/S0021889812002312

White, T. A., Mariani, V., Brehm, W., Yefanov, O., Barty, A., Beyerlein, K. R., Chervinskii, F., Galli, L., Gati, C., Nakane, T., Tolstikova, A., Yamashita, K., Yoon, C. H., Diederichs, K., & Chapman, H. N. (2016). Recent developments in CrystFEL. *J Appl Crystallogr*, *49*(Pt 2), 680-689. https://doi.org/10.1107/S1600576716004751

WHO, W. H. O. (2017). *WHO Publishes List of Bacteria for which New Antibiotics are Urgently Needed*. Retrieved 20.02.2023 from https://www.who.int/news/item/27-02-2017-who-publishes-list-of-bacteria-for-which-new-antibiotics-are-urgently-needed

WHO, W. H. O. (2019). 2019 antibacterial agents in clinical development: an analysis of the antibacterial clinical development pipeline.

Wiedorn, M. O., Oberthür, D., Bean, R., Schubert, R., Werner, N., Abbey, B., Aepfelbacher, M., Adriano, L., Allahgholi, A., Al-Qudami, N., Andreasson, J., Aplin, S., Awel, S., Ayyer, K., Bajt, S., Barák, I., Bari, S., Bielecki, J., Botha, S., . . . Barty, A. (2018). Megahertz serial crystallography. *Nature Communications*, *9*(1). https://doi.org/10.1038/s41467-018-06156-7

Wilamowski, M., Sherrell, D., Kim, Y., Lavens, A., Henning, R., Lazarski, K., Shigemoto, A., Endres, M., Maltseva, N., & Babnigg, G. (2022). Time-resolved β-lactam cleavage by L1 metallo-β-lactamase. *Nature Communications*, *13*(1), 7379.

Wilamowski, M., Sherrell, D. A., Kim, Y., Lavens, A., Henning, R. W., Lazarski, K., Shigemoto, A., Endres, M., Maltseva, N., Babnigg, G., Burdette, S. C., Srajer, V., & Joachimiak, A. (2022). Time-resolved β-lactam cleavage by L1 metallo-β-lactamase. *Nature Communications*, *13*(1), 7379. https://doi.org/10.1038/s41467-022-35029-3

Williams, C. J., Headd, J. J., Moriarty, N. W., Prisant, M. G., Videau, L. L., Deis, L. N., Verma, V., Keedy, D. A., Hintze, B. J., & Chen, V. B. (2018). MolProbity: More and better reference data for improved all-atom structure validation. *Protein Science*, *27*(1), 293-315.

Winn, M. D., Ballard, C. C., Cowtan, K. D., Dodson, E. J., Emsley, P., Evans, P. R., Keegan, R. M., Krissinel, E. B., Leslie, A. G., & McCoy, A. (2011). Overview of the CCP4 suite and current developments. *Acta Crystallographica Section D: Biological Crystallography*, *67*(4), 235-242.

Wright, G. D. (2011). Molecular mechanisms of antibiotic resistance. *Chemical communications*, *47*(14), 4055-4061.

Yahav, D., Giske, C. G., Grāmatniece, A., Abodakpi, H., Tam, V. H., & Leibovici, L. (2020). New β-lactam–β-lactamase inhibitor combinations. *Clinical microbiology reviews*, *34*(1), e00115-00120.

Yang, J., Yan, R., Roy, A., Xu, D., Poisson, J., & Zhang, Y. (2015). The I-TASSER Suite: protein structure and function prediction. *Nature methods*, *12*(1), 7-8.

Yip, K. M., Fischer, N., Paknia, E., Chari, A., & Stark, H. (2020). Atomic-resolution protein structure determination by cryo-EM. *Nature*, *587*(7832), 157-161.

Yuan, L., Hansen, M. F., Røder, H. L., Wang, N., Burmølle, M., & He, G. (2020). Mixed-species biofilms in the food industry: Current knowledge and novel control strategies. *Critical Reviews in Food Science and Nutrition*, *60*(13), 2277-2293.

Zhanel, G. G., Chung, P., Adam, H., Zelenitsky, S., Denisuik, A., Schweizer, F., Lagacé-Wiens, P. R., Rubinstein, E., Gin, A. S., & Walkty, A. (2014).

Ceftolozane/tazobactam: a novel cephalosporin/β-lactamase inhibitor combination with activity against multidrug-resistant gram-negative bacilli. *Drugs*, *74*(1), 31-51.

Zhanel, G. G., Dueck, M., Hoban, D. J., Vercaigne, L. M., Embil, J. M., Gin, A. S., & Karlowsky, J. A. (2001). Review of macrolides and ketolides. *Drugs*, *61*(4), 443-498.

Zhanel, G. G., Lawrence, C. K., Adam, H., Schweizer, F., Zelenitsky, S., Zhanel, M., Lagacé-Wiens, P. R., Walkty, A., Denisuik, A., & Golden, A. (2018). Imipenem–relebactam and meropenem–vaborbactam: two novel carbapenem-β-lactamase inhibitor combinations. *Drugs*, *78*(1), 65-98.

Zhao, W.-H., & Hu, Z.-Q. (2013). Epidemiology and genetics of CTX-M extended-spectrum β-lactamases in Gram-negative bacteria. *Critical reviews in microbiology*, *39*(1), 79-101.

Zielinski, K. A., Prester, A., Andaleeb, H., Bui, S., Yefanov, O., Catapano, L., Henkel, A., Wiedorn, M. O., Lorbeer, O., Crosas, E., Meyer, J., Maleriani, V., Domracky, M., White, T. A., Fleckenstein, H., Sarrou, I., Werner, N., Betzel, C., Rohde, H., . . . Oberthuer, D. (2022). Rapid and efficient room-temperature serial synchrotron crystallography using the CFEL TapeDrive. *IUCrJ*, *9*(6), 778-791.

Zwama, M., & Nishino, K. (2021). Ever-adapting RND efflux pumps in Gram-negative multidrug-resistant pathogens: a race against time. *Antibiotics*, *10*(7), 774.

Appendix

A1. Supplementary figures

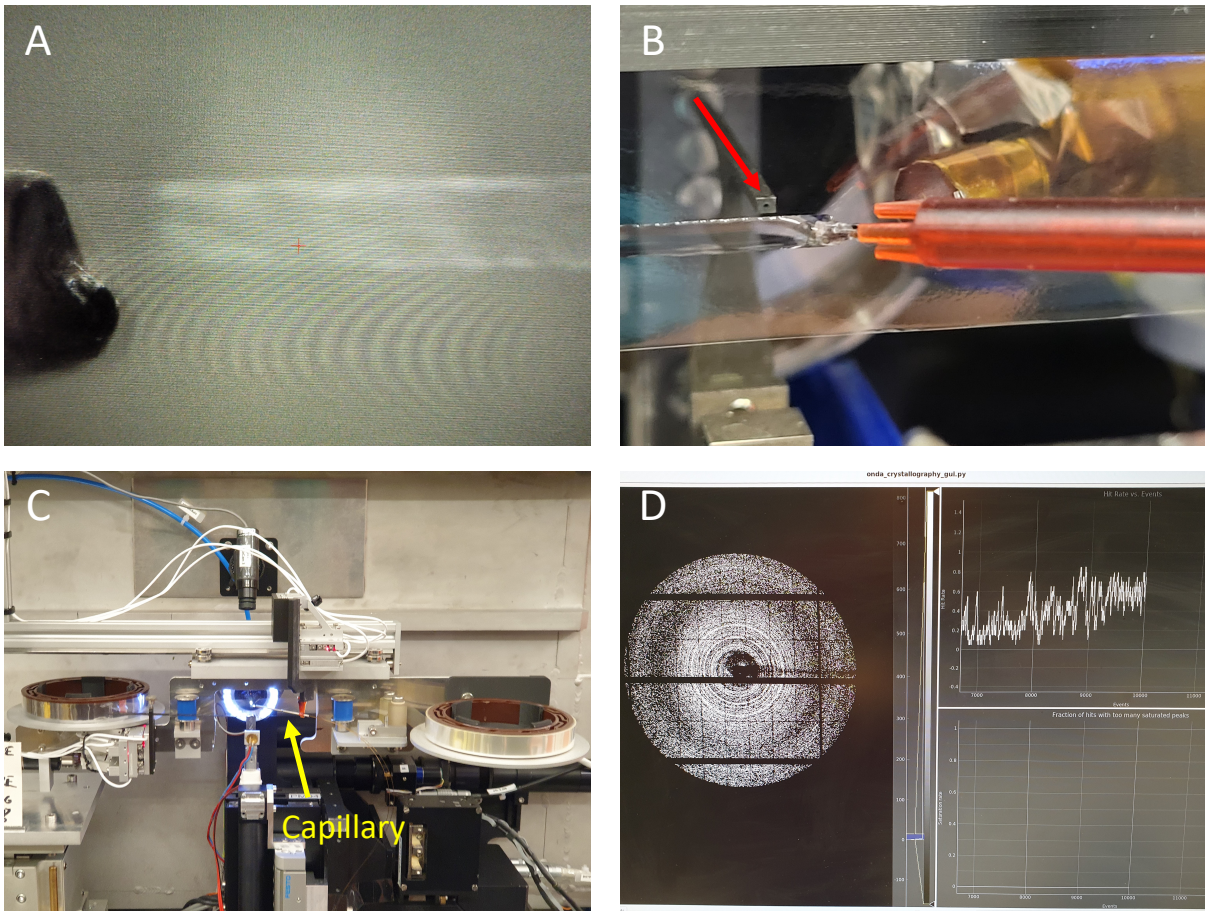

Figure S1: Photographs of the CFEL TapeDrive. (A) Image by in-line microscope of P11 beamline showing the stream of microcrystal suspension. The capillary through which the sample is applied to the tape is located on the left side of the image. The movement of the tape transports the microcrystal stream from the left side of the image to the right side, passing through the X-ray interaction region marked by the red cross. **(B)** Another picture of the capillary applying the microcrystal stream to the tape. The tape is moving in the left direction. The X-rays are emitted in the direction indicated by the red arrow. **(C)** General view of the TapeDrive setup. **(D)** Onda for real time monitoring of the experiments with a cumulative plot of the diffraction patterns (left) and a graph showing the hit rate (top right) and the hits with too many saturated peaks (bottom right).

```
        10         20         30         40         50         60
MVTKRVQRMM FAAAACIPLL LGSAPLYAQT SAVQQKLAAL EKSSGGRLGV ALIDTADNTQ

        70         80         90        100        110        120
VLYRGDERFP MCSTSKVMAA AAVLKQSETQ KQLLNQPVEI KPADLVNYNP IAEKHVNGTM

       130        140        150        160        170        180
TLAELSAAAL QYSDNTAMNK LIAQLGGPGG VTAFARAIGD ETFRLDRTEP TLNTAIPGDP

       190        200        210        220        230        240
RDTTTPRAMA QTLRQLTLGH ALGETQRAQL VTWLKGNTTG AASIRAGLPT SWTVGDKTGS

       250        260        270        280        290
GDYGTTNDIA VIWPQGRAPL VLVTYFTQPQ QNAESRRDVL ASAARIIAEG L
```

Figure S2: Amino acid sequence of CTX-M-14 β-lactamase.

Table S1: Molar extinction coefficients of 10 antibiotics.

Antibiotic	Molar extinction coefficient	Reference
ampicillin	$\varepsilon_{235nm} = -900\ M^{-1}cm^{-1}$	(Ishii et al., 2007)
benzylpenicillin	$\varepsilon_{233nm} = -780\ M^{-1}cm^{-1}$	(Ishii et al., 2007)
cefalotin	$\varepsilon_{262nm} = -7660\ M^{-1}cm^{-1}$	(Ishii et al., 2007)
cefdinir	$\varepsilon_{310nm} = -5390\ M^{-1}cm^{-1}$	(Ishii et al., 2007)
cefepime	$\varepsilon_{267nm} = -9120\ M^{-1}cm^{-1}$	(Ishii et al., 2007)
cefotaxime	$\varepsilon_{264nm} = -7250\ M^{-1}cm^{-1}$	(Ishii et al., 2007)
ceftazidime	$\varepsilon_{265nm} = -10300\ M^{-1}cm^{-1}$	(Ishii et al., 2007)
ceftriaxone	$\varepsilon_{256nm} = -25410\ M^{-1}cm^{-1}$	Determined experimentally
cefuroxime	$\varepsilon_{262nm} = -14550\ M^{-1}cm^{-1}$	Determined experimentally
piperacillin	$\varepsilon_{232nm} = -1640\ M^{-1}cm^{-1}$	(Ishii et al., 2007)

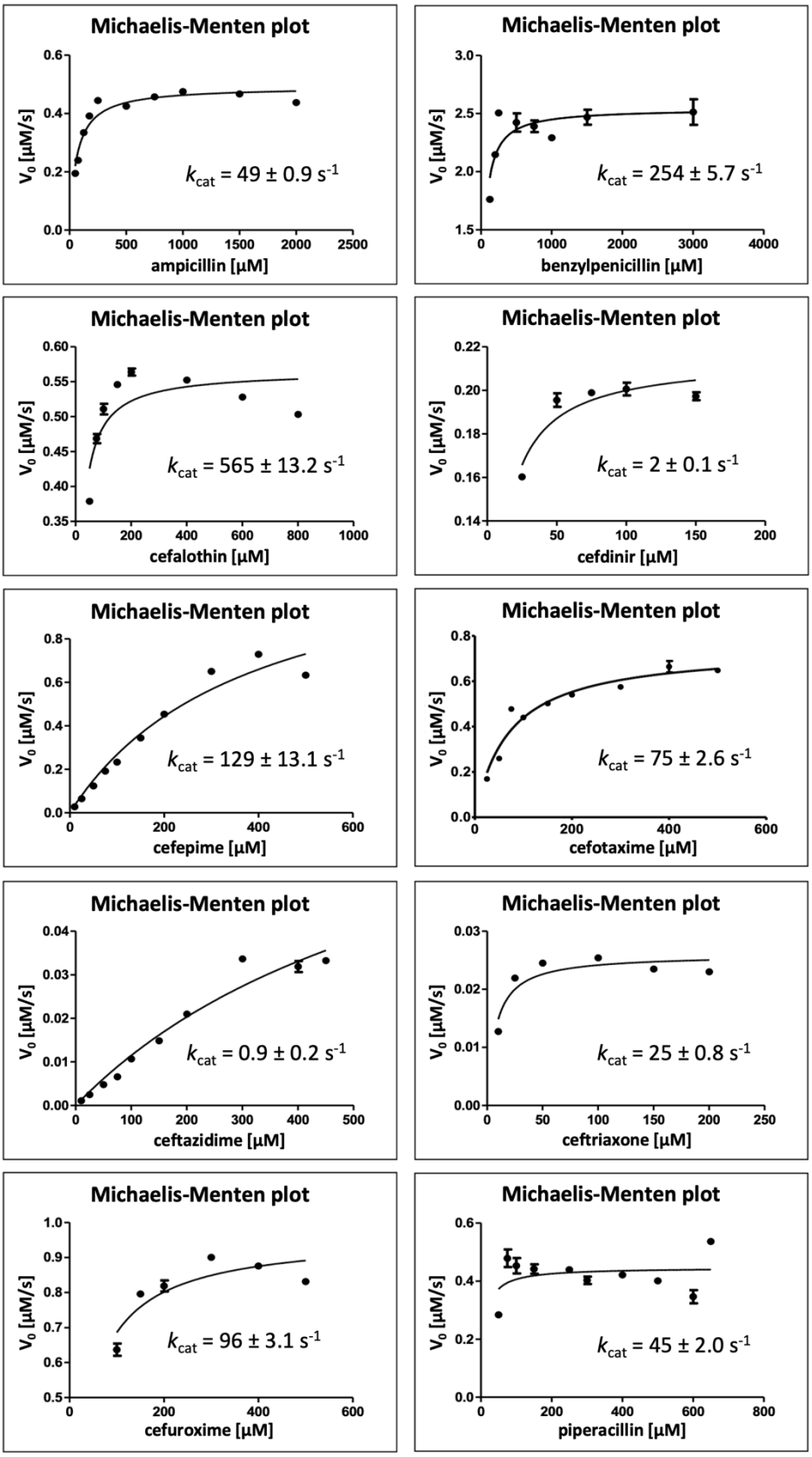

Figure S3: Michaelis-Menten plots of 10 antibiotics. The steady-state parameters k_{cat} and K_m have been determined at 28 °C and pH 6 (20mM MES buffer). Initial rates of enzymatic hydrolysis of antibiotics by CTX-M-14 were plotted against the corresponding concentration of the antibiotic. Steady-state parameters k_{cat} and K_m were calculated using the k_{cat} equation of GraphPad Prism.

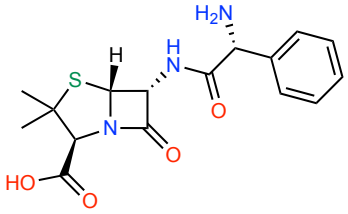

ampicillin; k_{cat} = 61 ± 0.9 s^{-1}

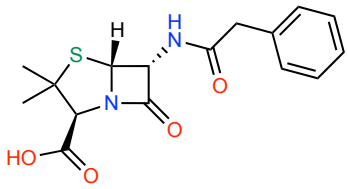

benzylpenicillin; k_{cat} = 254 ± 5.7 s^{-1}

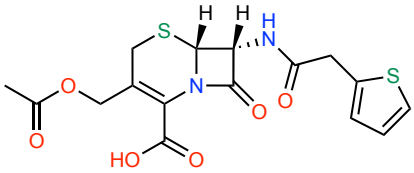

cefalotin; k_{cat} = 565 ± 13.2 s^{-1}

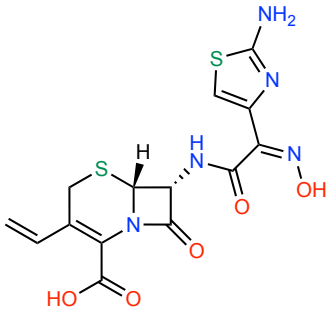

cefdinir; k_{cat} = 2 ± 0.1 s^{-1}

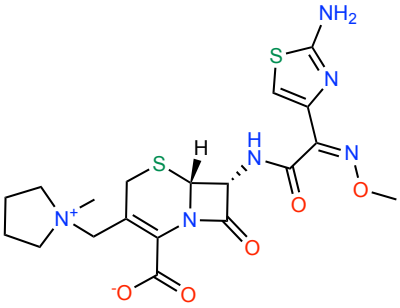

cefepime; k_{cat} = 129 ± 13.1 s^{-1}

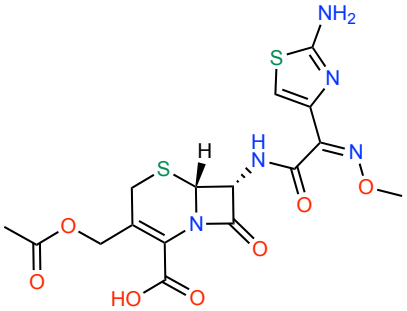

cefotaxime; k_{cat} = 75 ± 2.6 s^{-1}

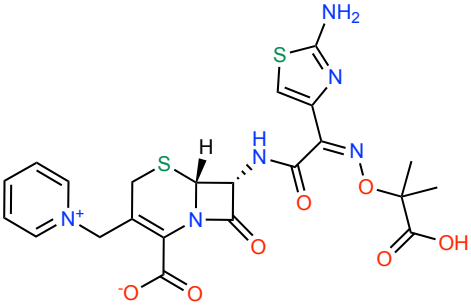

ceftazidime; k_{cat} = 0.9 ± 0.2 s^{-1}

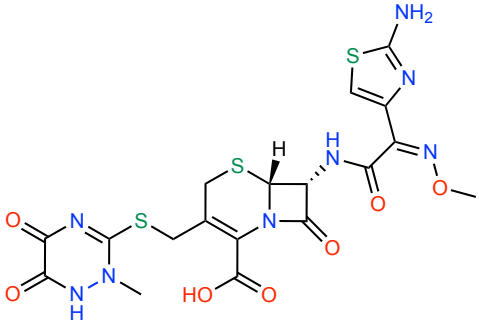

ceftriaxone; k_{cat} = 25 ± 0.8 s^{-1}

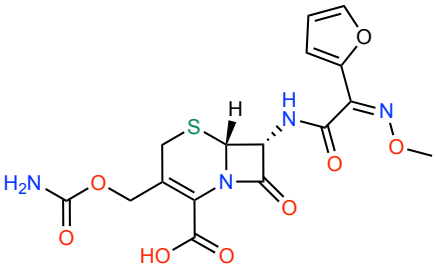

cefuroxime; k_{cat} = 96 ± 3.1 s^{-1}

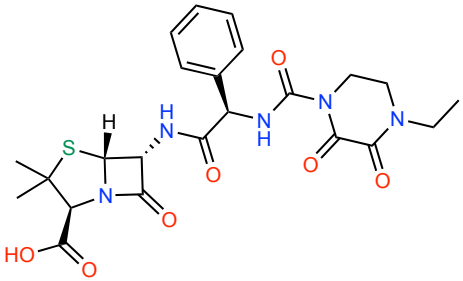

piperacillin; k_{cat} = 45 ± 2.0 s^{-1}

Figure S4: Chemical structures of 10 antibiotics and respective k_{cat} values.

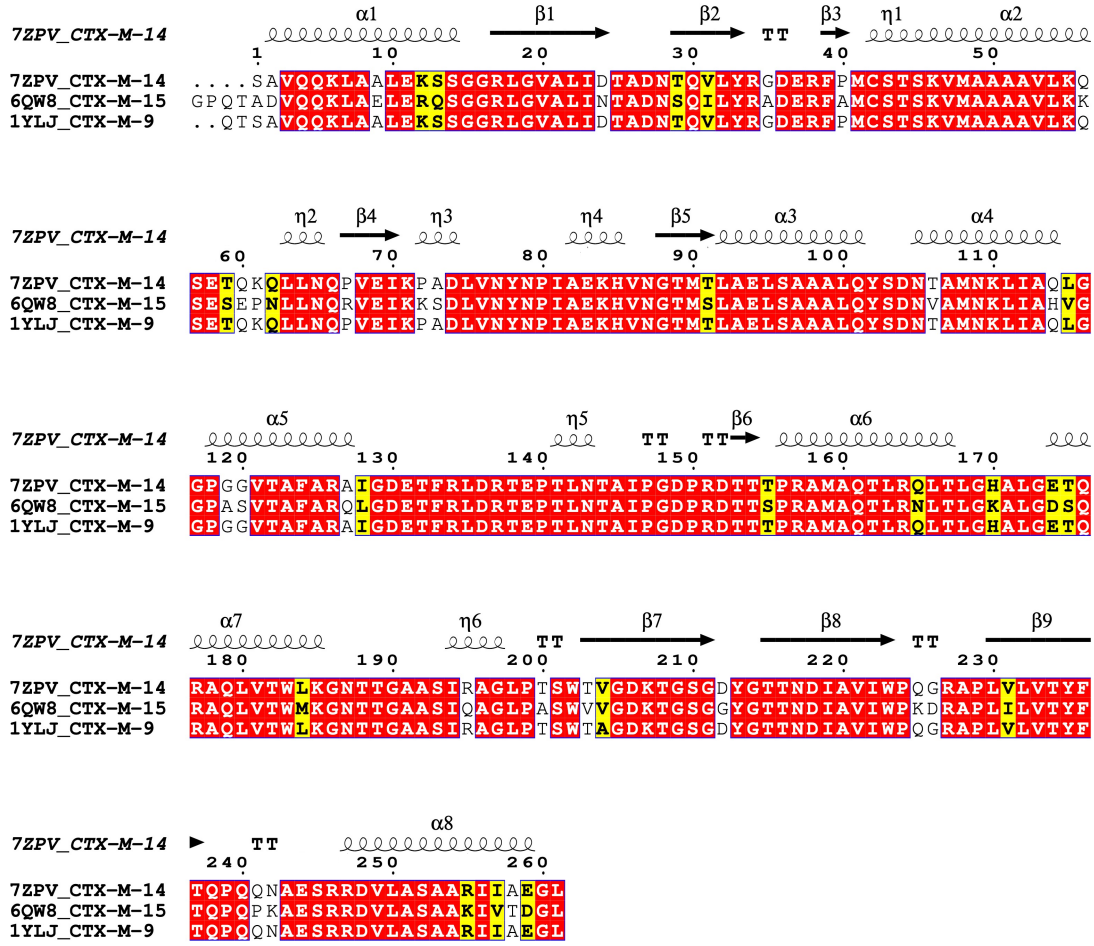

Percent Identity Matrix - created by Clustal2.1 #

1: 7ZPV_CTX-M-14	100.00	82.76	99.62
2: 6QW8_CTX-M-15	82.76	100.00	82.51
3: 1YLJ_CTX-M-9	99.62	82.51	100.00

Figure S5: Multiple sequence alignment of CTX-M-14 with related β-lactamases CTX-M-15 and CTX-M-9. Multiple sequence alignment was performed using Clustal Omega (Madeira et al., 2022) and the graphical representation was generated using ESPript 3.0 (Robert & Gouet, 2014). Identical amino acid residues are highlighted with a red background and similar amino acid residues with a yellow background. Secondary structure of CTX-M-14 7zpv is displayed with α-helices (spirals, α), 3_{10} helices (spirals, η), β-strands (arrows, β) and turns (TT). The corresponding percent identity matrix reveals an identity of 82.76 % for CTX-M-15 and 99.62 % for CTX-M-9 compared to CTX-M-14.

A2. Chemicals and Hazards

A2.1. Chemicals

Compound	CAS-No.	Supplier	GHS hazard	Hazard Statements	Precautionary Statements
Acetic acid	64-19-7	Chem-solute	GHS02 GHS05	H226, H314	P280, P305+351+338, P310
Acrylamide 30 %	79-06-1	Carl Roth	GHS06 GHS08	H301, H312, H315, H317, H319, H332, H340, H350, H361f, H372	P201, P280, P301+310, P305+351+338, P308+313
N,N'-Methylen-bis-acrylamide	110-26-9	Carl Roth	GHS06 GHS08	H301, H340	P202, P264, P270, P280, P301+310, P405
Agar	9002-18-0	Carl Roth	-	-	-
Agarose	9012-36-6	Lonza	-	-	-
Ampicillin sodium salt	69-52-3	Sigma	GHS08	H334, H317	P280, P261, P302+352, P342+311
Ammonium persulfate (APS)	7727-54-0	Carl Roth	GHS03 GHS07 GHS08	H272, H302, H315, H317, H319, H334, H335	P280, P305+351+338, P302+352, P304+341, P342+311
Avibactam sodium salt	1192491-61-4	Hycultec	GHS08	H317, H334	P261, P272, P280, P285, P302+352, P304+340, P333+313, P342+311, P362+364
Boric acid	10043-35-3	Sigma	GHS08	H360FD	P201, P280, P308+313
Bortezomib	179324-69-7	Merck	GHS06 GHS08	H330, H372, H301+311	P280, P302+352, P304+340, P310

Compound	CAS-No.	Supplier	GHS hazard	Hazard Statements	Precautionary Statements
Bromphenol blue	115-39-9	Applichem	-	-	-
BSA	9048-46-8	Serva	-	-	-
Calcium chloride	10043-52-4	Merck	GHS07	H319	P305+351+338
Cefalotin sodium salt	58-71-9	Sigma	GHS08	H317, H334	P261, P280, P342+311
Cefdinir	91832-40-5	Sigma	-	-	-
Cefepime hydrochloride	123171-59-5	Sigma	-	-	-
Cefotaxime sodium	64485-93-4	Hycultec	GHS08	H317 H334	P261, P280, P342+P311
Ceftazidime	72558-82-8	Hycultec	GHS08	H317 H334	P261, P272, P280, P284, P302+352, P333+313
Ceftriaxone sodium salt	74578-69-1	Hycultec	GHS07 GHS08	H315, H317, H319, H334, H335	P260, P264, P280, P305+351+338
Cefuroxime sodium salt	56238-63-2	Sigma	GHS07	H317	P261, P272, P280, P302+352, P333+313, P362+364
Chloramphenicol	56-75-7	Sigma	-	-	-
Citric acid	77-92-9	Sigma	GHS05	H318	P305+351+338, P311
Coomassie Brilliant Blue R250	6104-59-2	Serva	-	-	-
DTT	3483-12-3	Applichem	GHS07	H302, H315, H319, H335	P302+352, P305+351+338
EDTA	60-00-4	Sigma	GHS07	H319	P305+351+338
Ethanol	64-17-5	Carl Roth	GHS02	H225	P210
Glycerol	56-81-5	Sigma	-	-	-
Hydrochloric acid >25 %	7647-01-0	Merck	GHS05 GHS07	H314, H335	P261, P280, P310, P305+351+338
Imidazole	288-32-4	Carl Roth	GHS05 GHS06 GHS08	H301, H314, H361	P260, P281, P303+361+353, P301+330+3 31, P305+351+3 38, P308+313
IPTG	367-93-1	Thermo Fisher	-	-	-

Compound	CAS-No.	Supplier	GHS hazard	Hazard Statements	Precautionary Statements
Isopropanol	67-63-0	Carl Roth	GHS02 GHS07	H225, H319, H336.	P210, P233, P305+351+338
Ixazomib	1072833-77-2	AmBeed	GHS07	H302, H315, H319, H335	P261, P305+351+338
KCl	7447-40-7	Carl Roth	-	-	-
Lithium Dodecyl Sulfate	2044-56-6	Thermo Fisher	GHS07	H315 H319	P264 P280 P302+352 P337+313 P362+364 P332+313
Lithium sulfate	10102-25-7	Merck	GHS07	H302	-
Magnesium chloride	7786-30-3	Carl Roth	-	-	-
2-Mercaptoethanol	60-24-2	Carl Roth	GHS06 GHS09	H302, H411, H315, H335, H311, H319	P280, P312, P302+350, P261, P273, P301+312, P305+351+338
MES	4432-31-9	Sigma	GHS07	H315, H319, H336	P261, P305+351+339
Methanol	67-56-1	Carl Roth	GHS02 GHS06 GHS08	H225, H301 H311 H331	P210, P270, P280, P303+361+353, P304+340, P308+311
NuPage MES SDS running buffer (20x)	-	Thermo Scientific	-	H316	P302+350
NuPage LDS sample buffer (4x)	-	Thermo Scientific	-	H316	P332+313
RedSafe	-	Intron	-	-	-
Relebactam	1174018-99-5	MedChem Express	GHS07 GHS09	H302, H410	P264, P270, P273 P301+312, P330, P391, P501
Sodium acetate	127-09-3	Applichem	-	-	-
Sodium chloride	7647-14-5	Carl Roth	-	-	-
Sodium dihydrogen phosphate	10049-21-5	Applichem	-	-	-
Sodium phosphate dibasic	7558-79-4	Sigma	-	-	-

Compound	CAS-No.	Supplier	GHS hazard	Hazard Statements	Precautionary Statements
Sodium hydroxide	1310-73-2	Merck	GHS05	H314	P280, P310, P305+351+338
Ni(II)SO4	10101-97-0	Applichem	GHS07 GHS08 GHS09	H302+332, H315, H317, H334, H341, H350i, H360d, H372 H410	P201, P261, P273, P280, P284, P304+340+312
PEG 8000	25322-68-3	Sigma	-	-	-
Penicillin G sodium salt	69-57-8	Sigma	GHS07	H317	P261, P272, P280, P302+352, P333+313, P362+364
Piperacillin sodium salt	59703-84-3	Sigma	-	-	-
PMSF	329-98-6	Applichem	GHS06 GHS05	H301, H314	P280, P305+351+338, P310
Relebactam	1174018-99-5	Hycultec	-	-	-
SDS	151-21-3	Sigma	GHS02 GHS06	H228, H302, H311, H315, H319, H335	P210, P261, P280, P312, P305+351+338
Sodium borate	1303-96-4	Sigma	GHS08	H360FD	P201, P308+313
Sodium citrate	6132-04-3	Sigma	-	-	-
Tazobactam	89786-04-9	Hycultec	-	-	-
TEMED	110-18-9	Merck	GHS02 GHS05 GHS07	H225, H302, H314, H332	P261, P280, P305+351+338
Tris	1185-53-1	Fluka	GHS07	H315, H319, H335	P261, P305+351+338

A2.2. GHS and Risk Symbols

Figure Appendix 1: GHS pictograms

(https://unece.org/transportdangerous-goods/ghs-pictograms)

A2.3. GHS Hazard Statements.

H225	Highly flammable liquid and vapor
H226	Flammable liquid and vapor
H228	Flammable solid
H272	May intensify fire; oxidizer
H290	May be corrosive to metals
H301	Toxic if swallowed
H302	Harmful if swallowed
H303	May be harmful if swallowed
H311	Toxic in contact with skin
H312	Harmful in contact with skin
H313	May be harmful in contact with skin
H314	Causes severe skin burns and eye damage
H315	Causes skin irritation
H316	Causes mild skin irritation
H317	May cause an allergic skin reaction
H318	Causes serious eye damage
H319	Causes serious eye irritation
H330	Fatal if inhaled
H331	Toxic if inhaled
H332	Harmful if inhaled
H333	May be harmful if inhaled
H334	May cause allergy or asthma symptoms or breathing difficulties if inhaled
H335	May cause respiratory irritation
H336	May cause drowsiness or dizziness
H340	May cause genetic defects
H341	Suspected of causing genetic defects
H350	May cause cancer
H350i	May cause cancer by inhalation
H360	May damage fertility or the unborn child
H360D	May damage the unborn child
H360F	May damage fertility
H360Fd	May damage fertility. Suspected of damaging the unborn child

H360FD	May damage fertility. May damage the unborn child
H361	Suspected of damaging fertility or the unborn child
H361d	Suspected of damaging the unborn child.
H361f	Suspected of damaging fertility
H370	Cause damage to organs
H372	Causes damage to organs through prolonged or repeated exposure
H373	May cause damage to organs through prolonged or repeated exposure.
H400	Very toxic to aquatic life with long-lasting effects
H410	Very toxic to aquatic life with long lasting effects
H411	Toxic to aquatic life with long lasting effects
H412	Harmful to aquatic life with long lasting effects.

A2.4. GHS Precautionary Statements.

P101	If medical advice is needed, have product container or label at hand
P201	Obtain special instructions before use
P210	Keep away from heat/sparks/open flames/hot surfaces. No smoking
P233	Keep container tightly closed
P260	Do not breathe dust/fume/gas/mist/vapors/spray
P261	Avoid breathing dust/fume/gas/mist/vapors/spray
P264	Wash thoroughly after handling
P270	Do not eat, drink or smoke when using this product
P272	Contaminated work clothing should not be allowed out of the workplace.
P273	Avoid release to the environment
P281	Use personal protective equipment as required
P280	Wear protective gloves/protective clothing/eye protection/face protection
P284	Wear respiratory protection
P301+P310	IF SWALLOWED: Immediately call a POISON CENTER or doctor/physician
P301+P312	IF SWALLOWED: Call a POISON CENTER or doctor/physician if you feel unwell
P301+P330+P331	IF SWALLOWED: Rinse mouth. Do NOT induce vomiting
P302+P352	IF ON SKIN: Wash with soap and water
P303+P361+P353	IF ON SKIN (or hair): Remove/Take off immediately all contaminated clothing. Rinse skin with water/shower
P304+P341	IF INHALED: lf breathing is difficult, remove victim to fresh air and keep at rest in a position comfortable for breathing
P305+P351+P338	IF IN EYES: Rinse cautiously with water for several minutes. Remove contact lenses if present and easy to do - continue rinsing
P308+P313	IF exposed or concerned: Get medical advice/attention
P309	IF exposed or you feel unwell
P309+P311	IF exposed or you feel unwell: Call a POISON CENTER or doctor/physician
P310	Immediately call a POISON CENTER or doctor/physician
P311	Call a POISON CENTER or doctor/physician

P312	Call a POISON CENTER or doctor/physician if you feel unwell
P321	Specific treatment (see respective MSDS)
P330	Rinse mouth
P332+P313	lf skin irritation occurs: Get medical advice/attention
P333+P313	If skin irritation or rash occurs: Get medical advice/attention
P337+P313	If eye irritation persists: Get medical advice/attention.
P342+P311	Call a POISON CENTER or doctor/physician
P362+P364	Take off contaminated clothing and wash before reuse
P370+P378	In case of fire: Use for extinction: Alcohol resistant foam.
P370+P378	In case of fire: Use for extinction: Fire-extinguishing powder.
P370+P378	In case of fire: Use for extinction: Carbon dioxide.
P391	Collect spillage.
P405	Store locked up
P501	Dispose of contents/container in accordance with local/regional/national/international regulations

A3. List of figures

A4. List of supplementary figures

A5. List of tables

Acknowledgements

I would like to sincerely thank my supervisor Prof. Dr. Holger Rohde for the opportunity to work in his research group at the Institute of Medical Microbiology, Virology and Hygiene at the University Medical Center Hamburg-Eppendorf (UKE) and pursue a PhD on such an exciting topic at the University of Hamburg (UHH). I would like to sincerely thank him for the excellent supervision at all times and the guidance for independent scientific work as well as the confidence in my abilities.

Likewise, I would like to thank Prof. Dr. Dr. Christian Betzel for the excellent co-supervision, the support throughout the project and the opportunity to use the laboratories and expertise of his research group. Such interdisciplinary work, combining microbiology, biochemistry and structural biology would not have been possible without this supportive supervision.

In this context, I would like to thank both my supervisors for preparing the dissertation reports. Of course, I would also like to thank Prof. Dr. Ralph Holl and Dr. Thomas Hackl for their commitment to the defense committee of the disputation.

I would also like to thank PD Dr. Markus Perbandt for teaching me all the crystallographic methods from crystallization to PDB deposition, and for helping me with the project planning, as well as for all the inspiration and support that helped my work progress.

I would like to thank Dr. Nadine Werner for the great preliminary work on this project and for all the support in the initial phase. Another thank you is due to the whole research group of Prof. Christian Betzel who always welcomed me very kindly and always supported me.

All the measurements with the TapeDrive would not have been possible without the support of Dr. Dominik Oberthuer, his colleagues and the P11 beamline staff (DESY). In particular, I would like to thank Marina Galchenkova for her support with the processing of all the TapeDrive serial crystallography data and Kara Zielinski and Alessandra Henkel for their support during beamtimes.

Furthermore, I would like to thank Dr. Eike Schulz for the opportunity to use additional time-resolved crystallography methods, for the support and the strong interest towards solving the enzymatic mechanism. I am also grateful to be able to continue working on this exciting

project in his group. In addition, thanks are also due to Prof. Dr. Arwen Pearson, Dr. Pedram Mehrabi, and Dr. David von Stetten for their support at T-REXX beamtimes.

I would like to thank Prof. em. Dr. Winfried Hinrichs for the many helpful conversations and support in manuscript writing.

A big thank you also to Dr. Henning Büttner, who introduced me very well to the protein methods of the research group and quickly left me in charge of many tasks.

I would also like to thank Prof. Dr. Martin Aepfelbacher for giving me the opportunity to work at the Institute of Medical Microbiology, Virology and Hygiene. He also founded the Infectophysics consortium, which facilitated scientific exchange with researchers in complementary fields to support our research. In this context, I would also like to thank the Joachim-Herz-Foundation for its financial support.

Weiterhin möchte ich mich bei allen Mitarbeitern der AG Rohde und des gesamten Instituts für Medizinische Mikrobiologie, Virologie und Hygiene für die großartige Atmosphäre, die Hilfsbereitschaft und die Unterstützung aber vor allem auch für die vielen außeruniversitären Aktivitäten bedanken. Ich hatte immer eine fantastische Zeit mit euch. An dieser Stelle möchte ich mich herzlich bei Samira, meiner Labor-Platz-Nachbarin und Mitstreiterin und Paul, meinem Boulder-Schrauber-Fahrrad-Partner, für die unfassbar schöne Zeit und die vielen lustigen und unvergesslichen Momente im Labor und in der Freizeit bedanken. Ich möchte mich ebenfalls bei Vero bedanken, sowohl für ihre Hilfsbereitschaft als auch für die unterhaltsamen Momente an der ÄKTA. Mit diesen Kollegen ist die Arbeit direkt viel schöner!

Besonderer Dank gilt meinen Eltern Olga und Alexander, meiner Schwester Elisabeth und meinen Freunden für ihr Interesse an meiner Arbeit und die großartige Unterstützung in allen Lebenslagen. Ganz besonders möchte ich mich bei Emily bedanken. Wenn ich mit dir zusammen bin, ist alles andere vergessen. Die Ruhe und Kraft, die du mir gibst, ist einfach wunderschön.

Eidesstattliche Erklärung

„Hiermit erkläre ich an Eides statt, dass ich die vorliegende Dissertationsschrift selbst verfasst und keine anderen als die angegebenen Quellen und Hilfsmittel benutzt habe. Ich versichere, dass das gebundene Exemplar der Dissertation und das in elektronischer Form eingereichte Dissertationsexemplar (über den Docata-Upload) und das bei der Fakultät (Promotionsbüro Chemie) zur Archivierung eingereichte gedruckte gebundene Exemplar der Dissertationsschrift identisch sind. Ich versichere, dass diese Dissertation nicht in einem früheren Promotionsverfahren eingereicht wurde."

Hamburg, 11.08.2023

Andreas Prester